DEVELOPMENT OF A FINITE ELEMENT MODELLING SYSTEM FOR PIEZOCOMPOSITE TRANSDUCERS

JEREMY T. BENNETT

Submitted in July 1995

for the degree of

Doctor of Philosophy

Ultrasonics Research Group,

Department of Electronic and Electrical Engineering,

The University of Strathclyde,

204 George Street, Glasgow G1 1XW,

Scotland, United Kingdom

List of Contents

Appendices

ACKNOWLEDGEMENTS

I would like to thank my supervisor, Professor Gordon Hayward, founder of the Ultrasonics Research Group at the University of Strathclyde, for his direction, support and enthusiasm during my three years of doctorate studies. My thanks also go to the members of the Ultrasonics Research Group for their comments on the finite element modelling and provision of experimental results. However, special mention must go to the following:

- Tony Gachagan, Robin Hamilton, Dave Hall and Dave Powell for using the finite element modelling in their own projects and publishing their results.
- John Hossack for issuing the challenge to do the work and develop the system.
- Greg Wojcik and Dave Vaughan for helping me to organise the PZ-Flex package into the system at the final hour.
- Wally Smith and Bob Ting for supplying experimental results for the 1-3 piezocomposite hydrophones.
- My father and my father-in-law for their comments on the writing of an engineering degree Thesis.

Of all the people involved with my work, my greatest thanks and appreciation goes to the lady who became my wife during the study period, Susanna, and hope that the completion of this Thesis will give her courage and determination to complete her own studies in the near future.

ABSTRACT

1-3 piezocomposites comprising of stiff piezoelectric ceramic rods embedded in a soft polymer matrix have considerable potential as the active component in ultrasonic systems for applications in such diverse fields as bio-medicine, SONAR and non-destructive testing. This is because of the ability to tailor the properties via adjustment of the ceramic pillar shape, size, type and distribution and by selection of the passive phase properties. This complex microstructure and its significant influence on resultant device performance has led to a requirement for sophisticated analytical tools to facilitate cost-effective optimisation at the design stage. This Thesis describes the use of finite element analysis to investigate the behaviour of 1-3 composites for different applications. Firstly, the influence of constituent material properties on the behaviour of thickness mode drive was studied via a combination of modal and harmonic analysis. This led to the creation of straightforward design rules relating to ceramic type, shape and distribution, in addition to the desired properties of the passive filler phase. The Thesis then describes the influence of mechanical loading and method of construction on composite transducer performance, over the complete range of volume fractions. Front face matching, fluid loading and mechanical damping via a backing block are considered and analysed with respect to composite transducer performance. This is extended using static analysis to include the behaviour of hydrostatic devices and the effect of adding stiffening plates. The theory is then augmented to encompass monolithic and diced imaging arrays. The influence of composite geometry, element dimensions and transducer separation is discussed with respect to sensitivity, cross-coupling and beam profile.

Throughout the Thesis, the analytical work is supported by experimental evidence. This involved the manufacture of a comprehensive range of devices, followed by experimental studies on performance. Impedance analysis, transmission/reception sensitivities, surface displacement profiles and beam characteristics were all evaluated and the results compared with theoretical predictions. It is considered that the work described within the Thesis makes a valuable and original contribution to the field of 1-3 connectivity composite transducers. It should constitute a basis for on-going theoretical work to improve further the performance of the devices.

MAIN FINDINGS OF THE WORK

The principal new findings of the work were:

- A set of finite element models for 1-3 piezocomposite transducers including the backing block, matching layer and fluid loading under operational conditions were developed. These were used to generate a set of design guidelines for 1-3 piezocomposite transducers.

- The main design guidelines were:
  - To obtain an undistorted thickness mode oscillation from a piezocomposite transducer, the aspect ratio of the material must be less than the "*Maximum Pillar Aspect Ratio*" (MPAR). Tables for the MPAR of different PZT-5A piezocomposites are given in Chapter 4.
  - The volume fraction for devices to be used as transmitters should be greater than or equal to 30%. The volume fraction for receivers should be between 20% and 70%. Considering the combined transmit/receive levels, the volume fraction for transceivers should be between 30% and 70%. If large bandwidth is important, the transceiver volume fraction should not be greater than 40%.
  - Low volume (<10%) fraction composites of PZT-5H make good hydrophones but the performance can be enhanced by the addition of cover plates. The aspect ratio of the ceramic pillars should be minimised and the polymer phase should be compliant and possess the minimum Poisson ratio.
  - The number of pillars under the electrode for an array element should be at least 4x4 pillars to obtain good sensitivity and sufficient dilation quality.

- For a piezocomposite with a high loss polymer, the material does not act as a homogeneous medium but as a set of ceramic pillars in a dense medium. However, the effect of the high damping is reduced by the addition of a backing block and a matching layer.

LIST OF SYMBOLS

Symbol	Description	Units
^	Denotes complex value	
–	Denotes homogenous value	
α	Normalised frequency	
β	Amplification co-efficient of thickness stress over transient hydrostatic pressure	
β_{ij}^{S}	Impermittivity measured under conditions of constant strain for a material	$m.F^{-1}$
Γ	Reflection co-efficient for a boundary between two materials	
γ	Ratio of widths of sections A and B of the unit cell for Haun-Newnham model	
ε_{ij}^{S}	Permittivity measured under conditions of constant strain for a material	$F.m^{-1}$
ζ_{nmat}	Damping co-efficient for a material	dB
θ	Angle for acoustic ray from the acoustic axis	
θ_Z	Phase angle between voltage and current of a transducer	
λ	Wavelength	m
v	Speed of propagation for a wave	$m.s^{-1}$
v_l	Speed of propagation for the longitudinal wave	$m.s^{-1}$
ρ	Density of a material	$Kg.m^{-3}$
ρ_R	Resistivity of a material	$\Omega.m^{-1}$
σ	Poisson ratio of a material	
υ	Ceramic volume fraction of the piezocomposite material	
ϕ	Turns ratio for ideal transformers in constrained-dimensional models	
χ	Amplification co-efficient for 1-3-1 connectivity composite configuration	
ω	Radial frequency of operation	Hz
A_{exp}	Surface area of a experimental transducer	m^2

A_t	Surface area of the transducer in a finite element model	m^2
C_0	Static capacitance of a transducer	F
c	Longitudinal speed of sound for a material	$m.s^{-1}$
c_{ij}^{D}	Elastic stiffness tensor measured under conditions of constant charge density of a material	Pa
c_{ij}^{E}	Elastic stiffness tensor measured under conditions of constant electric field of a material	Pa
D_i	Electric charge density in the *i* direction	$C.m^{-3}$
d_{ij}	Piezoelectric strain (charge) constant	$m.V^{-1}$
d_h	Hydrostatic piezoelectric strain (charge) constant	$m.V^{-1}$
E_i	Electric field vector in the *i* direction	$V.m^{-1}$
e_{ij}	Piezoelectric constant	
FX	Force applied or generated at the node in the *1* direction	N
FY	Force applied or generated at a node in the *2* direction	N
FZ	Force applied or generated at a node in the *3* direction	N
f	Frequency of operation	Hz
f_{elec}	Electrical resonance frequency	Hz
f_{mech}	Mechanical resonance frequency	Hz
$G(\omega)$	Conductance of a transducer with frequency	Ω^{-1}
g_{ij}	Piezoelectric voltage constant for a material	$V.(m.Pa)^{-1}$
g_h	Hydrostatic piezoelectric voltage constant for a material	$V.(m.Pa)^{-1}$
h_{ij}	Piezoelectric constant for a material	
$J(\omega)$	Reciprocity parameter with frequency	
k	Wavenumber for a material at a specific frequency	m^{-1}
k_t	Thickness mode electromechanical coupling co-efficient	
P	Power	W
ΔP	Transient hydrostatic pressure	Pa
p	Pressure at a node	Pa
Q	Charge produced at a node	C
Q_m	Mechanical quality factor	
S_{RX}	Receive sensitivity of a transducer	$V.Pa^{-1}$

S_{TX}	Transmit sensitivity of a transducer	$Pa.V^{-1}$
S_i	Strain in the *i* direction	
T_i	Stress in the *i* direction	Pa
T_3	Thickness stress	Pa
t	Time	s
t_3	Height of the active material	m
UX	Displacement of a node in the *1* direction	m
UY	Displacement of a node in the *2* direction	m
UZ	Displacement of a node in the *3* direction	m
V	Voltage at a node	V
Z	Specific acoustic impedance of a material	Rayls
Z_C	Specific acoustic impedance of the piezoelectric material	Rayls
z	Distance along the thickness direction	m

CHAPTER ONE

OVERVIEW OF WORK

CHAPTER OBJECTIVE

The objective of this Chapter is to define the mission and the goals of the work covered in this thesis. Ultrasound has been used in many applications in different fields and in most applications, transducers using piezoelectric materials are used to generate and detect the ultrasound. As more complex piezoelectric materials are being developed, the design of the transducers becomes a non-trivial task and modelling of the devices is necessary. In the past, constrained dimensional models have been used but these neglect many parameters of the design process. With the specifications for the transducers being pushed to the limits, these omitted parameters are becoming important and a more general modelling technique is required which incorporates all the necessary features. This thesis proposes the use of finite element modelling with emphasis on 1-3 connectivity composite materials. Contributions to the field of ultrasonic transducer design are also detailed in this Chapter.

1.1 MISSION STATEMENT

The objective of this thesis is to develop an operating system to tailor a general-purpose finite element (FE) package to the specific task of finite element modelling (FEM) of 1-3 piezocomposite transducers under different operating conditions. This includes the development and verification of the system around the general-purpose FE package, ANSYS [1], for the generation, solution and analysis of 1-3 piezocomposites models. The forms of analysis are to be: *modal* to determine the operating frequencies of the device; and *dynamic* incorporating loss to determine the operating characteristics of the device. Any limitations in the ANSYS package are to be identified and suggestions for overcoming these limitations are to be presented. Finally, the system is to be applied to the two application areas: hydrophone and array transducer design. Both are areas where classical constrained-dimensional modelling has been found to be inadequate.

1.2 POSITIONING OF WORK IN THE FIELD

Ultrasound has found widespread application in many fields including bio-medicine, sound navigation and ranging (SONAR) and non-destructive testing (NDT) [2]. In such applications, transducers use piezoelectric materials as the source of energy conversion between the electrical energy on the "dry side" and pressure energy on the "wet side". The transmitter when excited by an electrical stimulus, generates pressure or acoustic waves in the surrounding medium through a vibrating surface. These waves propagate through the medium and are refracted or reflected by any inhomogenieties. The energy contained within these waves can be evaluated at any point by inserting a receiver transducer and measuring the electrical energy generated from the transducer. For *pulse-echo* operation, a single transducer fulfils both roles and hence, is designed as a compromise between the two requirements. For *pitch-catch* operation, separate transducers fulfil the separate roles and hence, are designed to be optimal for the specific role.

Three types of piezoelectric materials are generally used for ultrasonic transducers [3]:

- Piezoelectric ceramics which are very efficient for the energy conversion but have a large acoustic mis-match with low-impedance media such as water and air.
- Piezoelectric polymers which are significantly less efficient but have a close acoustic match to water.
- Piezoelectric composites of ceramic and polymer which were developed as a compromise between the above two types. A well-designed composite will combine the best properties from the previous two types.

The work in this thesis will concentrate on acoustic operation into low-impedance media where the piezocomposite material is used as the active material. A more complete description of each material type is given in Chapter 2. As there are two materials included in the composite, an extra set of parameters are needed to specify the microstructure of the material:

- *Connectivity* which describes the number of dimensions through which each phase is connected. The most popular form is 1-3 connectivity which consists of ceramic pillars embedded in a polymer matrix as shown in Figure 1.1.
- *Volume Fraction* which is the ratio of the ceramic volume to that of the total composite.
- *Ceramic Pillar Shape.*
- *Pillar Aspect Ratio* which is the ratio of the width of the ceramic pillar to its height.

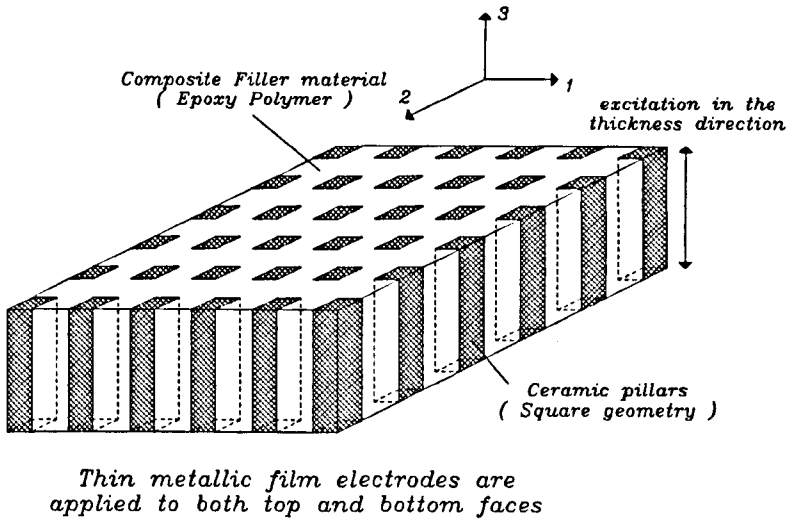

Figure 1.1: 1-3 Connectivity Ceramic/Polymer Composite

The behaviour of the transducer does not only depend on the behaviour of the piezoelectric material but also on ancillary components that can be used to modify the behaviour according to what is desired. As there are several components included in the transducer structure, modelling of the device under operating conditions is used extensively. However, simulation of transducer behaviour is not a trivial matter and is normally performed with the aid of a single or set of modelling techniques with which the designer can evaluate the prototype design without physically constructing the device. This makes the design process more streamlined and cost-effective [4]. It also allows transducers using innovative mechanisms to be tested in a quick and efficient manner. A good modelling technique will also allow the designer to examine the behaviour of the microstructure of the components in the transducer and not only of the whole device.

At present, most piezoelectric transducer modelling is done using constrained-dimensional models where the set of variables in the model has been reduced to a subset of variables of interest to the designer through the application of assumptions to the linear constitutive equations of piezoelectricity. Chapter 2 deals with these models in some depth including the Mason and KLM model. The derived models tend to be simple to implement and operate. The direct output of the modelling can

be interpreted readily by the operator but all the assumptions must be met for the modelling to be valid. This has led to the use of finite element analysis which does not have such restrictive assumptions but requires significantly more processing for solving the model and extracting the desired parameters from the model behaviour.

In the finite element analysis process, the device being simulated is partitioned into a series of elements of finite size where each element consists of a single material and has a single set of associated material properties. The equations that describe the behaviour of the element, can be derived prior to the analysis and can be incorporated into the modelling package. The equations for each of the elements are combined into a single system-wide matrix equation which can be solved using a standard matrix solution technique. From the solution, the behaviour of each element can be determined and from this, the behaviour of the whole device is derived. Finite element modelling has been applied to piezoelectricity for over a decade [5] and the theory has been well established. However, other aspects of the modelling of piezoelectric transducers such as fluid loading and the loss mechanisms within the transducer structure have not been finalised and are under current development. Several researchers have developed specialised FE codes for the design of piezoelectric transducers. These include the work performed for Siemens by Lerch [6] and the French package ATILA [7]. However, commercially available general-purpose FE packages such as ANSYS [1] have the necessary features to model transducers and are replacing individually-generated specialised codes as the packages in general use.

Any modelling process can be divided into three tasks:

- *Pre-processing* - where the model and its input parameters are defined. A set of equations describing the model and the boundary conditions can be generated at the end of the stage.
- *Model solution* - where the set of equations from the previous task is solved for the set of unknowns.

- *Post-processing* - where the data generated in the previous task is manipulated into the information required by the designer.

While the second task normally requires minimal interaction with the operator, the other two tasks are specific to the modelling application and require extensive interaction and effort for each individual configuration. The driving concept behind the work presented in this thesis was to developed an operating system around a general-purpose FE package to aid in the operation of the pre- and post-processing tasks. This would give the finite element technique the simplicity of the constrained-dimensional model but without the constraining assumptions.

1.3 REQUIREMENTS FOR THE MODELLING PACKAGE

For this work to be successful, the FE package must have several necessary features to model the piezoelectric transducers under operating conditions. These are:

- Piezoelectric material elements;
- Purely mechanical elements incorporating a fairly comprehensive loss mechanism;
- Fluid loading; and
- The ability to define electrical and mechanical boundary conditions.

These are covered in Chapter 3. This Chapter also covers the definition of the models for the pre-processing task and the possible integrated quantities that could be required by the operator. These integrated quantities are scalar values which describe the performance of the transducer and include:

- Coupling factor which is a measure of the energy conversion efficiency;
- Surface dilation quality which is a measure of the piston-like nature of the movement of the transducer front face.
- Transmit sensitivity and its associated bandwidth; and

- Receive sensitivity and its associated bandwidth.

While these values do not describe the behaviour of the microstructure of the transducer, the operator can investigate the behaviour of each individual element of the model for this information. However, such a process is too time-consuming to evaluate the influence of varying a large set of input parameters on the overall behaviour of the device.

An evaluation for 1-3 piezocomposite transducers and the effect of the design parameters on the transducer is detailed in Chapter 4. The major component of this work examines the influence of the microstructure on the performance of the device. This includes the influence of passive components of the finite element model which are:

- The matching layer which is used to match the acoustic impedance of the active material to that of the surrounding medium;
- The backing block which is used to reduce energy reverberations within the active material; and
- The loading of the surrounding fluid - this is also required to generate the pressure that is present in the fluid medium.

1.4 APPLICATIONS FOR THE FINITE ELEMENT MODELLING SYSTEM

The operating system can be applied to specific applications where constrained-dimensional modelling had been found to be inadequate for complete design. Chapter 5 covers the design of 1-3 piezocomposite hydrophones for operation below the thickness mode frequencies. The FE model was compared to experimental results and to the two different constrained-dimensional models and showed good correlation. A material selection process was undertaken using the FE model to determine the desired properties of each phase. The methods of further enhancing the performance

of the hydrophones were considered and the effect of electrical loading for low volume fraction piezocomposite on the performance figures was investigated.

Chapter 6 covers the design of 1-3 piezocomposite array transducers. 1-3 piezocomposite have an intrinsic advantage for array design over monolithic ceramic arrays in that the mechanical loss in the polymer matrix is significantly higher than in the ceramic. This implies that the shear wave propagation in the active material causing element cross-coupling is dramatically reduced in relation to the equivalent monolithic ceramic. It was found that the present version of the ANSYS package was inadequate for modelling the arrays because the fluid loading and the loss mechanism in the polymer had not been completely developed.

To overcome this problem, another FE package called PZ-Flex was incorporated into the operating system. This originally had been developed as a general-purpose wave propagation modelling package under the name of FLEX [8]. As each wave propagation problem has specific requirements, the package was modified accordingly for the modelling of ultrasonic transducer. Hence, PZ-Flex is a hybrid between general-purpose codes like ANSYS [1] and specialised codes such as ATILA [7]. Additional features of the package over that of ANSYS include a set of boundary conditions to allow modelling of the surrounding fluid, an advanced loss mechanism model for the polymer phase and the ability to model electrical components such as co-axial cables.

1.5 CONTRIBUTIONS TO THE FIELD OF TRANSDUCER DESIGN

The contributions made by this work are in the application of finite element modelling to the design of 1-3 piezocomposite transducers. However, much of the theory developed for the FE model can be applied to the design of other types of ultrasonic transducer as long as the FE package can model the different individual components required for such a model. Specifically, the contributions are:

- A model of the unit cell for 1-3 piezocomposite material was developed where the geometry is defined by parameters understood by the transducer designer.
- This model was modified to allow harmonic analysis of the unit cell with the incorporation of mechanical loss in the structure. From this, the behaviour of the device could be estimated over a wide band of frequencies.
- The ancillary components of the transducer, the matching layer, surrounding fluid and backing block were included in the finite element model and the model was verified against experiment where possible. This allowed the complete transducer to be modelled.
- A set of integrated output parameters were derived to allow rapid evaluation of the performance of the transducer under operating conditions and different designs.
- Different resonance modes within the 1-3 piezocomposites were investigated and compared to determine the desirable operating characteristics for a 1-3 piezocomposite transducer.
- The concept of maximum pillar aspect ratio was introduced and criteria for determining the values for different configurations were developed.
- The effect of the different ancillary components on the behaviour of the transducer was investigated. This allowed a set of design guidelines to be developed. From this, a 1-3 piezocomposite may be designed to meet a given specification.
- A FE hydrostatic model for 1-3 piezocomposites was developed. This allowed

the inclusion of stiffening plates into the model so that the performance could be compared to 1-3-1 piezocomposite hydrophones.

- The influence of different ceramics and polymer materials on the performance of the hydrophones was investigated to determined the desirable properties of each phase.
- The effect of electrical loading on the hydrostatic voltage response was considered and an equation allowing the simulated value to be modified was derived.
- A FE model for piezocomposite array transducers was developed which could model different numbers of pillars under the electrode and different numbers of pillars between the elements.
- An algorithm for the calculation of the beam profile of an transducer array element was derived and the assumptions for the algorithm were included in the definition of the model. This has since been incorporated in the next revision of the PZ-Flex code by the developers.
- An investigation into the influence of the number of pillars under the electrode on different performance criteria for the behaviour of a transducer element was performed. This allowed the development of a set of design guidelines.
- The properties of different piezoceramics and other materials used in the transducer designs were collected and collated. The different properties were checked for consistency.

The vast majority of the contributions have been of a theoretical nature and no design for specific applications have been made in the course of the study. This was because the work dealt with the development of a set of innovative theoretical models. These can be considered as state of the art as evidenced by the publications listed in Section 1.5.1. For example, three papers detailing investigations using the FEM were accepted for presentation at the refereed 1994 IEEE Ultrasonic International Symposium, the premier conference in the field of study.

1.5.1 References Published from the Thesis

A. D.D.N.Hall, J.T.Bennett and G.Hayward, "The Design and Evaluation of Ultrasonic Arrays using 1-3 Connectivity Composites", *SPIE ISP*, 1992, Vol 1733, Ch 29, pp 216-227.

B. J.Bennett, R.Hamilton and G.Hayward, "Finite Element Modelling on 1-3 Piezocomposite for Underwater Applications", *Proc. IEEE Ultrasonic Symposium*, Baltimore, MD, USA, 1993, pp 1113-1117

C. G.Hayward and J.Bennett, "Assessing the Influence of Pillar Aspect Ratio on the Behaviour of 1-3 Connectivity Composite Transducers", *Proc. of 2nd European Conference on Underwater Acoustics*, Vol I, pp 503-508, Copenhagen, Denmark, July 1994.

D. J.Bennett and G.Hayward, "Design of 1-3 Piezocomposite Hydrostatic Transducers using Finite Element Analysis", *Proc. IEEE Ultrasonic Symposium*, Cannes, France 1994, pp 979-982

E. A.Gachagan, J.Bennett and G.Hayward, "A Finite Element Modelling Approach into the Influence of Mechanical Matching and Damping in 1-3 Piezocomposites", *Proc. IEEE Ultrasonic Symposium*, Cannes, France 1994, pp 995-998

F. J.Hyslop, J.Bennett and G.Hayward, "An Investigation into the Design of High Frequency Two-Dimensional Arrays", *Proc. IEEE Ultrasonic Symposium*, Cannes, France 1994., pp 1515-1518

G. G.Hayward, J.Bennett and R.Hamilton, "A Theoretical Study on the Influence of Some Constituent Material Properties on the Behaviour of 1-3 Connectivity Composite Transducers", Accepted for publication to *J.Acoust.Soc.Amer.*

H. G.Hayward and J.Bennett, "The Influence of Pillar Aspect Ratio on the Behaviour of 1-3 Connectivity Composite Transducers", Accepted for publication to *IEEE UFFC.*

I. J.Bennett and G.Hayward, "Design of High-Frequency Monolithic Ultrasonic Arrays using 1-3 Piezocomposite", *Proc. IEEE Ultrasonic Symposium*, November 1995 Seattle, WA, USA, 1995.

J. J.Bennett and G.Hayward, "Design of 1-3 Piezocomposite Hydrophones using Finite Element Analysis", Submitted for publication to *IEEE UFFC.*

CHAPTER TWO

MODELLING TECHNIQUES FOR PIEZOELECTRIC TRANSDUCERS

CHAPTER OBJECTIVE

The purpose of this Chapter is to review the research done on piezoelectric ultrasonic transducers which is pertinent to the work presented in this thesis. This excludes details specific to finite element modelling which are discussed in the next Chapter. From the fundamental concept of piezoelectricity and the constitutive linear equations, a list of selection criteria for comparing different piezoelectric materials can be generated and the optimal material chosen for a specific application. The modelling of piezoelectric materials has been in general performed using constrained-dimensional techniques where the linear equations are simplified through the application of constraints to reduce the number of variables or dimensionality of the system. These models may be also used to determine the design parameters for the ancillary components of the matching layer and backing block. Appraising the different aspects of the research covered in this Chapter, it is possible to generate a list of desired features for the finite element model of the 1-3 piezocomposite transducers that cannot be included in the current constrained-dimensional models.

2.1 PIEZOELECTRICITY

Most ultrasonic transducers utilise a piezoelectric or ferroelectric material which displays the piezoelectric effect, as the active component. The direct piezoelectric effect [9] is observed when external mechanical forces deform the shape of the piezoelectric material and this is accompanied by the generation of charge at the surface of the material. Similarly, the inverse effect occurs when the shape of the material is deformed by an applied electric field (which can be considered as the deposition of charge on the surface). There are few naturally occurring piezoelectric materials of which the commonest is quartz whose piezoelectricity was first observed by the Curies in 1880. A ferroelectric crystal possesses an internal dielectric moment under static conditions (no applied electric field) and this moment is constant within localised regions called *domains*. The crystal will normally have no net polarization because of the random alignment of these moments. However, if the crystal is heated to its Curie temperature and an electric field is applied across the crystal, the domains will tend to align with the field. If the electric field is maintained as the crystal is cooled below its Curie temperature, these domains will keep their alignment and the crystal becomes piezoelectric. The above process is called *poling*.

The electric and mechanical behaviour of any piezoelectric material can be described in tensor form [5] by the linear simultaneous equations:

$$\begin{aligned} \underline{T} &= [c^E]\underline{S} - [e]\underline{E} \\ \underline{D} &= [e]^t\underline{S} + [\varepsilon^S]\underline{E} \end{aligned} \qquad \textbf{Eqn. 2.1}$$

where $\underline{T}$ is the mechanical stress tensor;

$\underline{D}$ is the electric charge density tensor;

$\underline{S}$ is the mechanical strain tensor;

$\underline{E}$ is the electric field tensor;

$[c^E]$ denotes the elastic stiffness tensor where the superscript E implies that it is evaluated at constant electric field to remove the influence of the electric

field on the behaviour of piezoelectric material (normally the electrodes are short-circuited forcing a constant zero electric field to exist);

[e] denotes the piezoelectric tensor and the superscripted ^{t} indicates transpose; and

[ε^S] denotes the dielectric tensor where the superscript S implies that it is evaluated at constant mechanical strain to remove the influence of the movement (normally the material is constrained to have no movement and hence no strain which is constant).

The scalar values from each tensor are differentiated by subscripts from the reduced matrix notation of which there are six possible directions. The *3* direction is taken as the direction of the alignment of the dipoles and hence the poled direction. The *1* and *2* directions define the planes at 90° to the *3* direction. The directions *4*, *5* and *6* are the rotations about the *1*, *2* and *3* directions respectively as shown in Figure 2.1.

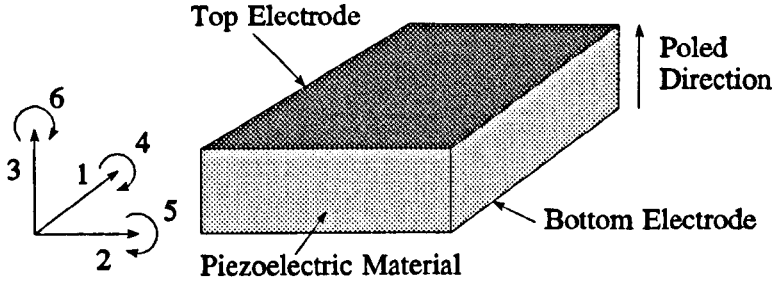

Figure 2.1: Subscripts used for Piezoelectric Notation

Some of the parameters contained in Equation 2.1 are difficult to measure and hence, the static piezoelectric activity of a material can be fully characterised by the following:

- Piezoelectric strain constant (d_{ij}) which gives an indication of the efficiency of the inverse piezoelectric effect and indicates behaviour of the material under transmit conditions. With the top and bottom electrode under open-circuit conditions, the constant is given by the strain produced by an applied

unit electric field and under short-circuit conditions, the constant is given by the charge density produced in the electrodes by an applied unit stress. The values are normally specified in meters per volt or coulombs per meter.

- Piezoelectric voltage constant (g_{ij}) which gives an indication of the efficiency of the direct piezoelectric effect and indicates the behaviour under receive conditions. With the top and bottom electrodes under open-circuit conditions, the constant is calculated as the induced electric field produced by an applied unit stress and under short-circuit conditions, the constant is given by the strain developed produced by applied unit charge density being present at the electrodes. The values are normally specified in volt meter per newton or meter per coulomb.

When two subscripts are given such as *ij*, the independent force is applied in the *j* direction and the resultant reaction is in the *i* direction. Thus g_{31} is equal to the ratio of the electric field produced in *3* direction to the force applied in the *1* direction. The two piezoelectric constants described above are related by the permittivity of the material:

$$d_{ij} = g_{ij}\varepsilon_{ii} \qquad \textbf{Eqn. 2.2}$$

The total efficiency of the material under different operating conditions for the thickness direction is indicated by the product of the two constants for the thickness direction and is called the *Figure of Merit* (FOM) of the particular piezoelectric material:

$$FOM = d_{33}g_{33} \qquad \textbf{Eqn. 2.3}$$

Another indicator of operational efficiency of the material is the electromechanical coupling co-efficient (k_{ij}) which represents the fraction of electrical energy converted into mechanical energy in a single frequency cycle. There are many methods of calculating this parameter and several will be discussed in later sections of the thesis. It is important to note that the value of the subscripts is chosen on the geometry of

the material and the direction in which it must operate. For this thesis, most transducer will be operated at their thickness mode making the thickness mode coupling co-efficient (k_t) the desired output parameter. Other important electromechanical coupling co-efficients are:

- k_{33} which is associated with a thickness mode that is laterally unclamped as would be the case for a thin long pillar; and
- k_{11} which is associated with the radial modes of the transducer.

2.1.1 Piezoelectric materials

Several criteria are considered when selecting an appropriate piezoelectric material for a transducer system [10]:

- High electromechanical coupling efficiency - to maximise the energy conversion to reduce the required input energy and reduce overheating of the material.
- Optimised acoustic matching to the load medium - to maximise the energy transfer across the boundary of the transducer and the medium.
- High electrical permittivity - to reduce the input impedance of the transducer and allow optimal electrical matching to the electrical sub-systems. This is of particular importance for arrays where the element size is relatively small to the height of the material and hence, have high electrical impedance.
- Low lateral coupling (d_{31}, g_{31}) to the thickness mode - to reduce the effect of the transducer geometry on the performance.

The most common piezoelectric material group is the piezoelectric ceramics which are characterised by:

- high electromechanical coupling - values can exceed 0.5 for plates (k_t) and up to 0.8 for the isolated pillars (k_{33}).

- high permittivity (ε_R ~ 140-1700) which implies good electrical matching.
- high specific acoustic impedance (Z > 25 MRayl) - the specific acoustic impedance of a material is the resistance experienced by a plane acoustic wave propagating through the material. Its importance is that the transmission and reflection of energy at the interface between two materials is purely a function of the two specific acoustic impedances involved. The high impedance of the piezoceramics implies a large acoustic mismatch when the transducer is operating into a low impedance medium such as water (1.5 MRayl) or air (420 Rayl) causing a drop in operational bandwidth and sensitivity.

The most widely used piezoceramics are the lead zirconate titanates (PZT) whose properties are adjusted by varying the zirconium to titanium ratio and by introducing small amounts of impurities. All the piezoceramics that fall in this group are denoted by their Vernitron names for the purpose of the thesis. These piezoceramics exhibit exceedingly high coupling factors (up to 0.8) but also high lateral coupling which limits the geometry of the transducer. An example of this group is PZT-4 or Navy type I which produces large mechanical drive amplitudes while maintaining low mechanical loss. In contrast, the PZT-5 family has significantly high internal losses and hence, lower quality factor. PZT-5A is commonly used as the manufacturing process has been well established but this material is being superseded by PZT-5H which has almost twice the dielectric constant and increased coupling co-efficients. A disadvantage with PZT-5H is the lower Curie temperature which means the properties of the material are not as stable with time as those of PZT-5A.

Barium titanate (BT) is characterised by intermediate electromechanical coupling in conjunction with a relatively high dielectric constant and reproducibility of manufacture. The high bulk wave velocity can be attractive for applications that require thick dimensions. Modified lead titanates (MPT) were developed [11] as an alternative and demonstrate negligible d_{31} and g_{31} at the expense of slightly reduced electromechanical coupling efficiency and significantly reduced permittivity. Another

piezoceramic with low lateral coupling is lead metaniobate (PmN) which has the added advantage of a high Curie temperature allowing application for high-temperature operation. It also has high internal loss.

Piezoelectric polymer materials such as polyvinylidene fluoride (PVDF) [12], were developed to overcome the problem of the mechanical impedance mismatch. They are characterised by a low specific acoustic impedance, relatively low electromechanical coupling (0.4), very low lateral coupling but small permittivity (ε_R^T=12.4). This means that while they can be used to construct efficient receivers, they are not well suited to transmitter applications. Even as receivers, piezopolymers place demands on the electrical circuitry because of the low permittivity. The piezoelectric action can be improved by the incorporation of co-polymers and modern innovation has allowed the manufacture of thick (100 μm) layers.

Modern piezoelectric ceramic-polymer composites were developed [13] as a compromise between the two material types (i.e piezoceramics and polymers) in the hope of combining the desirable properties of each phase. There are many possible methods of connecting the two phases and are described according to the number of dimensions each phase travels through the entire composite. If it is possible to enter the sample on a line parallel to the x-axis and exit the other side of the sample without having left the phase material, that phase material is said to be connected in the 'x' direction. The first number is the connectivity of the ceramic and the second is that of the polymer. Hence 2-2 connectivity piezoceramic-polymer composite implies that the structure consists of alternating plates of ceramic and polymer. 1-3 connectivity implies that the ceramic is connected in only one dimension, normally the *3* direction while the polymer is connected in all three. The importance of connectivity is that it governs whether material properties tend to be summed in series or in parallel. A 1-3 piezocomposite consisting of ceramic pillars embedded in a polymer matrix will act as if the resultant material stiffnesses are in parallel in the *3* directions and in series for the other two directions as shown in Figure 2.2.

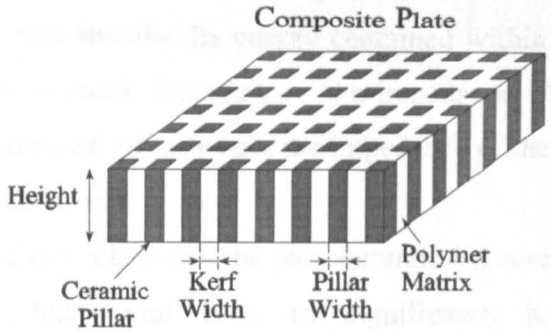

Figure 2.2: Microstructure of 1-3 Piezocomposite

The piezocomposites with which this thesis is concerned, are 1-3 connectivity types where most of the current research is directed [3]. Several parameters are used to characterise the material:

- Ceramic material - normally one of the lead zirconate titanate (PZT) piezoceramics as the polymer phase tends to reduce the debilitating effect of the lateral coupling;
- Polymer material - the material is selected to tailor the properties of the piezoceramic to the required operating conditions.
- Volume fraction - the ratio of the volume of the ceramic phase to the total volume of the material.
- Pillar aspect ratio - is defined for the purpose of this thesis as the ratio of the width of the ceramic pillar to its height and is normally less than one.

Assuming the ceramic pillars are squares, the above parameters are sufficient to define the micro-structure of the material. The generic properties of a well-designed 1-3 piezocomposite are:

- Very high thickness-mode electromechanical coupling efficiency - in many cases, it exceeds that of the original piezoceramic as the ceramic rods are not laterally clamped, allowing efficient operation.

- Relative low lateral coupling - the polymer is more mechanically lossy than the ceramic and absorbs the energy contained within the lateral modes;
- Low specific acoustic impedance - the impedance will be a combination of the two constituent values where the impedance of the polymer can be similar to that of water; and
- Low permittivity relative to the piezoceramic because the polymer has a low permittivity, but overall it is still significantly higher than that of the piezopolymers.

2.1.2 Polymer Properties

As mentioned above, there are two constituent phases to the 1-3 piezocomposite: the piezoceramic phase which is chosen for its high coupling co-efficient and high permittivity; and the polymer phase which is chosen for its mechanical properties. Polymers can exist in several states [14] and at room temperature, the polymer will typically exhibit a frequency-dependent modulus that is high (approximately 1 GPa) in the high-frequency glassy state but low (several MPa) in the low-frequency rubbery state. The S-shaped curve will have, around the transition frequency, a region termed the glass-to-rubber transition region as illustrated in an example curve in Figure 2.3. The second curve is that of damping which also varies with frequency. There are four operating regions [15]:

- Flow region - where the molecules in the polymer rearrange to absorb any applied stress. Hence, the material is very compliant at low frequencies.
- Rubber region - where the molecules can move in an unrestrained manner with the applied stress. Hence, the polymer is compliant with a relative high loss.
- Glass-rubber transition region - where the molecules in the polymer can no longer act in an unrestrained manner. Hence, the polymer becomes stiffer and the loss increases.

- Glassy region - where the molecules cannot react with the applied stress. Hence, the material is relatively stiff but has low mechanical loss.

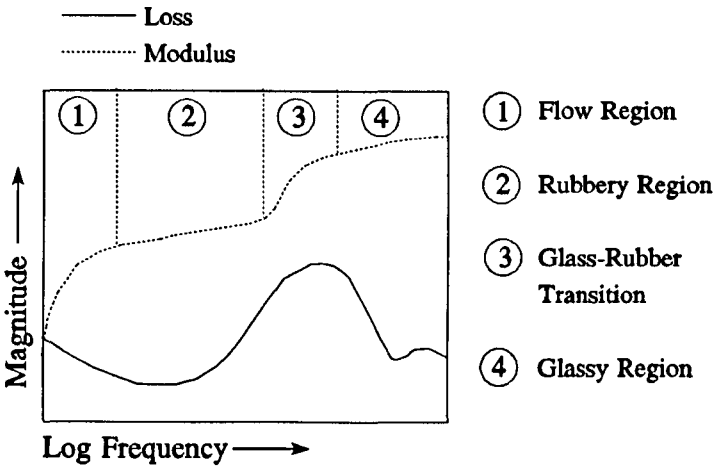

Figure 2.3: Frequency-dependent Behaviour of Polymers

Hence, the operational modulus is not only a function of the polymer material but also the operating frequency relative to the transition region. As the material hardens with increase in frequency, the Poisson ratio changes from approximately 0.5 for a soft rubber to approximately 0.35 for a hard resin. The polymer properties have a similar response to temperature change.

This is because polymers exhibit viscoelastic behaviour. Many solids such as metals and ceramics, exhibit pure elastic effects when deformed to low levels of strain. They behave as ideal Hookean elements in that the resulting strain is in phase with the stress and is independent of the stress history. In contrast, many fluids behave in a purely viscous fashion as ideal Newtonian elements where the rate of deformation is proportional to the rate of stress and hence, in a harmonic system, the strain lags the stress by 90°. If an ideal elastic element is placed in series with an ideal viscous element, a Maxwell element [14] is formed where the stress in both elements is equal and the resultant strain of the element is the sum of the strains of the two elements. If a ideal elastic element is placed in parallel with an ideal viscous element, a Voigt element is formed where the strain in both elements is equal and the resultant stress

of the element is the sum of the stresses of the two elements. The simplest possible model for the mechanical behaviour of a viscoelastic polymer is a Maxwell element in series with a Voigt element as shown in Figure 2.4.

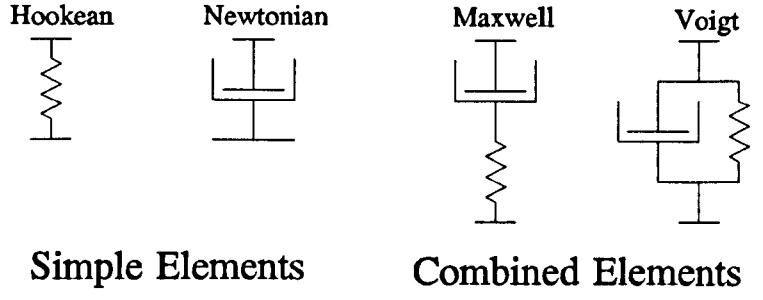

Figure 2.4: Different Combinational Elements

In practice, the polymer can be modelled as a material where the strain lags the stress by a constant phase, ε, less than 90°. The tangent of this angle is called the *loss tangent* and is used to define the damping within the polymer. The mechanical properties that are sufficient to characterise the material, are the bulk modulus, $\hat{K}$, and the shear modulus, $\hat{G}$ where the circumflex indicates a complex quantity throughout the thesis. Each modulus has an associated wave mechanism and hence, an associated attenuation co-efficient which are not necessarily equal. These co-efficients are calculated from the loss tangent, the density of the polymer and the frequency of operation. Therefore, while the mechanical losses present in a piezoelectric ceramic are negligible except at very high frequencies, the losses within the polymer must be included in any model to obtain accurate results.

A special range of polymers called electronic resins, have been developed for incorporation within electrical systems. These have very low permittivity ($\varepsilon_R \approx 4$) so as to act as an insulator but also have low dielectric loss. Hence, in a piezocomposite

material model, the dielectric properties of polymer can be assumed zero relative to the piezoceramic except at very low volume fractions and so the polymer can be modelled as a purely mechanical material. Two polymers are currently in use by the Ultrasonics Research Group at the University of Strathclyde: Ciba-Geigy CY1301/HY1300 named hardset epoxy as it is stiff at room temperature; and Ciba-Geigy CY208/HY956 named softset epoxy as it is flexible at room temperature. The properties of each is described in Appendix B and they were used for the modelling in the following Chapters.

2.2 CONSTRAINED-DIMENSIONAL MODELLING

The classical modelling technique for ultrasonic transducers has been to constrain the behaviour of the transducer to occur only in specific dimensions. The simplest method is to constrain the *1* and *2* directions to have no motion so that the behaviour is represented purely by the thickness mode resonances of the device. This implies several assumptions [16]:

1. The lateral dimensions are sufficiently large (at least ten times of the height of the active material) so that no lateral mode degrades the thickness mode operation of the transducer. This has the following implications:
   - Zero electric field components in the *1* and *2* directions.
   - Zero motion in the *1* and *2* directions.
   - No shear motion occurs within the transducer.
2. Each mode is assumed to be isolated from any other mode and to act independently.
3. All vector fields present in the transducer have no variation in the lateral dimensions and hence, can be represented by a single scalar value in the *3* direction.

The models developed from the above assumptions can be extended to include all the other components involved in the transducer design such as firing circuitry and

matching layers. Each mechanical component of the transducer is modelled as a layer of finite thickness but infinite width dimensions. The piezoelectric relationship for pure thickness mode operation of the layer l in the Laplace domain as defined by Redwood [17], is:

$$\begin{aligned} T_3^l &= c_{33}^{D,l} S_3^l - h_{33}^l D_3^l \\ E_3^l &= -h_{33}^l S_3^l - \beta_{33}^{S,l} D_3^l \end{aligned} \qquad \textbf{Eqn. 2.4}$$

The introduced parameters are derived from the original equation and are given by:

$$\begin{aligned} c_{33}^{D,l} &= c_{33}^{E,l} + \frac{\left(e_{33}^l\right)^2}{\varepsilon_{33}^{S,l}} \\ h_{33}^l &= \frac{e_{33}^l}{\varepsilon_{33}^{S,l}} \\ \beta_{33}^{S,l} &= \frac{1}{\varepsilon_{33}^{S,l}} \end{aligned} \qquad \textbf{Eqn. 2.5}$$

Non-piezoelectric or passive layers are assumed to be isotropic and can be represented by Hooke's law:

$$T_3^l = c_{11}^l S_3^l \qquad \textbf{Eqn. 2.6}$$

for a purely mechanical layer. Electrical loading on the active material can be incorporated within Equation (2.4) and solved conveniently by transformation into the Laplace transform. These equations can be modified by considering the plane waves that will propagate through each layer at a single frequency. A set of simultaneous equations is generated in terms of transmission and reflection co-efficients by assuming continuity of force and particle displacement at the boundaries between different layers. These equations are solved using matrix evaluation technique as discussed in Chapter 3 and the desired parameters describing the dynamic operation of the transducer can be calculated as was done by Hayward [16].

It can be seen that constrained-dimensional modelling produces much simpler equations with far fewer unknowns than the complete situation. Consequently, the

models are simpler to solve than those derived from the complete set of equations but produce similar results if there is insignificant movement in the *1* and *2* direction. There is current research into generating models of piezoceramics which include the lateral coupling into the thickness mode operation [18], but several assumptions are still required concerning the geometry of the material. As finite element analysis includes the geometry of the material within the model, no similar assumption are required. Hence finite element modelling can be used to determine under what conditions the assumptions made to derive the constrained-dimensional models are valid.

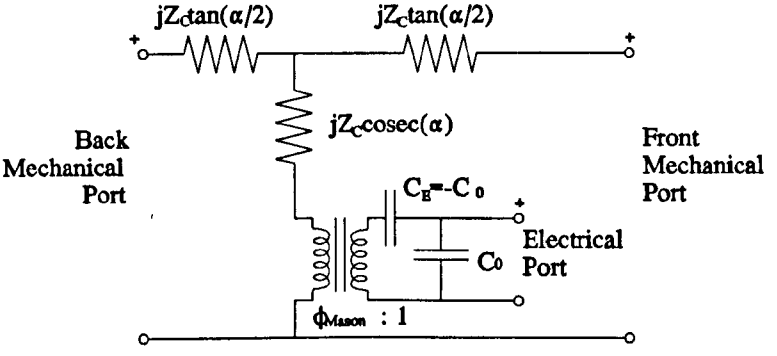

Figure 2.5: Mason's Electrical Equivalent Model

It is pertinent to mention that several researchers have developed electrical analogues for the piezoelectric transducer including the two most significant: the Mason's model and the Krimholtz, Leedom and Matthaei (KLM) model. Mason derived a three port network shown in Figure 2.5, from Equation 2.1 [19]. The transmission lines in the mechanical region of the circuit represents the time delay for the mechanical waves to travel through the piezoelectric layer where

- Z_C is the acoustic impedance of the piezoelectric material; and
- α is the normalised radial frequency and is given by the expression:

$$\alpha = \frac{\pi\omega}{\omega_{mech}} \qquad \textbf{Eqn. 2.7}$$

where ω is the operating frequency; and

ω_{mech} is the radial mechanical resonance frequency.

The negative capacitance simulates the positive feedback of the secondary piezoelectric effect [16]. C_0 is the static capacitance of the transducer with no piezoelectric action and is given by:

$$C_0 = \varepsilon_{33}^{s} \frac{A}{t_3} \qquad \textbf{Eqn. 2.8}$$

where $\varepsilon_{33}{}^{s}$ is the permittivity under constant strain (no movement); and

A and t_3 are the area and height of the transducer respectively.

The ideal transformer represents the piezoelectric action of converting between the electrical and mechanical energy and its turns ratio is given as:

$$\phi_{Mason} = h_{33} C_0 \qquad \textbf{Eqn. 2.9}$$

where h_{33} is the piezoelectric current constant for the material.

Near any odd mechanical resonance [20], the model can be simplified into the static capacitance in parallel with a R-L-C branch as shown in Figure 2.6. It is this model that is used in the IEEE (Institute of Electrical and Electronic Engineers) Standard on Piezoelectric Measurement [21] and is used to derive the motional components of the transducer. The value of the resistor, R_1, depends on the losses within the transducer and the radiation resistance. The values for the equivalent capacitance and inductance are given by:

$$C_1 = \frac{1}{\pi^2 f_{mech} Z_C}$$
$$L_1 = \frac{Z_C}{4 f_{mech}} \qquad \textbf{Eqn. 2.10}$$

where f_{mech} is the mechanical resonance frequency of the device.

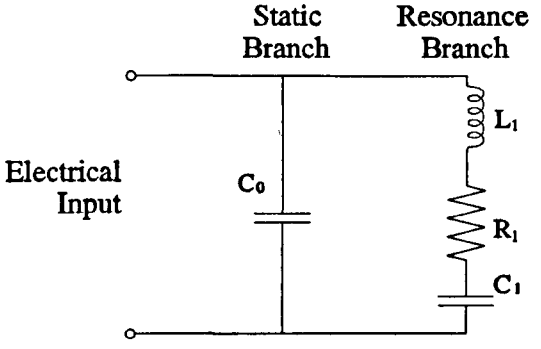

Figure 2.6: Model used by IEEE Standard

The KLM model [22] differs to the Mason model in that there is coupling between the electrical and mechanical domain at a single point rather than over a collection of components. This is done by having a frequency dependent turns ratio on the transformer. The KLM model is shown in Figure 2.7. The turns ratio is:

$$\phi_{KLM} = k_t \sqrt{\frac{\pi}{\omega_{mech} C_0 Z_C}} sinc\left(\frac{\omega}{2\omega_{mech}}\right) \qquad \textbf{Eqn. 2.11}$$

where ω_{mech} is the radial mechanical resonance frequency.

The additional reactance in series with the transformer can be modelled as a frequency dependent capacitor:

$$C' = -\frac{C_0}{k_t^2 sinc\left(\frac{\omega}{\omega_{mech}}\right)} \qquad \textbf{Eqn. 2.12}$$

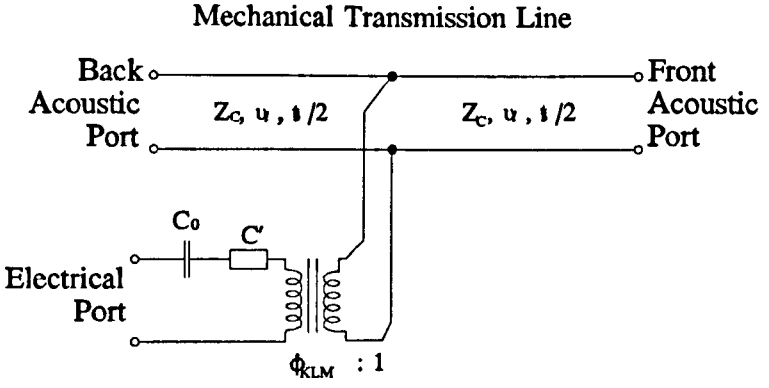

Figure 2.7: KLM Transmission Line Model

The mechanical section of the model is modelled as a set of transmission lines with impedance, Z_C, and speed of transmission, v_a, and length of $t_3/2$.

2.3 MODELLING OF ANCILLARY COMPONENTS

The previous sections have dealt with the active component of the transducer system. The practical behaviour of the transducer can be further enhanced by using extra components as shown in Figure 2.8.

The two principal features comprise additional matching layers and a backing block in order to develop a transducer with the following improved characteristics [23]:

- **Bandwidth** - The axial resolution of an acoustic imaging system is proportional to the bandwidth of the transducer.

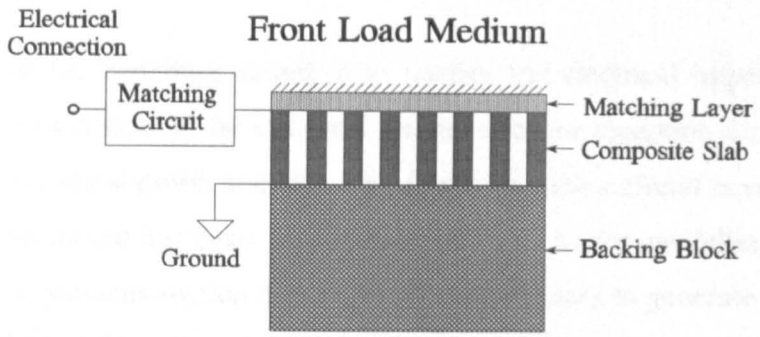

Figure 2.8: Extra Components on Transducer Model

- **Sensitivity** - The distance over which the transducer can transmit and receive is a function of the sensitivity.

The applications addressed in this thesis are associated mainly with low specific acoustic impedance media which means that generally there will be a large impedance mismatch between the active component of the transducer and the surrounding medium. The matching layer acts as an acoustic transformer between the front face of the piezoelectric material and the load while the backing block acts as a semi-infinite boundary with minimal mismatch for the back face of the piezoelectric material.

The properties of the surrounding medium affect the performance of the transducer as it acts as a mechanical load on the front of the transducer. When the medium is air, there is a large mis-match at the boundary between the device and the medium allowing Rayleigh waves to be sustained at the interface. However, for a water load, the mis-match can be small enough for any shear waves travelling at the boundary to couple with the fluid and produce propagating pressure waves in the water. This implies that not only the thickness modes but also the shear modes within the

composite matrix can generate acoustic energy in the fluid. Thus, it is important to include the fluid loading into any model.

The purpose of the matching circuit is to modify the electrical impedance of the transducer to match that of the electrical transmission or reception circuit so as to maximise the electrical power transfer. The design of such a circuit is not within the scope of this thesis but has been well researched [24]. As the modelling techniques discussed in the previous section use electrical circuit theory to generate the solution, the effect of the matching circuit can be easily incorporated into the model. It is done as an addition of electrical components to the electrical port of the appropriate model.

The effect of these two components on the transducer's performance can be examined by the application of wave propagation theory [19]. As mentioned in Section 2.2, if the lateral dimensions of the transducer are considered sufficiently large, the stress propagation through the mechanical part of a transducer system can be considered a plane wave that propagates with time. As the energy propagates as a mechanical wave, it will travel with a certain stress (T) and velocity (v) amplitude. These two quantities are related through the specific acoustic impedance (Z) of the constituent material:

$$Z = -\frac{T}{v} \qquad \textbf{Eqn. 2.13}$$

The wave motion at any one point (z) in space over time is represented by a forward travelling wave and a backward travelling wave. The specific acoustic impedance experienced by the forward wave is that of the material but because of its direction of travel, the backward wave has an associated specific acoustic impedance which is the negative value of impedance for the material. This can be represented mathematically as:

$$\hat{T}(z,t) = \left(T^F e^{-jkz} + T^B e^{jkz}\right)e^{j\omega t}$$
$$\hat{v}(z,t) = \left(v^F e^{-jkz} + v^B e^{jkz}\right)e^{j\omega t} \qquad \textbf{Eqn. 2.14}$$

where T^F and T^B is the stress amplitude of the forward and backward wave respectively;

v^F and v^B is the velocity of the forward and backward wave respectively;

ω is the operating radial frequency;

k is the wavenumber for the frequency and material and is equal to $2\pi/\lambda$; and

t and z are the position in time and space respectively.

For the following analysis, the $e^{j\omega t}$ term will be dropped from the equations and the waves will be evaluated at a single point in time.

2.3.1 Matching Layer Design

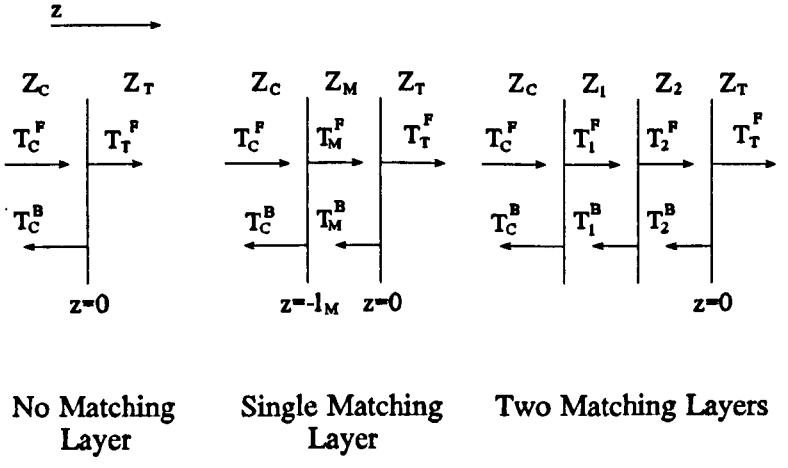

Figure 2.9: Effect of Matching Layers on Wave Propagation

The waves will propagate in an unimpeded form until there is a boundary between two layers as shown in Figure 2.9. For the active layer transmitting directly into the surrounding fluid, the boundary is that between a specific acoustic impedance of Z_C for the active layer and Z_L for the load medium. The fraction (Γ) of stress reflected

at the interface for z=0 is the ratio of the incident stress wave amplitude (T_C^F) to that of the reflected or backward wave (T_C^B):

$$\Gamma = \frac{T_C^B}{T_C^F} \qquad \textbf{Eqn. 2.15}$$

Equation (2.14) can be re-written in terms of Γ for the boundary for the active layer:

$$\begin{aligned} \hat{T}_C(z) &= T_C^F\left(e^{-jk_L z} + \Gamma e^{jk_L z}\right) \\ \hat{V}_C(z) &= -\frac{T_C^F}{Z_C}\left(e^{-jk_L z} - \Gamma e^{jk_L z}\right) \end{aligned} \qquad \textbf{Eqn. 2.16}$$

and for the load medium:

$$\begin{aligned} \hat{T}_L(z) &= T_L^F e^{-jk_L z} \\ \hat{V}_L(z) &= -\frac{T_L^F}{Z_L} e^{-jk_L z} \end{aligned} \qquad \textbf{Eqn. 2.17}$$

As the load medium is considered to be semi-infinite, there is no other boundary to generate a backward travelling wave in the load medium. The stress at each side of the interface (z=0) must be equal as the particles at the boundary can not vibrate with two different stress amplitudes. Equating the stress expressions of Equation (2.16) and (2.17):

$$T_L^F = T_C^F(1 + \Gamma) \qquad \textbf{Eqn. 2.18}$$

The velocities must also be equal:

$$-\frac{T_L^F}{Z_L} = -\frac{T_C^F}{Z_C}(1 - \Gamma) \qquad \textbf{Eqn. 2.19}$$

Equations (2.18) and (2.19) can be combined to obtain an expression for Γ:

$$\Gamma = \frac{Z_L - Z_C}{Z_L + Z_C} \qquad \textbf{Eqn. 2.20}$$

Thus if there is a large mismatch between the values of Z_C and Z_L, most of the stress in the forward travelling wave in the piezoelectric material is reflected at the boundary into a backward travelling wave. This stress will propagate within the active layer until it is absorbed by the mechanical loss mechanisms. A matching layer is used between the two impedances to reduce the reflection co-efficient and increase the fraction of stress transmitted from the active layer to the load medium for each wave.

The matching layer has two design parameters: a specific acoustic impedance of Z_M and width of l_M. Placing the boundary between the matching layer and the load medium at z=0, the specific acoustic impedance (Z_{in}) seen by the active layer at the boundary between it and the matching layer is:

$$Z_{in} = -\frac{\hat{T}_C(-l_M)}{\hat{v}_C(-l_M)} \qquad \textbf{Eqn. 2.21}$$

Considering the wave propagation within the matching layer and taking Γ_M to be the reflection co-efficient of the boundary at z=0:

$$\begin{aligned} \hat{T}_M(-l_M) &= T_M^F\left(e^{-jk_M(-l_M)} + \Gamma_M e^{jk_M(-l_M)}\right) \\ \hat{v}_M(-l_M) &= \frac{T_M^F}{Z_M}\left(e^{-jk_M(-l_M)} - \Gamma_M e^{jk_M(-l_M)}\right) \end{aligned} \qquad \textbf{Eqn. 2.22}$$

Using Equations (2.21) and (2.22) and equating the stress and velocities at the boundary, the expression for Z_{in} can be obtained as:

$$Z_{in} = Z_M\left(\frac{e^{jk_M l_M} + \Gamma_M e^{-jk_M l_M}}{e^{jk_M l_M} - \Gamma_M e^{-jk_M l_M}}\right) \qquad \textbf{Eqn. 2.23}$$

However:

$$\Gamma_M = \frac{Z_L - Z_M}{Z_L + Z_M} \qquad \textbf{Eqn. 2.24}$$

giving:

$$\begin{aligned} Z_{in} &= Z_M \left[\frac{(Z_L + Z_M)e^{jk_M l_M} + (Z_L - Z_M)e^{-jk_M l_M}}{(Z_L + Z_M)e^{jk_M l_M} - (Z_L - Z_M)e^{-jk_M l_M}} \right] \\ &= Z_M \left[\frac{Z_L \cos(k_M l_M) + jZ_M \sin(k_M l_M)}{Z_M \cos(k_M l_M) + jZ_L \sin(k_M l_M)} \right] \end{aligned} \qquad \textbf{Eqn. 2.25}$$

For the most efficient transfer of energy across the boundary, Z_{in} needs to be real as any imaginary components would indicate loss of energy. Considering the Equation, this can be easily achieved by either

- Setting the imaginary components to zero:

$$\sin(k_M l_M) = 0 \qquad \textbf{Eqn. 2.26}$$

From Equation (2.25), the expression for the load acoustic impedance would be:

$$Z_{in} = Z_L \qquad \textbf{Eqn. 2.27}$$

which would imply that the matching layer has no affect on the transducer behaviour. Hence, this solution can be ignored.

- Setting the real components to zero:

$$\begin{aligned} \cos(k_M l_M) &= 0 \\ \left(\frac{2\pi}{v_C}\right) l_M &= \frac{n\pi}{2} \quad \forall \quad n = 1,3,5,... \\ l_M &= \frac{v_C}{4}, \frac{3v_C}{4}, \frac{5v_C}{4} \end{aligned} \qquad \textbf{Eqn. 2.28}$$

From Equation (2.25), the expression for the load acoustic impedance would be:

$$Z_{in} = Z_M\left[\frac{jZ_M}{jZ_L}\right] = \frac{Z_M^2}{Z_L} \qquad \text{Eqn. 2.29}$$

The optimal value for Z_{in} is Z_C as this would make the reflection co-efficient at the boundary of the active layer zero. This gives a specific acoustic impedance for the matching layer of:

$$Z_M = \sqrt{Z_C Z_L} \qquad \text{Eqn. 2.30}$$

In summary, the optimal values for matching layer are:

- Thickness = $c_M/(2f)$ where c_M is the speed of sound in matching layer, taking the first solution from Equation (2.28).
- Specific acoustic impedance of $\sqrt{Z_C Z_L}$

These values are also valid for the transducer as a receiver as the specific acoustic impedance of the matching layer remains constant if Z_C and Z_L can be interchanged in Equation (2.27) without affecting the final value.

Jackson [25] extended this to include the design for multiple matching layers. Each layer optimises the transmission co-efficient between its two immediate neighbours. He showed that for *N* matching layers, the optimal specific acoustic impedance of *n*th layer, $Z_{n,N}$, is:

$$Z_{n,N} = \left(Z_C^{N+1-n}.Z_T^n\right)^{\frac{1}{N+1}} \qquad \text{Eqn. 2.31}$$

where n is the number of the layer counting from 1 for the layer attached to the active material to N for the layer in contact with the surrounding fluid.

As the number of layers is increased, the loading on the front surface of the active layer becomes matched which minimises the acoustic mismatch at the front face and increase the dynamic efficiency. In the case of the low volume fraction piezocomposites operating into a water medium, a single matching layer is normally sufficient but for operation into air, a second layer might be required. However, multiple matching layers are difficult to manufacture to the correct specification and do introduce a large component of loss in the device.

It is important to note that the theory presented in this section represents a starting point for the design of the matching layer for the transducer and not the optimal configuration. The thickness of the matching layer can be adjusted to introduce a resonance that is shifted slightly from the main thickness mode and hence, increase the bandwidth but at the expense of loss to maximum sensitivity. This operation is called *skewing*.

The addition of the matching layer introduces an additional resonator into the system which limits the maximum bandwidth achievable. The losses within the matching layer limits the maximum efficiency that can be achieved. Also as the height of the transducer has been increased, the transit time for a pulse to travel the length of the transducer has been increased. As the pulse is either absorbed by the backing block or the load medium, the ring-down time would have increased. All these considerations must be included in any modelling of piezoelectric transducers.

2.3.2 Design of Backing Block

The backing block provides the specific acoustic impedance for the back face of the transducer. If no block is used and hence the device is air-backed, the model can be considered as having a short-circuit (zero impedance) across the back acoustic port. This minimises the energy loss at the back boundary of the transducer thereby maximising the sensitivity but also causes the bandwidth to be narrow. For array configurations, a wide bandwidth is often more important than maximising the

sensitivity meaning that a high-impedance solid backing is used more frequently. To absorb all the stress energy that is incident on the back face of the active layer, the backing block must be the same specific acoustic impedance as the active layer. This configuration will give the system its maximum bandwidth but minimum sensitivity as most of the energy is absorbed by the backing block. The other disadvantage of such a configuration is that if the specific acoustic impedance is greater than that of the active layer, the reflection co-efficient becomes negative and the backward travelling wave will be inverted compared to the forward wave. The resonant nature of the active layer will change from a half-wave resonator to be a quarter-wave resonator. No strong resonance will be sustained at the half-wave frequency.

2.4 REQUIREMENTS FOR A PIEZOCOMPOSITE MODEL

Although constrained-dimensional modelling has been applied successfully for the design of 1-3 piezocomposite transducers as is shown in Chapter 4, there are assumptions about the microstructure of the piezocomposite that have to be fulfilled for the technique to be valid. Most of the models do not include any information concerning the internal geometry of the material other than the volume fraction. To define a constrained-dimensional model that does include these geometrical quantities would involve developing a technique very similar if not identical to finite element modelling. This technique is covered in greater detail in the next Chapter but it is suffice to say that finite element (FE) modelling is much more involved process than the constrained-dimensional modelling and should only be used when the simpler modelling techniques are deemed inadequate by the designer. Therefore the finite element model of a 1-3 piezocomposite transducer must supply more information to the operator and require fewer assumptions to be valid, for the technique to be useful in modelling 1-3 piezocomposite transducers.

The features for the definition phase of the modelling must include:

- A separate definition for the ceramic pillar and the surrounding polymer matrix - separate material parameters including damping co-efficients must be defined for each phase.
- A definition for matching layers and backing blocks which are used as mechanical enhancements to the performance of the device.
- A definition for the fluid medium to incorporate the effect of the fluid loading on the behaviour of the device.

2.5 CONCLUDING REMARKS

The aim of this Chapter was to introduce the concepts that would be used throughout this thesis for the operation and modelling of ultrasonic transducers. The transducers that are considered in this thesis, use the piezoelectric effect to both generate and measure acoustic pressure waves. There are three main type of piezoelectric materials: piezoceramic which are efficient but have large acoustic mis-match to low impedance loads; piezopolymers which are not as efficient but have a good acoustic match; and piezocomposite which, if designed well, combine the best properties of the other two groups.

Transducers are generally complex structures and require modelling to completely understand their behaviour. Most modelling has been performed using constrained-dimensional techniques where assumptions are made to reduce the number of unknowns in the system. However, finite element modelling does not have these restrictive assumptions so can be applied to situations where the validity of the other methods is in doubt. The concept of ancillary components was introduced and the different components were analysed. It was also shown why these must be included in the finite element model for a complete analysis of the system. Having considered all these different items and concepts, the features required to make the finite element modelling applicable, were detailed.

CHAPTER THREE

DEVELOPMENT OF THE FINITE ELEMENT MODELS

CHAPTER OBJECTIVE

The objective of this Chapter is to cover the development of the finite element model for a 1-3 piezocomposite transducer that will be used for the remainder of the thesis. It will be shown that the finite element modelling process can be divided into three phases: pre-processing where the geometrical and material properties of the transducer components are defined; solution where the behaviour of each node and element of the model is estimated; and post-processing where this behaviour is used to calculate a set of integrated output parameters which define the behaviour of the transducer as a whole. The list of desired features, both for pre-processing and for post-processing, have been defined in Chapter 2 and are incorporated into the finite element model. The implementation of each will be considered and verified by experiment where possible. Boundary conditions are of prime importance to the model definition in that they can be used to minimise the model size but keep the response of the model close to that of the practical device. The effect of boundary conditions are investigated and sets are chosen to represent the different possible operating conditions of the transducer.

3.1 OVERVIEW OF THE FINITE ELEMENT PACKAGES

The finite element method (FEM) [26] is a numerical procedure used for solving the differential equations encountered in a variety of engineering applications. The method was first applied to the aerospace industry in the early 1950's but came into use with other application areas when it was shown that the method was a variation of the Raleigh-Ritz procedure of minimising the potential energy of a system. When it was further demonstrated that the finite element equations could be derived by using a weighted residual procedure such as Galerkin's method and hence, be applied to any system of differential equations, FEM became more popular. In conjunction to these developments has been the microcomputer revolution enabling such a complex analysis technique as finite element modelling to be done far more cheaply and quickly compared to computers available during the initial development stages of FEM.

The finite element package used for the majority of this thesis was ANSYS produced by Swanson Associates of Houston, PA, USA and is one of the finite element (FE) packages currently being used by the University of Strathclyde. At the time of writing, the currently available version was 5.0A+. Although the package was not specifically developed for ultrasonic transducer modelling, it does incorporate piezoelectric and fluid elements making it suitable. However, it did have certain drawbacks, each of which will be highlighted later. There are specialised FE codes for ultrasonic transducer modelling such as ATILA but these package do not have the on-going financial support given to the large commercial codes. However the models are very similar between the different packages to the extent that the models developed in this Chapter can be converted to most FE packages. It is pertinent to mention that the ANSYS package used was an academic version and the size of the model that could be analysed was limited to 1500 master degrees-of-freedom which restricted the size of the more complex models.

It was found that the ANSYS package could not model piezocomposite transducer arrays as required for the purpose of Chapter 6 of this thesis. Hence, another package called PZ-Flex supplied by Weidlinger Associates of Los Altos, CA, USA, was used but this package will only be discussed in connection with array models which is dealt with exclusively in Chapter 6. A comparison between the two packages has been included.

3.2 GENERAL CONCEPTS OF FINITE ELEMENT MODELLING

The fundamental concept of the finite element analysis is that any continuous quantity such as temperature, pressure or displacement, for a domain can be approximated by a discrete model composed of a set of piece-wise continuous functions defined over a finite number of sub-domains. The discrete model is constructed as follows:

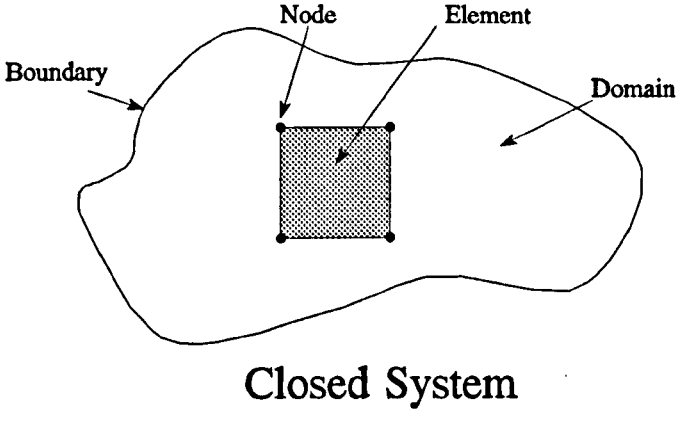

Figure 3.1: Concepts of Finite Element Modelling

- A finite number of discrete points called *nodes* are chosen within the domain.
- The value of the continuous quantity at each node is denoted as a *degree-of-freedom* (DOF) and is either set before or determined by the analysis process as an unknown.
- The domain is divided into a finite set of sub-domains called *elements* and at each vertex of the element, a node must exist. Certain elements allow nodes

to be present in the branches between the nodes to improve the accuracy of the interpolation of the quantities within the elements but none such elements were used in this work presented in this thesis. The partitioning procedure is called *meshing*.

- The continuous quantity is approximated through each element by interpolating polynomials called *shape functions*.

More than one quantity can be incorporated in the analysis as is the case for piezoelectric elements where both displacement and voltage are degrees of freedom at the nodes. Each element has a unique set of material properties which defines the relationship between each of its constituent nodes. The analysis is performed by creating and then solving a matrix equation describing these relationships, and it produces, as a result, the behaviour of the element at each of its nodes. The complete behaviour of the element is computed from this information and such parameters as the energy stored within the element can be generated.

For the analysis of piezoelectric transducers, there are three interacting physical systems: electrical, mechanical and fluid domains. This implies that each system cannot be analyzed as a separate entity from the others but all three must be solved simultaneously. There are two types of coupled systems as described by Zienkiewicz [27]:

- Class I : The coupled domains interact only at the boundary. This is the case with the mechanical and fluid domains at the fluid-structure interface. The solution for these boundary interaction is included as an option contained within the fluid elements.
- Class II : The coupled domains overlap and the coupling occurs through the differential governing equations describing different physical phenomena as is the case with the electrical and mechanical domains. Most finite element packages have a set of elements which combine the electrical and mechanical domains and are called multi-field solid elements.

Hence, the available degrees of freedom for each domain are:

- Mechanical displacement in each of the three dimensions, named UX, UY and UZ where the direction X, Y and Z are the *1*, *2* and *3* directions respectively;
- Electric potential or voltage (V) for the piezoelectric material within the model; and
- Pressure (p) for the fluid medium.

To each degree of freedom, there is a reaction:

- For each displacement, there is an associated mechanical force. The three forces are named FX, FY and FZ for each direction;
- To the electric potential, there is the reaction charge, Q; and
- To the pressure, there is the volume velocity. However, this can only be calculated for the element and not at the nodes as it is a volume quantity.

The forces and displacements can be partitioned into: values known before the analysis or set as part of the pre-processing stage; and values generated by the analysis. The equations governing piezoelectricity were derived from the law of conservation of momentum and the conservation of charge within a closed system [5]. For the mechanical domain, the conservation of energy takes the form of Hooke's law:

$$\underline{T} = [c]\underline{S} \qquad \textbf{Eqn. 3.1}$$

where $\underline{T}$ is the stress tensor containing the reaction forces, FX, FY and FZ;
[c] is the stiffness tensor which is given as one of the material properties specified for each mechanical element; and
$\underline{S}$ is the strain tensor containing the displacements, UX, UY and UZ, at the individual nodes.

Similarly, in the electrical domain, the law of conservation of charge takes the form of one of the fundamental relationships of electromagnetics:

$$\underline{D} = [\varepsilon]\underline{E} \qquad \textbf{Eqn. 3.2}$$

where $\underline{D}$ is the electric charge density tensor containing a function of the reaction charge;

$[\varepsilon]$ denotes the dielectric tensor which is defined by the material properties; and

$\underline{E}$ is the electric field tensor containing a function of the voltage, V, at the individual nodes.

The two domains are inter-related through the piezoelectric matrix giving the complete linear piezoelectric matrix equation as the following:

$$\begin{aligned} \underline{T} &= [c^E]\underline{S} - [e]\underline{E} \\ \underline{D} &= [e]'\underline{S} + [\varepsilon^S]\underline{E} \end{aligned} \qquad \textbf{Eqn. 3.3}$$

where [e] denotes the piezoelectric stress tensor which is defined by the material type;

the superscript ^{E} means under conditions of constant electric field;

the superscript ^{S} means under conditions of constant strain; and

the superscript ^{t} indicates the transpose of the matrix.

The basis for the derivation of the matrix equation for the finite element modelling was the variational principle of virtual (tending to zero) work. This states that, assuming the premise that a system will naturally seek equilibrium, the sum of work done by both the applied virtual forces and their reaction forces, and the stored potential energy generated by the virtual forces would be zero. The equations which represent the solid components of the model must be modified into a form that relates the degrees of freedom to their reaction forces. The strain and electric field tensors

for the *i*th element are related to the displacements and voltages through the shape functions mentioned earlier:

$$\underline{S_i} = \left[B_i^u\right]\underline{u_i}$$
$$\underline{E_i} = -\left[B_i^\phi\right]\underline{\phi_i} \qquad \textbf{Eqn. 3.4}$$

where $[B_i^u]$ is the shape function of the *i*th element in the mechanical domain;

$[B_i^\phi]$ is the shape function of the *i*th element in the electrical domain;

$\underline{u_i}$ is the tensor containing the mechanical displacements of the nodes that are associated with the *i*th element; and

$\underline{\phi_i}$ is the tensor containing the electrical displacements of the nodes that are associated with the *i*th element.

The application of the principle of variational work to the above equations yields the following equilibrium equations for the *i*th element:

$$\left[M_i^{uu}\right]\underline{\ddot{u}_i} + \left[C_i^{uu}\right]\underline{\dot{u}_i} + \left[K_i^{uu}\right]\underline{u_i} + \left[K_i^{u\phi}\right]\underline{\phi_i} = \underline{F_i}$$
$$\left[K_i^{u\phi}\right]^t\underline{u_i} + \left[K_i^{\phi\phi}\right]\underline{\phi_i} = \underline{Q_i} \qquad \textbf{Eqn. 3.5}$$

where $[K_i^{uu}]$ is the mechanical stiffness matrix derived from [c];

$[K_i^{u\phi}]$ is the piezoelectric stiffness matrix derived from [e];

$[K_i^{\phi\phi}]$ is the dielectric stiffness matrix derived from [ε];

$[C_i^{uu}]$ is the loss matrix;

$[M_i^{uu}]$ is the mass matrix derived from the mass of the element;

$\underline{F_i}$ is the combined reaction and applied force tensor;

$\underline{Q_i}$ is the combined reaction and applied charge tensor; and

each superscripted · indicates a time derivative.

The matrix equation for each element is combined to form a single large matrix representing the complete system to be modelled where each matrix is a system-wide matrix. It is of the form:

$$[M_{uu}]\ddot{\underline{u}} + [C_{uu}]\dot{\underline{u}} + \begin{bmatrix} [K_{uu}] & [K_{u\phi}] \\ [K_{u\phi}]^t & [K_{\phi\phi}] \end{bmatrix} \begin{bmatrix} \underline{u} \\ \underline{\phi} \end{bmatrix} = \begin{bmatrix} \underline{F} \\ \underline{Q} \end{bmatrix} \qquad \textbf{Eqn. 3.6}$$

As generally each element matrix is symmetrical, the system-wide matrices are normally symmetric allowing simpler matrix solution techniques to be used. The only unsymmetrical matrices encountered in the modelling are concerned with the fluid elements incorporating the fluid-structure interface.

The degrees of freedom are calculated from the solution of this equation and used to determine the behaviour of the elements and the device as a whole. Thus the finite element method can be divided into three phases as shown in Figure 3.2:

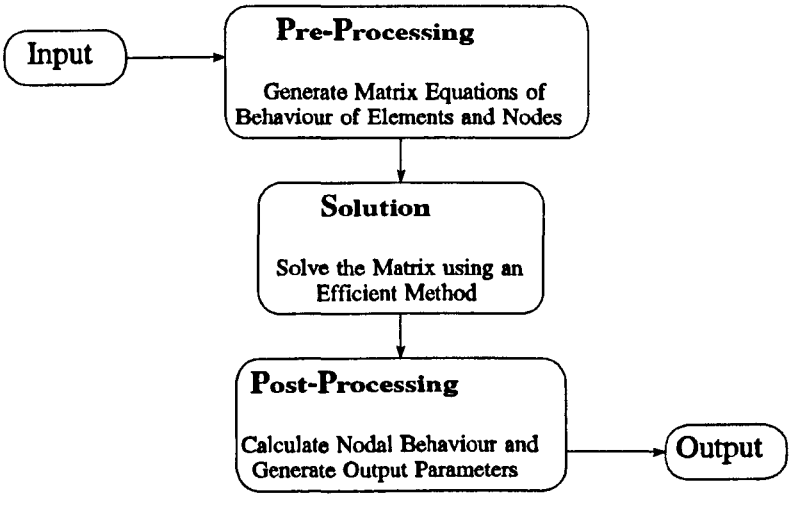

Figure 3.2: Flowchart of Modelling Process

- **Pre-processing** where the model is defined and all the material properties are specified. It is here that all the knowledge known before the analysis is supplied.
- **Solution** where the matrices are created and solved using one of the appropriate solution techniques.
- **Post-processing** where the results of the solution phase are analysed and the desired information is extracted and presented to the user.

The ANSYS package has several different modules to implement the above three processes. However, it was found that the desired output parameters were sufficiently far removed in calculation from the output of the analysis phase that a new post-processing module was developed for the purpose of this work to supersede the post-processing module of ANSYS. This meant that it could be optimised for each of the different forms of analysis performed. The module is discussed in Appendix A.

3.2.1 Elements in the Model

There are four element types from the ANSYS package that are used in the general finite element models for 1-3 piezocomposites. The names in the parentheses are the name of the material properties in the ANSYS package. The types are:

- **SOLID45** is a three-dimensional eight-node hexahedron that models the three displacement DOF's at each node. The material modelled with this element type is assumed to be isotropic so that the required properties are: elastic modulus (EX), Poisson ratio (NUXY) , density (DENS) and mechanical damping co-efficient (DAMP).

- **SOLID5** is a multi-field three-dimensional eight-node hexahedron. The fields incorporated into the element type are mechanical, electrical, temperature and magnetic. Temperature and magnetic degrees-of-freedom are set to zero at the start of the analysis to remove any influence on the behaviour of the transducer model. The required mechanical properties are: dielectric matrix (PERX), anisotropic mechanical stiffness matrix (ANEL), piezoelectric matrix (PIEZ), density (DENS) and mechanical damping co-efficient (DAMP).

- **FLUID30** is a three-dimensional eight-node hexahedron that models the fluid medium surrounding the transducer. The appropriate material properties are: speed of sound (SONC) and energy transmission co-efficient at any fluid-structure interface (MU).

- **LINK68** is a one-dimensional two-node link element that models electrical and temperature fields. The temperature degrees of freedom are set to zero so that the element acts as a purely resistive connection between two voltage degrees of freedom. The required properties are described in the Section 3.3.7. While it was not necessary, it was included in some models to ease the post-processing.

3.3 FINITE ELEMENT ANALYSIS TYPES

Equation (3.6) can be solved in several ways but sufficient constraints must be applied to ensure the matrix is non-singular. However care must be taken not to over-constrain the system forcing incorrect behaviour to result. While little can be assumed about the internal behaviour of the device, the behaviour at some of the boundaries is well-defined and can be defined during the pre-processing stage.

Once the model has been defined, it is analysed in the solution phase. There are several methods for performing this operation, the selection of which depends on the transducer operational conditions. For off-resonance operation, static analysis where the loss and mass matrix of the systems can be ignored, is applied. The resonances of the transducer are calculated from modal analysis of the system matrix equation. Finally to determine the performance of the transducer over a band of frequencies including any resonances, harmonic analysis utilising the complete set of matrices is used. The harmonic analysis allows the transmit and receive sensitivity of the transducer to be determined with the incorporation of electrical loading effects.

3.3.1 Boundary Conditions

To ensure the accurate results, the model must include the complete closed system because of the law of conservation of energy and of the fact that the principle of virtual work applies only to a closed system. This implies that the effect of any load media must be incorporated to complete the model and hence, the effect of a

decaying acoustic field extending to infinity needs to modelled [28]. This can be modelled as a fluid column with the pressure DOF set to zero at the open boundary. The effect is improved if an absorbing boundary is included at the boundary to simulate a non-reflecting surface. As these fluid media tend to be semi-infinite in nature meaning there is no reflected energy, special elements have been developed which model the medium purely as a boundary and a half-space behind it. These are called *boundary elements.* At the time of writing the thesis, the ANSYS package did not provide the necessary three-dimensional acoustic boundary elements but these will be included in a future revision of ANSYS V5.1 as the beta-release element, FLUID130, according to Rajakumar [29].

If the acoustic impedance of the surrounding medium is significantly different from the transducer, either much larger as would be the case for an extremely stiff material load or much lower as would be the case for in-air analysis, the boundary conditions are well defined as there is negligible energy transfer. For a *hard* boundary, there is zero strain (no movement) at the surface and for a *soft* boundary, there is zero stress (and accordingly zero pressure) at the surface. For the transducer systems studied in this thesis, none of the load media had higher acoustic impedances than the active material, so that hard boundaries were never encountered. However, many of the transducer systems were measured in air which is significantly softer than any of the piezoelectric materials.

The effect of the acoustic impedance, Z_{fluid}, of the fluid medium on the displacement of the surface of the transducer was analysed in Appendix C and the Equation C.10 for the surface displacement was derived. Considering this equation, it can be seen that if Z_{fluid} is extremely small compared to the piezoelectric charge constant of the piezoelectric material as is the case with in-air analysis, similar results would be obtained if Z_{fluid} is taken as zero. Hence, using a soft boundary would be an acceptable simplification. However, for in-water analysis where Z_{fluid} is approximately 1.5 MRayls, the frequency response would differ implying that the soft boundary could not be used and other methods discussed in Section 3.6.6 have to be used.

Boundary conditions in the mechanical domain are supplemented by electric potential boundary conditions applied at the:

- **Bottom Electrode** - the voltage DOFs in the plane of the bottom electrode are set to zero. This represents the electrical ground for the system.
- **Top Electrode** - the voltage DOFs in the plane of the top electrode are coupled so that their values are identical. This reduces the rank of the resultant matrix equation as only one of the voltage DOFs needs to be included in the analysis. For the simple case of no electrical circuit between the voltage source and the active electrode, the value of the voltage across the electrodes can be set to be a fixed 1 volt.

If there exists an axis of symmetry within the physical transducer, the forces across the boundary would be in equilibrium as identical conditions occur at each side of the axis. Hence, there would be no movement across it although there can be movement along the axis. The axis can be modelled by setting the displacement value across the axis to zero. Only the part of the model on one side needs to be modelled and the response of the other part would be identical. The axis becomes a boundary and is called a *symmetric boundary* of the model and is implemented in the ANSYS package by defining a plane to be a symmetric boundary. This simplification was proven mathematically in reference [7].

3.3.2 Static Analysis

If the dynamic frequency of operation is sufficiently small that the time derivatives of the DOFs approaches zero, the effect of the loss and mass matrix on the system can be ignored. Equation (3.6) can then be re-written as:

$$\begin{bmatrix} [K_{uu}] & [K_{u\phi}] \\ [K_{u\phi}]^t & [K_{\phi\phi}] \end{bmatrix} \begin{bmatrix} \underline{u} \\ \underline{\Phi} \end{bmatrix} = \begin{bmatrix} \underline{F} \\ \underline{Q} \end{bmatrix} \qquad \textbf{Eqn. 3.7}$$

As the vast majority of the nodes are not connected to all the other nodes but rather to their immediate neighbours, the matrices can be considered sparse allowing the use of *wavefront* or *frontal* methods [1] to solve the matrix equation. ANSYS includes a set of commands that attempts to optimise the ordering of the nodes to minimise the bandwidth of the matrix and speed the solution of the problem. The bandwidth or wavefront of the matrix is defined as the maximum number of non-zero DOFs in each row or column.

The standard method of solving the matrix equation, $[A]\underline{x} = \underline{b}$, on a computer system is LU or triangular decomposition which has three stages:

1. Factorize [A] into [L][U] where L is a lower triangular matrix and U is an upper triangular matrix. The two matrices are calculated from a set of iterative equations.
2. Solve for [Y] by forward substitution in $[Y] = [L]^{-1}\underline{b}$. Inverting triangular matrices is a far simpler task than inverting the original matrix, [A].
3. Solve for $\underline{x}$ by back substitution in $[U]\underline{x} = [Y]$.

This process is equivalent to performing Gaussian elimination but in a form that is more readily implemented on computer. However, most matrices involved with the finite element modelling are symmetric positive-definite which allows LU decomposition to be modified to the *Cholesky* decomposition [30] and requires half the number of operations that LU decomposition does as a symmetrical positive-definite matrix can be decomposed into a lower triangular matrix and its transpose: $[A] = [L][L]^t$.

Cholesky decomposition can be modified to account for the sparse matrix and then the number of operations is dependent on the wavefront. The solution of the matrix equation is the single most important component for finite element analysis as it is the most time-intensive part of the modelling and the most restrictive to the modelling. It is for this reason that the FE models are designed to have as few nodes and degrees of freedom as possible but still be representative of what they model.

3.3.3 Modal Analysis

The determination of the natural resonant mode frequencies and their associated shapes is a principal application of finite element analysis. For the derivation of the analysis method, free, undamped vibration is assumed in the ANSYS package i.e. $\underline{F} = \underline{0}$, $\underline{Q} = \underline{0}$ and $[C_{uu}] = [0]$. The second part of Equation (3.6) can be re-formulated using the process of *condensation* as:

$$\begin{aligned} [K_{u\phi}]^t \underline{u} + [K_{\phi\phi}]\underline{\phi} &= \underline{0} \\ \underline{\phi} &= -[K_{\phi\phi}]^{-1}[K_{u\phi}]^t \underline{u} \end{aligned} \qquad \textbf{Eqn. 3.8}$$

Hence the voltage tensor can be removed from the matrix equation leaving Equation (3.6) as:

$$\begin{aligned} [M_{uu}]\ddot{\underline{u}} + \left([K_{uu}] - [K_{u\phi}][K_{\phi\phi}]^{-1}[K_{u\phi}]^t\right)\underline{u} &= \underline{0} \\ [M_{uu}]\ddot{\underline{u}} + [\bar{K}]\underline{u} &= \underline{0} \end{aligned} \qquad \textbf{Eqn. 3.9}$$

where $[\bar{K}]$ is the apparent stiffness matrix of the system.

All components of the displacement tensor $\underline{u}_i$ are considered to oscillate at the *i*th natural frequency of the device so that this tensor can be partitioned as:

$$\underline{u}_i = \underline{\psi}_i \cos(\omega_i t) \qquad \textbf{Eqn. 3.10}$$

where ω_i is the radial frequency of the *i*th natural mode; and

$\underline{\omega_i}$ is the eigenvector of the *i*th mode and represents the mode shape at that mode. Its components are real as no loss is included in the analysis.

The second derivative of the displacement tensor is then:

$$\underline{\ddot{u}_i} = -\omega_i^2 \underline{u_i} \qquad \textbf{Eqn. 3.11}$$

yielding the matrix form:

$$\left([\bar{K}] - \omega_i^2[M_{uu}]\right)\underline{u_i} = \underline{0} \qquad \textbf{Eqn. 3.12}$$

A condition for non-trivial solutions of Equation (3.12) is that the determinant must be zero:

$$\left|[\bar{K}] - \xi_i[M_{uu}]\right| = 0 \qquad \textbf{Eqn. 3.13}$$

where $\xi_i = \omega_i^2$. This is a form of an eigenvalue equation with solution set $\underline{\xi}$.

There are several methods of estimating the eigenvalues and their associated eigenvectors for symmetric positive definite matrices [30]. The standard hand-operated method of determining the characteristic equation is not applicable for the large matrices that are encountered in finite element analysis and hence, the matrix is normally passed through an orthogonal transformation to obtain a form where the eigenvalues can be easily determined. The transformation does not modify the eigenvalues of the equation because of its orthogonality. The eigenvectors are then given by substitution of the eigenvalues back into the original matrix equation. However, the calculation of the eigenvalues is approximate and inverse iteration is normally used to improve the estimate of the associated eigenvector. If the eigenvalue is not the largest, then convergence towards the eigenvector would be slow. The rate of convergence is increased by using the modified inverse matrix:

$$[\bar{A}]_i = ([\bar{K}] - \xi_i[M_{uu}])^{-1} \qquad \textbf{Eqn. 3.14}$$

where ξ_i is the estimate of the eigenvalue.

The classical orthogonal transformation method called Jacobi diagonalization transforms the matrix into a diagonal form by iteratively removing off-diagonal terms through the rotation of specific matrix columns. As the diagonal elements of a diagonal matrix are the eigenvalues, this iterative method will converge on the solution. It has been shown that each rotation increases the sum of the squares of the diagonal terms and decreases the sum of squares of the off-diagonal terms indicating the method does converge eventually. The rate of convergence is improved by selecting the off-diagonal term with the largest magnitude at each iteration. The main application of this method is to small matrices or matrices with small off-diagonal terms which are conditions that are seldom met in finite element analysis. Householder tridiagonalization is a method used by many FE packages. In this method, the matrix is transformed to a tridiagonal matrix from which the eigenvalues can be calculated directly. Each step of the transformation removes a column of the matrix except for the diagonal and super-diagonal terms. Thus the method is non-iterative and the transformation is only applied *N-1* times for a rank *N* matrix.

Even though the displacements in mode shapes are named as such, they do not represent the true displacements but rather relative amplitudes of displacement for each natural frequency. This is considered for the post-processing of modal analysis results and shows the reason for the more advanced analysis discussed in the following Section.

3.3.4 Harmonic Analysis

In harmonic analysis, the excitation is assumed to occur at a single radial frequency, ω. Then the components of the displacement, voltage, force and charge tensors can be represented as a complex amplitude and an exponential time-varying term, $e^{j\omega t}$. The ANSYS package allows loss in the form of the mechanical loss matrix, $[C_{uu}]$ which is defined as:

$$[C_{uu}] = \alpha[M_{uu}] + \sum_{nmat=1}^{NMAT} \beta_{nmat}\left[K_{nmat}^{uu}\right] \qquad \textbf{Eqn. 3.15}$$

where α and β_{nmat} are the Rayleigh damping constants;

NMAT is the number of materials present in the model;

$[K_{nmat}{}^{uu}]$ is the stiffness matrix for all the elements consisting of material *nmat*; and

β_{nmat} is the damping constant associated with material *nmat*.

α represents inertial damping which is inversely proportional to frequency and depends on the mass distribution of the model. β_{nmat} represents structural damping which is inherent in every mechanical body and is directly proportional to frequency. In the ANSYS package, α could be set for a model but not for an individual material. Hence, more emphasis for the model damping was placed on β_{nmat} which could be adjusted for individual materials.

The damping co-efficient, ζ_{nmat}, for the material *nmat* used in this thesis is related to the structural damping by the formula:

$$\zeta_{nmat} = 10\log_{10}(\beta_{nmat}) \qquad \textbf{Eqn. 3.16}$$

and is expressed in decibels.

For an input scalar value of ω, the left hand side of the matrix Equation (3.6) can be combined into a single matrix giving a final form $[A]\underline{x} = \underline{b}$. Then the matrix solution techniques discussed in Section 3.3.2 can be utilised with the consideration that the scalars within the matrices are complex values.

An advantage of harmonic analysis is that harmonic load conditions can be applied to the model to simulate the transducer under operation. An acoustic transducer has two main functions:

- Conversion of input electrical power to output acoustic power. It is measured as transmit sensitivity and is discussed in Section 3.3.5.
- Conversion of incident acoustic power to output electrical power. It is measured as receive sensitivity and is discussed in Section 3.3.6.

If the transducer is operated in the pulse-echo mode of operation, the transmit and receive responses for the single transducer are combined by multiplying the sensitivities to obtain the voltage-to-voltage response. The pitch-catch response for a separate transmitter and receiver is generated in a similar manner by combining the transmit response of the transmitter and the receive response of the receiver. This neglects any attenuation that occurs in the medium between the transmitter and receiver.

3.3.5 Transmission Analysis

Bobber [31] defined the transmit sensitivity of a transducer in terms of the transmitting voltage response (TVR) or the transmitting current response (TCR). TVR is the ratio of the acoustic pressure produced in the fluid at a distance of 1 metre from the acoustic centre of the transducer along its acoustic axis to the input voltage at the electrical port of the transducer. TCR has a similar definition but the input current is substituted for the input voltage. The finite element model simulates a small section of the transducer to emulate the behaviour of the whole transducer. As this analysis does not include any of the edge effects of the plate, it is equivalent to assuming that the active layer extends to infinity in the lateral directions. For such an arrangement, the pressure produced at the surface of the transducer will propagate with no spherical or cylindrical spreading. If it is assumed that there is no attenuation of the acoustic wave with distance, the average pressure at the transducer surface will be the same as the pressure at 1 metre. Then, the transmit sensitivity, $S_{TX}(\omega)$, can be calculated as the ratio of the resultant pressure, $\bar{p}_{out}(\omega)$, at the surface of the

transducer to the magnitude of the voltage, $|\hat{V}_{in}(\omega)|$, applied across the two electrodes at the frequency, ω, giving the expression:

$$S_{TX}(\omega) = \frac{\overline{P}_{out}(\omega)}{|\hat{V}_{in}(\omega)|} \qquad \textbf{Eqn. 3.17}$$

As can be seen in Figure 3.3, the model is sufficient to include all the values necessary to calculate the sensitivity.

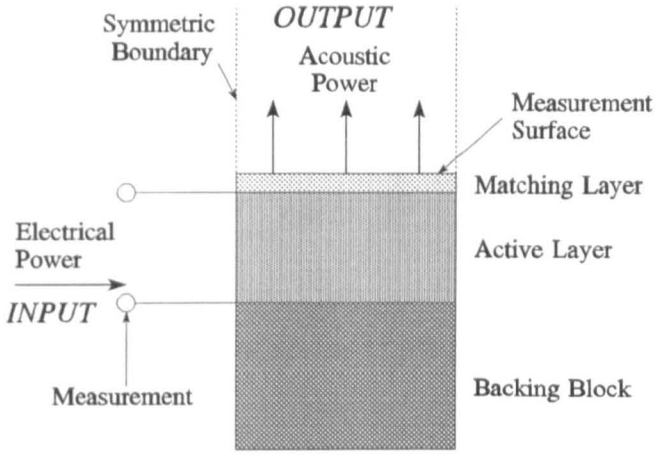

Figure 3.3: Evaluation of the Transmit Sensitivity

The resultant pressure used in Equation (3.17) is calculated as the root-mean-square result for the values produced at the all the nodes on the surface of the transducer as the acoustic energy contained within an acoustic wave is proportional to the square of the magnitude of local pressure transient, $\hat{p}_{out}(\underline{r},\omega)$. In the context of the finite element model, the acoustic power, $\hat{P}_n(\omega)$, flowing through the surrounding area, A_n, of the *n*th node is given by:

$$P_n(\omega) = \frac{|\hat{p}_n(\omega)|^2 . A_n}{Z_{fluid}} \qquad \textbf{Eqn. 3.18}$$

where $\hat{p}_n(\omega)$ is the complex pressure output from the node; and

Z_{fluid} is the specific acoustic impedance of the fluid load.

The total power output, $\hat{P}^{out}_{acoustic}(\omega)$, across the surface of the transducer is the integral over the surface of the power produced around each node:

$$\hat{P}^{out}_{acoustic}(\omega) = \frac{\sum_{n=1}^{NODE} \left(|\hat{p}_n(\omega)|^2 . A_n \right)}{Z_{fluid}} \qquad \textbf{Eqn. 3.19}$$

where NODE is the number of nodes on the surface of the transducer model.

The average acoustic intensity across the surface which is given by the acoustic power per unit area, can be calculated as:

$$\begin{aligned} \bar{I}_{acoustic}(\omega) &= \frac{\bar{p}_{out}(\omega)^2}{Z_{fluid}} \\ &= \frac{\sum_{n=1}^{NODE} \left(|\hat{p}_n(\omega)|^2 . A_n \right)}{Z_{fluid} . \sum_{n=1}^{NODE} A_n} \end{aligned} \qquad \textbf{Eqn. 3.20}$$

where $\bar{p}_{out}(\omega)$ is the equivalent average pressure output required to generate the same acoustic intensity. Rearranging Equation (3.20) yields:

$$\bar{p}_{out}(\omega) = \sqrt{\frac{\sum_{node=1}^{NODE} \left(|p_{node}(\omega)|^2 . A_{node} \right)}{\sum_{node=1}^{NODE} A_{node}}} \qquad \textbf{Eqn. 3.21}$$

and this is the formula used to calculate the pressure term in Equation (3.17).

It is important to note that Equation (3.17) neglects the energy dissipated from the back surface of the transducer as it is assumed to be absorbed by the structures surrounding the transducer and hence, cannot be included in the sensitivity calculation.

The transmit sensitivity is normally expressed in decibels relative to 1 $\mu Pa.V^{-1}$ and is called Transmitting Voltage Response (TVR) [7]:

$$TVR(\omega) = 20\log_{10}\left(S_{TX}(\omega)\right) + 120\ dB\ re\ 1\mu Pa.V^{-1} \qquad \textbf{Eqn. 3.22}$$

As the ANSYS package does not implement losses within the fluid, the fluid is considered lossless at the surface of the transducer. Then the specific acoustic impedance of the field can be assumed to be real according to Kossoff [32] and equal to the product of the density of the fluid and the speed of sound within the fluid.

A problem that was encountered for models which utilise the soft boundary condition to simulate a semi-infinite air medium, was that no pressures were produced by the analysis. However, the output pressure could be calculated from the displacements across the boundary using the formula:

$$\hat{p}_n(\omega) = j\omega Z_{air} \hat{D}_n(\omega) \qquad \textbf{Eqn. 3.23}$$

where $\hat{p}_n(\omega)$ is the normal pressure produced at the surface of the transducer;

Z_{air} is normally taken as 423 Rayl; and

$\hat{D}_n(\omega)$ is the complex displacement in the *3* direction at node *n*.

3.3.6 Reception Analysis

It was initially thought that a modification of the complete transmitter model could be utilised to implement the receive scenario of a pressure wave impinging on the front surface of the transducer. Then the receive sensitivity of the transducer would be calculated as the magnitude of the voltage produced by an incoming wave of unity pressure. This meant that the construction of the model would remain essentially the same as for the transmitter model.

However, the problem of defining the unity pressure front remained. It could have been designated as a plane in front of the transducer but this would negate the effect of the absorbing boundary condition in the fluid to simulate a fluid half-space on the front surface of the transducer. The impinging pressure wave could not be converted into a displacement at the surface as the secondary piezoelectric effect within the active layer produces a negative pressure within the device which would result in a reduced resultant pressure at the transducer surface. A possible solution is to assume that there exists infinite electrical resistance between the electrodes to minimise the secondary piezoelectric action implying that the pressure at the surface of the transducer can be taken as that of the incoming pressure wave. This is restrictive and not accurate as it represents a single possible electrical load case. Another solution to the definition of the receiver model is to use a time-gated pressure wave and implement the model in the time domain. Then the concept of an semi-infinite half-space is no longer required. This is a valid solution but would require significantly more processing than using a frequency-domain model for a similar frequency analysis as performed in the previous Section. So, in summary, there is no obvious receiver model for this application.

However, the Rayleigh reciprocity theorem [31] presented a possible solution. This states that, in any system composed of linear bilateral impedances, if a force E is applied in any branch A and the response I is measured in any branch B, their ratio will be equal to the ratio obtained if the force E is applied in the branch B and the response I is measured in branch A. According to Beranek [33], this implies that there is a reciprocity constant, J(ω), for which the following two expressions hold true:

$$\begin{aligned} \left|\bar{P}_{out}(\omega)\right| &= J(\omega)\left|\hat{I}_{in}(\omega)\right| \\ \left|\hat{V}_{out}(\omega)\right| &= J(\omega)\left|\bar{U}_{in}(\omega)\right| \end{aligned} \qquad \textbf{Eqn. 3.24}$$

where $\hat{I}_{in}(\omega)$ is the input complex current generated by the input voltage;

$\hat{V}_{out}(\omega)$ is the output complex voltage generated under receive conditions;

and

$\bar{U}_{in}(\omega)$ is the input volume velocity of the acoustic wave impinging on the transducer under receiver conditions.

These expressions can be modified to calculate the receive sensitivity. The first is related to the transmit sensitivity through Ohm's law:

$$\left|\hat{I}_{in}(\omega)\right| = \frac{\left|\hat{V}_{in}(\omega)\right|}{\left|\hat{Z}_T(\omega)\right|} \qquad \textbf{Eqn. 3.25}$$

where $\hat{Z}_T(\omega)$ is the complex electrical impedance of the transducer.

Hence, the reciprocity parameter can be calculated as:

$$J(\omega) = \frac{|\bar{P}_{out}(\omega)|}{|\hat{V}_{in}(\omega)|}.|\hat{Z}_T(\omega)| \qquad \text{Eqn. 3.26}$$

$$= S_{TX}(\omega).|\hat{Z}_T(\omega)|$$

Similarly, from Beranek[33]:

$$\bar{U}_{in}(\omega) = \frac{\bar{p}_{in}(\omega).A_t}{Z_{fluid}} \qquad \text{Eqn. 3.27}$$

where $\bar{p}_{in}(\omega)$ is the pressure impinging on the surface of the transducer during reception and is taken as a constant across the surface; and

A_t is the area of the transducer model.

Then, from Equation (3.24):

$$\frac{|\hat{V}_{out}(\omega)|}{|\bar{p}_{in}(\omega)|} = \frac{J(\omega)A_t}{Z_{fluid}} \qquad \text{Eqn. 3.28}$$

The receive sensitivity, $S_{RX}(\omega)$, is defined as the voltage generated between the electrodes by a unity pressure wave impinging on the front face of the transducer:

$$S_{RX}(\omega) = \frac{|\hat{V}_{out}(\omega)|}{|\bar{p}_{in}(\omega)|} \qquad \text{Eqn. 3.29}$$

Substituting this definition into a combination of Equations (3.26) and (3.28) gives:

$$S_{RX}(\omega) = \frac{|\hat{Z}_T(\omega)|A_t}{Z_{fluid}}.S_{TX}(\omega) \qquad \text{Eqn. 3.30}$$

which allows the receive sensitivity to be generated from the results of the transmit model scenario.

The receive sensitivity can be expressed in terms of decibels relative to 1 V.μPa^{-1} and is called the Far-Field Voltage Sensitivity (FFVS):

$$FFVS(\omega) = TVR(\omega) - 240 + 20\log_{10}\left(\frac{|\hat{Z}_T(\omega)|A_t}{Z_{fluid}}\right) dB\ re\ 1V.\mu Pa^{-1} \qquad \textbf{Eqn. 3.31}$$

The bandwidth for both the transmit and receive sensitivity are calculated as the -3 dB fractional bandwidth and is expressed as a percentage. The centre frequency for each sensitivity is taken as the frequency of maximum value and is the frequency by which the bandwidth is divided to generate the fractional bandwidth. The transmit bandwidth is denoted by BW(TX) and receive bandwidth is denoted by BW(RX) for the purpose of the thesis.

In conclusion, there is no requirement to produce a frequency-domain finite element receiver model and only a transmit model needs to be implemented to obtain both the transmit and receive sensitivities of the transducer system. The reciprocity parameter, J(ω), is a single quantity that indicates the performance of the transducer and can be used to compare different transducer configurations. However, it cannot be measured easily experimentally but can only be derived.

3.3.7 Electrical Loading of the Transducer

Electrical loading was introduced into the finite element model through the use of the thermal-electric element, LINK68. The resistance of the element in the model is determined by the formula:

$$R = \frac{\rho_R l}{A_X} \qquad \textbf{Eqn. 3.32}$$

where R is the resistance of the element;

ρ_R is the resistivity of the material in the element;

l is the length of the element; and

A_X is the cross-sectional area of the element.

The element does not directly affect the mechanical domain of the model but exists in the three dimensional model in that it connects two nodes together. For ease of use, the cross-sectional area is set to be identical to the length making the resistance equal to the resistivity of the material. The element is placed with one node on the top electrode and the other node created remotely from the model. Then the input voltage is applied to the new created node. The effect of the resistor on the device performance is minimal as the response of the transducer is normalised to the voltage that appears at the electrodes in the post-processing stage.

3.4 POST-PROCESSING OF RESULTS

The final stage of the modelling process is to extract the desired information from the computed model and present it in a form that can be understood by the user. To achieve this, a suite of software programs was developed which processed the result file from the solution phase to produce the required data for each type of analysis. These programs are outlined in appendix A and all the graphs displaying finite element results in this thesis were obtained with the aid of these programs.

3.4.1 Information gained from Modal Analysis

As mentioned earlier in this Chapter, modal analysis produces both the mode shapes and natural frequencies of the transducer under different resonant conditions. Employing this technique, the resonant and anti-resonant frequencies of a particular mode are obtained by applying appropriate voltage boundary conditions. The resonant or electrical resonance frequencies are estimated by short-circuiting the two electrodes which is achieved by setting the voltage at the top electrode to be zero. The anti-resonant or mechanical resonance frequencies are estimated by leaving the electrodes isolated and hence, open-circuited. The electromechanical coupling factor for each mode can be calculated for each mode by using the formula [9]:

$$k_t^2 = \frac{\pi}{2}\frac{f_{elec}}{f_{mech}} cotan\left(\frac{\pi}{2}\frac{f_{elec}}{f_{mech}}\right) \qquad \textbf{Eqn. 3.33}$$

where f_{elec} and f_{mech} are the electrical and mechanical resonance frequencies of the mode respectively.

This information gives the strength of coupling for each mode but not the "desirability" or *quality* of the mode. Even though the absolute displacements cannot be calculated from the modal analysis, the displacements are in the correct ratio to each other. Hence, the surface dilation quality (Q_{dil}) [6], describing the uniformity of the surface displacement, can be calculated. This defines the piston-like nature of the transducer by examining the UZ displacements at each node on a user-defined surface of the transducer. Dilation qualities approaching unity indicates uniform surface dilation of both phases and confirm that the composite is operating as an effective homogenous medium. When the thickness mode is coupled with lateral modes, parts of the surface can vibrate in anti-phase drawing Q_{dil} towards zero. The surface dilation quality can be calculated as:

$$Q_{dil}(\omega_i) = \frac{\sum_{n=1}^{NODE} D_n(\omega_i) A_n}{D_{max}(\omega_i) \sum_{n=1}^{NODE} A_n} \qquad \textbf{Eqn. 3.34}$$

where ω_i is the radial frequency of the *i*th mode;

D_n is the nodal displacement in the *3* direction of the *n*th surface node; and

D_{max} is the maximum nodal displacement on the surface.

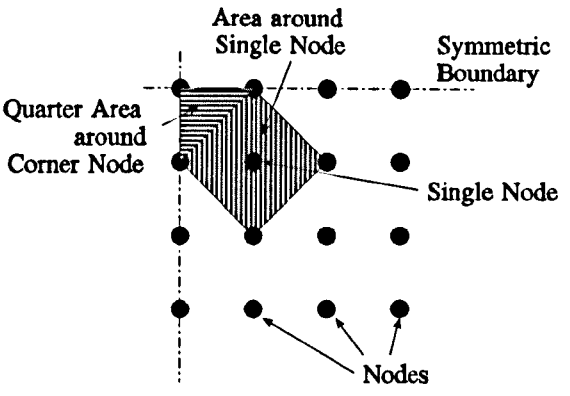

Figure 3.4: The area surrounding a node of an element

The area, A_n, surrounding a node is calculated as the region bounded by its nearest neighbours as shown in Figure 3.4. This method is valid except at symmetrical boundaries where the node is not be completely surrounded by neighbours. This is corrected by doubling the area for every symmetrical boundary on which the node exists.

As the areas surrounding each of the nodes overlaps with its four neighbours, the summation of the area is not the total surface area of the model, A_t, but rather a multiple of the area. However this is accounted for in Equation (3.34).

3.4.2 Information gained from Harmonic Analysis

The operating electrical impedance of the model can be calculated by noting that in a harmonic situation, the current and charge are related by:

$$\hat{I}(\omega) = j\omega\hat{Q}(\omega) \qquad \textbf{Eqn. 3.35}$$

where $\hat{I}(\omega)$ is the electrical current entering the transducer; and

$\hat{Q}(\omega)$ is the reaction charge to the electric potential generated.

However, since only part of the transducer is modelled, the charge of the model needs to be modified to be the total charge, $\hat{Q}_{exp}(\omega)$, of the transducer through normalisation by the surface area of the physical transducer, A_{exp} as:

$$\hat{Q}_{exp}(\omega) = \hat{Q}(\omega)\frac{A_{exp}}{A_t} \qquad \textbf{Eqn. 3.36}$$

Hence, the electrical impedance equation for the transducer being modelled for both transmission and reception conditions, is:

$$\hat{Z}_T(\omega) = \frac{\hat{V}(\omega)A_t}{j\omega\hat{Q}(\omega)A_{exp}} \qquad \textbf{Eqn. 3.37}$$

where $\hat{V}(\omega)$ is the applied complex voltage.

The dilation quality factor can be generated as detailed in the previous Section but is calculated as a function of frequency rather than at individual resonance modes. The final parameter is average displacement of the surface per volt of applied electric potential and is given by the formula:

$$\left|\hat{d}_{ave}(\omega)\right| = \frac{\left|\hat{D}_n(\omega)\right|_{max} Q_{dil}(\omega)}{\left|\hat{V}(\omega)\right|} \qquad \textbf{Eqn. 3.38}$$

where $\left|\hat{d}_{ave}(\omega)\right|$ is the average surface displacement of the surface in the *3* direction;

and

$\left|\hat{D}_n(\omega)\right|_{max}$ is the maximum amplitude of displacement for any node at the surface.

3.5 SINGLE PIEZOELECTRIC MATERIAL MODEL

This Section covers the verification of the general finite element models for piezoelectricity and the assumptions made to generate the transducer model. The simplest piezoelectric model is that of single piezoelectric crystal. The models examined in this Section consist of different shapes of the piezoceramic, PZT-5A, which are shown in Figure 3.5. Each shapes introduces resonances whose frequencies can be estimated theoretically and measured experimentally.

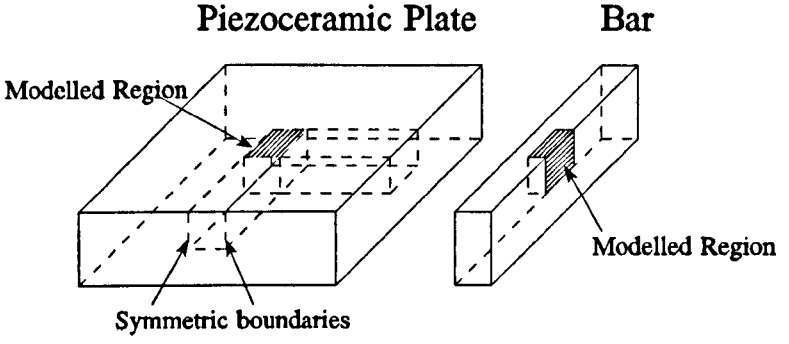

Figure 3.5: Shapes of Piezoceramic Models

3.5.1 Piezoelectric Plate Model

The first model to be examined was that of an infinite plate of PZT-5A piezoceramic. As the plate is infinite in the *1* and *2* directions, the plate can only expand and contract in the *3* direction. This model was to test the piezoelectric element SOLID5 and to verify the assumption of a soft boundary against experiment for in-air analysis. All resonances modes of such a plate occur purely in the *3* or thickness direction. The simple model can be analyzed theoretically to obtain the resonance frequencies and surface displacements. From wave theory, the *n*th harmonic of the mechanical resonance occurs at:

$$f_{mech}^{n} = \frac{n\nu}{2t_3} \quad \forall\ n = 1,3,5,... \qquad \textbf{Eqn. 3.39}$$

where ν is the speed of sound in the *3* direction and is 4323m.s^{-1} for PZT-5A; and

t_3 is the thickness of the plate.

There are nulls in the response spectrum at the even harmonics. The electrical resonances can be generated using Equation (3.33) as the thickness mode coupling factor for PZT-5A is 0.486.

The behaviour of the piezoelectric plate was generated from the theory derived in Appendix C. The results generated by the finite element analysis using the material parameters specified in Appendix B were compared to the theory derived in Appendix C for the behaviour of a piezoelectric plate. A piezoceramic plate of PZT-5A, height of 1.0 mm, has a theoretical fundamental electrical resonance of 1.974 MHz and mechanical resonance of 2.161 MHz. The modal analysis of the finite element model produced an electrical resonance of 1.974 MHz and mechanical resonance of 2.218 MHz which closely matches the theoretical analysis.

3.5.2 Piezoelectric Bar Model

For a bar, there is not only the thickness mode resonances as with a infinite plate but also resonances in the finite width dimension shown in Figure 3.5. The two types of modes can couple to shift the resonance frequencies. Results for the simulation of the piezoelectric bars are detailed in Table 3.2 to 3.5. The frequencies displayed in the Tables are given in kilohertz. Five bars of PZT-5A ceramic were characterised and modelled. The lengths of all the bars were sufficient that there were no significant length modes in the frequency range of interest. So only the height and width of the bars have been specified. The dimensions are given in Table 3.1.

The tables show good correlation between the experimental results and those produced by the finite element model. Discrepancies between the two sets can be explained by the fact that the manufacturer's data for the material properties was used for the finite element model and the values in practice can vary by as much as 10% between batches.

Table 3.1: Dimensions of Each Bar

Bar	Height (mm)	Width (mm)
1	7.88	1.88
2	7.84	2.94
3	7.89	3.67
4	7.87	4.49
5	7.87	5.37

Table 3.2: Fundamental Thickness Mode Electrical Resonance Frequencies

Bar	Experimental	Modal Analysis	%error	Harmonic Analysis	%error
1	199	190	-4.7	188	-5.5
2	197	188	-4.6	189	-4.1
3	191	184	-3.7	185	-3.1
4	187	181	-3.2	179	-4.3
5	177	175	-1.1	175	-1.1

Table 3.3: Fundamental Thickness Mode Mechanical Resonance Frequencies

Bar	Experimental	Modal Analysis	%error	Harmonic Analysis	%error
1	238	243	+2.1	238	0.0
2	238	242	+1.7	238	0.0
3	235	238	+1.3	235	0.0
4	232	233	+0.4	228	-1.7
5	221	224	+1.4	222	+0.5

Table 3.4: Fundamental Width Mode Electrical Resonance Frequencies

Bar	Experimental	Modal Analysis	%error	Harmonic Analysis	%error
1	642	693	+7.9	648	+0.9
2	510	520	+1.9	515	+1.0
3	400	413	+3.3	407	+1.8
4	324	333	+2.8	327	+0.9
5	273	277	+1.5	273	0.0

Table 3.5: Fundamental Width Mode Mechanical Resonance Frequencies

Bar	Experimental	Modal Analysis	%error	Harmonic Analysis	%error
1	655	707	+7.9	655	0.0
2	522	530	+1.5	527	+1.0
3	404	417	+3.2	416	+3.0
4	331	337	+1.8	338	+2.1
5	277	283	+2.2	281	+1.4

3.6 1-3 CONNECTIVITY PIEZOCOMPOSITE MODELS

The main purpose of this thesis was to analyse the behaviour of 1-3 piezocomposite transducer for different applications using the finite element modelling. The starting point was the eighth-symmetry model verified through extensive comparison with experiment by Hossack [34]. As the model used by Hossack was extended for the work, the original model is covered briefly in Section 3.6.1. The extra components of a backing block, matching layers and fluid loading were included to allow the transducer to be simulated in its operating environment. The effect of each component on the behaviour of the transducer system was verified with experiment where possible. Hence, the output from this Section is the complete finite element model that was used to generate a set of design guidelines for 1-3 piezocomposite transducers.

3.6.1 Eighth-Symmetry Finite Element Model

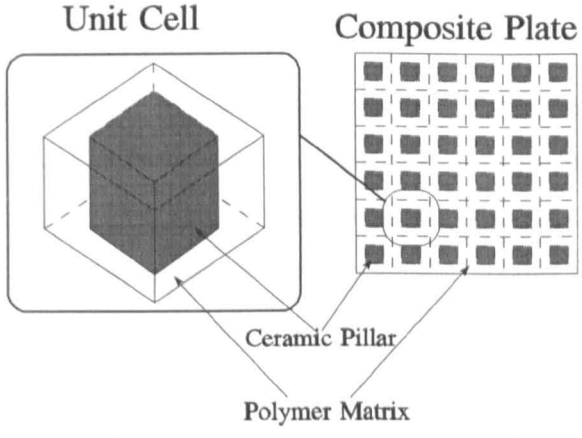

Figure 3.6: Unit Cell of Piezocomposite Plate

The simplest form of a finite element model for a 1-3 piezocomposite plate is that of the eight-symmetry model developed by Hossack and Hayward [35]. The composite plate can be divided into a set of unit cells, each of which consisting of a single piezoceramic pillar with its surrounding polymer as shown in Figure 3.6.

The behaviour of the unit cell is assumed to be indicative of the response of the each of the unit cells in the entire plate. As the unit cell is symmetrical about all three axes, only an eighth of the cell needs to be modelled, as detailed in Figure 3.7. There are five symmetric axes in the model: x=0; y=0; z=0; x=t2; and y=t2. The model is only free to move at the surface z=h2.

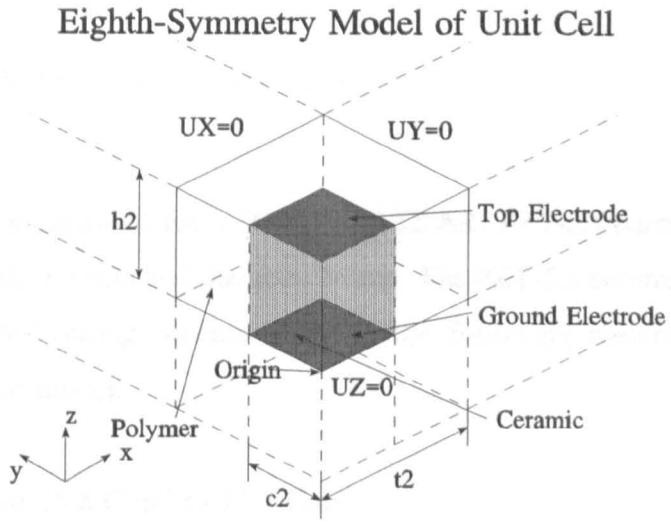

Figure 3.7: Eighth-symmetry Finite Element Model

The electrodes were placed at the surfaces, 0V at z=0 for the ground electrode and 1V at z=h2 for the live electrode. This is equivalent of applying 2V across the full height of the transducer but this is accounted in the post-processing. The internal geometry of the 1-3 piezocomposite finite element model is defined by three parameters for a square pillar:

- **Ceramic Half-Width (c2)** - half-width of the ceramic pillar;
- **Cell Half-Width (t2)** - half-width of the unit cell; and
- **Half-Height (h2)** - half-height of the unit cell.

From these three parameters, the following values can be calculated:

- Percentage Volume Fraction: $VF = \left(\frac{c2}{t2}\right)^2 \times 100\%$;

- Aspect Ratio: $AR = \frac{c2}{h2}$; and

- Kerf Width: $KW = 2(t2 - c2)$

The model was analysed for a 50% VF, 0.22 AR, PZT-5A/hardset piezocomposite disc with height 3.3 mm and diameter 30mm. The PZT-5A ceramic in the pillars was slightly depoled during manufacture and the following material properties were modified in the model:

- e_{33} from 15.8 $C.m^{-1}$ to 14.5 $C.m^{-1}$
- c_{33}^{E} from 11.1 GPa to 12.0 GPa

The impedance profile from experiment and the finite element model for in-air analysis are compared in Figure 3.8 where it can be seen that there is excellent correlation between the finite element model and experiment. The ordinate axis in Figure 3.8 is given in decibels relative to 1Ω so that the magnitude at the electrical resonance can be seen clearly and can be compared to the magnitude of the mechanical resonance. Also the position of the electrical resonance is well-defined on the curve. If a linear scale is used, the impedance magnitude of the mechanical resonance is normally so much larger than that of the electrical resonance that the magnitude of the electrical resonance is indicated as zero on the curve. This practice is similar to that adopted by Lerch [6]. The results from the linear systems model, one of the constrained-dimensional models, was included to show that in the case of uni-modal response as shown in Figure 3.8, such models do produce the correct results. Figure 3.13 shown in Section 3.6.4 is an example where the piezocomposite

does not display uni-modal response and the linear systems model did not produce good correlation with experiment. The meshing was the same as used by Hossack.

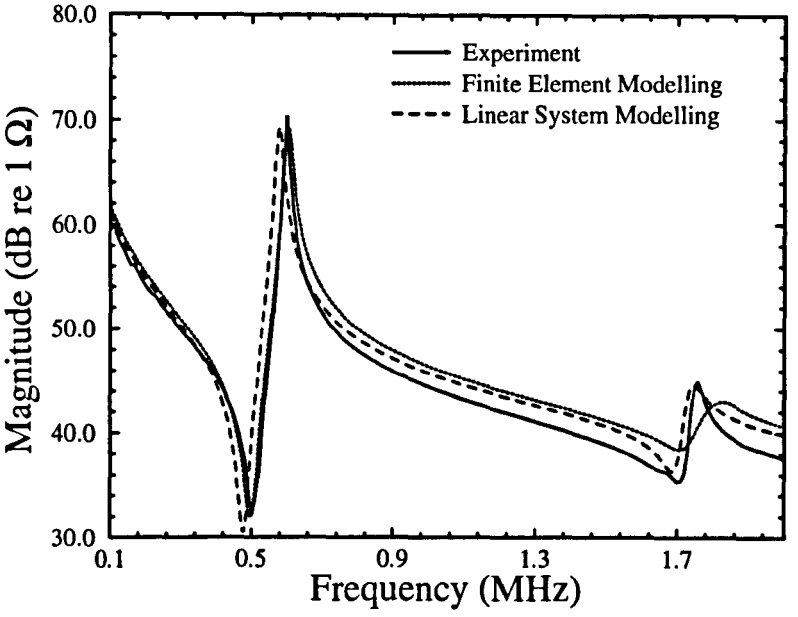

Figure 3.8: Impedance Profile of 50% VF 0.2 AR PZT-5A/hardset Composite

3.6.2 Implementation of Pillar Shape

An investigation into the effect of different pillar shapes on the frequencies of lateral modes relative to that of the thickness mode was performed and is detailed in Chapter 4. The structure described previously is not only valid for pillars with square cross-sections but also for cylindrical and triangular pillars that were included in the investigation. For these types of pillar shape, the definition of pillar width is modified according to the shape:

- For the cylindrical pillars, the modified expressions are:

$$AR_{cyl} = \frac{\phi}{height}$$

$$VF_{cyl} = \frac{\pi\phi^2}{4d_\phi^2}$$

- For the triangular pillars, the modified expressions are:

$$AR_{tri} = \frac{\min(b,c)}{height}$$

$$VF_{tri} = \frac{b^2}{2d_b^2} = \frac{c^2}{2d_c^2}$$

where min(b,c) is the minimum of b and c.

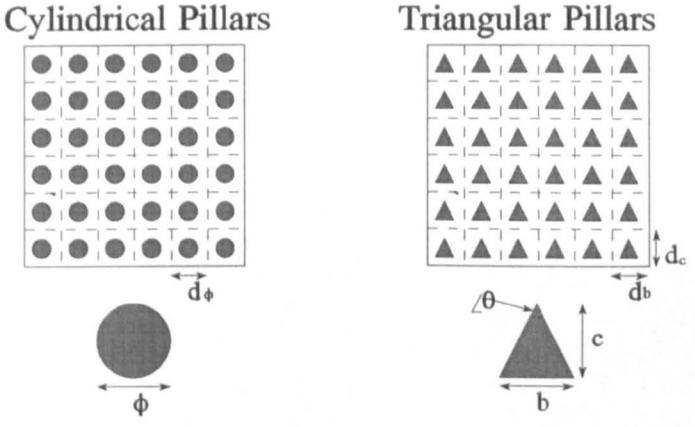

Figure 3.9: Pillar Shapes for Piezocomposites

The definitions of the symbols are illustrated in Figure 3.9. The triangular pillars are isosceles indicating that the exact shape is defined by a single angle, θ, and that the cross-section is only symmetrical about a single axis and not both as is the case with the other two pillar shapes. Hence, a quarter-symmetry model was used and the UZ degree of freedom for each node on the x=0 plane was coupled to have the same value as the corresponding node on the x=t plane. This was to simulate the identical movement that would experience by these two planes in the piezocomposite plate.

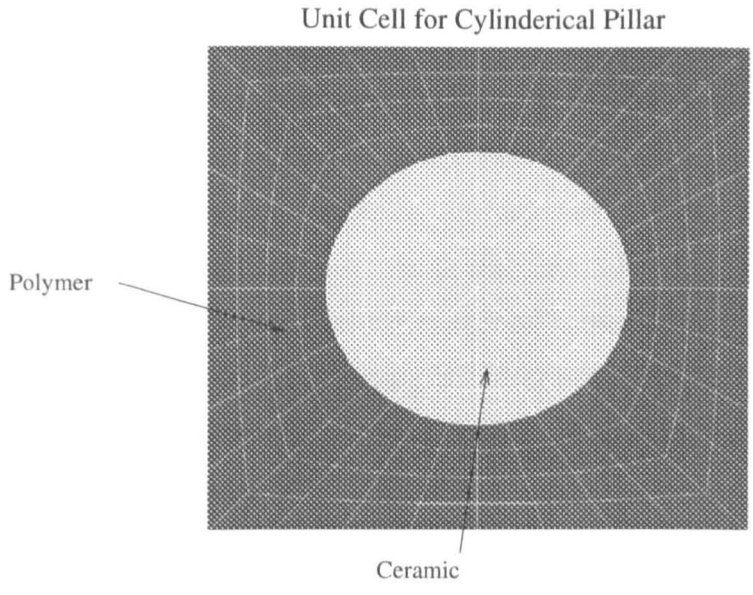

Figure 3.10: Cylinderical Pillar in Unit Cell

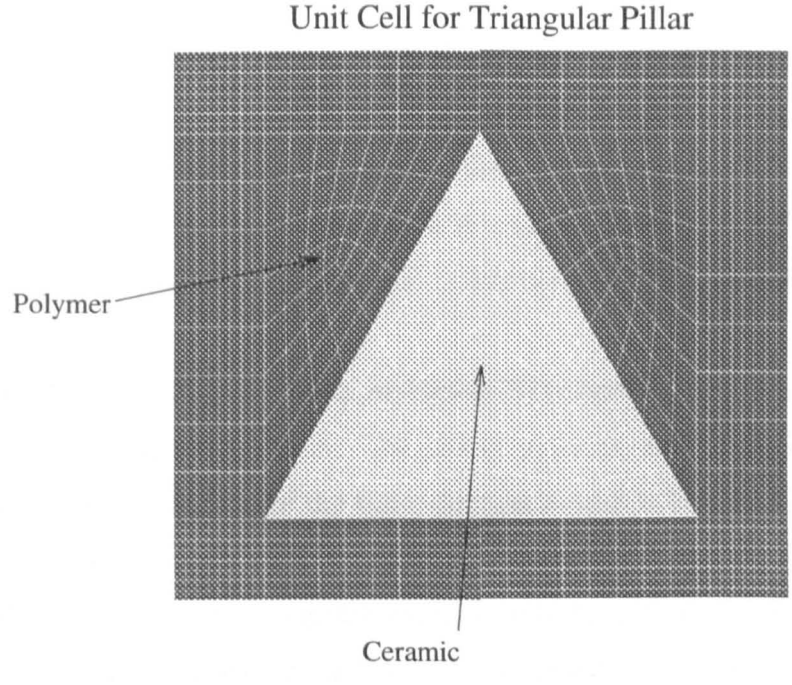

Figure 3.11: Triangular Pillar in Unit Cell

The shape is not "flipped" as with the symmetric shapes but replicated implying the response at each boundary is identical.

A point to consider when meshing these shapes, is that the elements can no longer be cuboidal as with the square pillar geometry. Hence, the shape and distribution of the elements becomes important. While the operator can attempt to define his own mesh, most commercial packages will mesh the elements about the geometrical centroid of the shape being meshed which in general is the optimal mesh. Examples of the meshing for the cylinders and triangles are shown in Figures 3.10 and 3.11. These figures were obtained directly from the ANSYS packages and were the meshes used for the simulations presented in Chapter 4.

3.6.3 Inclusion of Ancillary Components

As was discussed in the previous Chapter, ancillary components such as backing blocks and matching layers can be incorporated into the transducer system to further modify and enhance the transducer performance for a specific application. The addition of each component to the finite element model is verified by comparison of the response of the new model to experiment and the linear systems model (LSM) of 1-3 piezocomposite transducers detailed in Hayward and Hossack [36]. The LSM has been extensively verified for uni-modal behaviour of the piezocomposite.

An example of the models is shown in Figure 3.12 showing the position of the backing block and matching layer. The linear systems model is included for comparison. From examination of the finite element model in Figure 3.12, it can be seen that the model does not retain its symmetry about the *1-2* plane (z=0) and the compact nature of the eighth-symmetry model cannot be utilised. This implies that the full height of the composite plate has to be modelled so that the backing block can be added below (in terms of the *3* axis) the plate and a matching layer above the plate. The new model is named the *full-height* model to differentiate it from the eighth-symmetry model.

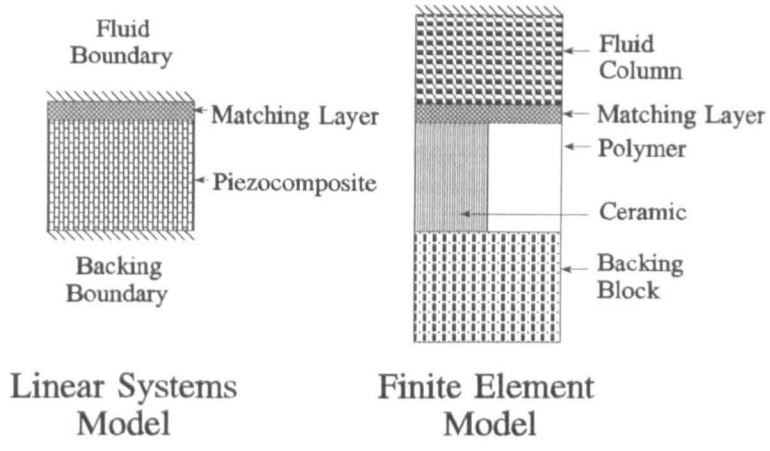

Figure 3.12: Ancillary Components of Finite Element Model

Electrode and bonding effects weere ignored as these layers could be constructed to be sufficiently to have no influence on the behaviour of the device. The validity of removing the symmetric axis was tested by comparing the results from four separate analysis of the same composite structure: modal and harmonic analysis of the eighth-symmetry model; and modal and harmonic analysis of the quarter-symmetry model. Minimal loss was not included for the harmonic analysis so it would produce similar results to the modal analysis. The finite element model piezocomposite was 25% volume fraction (VF), 0.1 aspect ratio (AR), PZT-5A/Hardset composite plate of height 1.0 mm and the results are given in Table 3.6.

It can be observed that the results have not varied between the two models. However, the modal and harmonic analysis of the same model do not produce identical results. This is because the calculation of the matrices differs between the two analysis types producing different rounding errors and hence different results. As the number of nodes in the finite element model is finite and the number of possible points in the transducer is infinite, there is normally a small error of undeterminable quantity in the frequency location of the modes. Ostergraad and Pawlak [37] discussed this phenomena in some more detail.

Table 3.6: Comparison of Results from Different FE Models

Type of Finite Element Model	Electrical Resonance (MHz)	Mechanical Resonance (MHz)	Dilation Quality at f_{elec}	Dilation Quality at f_{mech}
Eighth Symmetry Modal Analysis	1.388	1.712	0.963	0.953
Quarter Symmetry Modal Analysis	1.388	1.712	0.963	0.953
Eighth Symmetry Harmonic Analysis	1.374	1.727	0.953	0.994
Quarter Symmetry Harmonic Analysis	1.374	1.727	0.953	0.994

The example configuration of 25% VF was selected for analysis in Table 3.6 because the width of the ceramic pillar is the same as the width of the polymer matrix between the pillars. The same 25% VF 0.1 AR configuration is used to analyse the effect of the addition of the ancillary components on the behaviour of the device. Both the hardset configuration analysed in Table 3.6 and the equivalent softset configuration are used in the subsequent Sections with the thickness of the piezocomposites fixed at 1.0 mm. The operational parameters for the two simulation test devices are:

Table 3.7: Operational Parameters for Test Configurations

Parameter	25% VF 0.1 AR PZT-5A/Hardset	25% VF 0.1 AR PZT-5A/Softset
f_{elec} (MHz)	1.374	1.296
f_{mech} (MHz)	1.727	1.623
Z_C (MRayls)	9.500	9.147

3.6.4 Implementation of the Backing Block

The linear systems model (LSM) implemented the backing block as a boundary condition with a reflection and transmission co-efficient defined by the acoustic impedance of the block and that of the piezoelectric material. This emulates an ideal backing block but there is no equivalent condition available in the ANSYS package. Hence, the backing block was implemented as it would be constructed in practice, with finite thickness and high damping. An impedance profile of 20% VF 0.24 AR PZT-5A/hardset piezocomposite shown in Figure 3.13 was analysed with both finite element analysis and the LSM in Gachagan et al. [38]. The particular configuration exhibits mode coupling between the thickness mode and the first inter-pillar mode which cannot be modelled by the LSM. This illustrates an advantage of the FEM over constrained-dimensional modelling. It can be seen from these results that the finite element analysis produce improved correlation with experiment.

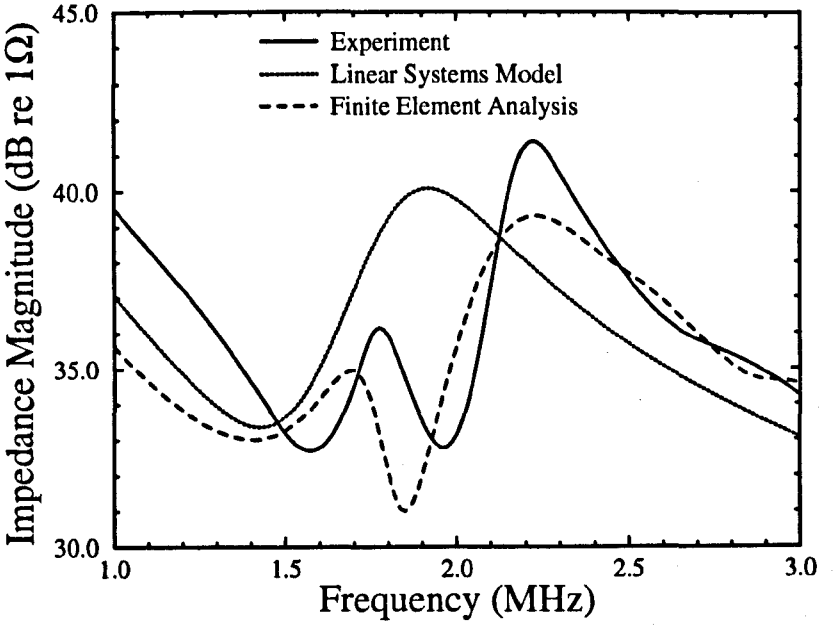

Figure 3.13: Impedance Profile of 20% VF 0.24 AR PZT-5A/Hardset Piezocomposite

The parameters that have been chosen to characterise the backing block construction are:

- Specific acoustic impedance;
- Height of the backing block; and
- Damping co-efficient of the material.

The backing block is assumed to be constructed from tungsten loaded softset epoxy. It is also assumed the addition of the tungsten powder to the epoxy increases the speed of sound and the density of the backing block material by the same fraction. The density of softset is 1150 $Kg.m^{-3}$ and longitudinal wave velocity is 1820 $m.s^{-1}$ giving a specific acoustic impedance of 2.093 MRayls. Taking ϕ as the ratio of the desired specific acoustic impedance to that of the softset epoxy, then the density of the backing material would be $1150\sqrt{\phi}$ $Kg.m^{-3}$ and the elastic modulus would be $1.8\phi\sqrt{\phi}$ MPa. The Poisson ratio is assumed to be unchanged at 0.40.

The effect of damping co-efficient was analysed initially as its influence was considered to be independent of the specific configuration. The purpose of this analysis was to determine a valid value for the co-efficient that could be used in all subsequent analyses. The characterising quantity was chosen to be the frequency for which the transmission sensitivity of the device is a maximum and was used by Gururaja et al. [39]. For the unbacked device with very low loss, this frequency is identical to the electrical resonance frequency. However, with the extra damping caused by the addition of the backing block, the two frequencies diverge and the easier of the two to locate, both experimentally and with simulation, is the frequency of maximum transmission. For this set of simulations, the backing block was placed at both the bottom and top surface of the transducer. This was because if the backing block was not added to the top surface for high damping cases, the piezoelectric material would vibrate independently of the block producing results which could be

mis-interpreted. The specific acoustic impedance and height of the backing block for the hardset configuration of Table 3.8 was selected as 4 MRayls and 2 mm respectively in this analysis. The damping co-efficient, ζ, was varied from -10 dB to -100 dB and the results are plotted in Figure 3.14. The dotted line shows that the linear systems model produced a frequency of 1.470 MHz as the frequency of maximum transmission if the backing block is considered as a boundary condition as shown in Figure 3.12.

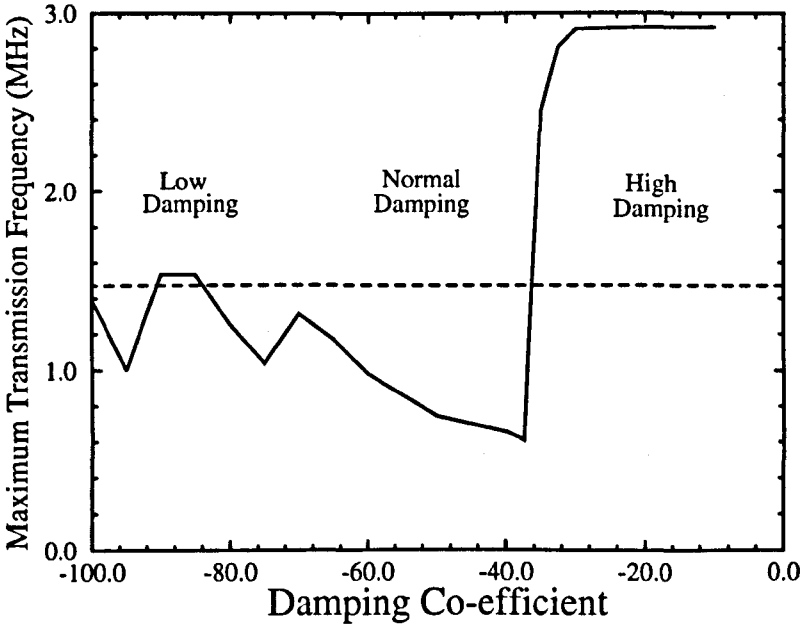

Figure 3.14: Effect of Damping in the Backing Block

The graph in the Figure can be divided into three regions:

- *High damping (ζ > -40 dB)* where the damping in the backing block is sufficiently high to influence the specific acoustic impedance of the material through the modification of the group velocity relative to the phase velocity. The specific acoustic impedance of a material is proportional to the group velocity of acoustic wave travelling through the material. From Ingard [40], under conditions of zero damping, the group velocity, v_g, and the phase velocity, v_p, are identical for an isotropic material:

$$v_g = \frac{\partial \omega}{\partial k}$$
$$but\ \omega = v_p.k \qquad \textbf{Eqn. 3.40}$$
$$\therefore v_g = v_p$$

where k is the wave number for the acoustic wave.

Hence, the specific acoustic impedance is normally calculated using the phase velocity rather than the group velocity as the phase velocity can be derived theoretically from the stiffness and density of the material. However, the damping in the material introduces an imaginary component to the wavenumber:

$$\omega = v_p k(1 + j\beta_{nmat}) \qquad \textbf{Eqn. 3.41}$$
$$\frac{\partial \omega}{\partial k} = v_p(1 + j\beta_{nmat})$$

where β_{nmat} represents the damping in the material.

If the damping in the material is large, the velocities will differ and the effective specific acoustic impedance of the material is increased compared to that calculated from the density and phase velocity. In the high damping region of the curve, the impedance of the block has exceeded that of the piezocomposite changing the resonance condition of the transducer from half-wavelength to quarter-wavelength. This is shown by the sharp increase in maximum transmission frequency to just less than 3.0 MHz from 1.470 MHz.

- *Low Damping (ζ < -70 dB)* where the damping is insufficient to absorb all the energy contained within the pressure waves entering the backing block. The pressure waves are reflected from the back face of the backing block and travel back into the piezocomposite material. This is shown by the rapid shifting of the frequency in this region as the position of the resonances within the block are changed by the damping co-efficient. This can be corrected by extending the backing block but this

increases the size of the model for no significant gain over operating in the middle region.

- *Normal Damping (40 dB < ζ < 70 dB)* where neither damping or the resonance effect dominates the frequency of operation. The damping co-efficient was chosen to be in this region and was selected as 70 dB for the finite element model. This produces a small downward shift of frequency compared to the linear systems model but any high value would produce resonance in the backing block. This is an important consideration when comparing the results of the finite element model to those produced by a constrained-dimensional modelling approach.

As the function of the backing block is to absorb energy from the piezoelectric material, a backed transducer should have a large bandwidth but lower sensitivity compared to the equivalent unbacked transducer. Figure 3.15(a) and 3.15(b) show the transmit and receive sensitivity with the specific acoustic impedance of the backing to that of the piezocomposite. Figure 3.15(c) and 3.15(d) show the associated percentage fractional bandwidth with each case. The simulations were repeated with softset for the filler material and the results are shown as a dotted line as opposed to the solid line for the results of the PZT-5A/hardset configurations. This shows that the backing block has the anticipated effect of increasing the operational bandwidth with an accompanying drop in sensitivity. The bandwidth and sensitivity curves have been combined through multiplication into Figure 3.15(e) and 3.15(f). The curves represent the product of the sensitivity and fractional bandwidth normalised so that the maximum value over both sets of simulations is 1.0. The unbacked cases were not included as these have about four times the product and if included, would reduce the displayed detail. While the product does increase with backing impedance, the change is small above 3 MRayls showing that the reduction in sensitivity is similar to the increase in bandwidth. Figure 3.15(a) and 3.15(c) illustrate that the backing impedance acts as a compromise to maximise the sensitivity-bandwidth product. An increase in the impedance value would increase the operational bandwidth while a decrease would increase the operational sensitivity. However, the compromise should

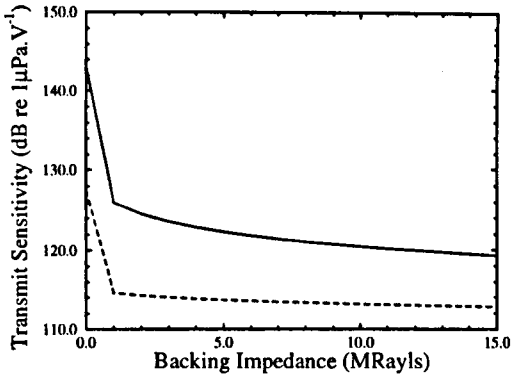

(a) Transmission

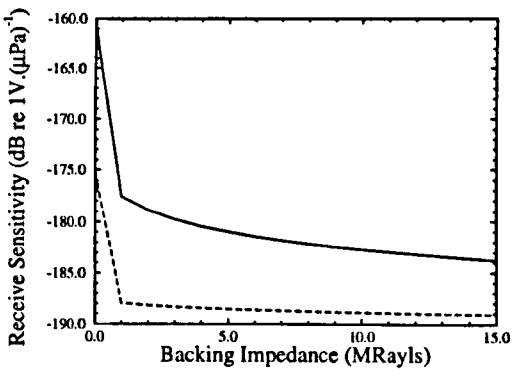

(b) Reception

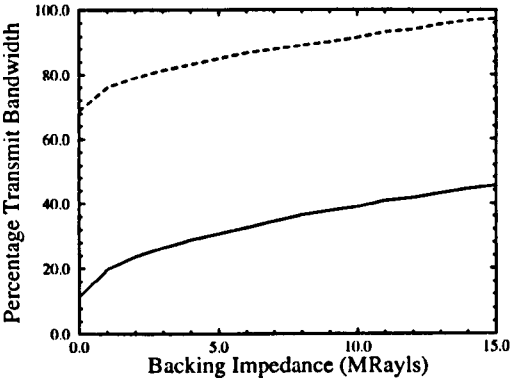

(c) Transmission

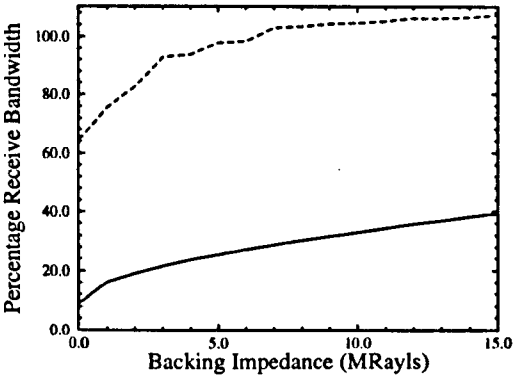

(d) Reception

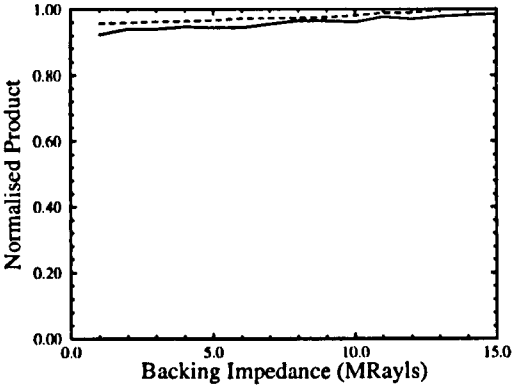

(e) Transmission

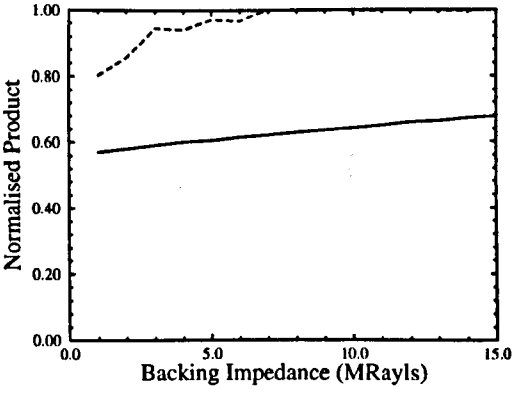

(f) Reception

Figure 3.15: Effect of Damping Impedance on Transmission and Reception

Key: Hardset Composite ——
Softset Composite - - -

be weighted towards higher sensitivity to increase the signal to noise ratio of the system indicating that the selection for the required backing impedance was between 3.0 and 5.0 MRayls. In Hall [41], the guideline for selecting the impedance of the backing block was to take half that of the active material. For this specific example, this would have been 4.75 MRayls which falls in the compromise region chosen from Figure 3.15. The designer would be wise to ensure that if the value is going to be shifted from half that of the active material, it should err in the direction of lower values.

In absorbing energy from the active material, the backing shifts the centre frequency of operation for the transducer. Figure 3.16 shows the frequency of maximum transmit sensitivity with different backing impedances for the hardset and softset configurations for the 25% VF 0.1 AR piezocomposite material.

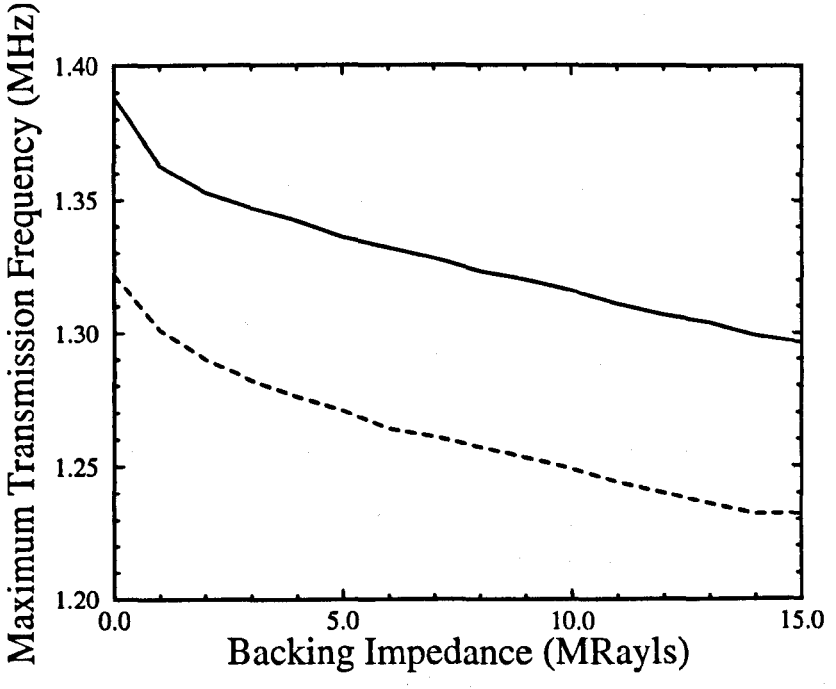

Figure 3.16: Effect of Backing Impedance on Frequency of Maximum Transmission

3.6.5 Implementation of the Matching Layer

The implementation of the matching layer for the finite element model is similar to that for the constrained dimensional model. It is a layer of material added to the top of the piezoelectric material and is meshed to be 1 element thick. The addition of the matching layer introduces extra resonances to the impedance profile of the transducer caused by the inclusion of an extra boundary. Usually, there would be a single extra resonance in the operational frequency range of the thickness mode as shown in Figure 3.17. Here, the transducer was 2.82 mm thick 40% VF, 0.14 AR, PZT-5A/hardset composite with a 1.29mm thick slice of hardset on one surface as a matching layer into an air medium.

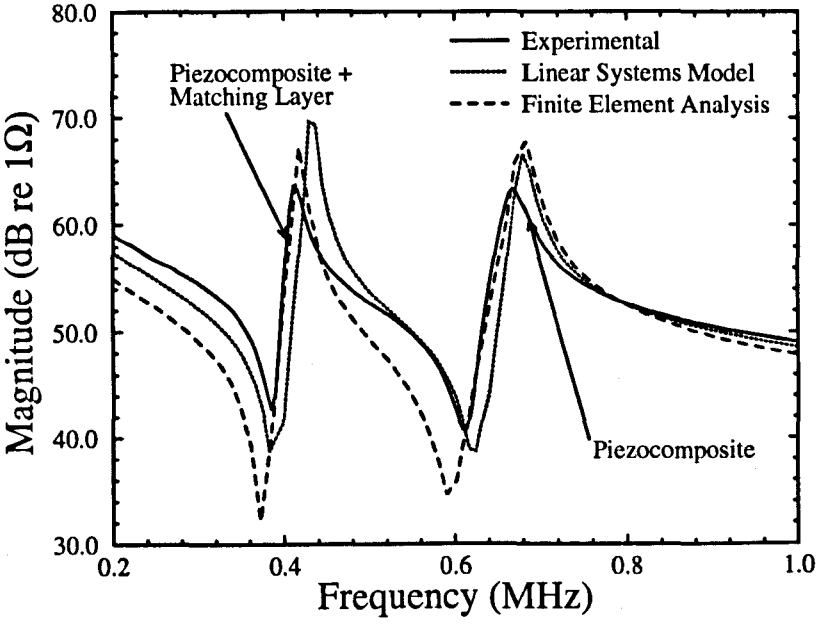

Figure 3.17: Impedance Profile of 40% VF 0.14 AR PZT-5A/Hardset Composite with Matching Layer

The resonance in the region of 400 kHz is the fundamental thickness mode of the piezocomposite and the matching layer and the resonance in the region of 700 kHz is the fundamental thickness mode of the piezocomposite by itself. The thickness mode resonance of the matching layer occurs at a frequency greater than 1.0 MHz.

Gachagan [38] has made an investigation to examine the effect of using different practical materials in the matching layer for a standard piezocomposite transducer whose impedance profile is shown in Figure 3.17.

He compared the results from the linear systems model and the finite element model derived in this Chapter to experimental results. The four materials are given in Table 3.8 and the thickness of each material was designed to approximate quarter-wavelength conditions at 587 kHz. In addition to the single matching layers, a silicone rubber/perspex matching layer combination was examined to consider where double matching layers gave an increase in performance.

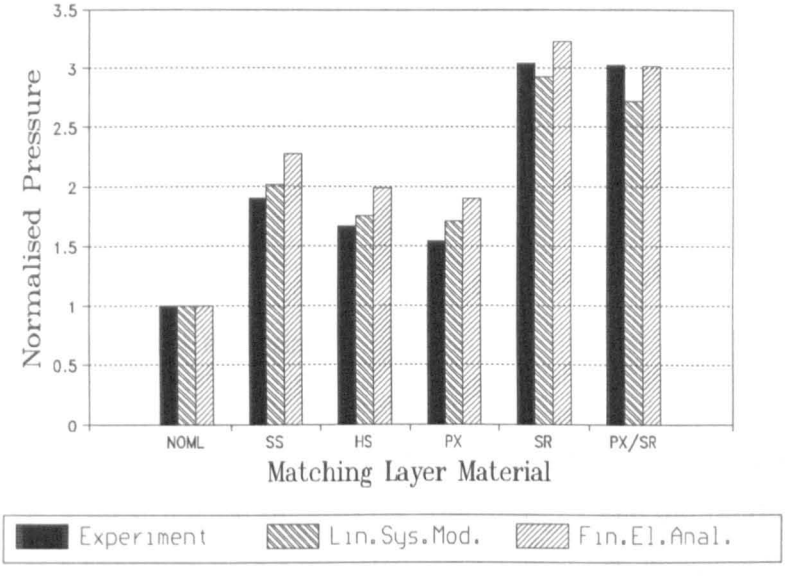

Figure 3.18: Various Matching Layer Configurations in Transmission

Table 3.8: Matching Layer Materials

	Material	Label	Z(MRayls)
1	Softset	SS	2.23
2	Hardset	HS	2.85
3	Perspex	PX	3.29
4	Silicone Rubber	SR	1.05

Figure 3.18 shows the results of the analysis in which the pressure output values are normalised to that of the un-matched case, indicated by NOML. Good correlation between the finite element theory and experiment can be readily observed. This shows that the required specific acoustic impedance of the matching layer should be as close as possible to that predicted by Eqn 2.31 as can be seen by the good response from the silicone rubber.

3.6.6 Inclusion of Fluid Boundary

As explained in Section 3.3.1, the required boundary fluid elements were not available in the present release of ANSYS. This implied that the fluid could not be implemented as a boundary with a reflection co-efficient which would have been the optimal method and was the method used by the linear systems model. However, the ANSYS package has fluid elements with which boundaries can be implemented through the use of the property called MU [1]. It can be varied between 0.0 for a reflecting boundary and 1.0 for an absorbing boundary. For the boundary between the transducer and the fluid, MU is set to the ratios of the specific acoustic impedance:

$$MU = \frac{Z_{fluid}}{Z_C} \qquad \textbf{Eqn. 3.42}$$

where Z_{fluid} is the specific acoustic impedance of the fluid medium; and

Z_C is the specific acoustic impedance of the piezoelectric material.

It can be seen that the value of MU for the boundary between the ceramic phase and the fluid would be different from the value for the boundary between the polymer phase and the fluid. This is because the polymer has a lower specific acoustic impedance than the ceramic. Four different implementations for the fluid loading were developed and compared with each other and experiment in attempt to incorporate fluid loading into the finite element model. The experimental device was a 50% VF 0.22 AR PZT-5A/hardset piezocomposite operating into castor oil. The oil was used because it is an electrical insulator unlike water but has similar acoustic properties to water. This meant that a housing was not required to protect the electrodes of the transducer for the measurement but the behaviour of the device would be similar to that with water loading. The properties of castor oil and water are defined in Selfridge [42] and the specific acoustic impedance of the oil is 1.48 MRayls compared to 1.50 MRayls for water. Figure 3.19 shows two-dimensional representations for implementation of the fluid column for the four different models. The impedance profile obtained from each model is shown in the different graphs of Figure 3.20 and the dilation quality is shown in the different graphs for Figure 3.21. Figure 3.20 also contains the impedance profile for the experimental device measured in castor oil. The models were as follows:

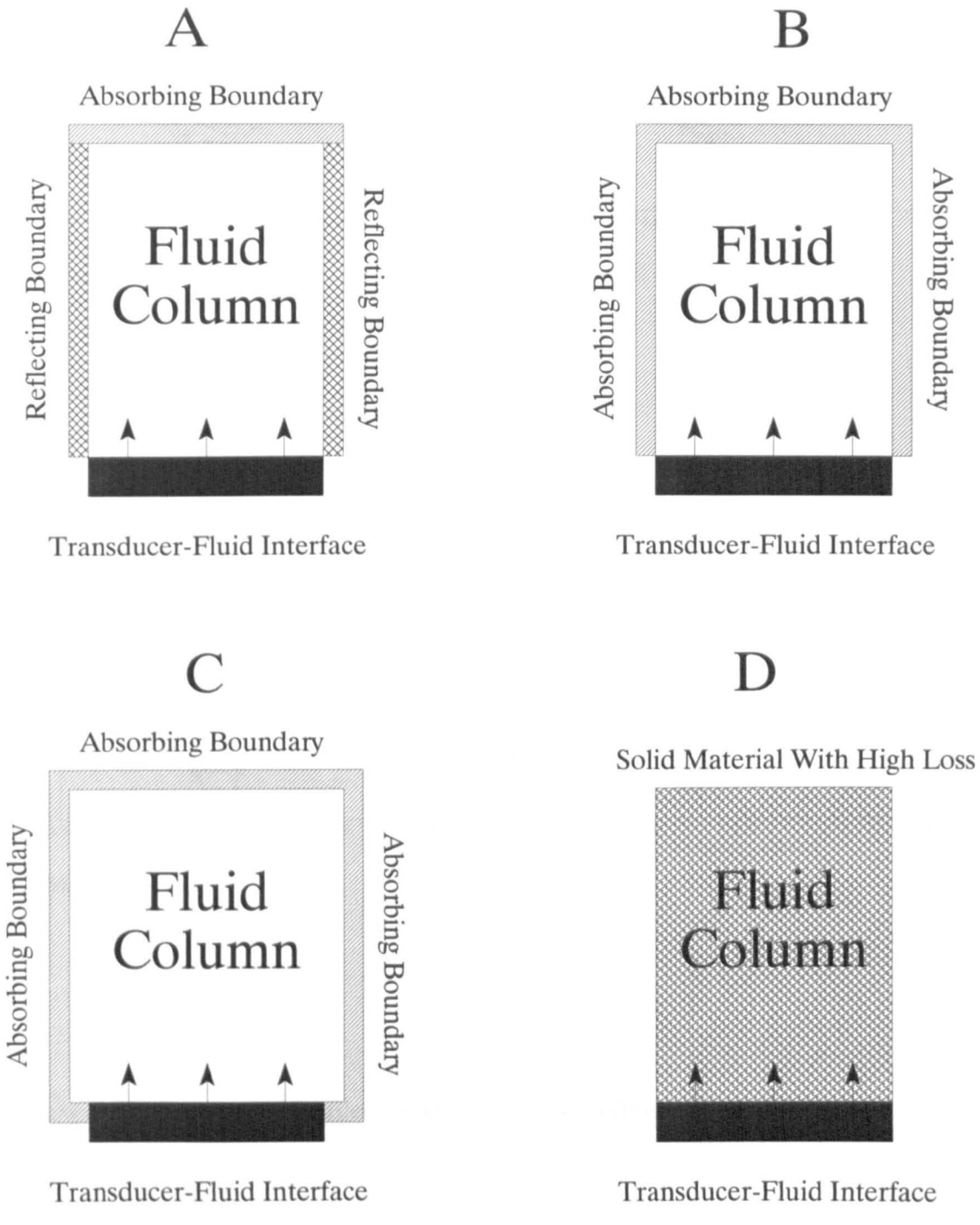

Figure 3.19: Different Implementations of the Fluid Column

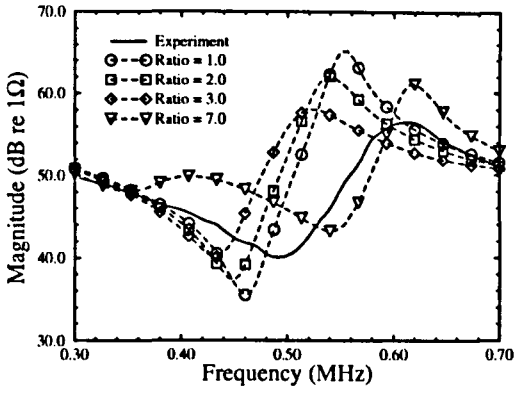

(a) Model A

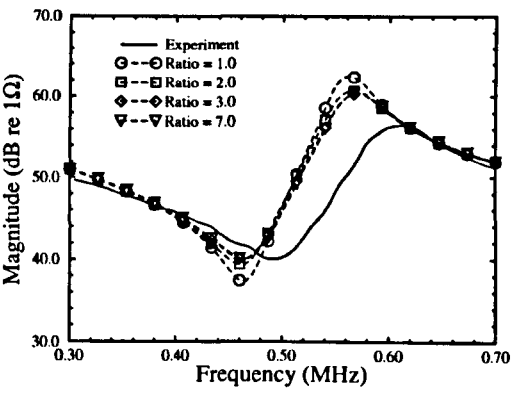

(b) Model B

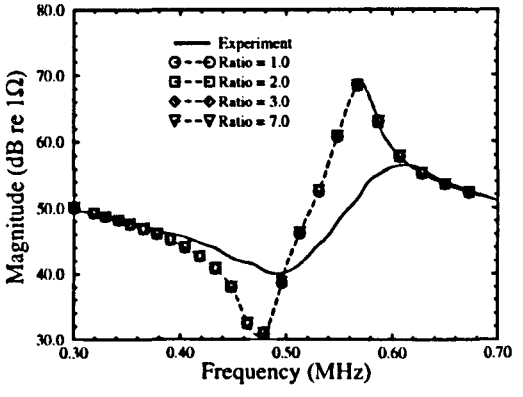

(c) Model C

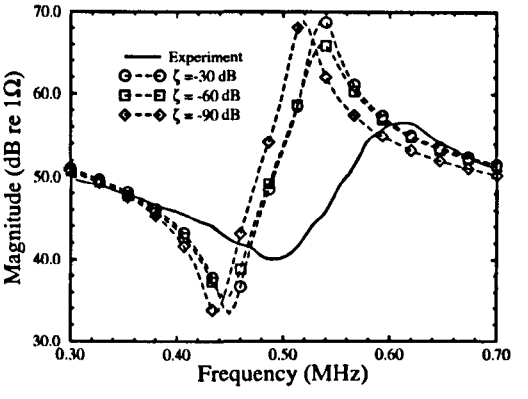

(d) Model D

Figure 3.20: Impedance Profiles Generated by the Different Models

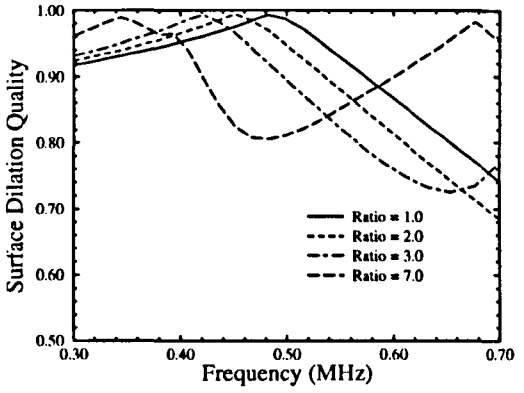

(a) Model A

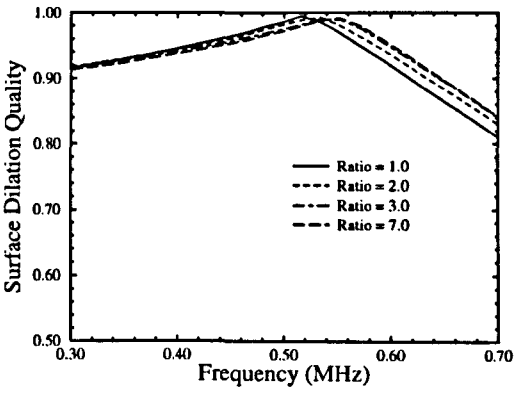

(b) Model B

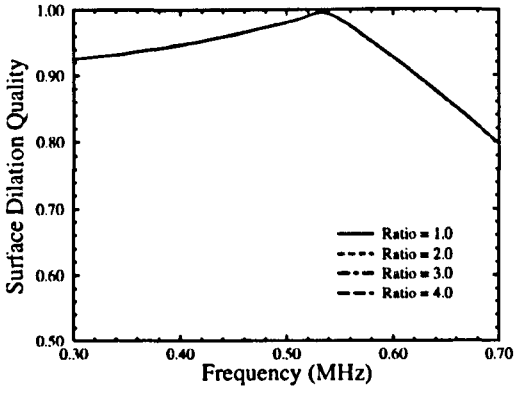

(c) Model C

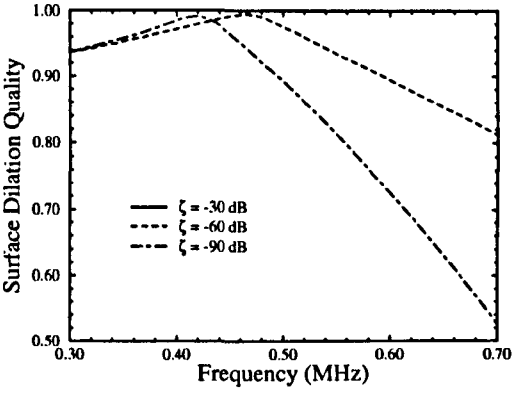

(d) Model D

Figure 3.21: Surface Dilation Qualities Generated by the Different Models

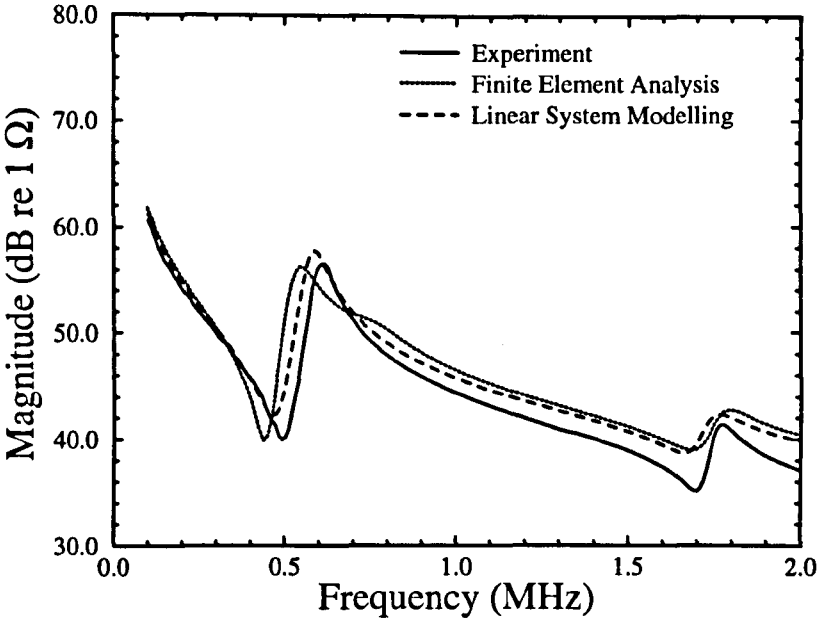

Figure 3.22: Impedance Profile of 50% VF 0.22 AR PZT-5A/Hardset Composite in Castor Oil

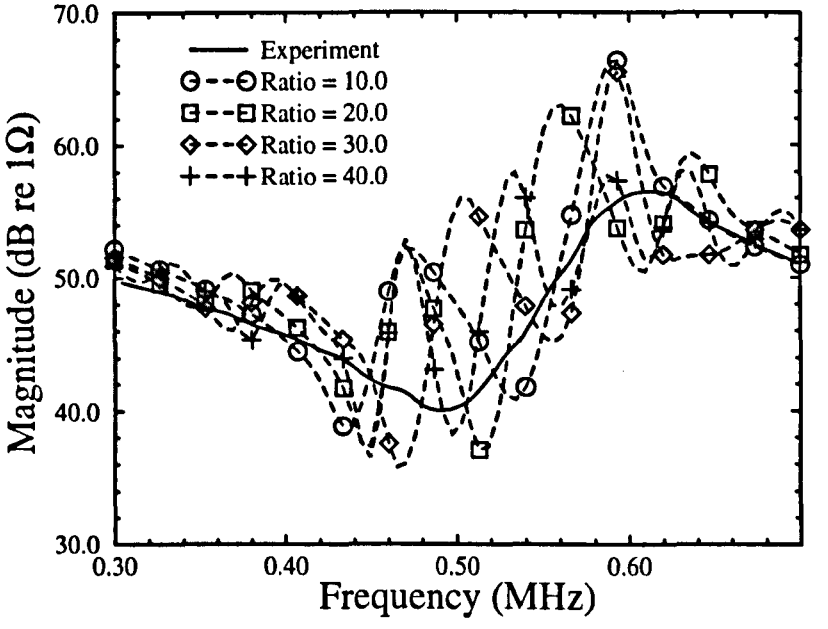

Figure 3.23: Impedance Profile of 50% VF 0.22 AR PZT-5A/Hardset Composite in Castor Oil

A. The fluid column was implemented as suggested by Rajakumar [28]. Reflecting boundaries were placed on the sides of the column to simulate the symmetric axes on the model of the transducer. An absorbing boundary was placed at the open top side of the column. It was found that the shape of the fluid elements was very important in determining the behaviour of the whole finite element model. The shape was selected as a cuboidal rectangle where the width and length were identical and fixed by the size of the elements in the transducer model. The height was specified as a ratio to the width of the element. Simulations with different ratios ranging from 1.0 to 7.0 were performed. The impedance profiles are shown in Figure 3.20(a) and the surface dilation qualities are shown in Figure 3.21(a). None of the simulations produced reasonable correlation with the impedance profile of the experimental transducer. The best responses was obtained with the smaller ratios. The models with high ratios produced extraneous fluctuations in the impedance profile that did not exist in practice. It was found through simulation that a certain ratio could be selected to produce a reasonable correlation with both the experimental transducer and the results from the linear systems model as shown in Figure 3.22. This is not an acceptable solution to the problem as the ratio is specific to the scenario and requires an experimental trace to determine the optimal ratio. Thus, a new formulation for the fluid column was required and this is described in the following paragraphs. The effect of extremely large ratios can be seen in Figure 3.23 where there are many extra fluctuations in the response.

B. The reflecting boundaries on the side of the columns for the previous model did not sufficiently constrain the model which lead to the appearance of extraneous fluctuations in the impedance profile and dilation quality. These boundaries were replaced by absorbing boundaries in an attempt to reduce the resonances within the fluid column. The impedance profile produced from this model are shown in Figure 3.20(b) and was similar to that from model A but the dilation qualities in Figure 3.21(b) show that the fluctuations no longer existed. The ratios for the simulations was varied between 1.0 and 7.0 as with the simulations for Model A. However, the positions of the thickness mode resonance have been shifted down relative to model

A from which it can be concluded that the fluid column is over-constrained. Another point is that the model response is not as sensitive to the height-to-width ratio of the fluid elements which is an advantage over model A.

C. Model C represents a compromise between model A and model B in attempt to neither under - or over-constrain the fluid column with its boundary conditions. The absorbing boundary conditions of model B were retained but the size of the fluid column was increased by increasing the width. This had the disadvantage over the previous models that there are more elements in the model. However, there is no significant improvement in the modelling of the fluid loading as can be seen in Figure 3.20(c) for the impedance traces and Figure 3.21(c) for the dilation quality. Also this modelling system is insensitive to the ratio of the fluid element which was found to be very important in Chapter 6.

D. The final configuration was to implement the fluid as a solid with the same properties as the fluid. As fluids cannot sustain shear modes because they do not have a fixed lattice, the Poisson ratio in the fluid column was set to 0.0. The stiffness of the solid can be calculated from the density and speed of sound for the fluid. For the castor oil medium, the Young's modulus has a value of 2.25 MPa. The effect of a half-space can be duplicated by introducing a large loss co-efficient to the material so that no energy is reflected back into the transducer from the solid material. Hence, this implementation is very similar to that of the backing block. While the impedance traces shown in Figure 3.20(d) are similar to the experiment and those produced by the other models, the dilation quality in Figure 3.21(d) was too dependent on the damping co-efficient in the fluid material for meaningful information to be obtained. The reason why the dilation quality curve for the damping co-efficient of -30 could not be observed was because it had a value of 1.000 for all frequencies. It was shown in Figure 3.14 that the damping co-efficient in the surrounding components can modify the complete behaviour of the device.

In conclusion, it was decided to use the fluid model C for the analysis of the effect of the fluid loading in Section 4.5.3. The model did not produce extraneous fluctuations in the fluid column if the fluid elements were kept cuboidal, as did the model A. It was insensitive to the ratio of the height to width of the fluid element which model B was not, and the results were not dependent on the damping as was model D. The selection of model C was confirmed in the modelling of transducer arrays. However, it did not correctly locate the resonant frequencies and so can only be used for determining the effect of varying different parameters rather than the modelling of exact configurations. Once there is a new release of ANSYS with the boundary element for the fluid, a new model of fluid column can be attempted and a full investigation undertaken.

3.6.7 Electrical Loading of the Transducer

The effect of the loading was evaluated by modelling a 25% VF, 0.1 AR, PZT-5A/hardset 1-3 piezocomposite under different electrical loadings. Four cases were simulated:

(a) 1 volt of potential difference was applied directly to the electrodes - this was to simulate a zero output resistance for the voltage source;

(b) 1 volt of potential difference was applied with a 50Ω resistor in series with the transducer;

(c) 1 volt of potential difference was applied with a 1MΩ resistor in series with the transducer; and

(d) 1 coulomb of free charge was applied directly to the top electrode - this was to simulate a current source with infinite output resistance.

The static capacitance, electrical impedance at the electrical resonance and mechanical resonances were compared for each case in Table 3.9. The results from all cases were identical showing that the electrical loading does not affect the behaviour of the transducer model. The electrical loading does affect the experimental

measurement of the transducer's performance as the measurement system cannot measure the impedance of the transducer at its terminals but does included the impedance of the electronic circuitry.

Table 3.9: Comparison of Different Electrical Loading

Case	Static Capacitance (pF)	Impedance at f_{elec} (ohms)	Impedance at f_{mech} (ohms)
(a)	6.36	7962∠-27.2°	87700∠-26.6°
(b)	6.36	7962∠-27.2°	87700∠-26.6°
(c)	6.36	7962∠-27.2°	87700∠-26.6°
(d)	6.36	7962∠-27.2°	87700∠-26.6°

The resistor element was included in most models as it facilitated the calculation of the current passing through the transducer as all the charge entering the device had to pass through the resistor. It also allowed the designer to uniquely define the active electrode for identification in the post-processing stage of the analysis.

3.7 CONCLUDING REMARKS

This Chapter described the general concepts of finite element modelling in the form that is applied to many engineering fields. From this discussion, the finite element analysis could be divided into three phases: pre-processing where the model and material parameters were defined; solution where the finite element matrix was solved; and post-processing where the desired information was extracted and presented to the user. The different analysis types were detailed: static analysis; modal analysis and harmonic analysis. The transmit and receive sensitivity could be generated from the harmonic analysis. Integrated parameters for each type of analysis to allow comparison between different configurations were described.

The finite element modelling of piezoelectricity was verified by comparing the generated response of different shapes of the piezoceramic, PZT-5A, with the experimental response. This included the development of an expression for displacement at the surface of the transducer as a function of voltage at different frequencies. The model was extended to incorporate the geometrical properties of the 1-3 piezocomposite material including different shaped ceramic pillars. The ancillary components of backing blocks and matching layers were added to the model and the new models were verified. Finally several attempts were made to incorporate fluid loading into the modelling using standard element types but no ideal solution could be found. However, the final solution was sufficient to determine trends in the integrated parameters for different properties. The selected model was C where the fluid column was such that none of the absorbing boundaries are in contact with the transducer surface. The electrical loading of the electronic circuit was shown not to influence the calculation of the transducer impedance and hence does not need to be included in the modelling.

CHAPTER FOUR

MODELLING OF 1-3 PIEZOCOMPOSITES USING THE FINITE ELEMENT METHOD

CHAPTER OBJECTIVE

The aim of this Chapter is to apply the finite element model developed in Chapter 3 to generate a design methodology for 1-3 piezocomposite transducers and from this, produce a set of design guidelines. The restriction on the microstructure of the piezocomposite can be evaluated by the relative position of the thickness mode to that of the lateral modes caused by the lattice structure. These modal frequencies and the associated coupling of the mode are affected by damping within the polymer matrix which indicates that mechanical loss must be included. The design of ancillary components in the system such as the matching layer and backing block must also be included in the process. Finally the influence of the fluid loading on the dilation quality also requires quantification.

4.1 UNI-DIMENSIONAL MODELLING APPROACH

Much research has been performed in the modelling of 1-3 piezocomposites as a homogenous medium, that can be incorporated into a constrained-dimensional modelling scheme as discussed in Chapter 2. The most successful to date has been the isostrain model of Smith and Auld [43] and the model has been incorporated into the linear systems modelling scheme by Hayward and Hossack [36]. The approach taken by this method was to derive expressions for the parameters of the equivalent homogenous material that would behave in an identical fashion to the 1-3 piezocomposite. The assumptions used for constrained-dimensional modelling discussed in Chapter 2 were used in the derivation and only the *33* components of the equivalent parameters were derived.

4.1.1 Isostrain Model of Smith and Auld

The full derivation of the isostrain model is detailed in Smith and Auld [43]. Any parameter with a superscript *p* is associated with the polymer phase while any other parameter is associated with the ceramic phase. In summary, the expressions for the fundamental properties were [34]:

$$\bar{c}_{33}^{E} = \upsilon\left[c_{33}^{E} - \frac{2\left(c_{13}^{E} - c_{12}^{p}\right)^2}{\bar{c}(\upsilon)}\right] + (1 - \upsilon)c_{11}^{p}$$

$$\bar{e}_{33} = \upsilon\left[e_{33} - \frac{2e_{31}\left(c_{13}^{E} - c_{12}^{p}\right)}{\bar{c}(\upsilon)}\right] \qquad \textbf{Eqn. 4.1}$$

$$\bar{\varepsilon}_{33}^{S} = \upsilon\left[\varepsilon_{33}^{S} + \frac{2e_{31}^2}{\bar{c}(\upsilon)}\right] + (1 - \upsilon)\varepsilon_{11}^{p}$$

where $\bar{c}(\upsilon) = c_{11}^{E} + c_{12}^{E} + \frac{\upsilon}{(1-\upsilon)}\left(c_{11}^{p} + c_{12}^{p}\right)$;

υ is the ceramic volume fraction (VF); and

the bar on the left hand side of each equation denotes the equivalent parameter.

The parameters for the constrained model for application in the modelling schemes presented in Chapter 2 are the following:

$$\bar{\beta}_{33}^{S} = \frac{1}{\bar{\varepsilon}_{33}^{S}}$$
$$h_{33} = \bar{e}_{33}\bar{\beta}_{33}^{S} \qquad \textbf{Eqn. 4.2}$$
$$\bar{c}_{33}^{D} = \bar{c}_{33}^{E} + \bar{e}_{33}\bar{h}_{33}$$

The density of the homogenous material is defined as:

$$\bar{\rho} = \upsilon\rho^{c} + (1-\upsilon)\rho^{p} \qquad \textbf{Eqn. 4.3}$$

where ρ^{c} is the density of the ceramic phase; and

ρ^{p} is the density of the polymer phase.

If the transducer being evaluated is a single layer of the 1-3 piezocomposite with no matching layers or backing blocks, the integrated homogenous operating parameters are:

- Thickness mode coupling factor: $\bar{k}_{t} = \frac{\bar{h}_{33}}{\sqrt{\bar{c}_{33}^{D}\,\bar{\beta}_{33}^{S}}}$

- Specific acoustic impedance: $\bar{Z} = \sqrt{\bar{c}_{33}^{D}\,\bar{\rho}}$

- Longitudinal speed of sound: $\bar{v}_l = \sqrt{\frac{\bar{c}_{33}^{D}}{\bar{\rho}}}$

In deriving the expressions, the following assumptions were made:

1. There was no movement, electrical or mechanical, in the *1* and *2* directions.
2. All oscillations in the transducer's behaviour would be thickness (*3*) direction so that:
- Uniform electroding with no fringing effects implying $E_1 = E_2 = D_1 = D_2 = 0$
- There would be no shear motion within the composite.
3. The two phases in the composite would act as if they were connected in parallel in the *3* direction so that the thickness strain of the two phases is equal and the thickness stresses are averaged over the surface.
4. The two phases in the composite would act as if they were connected in series for the *1* and *2* directions so that the lateral strains of the two phases are averaged through the height and the lateral stresses are equal.

Hashimoto and Yamaguchi derived similar results to those of the isostrain model using a different approach. They partitioned the elastic matrix equations into two parts: unknown and known quantities as shown in Oakley [44]. By making similar assumptions to Smith, the equivalent parameters for the piezocomposites were developed through matrix manipulation. The elements of the system matrices which were ignored by the isostrain approach such as c_{44} and c_{13}, were obtained through this technique. However, the method was developed for one-dimensional composites such as 2-2 connectivity and the extension to two-dimensional 1-3 composites while possible, produced clumsy equations that had to be solved using iterative methods [34]. Such an algorithm would have no inherent advantage over the finite element method as it was no simpler to implement or quicker to solve. Hence, the isostrain approach remains the superior of the two constrained-dimensional modelling

techniques for piezocomposites and was used in the comparison with the finite element analysis results in this Chapter.

4.1.2 Results Obtained using the Isostrain Model

The isostrain model has been verified experimentally by Hayward [36] and applied to the design of 1-3 piezocomposites [45]. This Section will illustrate the model graphically for different volume fractions and compared the response of the model with that of the FE model. The two piezocomposites simulated were a PZT-5A/hardset composite and a PZT-5A/softset composite, both with pillar aspect ratios (AR) of 0.10 for volume fractions from 0% to 100%.

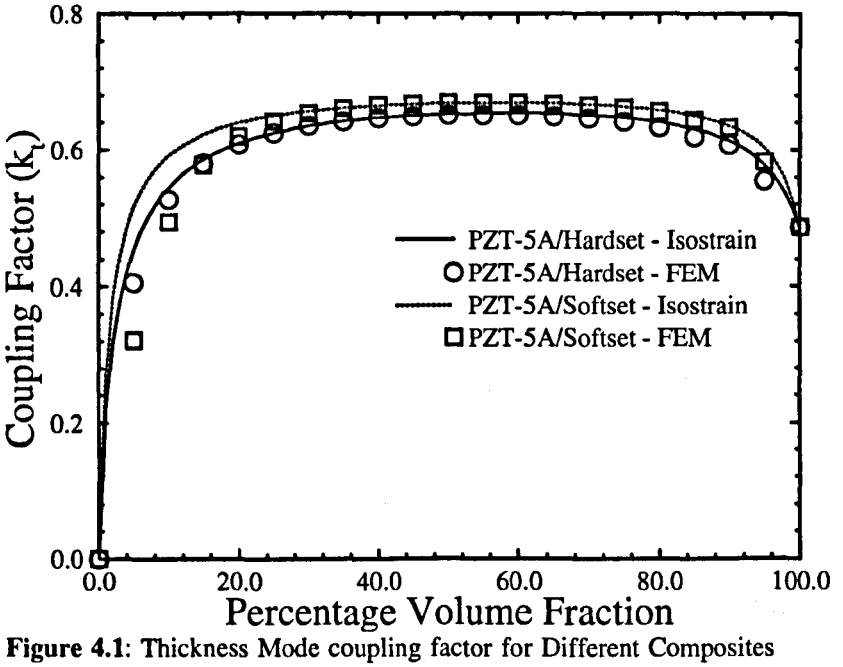

Figure 4.1: Thickness Mode coupling factor for Different Composites

The integrated operating parameters were extracted from the results of the finite element analysis and compared to the isostrain model results in Figure 4.1 for thickness mode coupling factor and Figure 4.2 for longitudinal speed of sound. At all but the lowest volume fraction, the coupling factor exceeds that of the constituent ceramic demonstrating an advantage of the piezocomposite material over the piezoceramics. It can be observed that the more compliant polymer, *softset*, promoted a better response than that of *hardset*.

At low volume fractions, the correlation between the isostrain model and the finite element model decreased because the inter-pillar modes couple with the thickness mode decreasing the efficiency of the mode. This introduces the concept of maximum pillar aspect ratio which is discussed further in Section 4.3. For efficient operation of composites below 10% volume fraction, the aspect ratio must be less than 0.10. A similar but not as marked effect occurs at the highest volume fractions. As the polymer between the ceramic pillars is so thin compared to the width of the pillars, it moves in unison with the ceramic making the material act as a monolithic plate.

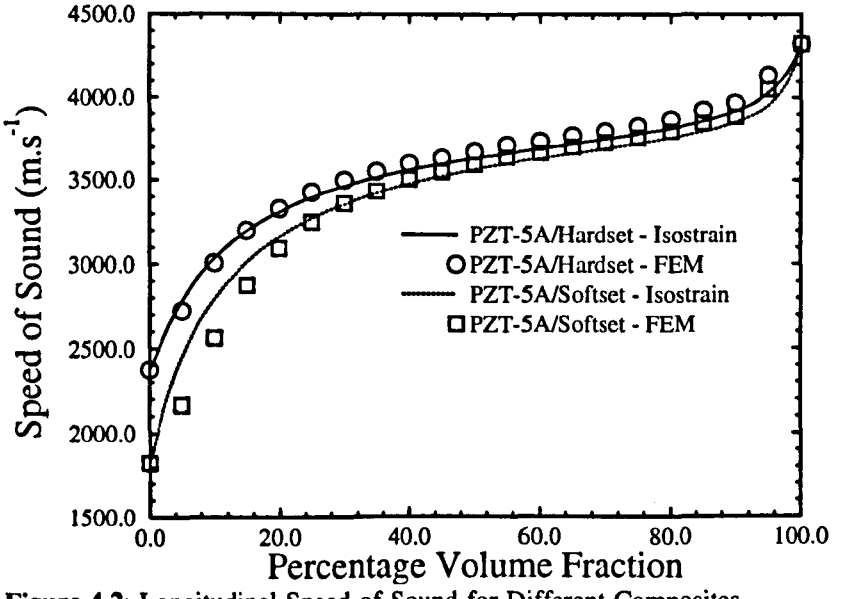

Figure 4.2: Longitudinal Speed of Sound for Different Composites

The next parameter, longitudinal wave speed, determines both the operating thickness and the acoustic impedance of the composite as the other variable in the appropriate equations is the density of the material which is the summation of the fractions of each density. The curve demonstrated an almost linear response except at very low and very high volume fractions.

Again at very low and very high volume fractions, the correlations between the models decreased for the same reasons discussed previously. The speed was estimated from the FE model by the formula:

$$v_l = 2t_3 f_{mech} \qquad \text{Eqn. 4.4}$$

where t_3 is the height of the transducer and kept at 0.5 mm for the simulations.

4.2 RESONANCE MODES WITHIN THE PIEZOCOMPOSITE MATRIX

A major advantage of the 1-3 piezocomposite material over the piezoceramics and piezopolymers is the number of design parameters that can be adjusted to modify the behaviour of the material. To understand the process of how these parameters affect the behaviour, the position and electro-mechanical coupling factor of each resonance mode must be determined. There are four major types of modal mechanisms present in the structure, two arising because of the external dimensions (macrostructure) of the matrix and two arising because of the internal geometry (microstructure) of the matrix:

A. **Width-dilational modes** - these occur because of the finite lateral dimensions of the piezocomposite plate. Consequently the fundamental plate mode is normally observed at a frequency far below that of the normal operating frequency band and can be ignored for most applications. An advantage of 1-3 piezoceramics over the original ceramic material is that as the ceramic phase is not connected in the *1* or *2* directions and since the polymer phase is significantly damped compared to the ceramic phase, the polymer matrix reduces the energy contained within these modes ensuring that the harmonics are weakly coupled.

B. **Thickness modes** - these occur because of the finite thickness of the structure. The fundamental frequency is that for which the wavelength of the extensional wave travelling in the *3* direction is twice that of the height of the plate allowing antinodes in the stress to occur at the plate surfaces. Hence, the position of these modes depends on the longitudinal speed within the structure. Other thickness modes occur at the odd harmonics of the fundamental but become increasingly weakly coupled at the higher harmonics because of increased mechanical damping with frequency.

C. **Inter-pillar resonances** - these occur because of the periodic spacing of the stiff ceramic pillars within the significantly more compliant polymer matrix. The position of these modes is determined by the inter-pillar spacing, the pillar shape used and the shear velocity of the polymer phase.

D. **Intra-pillar resonances** - these occur because of the finite lateral dimensions of the ceramic pillars and become important when the lateral dimensions of the pillar are in the same range as the height or, for pillar aspect ratios of between 0.50 and 2.00.

The isostrain model was derived with the equivalent assumption that the only modes that exist within the material are of type B or thickness modes.

4.2.1 Width-Dilational Mode Resonances

These are characterised as mechanical motion in the *1* and *2* direction when driven by an electric field in the *3* direction and are defined mainly by the elastic modulus of the polymer as well as the mass loading of the ceramic pillars [46]. For circular plates, the mode is associated with the diameter and for rectangular plates, there is a mode associated with each width dimension. The planar coupling co-efficient is found to be significantly less than the thickness-mode coupling co-efficient and the resultant movement in the *3* direction is minimal compared to that experienced at the thickness mode frequency.

As the polymer matrix cannot sustain a strongly coupled mode, the harmonics of the plate mode do not influence the performance of the 1-3 piezocomposite as they would for a PZT-5A piezoceramic material. A series of finite element simulations on a plate of 1-3 piezocomposite material was performed to determine the effect of the dimensions of the plate on the width mode. The width, height and volume fraction of the plate were varied and the fundamental mode was determined from modal analysis. The fundamental thickness mode occurred at a frequency higher than the plate mode for most simulations so there was minimal coupling between the two

Table 4.1: Mechanical Resonance Frequency of Width-Dilational Modes

Volume Fraction	Height (mm)	Width (mm)	f_{plate} (kHz)	f_{thick} (kHz)
20%	1.0	6.0	1615	1369
20%	1.0	12.0	782	1369
20%	1.0	18.0	518	1369
20%	1.0	24.0	386	1369
30%	1.0	6.0	1574	1404
40%	1.0	6.0	1593	1430
50%	1.0	6.0	1635	1453
20%	2.0	6.0	1669	685
20%	3.0	6.0	1694	456
20%	4.0	6.0	1697	342
20%	1.0	8.0	1222	1369
20%	1.0	10.0	992	1369
20%	1.0	12.0	847	1369

types of modes. Also, as modal analysis does not include loss, it does not couple independent modes. As the number of active degrees of freedom was restricted by the ANSYS package, an indicative set of DOFs was chosen from the total set of DOFs. The DOFs in the selective set are called master degrees of freedom (MDOFs) and the remaining degrees of freedom are called slave degrees of freedom (SDOFs). The matrix equation is partitioned into two sub-equations, one containing the MDOFs and the other the SDOFs. The latter is redefined in terms of the former reducing the number of DOFs in the final matrix equation. This process is called *Guyan Reduction* [47] and significantly reduces the size of the problem with minimal loss of accuracy if the master set is well-chosen. The ANSYS package has a command to select the master set from the available degrees-of-freedom. Using this reduction does have the implication that the value of the resonance frequencies becomes less accurate with

increase in the original problem size but does allow large problems to solved with a restrictive DOF set. Another innovation in the model used for these simulations was the zero-stress boundaries used for the *1* and *2* direction as these represent the physical boundaries of the transducer. The analysis was also only performed for the mechanical resonance frequency by keeping the electrodes open-circuited. The results are summarised in Table 4.1 and the fundamental thickness mode frequency was also included to illustrate the separation of the width-dilational mode and the thickness mode. It can be seen from the Table that within the limits of the simulation accuracy, the frequencies of the modes were independent of the height and the ceramic volume fraction. This implied that the width-extensional modes for 1-3 piezocomposites were sustained purely within the polymer phases and were dependent on the width dimensions of the plate.

The plate modelled in the simulations are significantly smaller than those used in practical transducers implying the plate mode frequencies would be much less than in Table 4.1. Hence, the lateral dimensions of the piezocomposite material can be ignored in the model as they have minimal effect on the thickness mode operation of the piezocomposite material as long as the plate is large relative to its thickness.

4.2.2 Thickness Mode Resonances

For this mode, the ceramic rods vibrate in their length (height) mode. Experimentally, the thickness-mode coupling factor can be determined from the complex impedance curve of the material according to Equation (3.33) where:

- The electrical resonance frequency, f_{elec}, is the frequency of minimum impedance and is the resonant frequency of the unit cell when the electrodes are short-circuited. This is usually close to the optimal frequency for transmission.

- The mechanical resonance frequency, f_{mech}, is the frequency of maximum impedance and is the resonant frequency of the unit cell when the electrodes are open-circuited. This is normally the optimal frequency for reception.

The influence of both the low-frequency width-extensional mode and thickness mode on the electrical impedance is shown in Figure 4.3. The impedance profile is of a 50% VF, 0.22 AR, 3.3 mm high, 30 mm diameter disc PZT-5A/hardset piezocomposite. The two modes have been labelled on the graph. As can be seen from the curve, the harmonics of the plate modes are not strongly coupled. This is because of the high damping in the polymer and illustrates one of the advantages of 1-3 piezocomposites over monolithic ceramic for the active material.

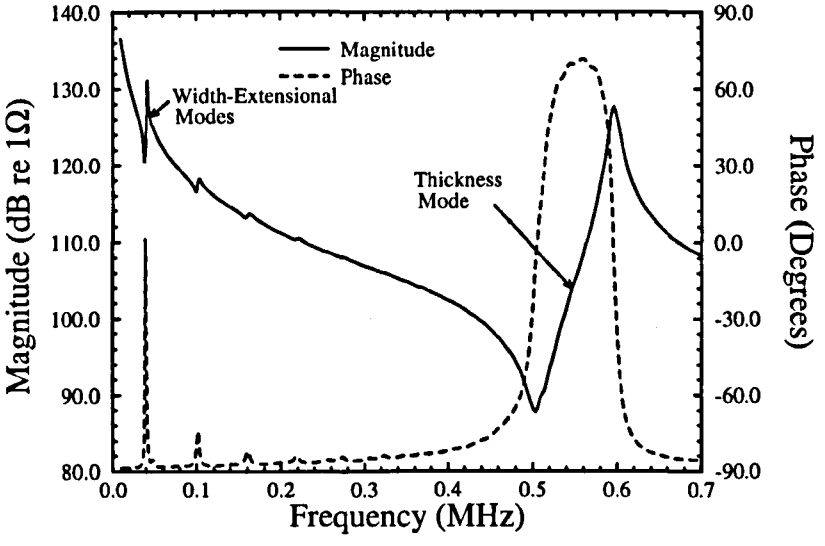

Figure 4.3: Impedance Profile of 50% VF 0.22 AR Piezocomposite

4.2.3 Inter-Pillar Resonances

As the ceramic pillars vibrate in the *3* direction, planar shear waves are excited within the polymer matrix in the *1* and *2* directions. At certain frequencies dependent on the spacing, these waves will interfere constructively because of the lattice structure. This behaviour was explained using Brillouin scattering theory by Auld and Wang [48], provided that the following physical constraints were valid:

- The width of the ceramic pillars is relatively small compared to the inter-pillar distance, d_p, and the height of the plate is greater than the pillar spacing so that the structure approximates that of a Brillouin lattice.
- The transverse wavelength for the operating frequency is comparable with the composite pillar periodicity. If the wavelength is too great, then Smith's assumption of sufficiently fine pillar spacing becomes valid and the composite acts as a homogenous material. Using laser probe measurements, Gururaju et al. [46] estimated that this conditions occurs when the transverse wavelength is more than three times the periodicity.
- The damping within the polymer is sufficiently low that a transverse wave can be sustained within the matrix. If this was not valid, then no modes can exist within the polymer and the width-extensional and inter-pillar modes do not affect the behaviour of the piezocomposite.

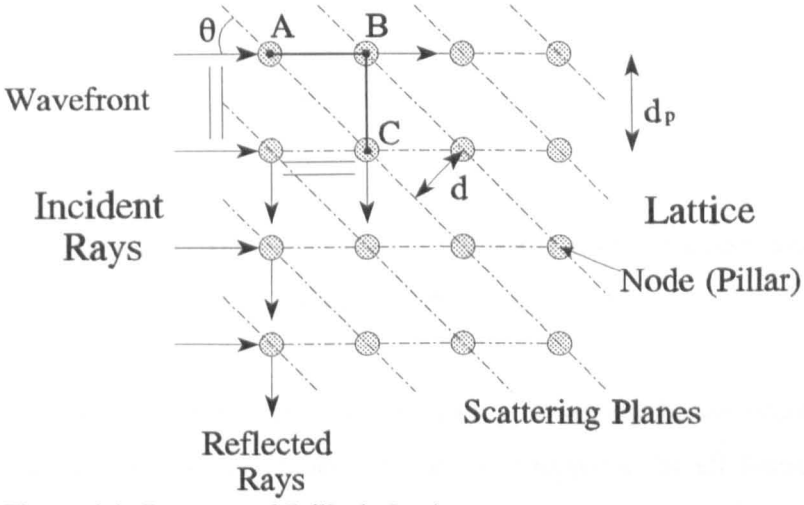

Figure 4.4: Geometry of Brillouin Lattice

Brillouin lattices exhibit Bragg scattering which is a concept that originated from X-ray diffraction in crystal lattices. The internal geometrical dimensions of the individual unit cells is ignored and the crystal lattice can be represented as a two-dimensional lattice for a uniform periodic structure as shown in Figure 4.4.

The diffracted rays combine to produce a maximum intensity when the path difference (ABC in the diagram) is an integral number of wavelengths as can be seen

from Figure 4.5. This diagram is simplified version of Figure 4.4 and has been rotated so that the diffracting planes are horizontal. The position of A, B, and C can be easily seen in relationship with each other. Each point represents a stiff ceramic pillar in a soft polymer matrix.

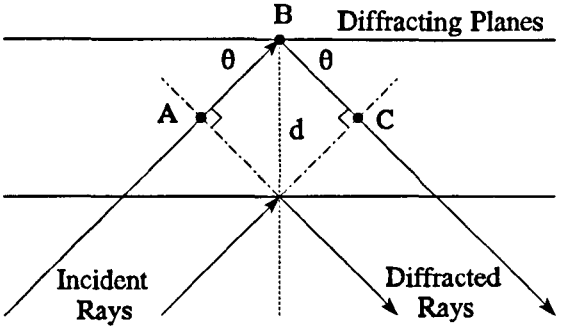

Figure 4.5: Simplified Diagram of Diffraction Process

Mathematically, this is represented by the Bragg Equation:

$$\underline{AB} + \underline{BC} = m\lambda$$
$$2d\sin\theta = m\lambda \quad \forall\ m=1,2,3,... \qquad \textbf{Eqn. 4.5}$$

where d is the distance between the scattering planes;

θ is the angle between the incident ray and scattering plane; and

λ is the wavelength of the propagating ray.

For the composite material, the incident ray is assumed to be produced by the vibrating ceramic pillars and hence, the waves propagate in all lateral directions. Considering the regular lattice, the valid angles for which constructive scattering will occur between pillars spaced at identical distances, can only be 90° for the vertical plane and 45° for the diagonal plane. There would be no scattering for an angle of 0° as sin(0°)=0. Each case is be examined separately where the spacing, *d*, of Equation (4.5) is taken as the inter-pillar spacing.

A. For the vertical planes, Bragg scattering will occur for:

$$\begin{aligned} 2d_p \sin(90^o) &= m v_s \\ 2d_p &= m v_s \\ f_v^m &= \frac{m v_s}{2d_p} \end{aligned} \qquad \textbf{Eqn. 4.6}$$

where d_p is the centre-to-centre distance between the pillars;

f_v^m is the resonance frequencies of the vertical plane modes; and

v_s is the shear wave velocity in the polymer.

B. For the diagonal planes, Bragg scattering will occur for:

$$\begin{aligned} 2\left(\frac{d_p}{\sqrt{2}}\right)\sin(45^o) &= m v_s \\ d_p &= m v_s \\ f_d^m &= \frac{m v_s}{d_p} \end{aligned} \qquad \textbf{Eqn. 4.7}$$

where f_d^m is the frequencies of the diagonal modes.

Consequently, the shear waves propagating with wavelengths, d_p, $d_p/2$, $d_p/3$ will scatter both into the vertical and diagonal planes and hence produce a strong vibrational mode. The odd harmonics of the vertical plane resonances would be destructively interfered by the waves produced from the neighbouring pillars and would not be strongly coupled. An example of an inter-pillar mode is illustrated by the surface displacement profile of the fundamental resonance as shown in Figure 4.6.

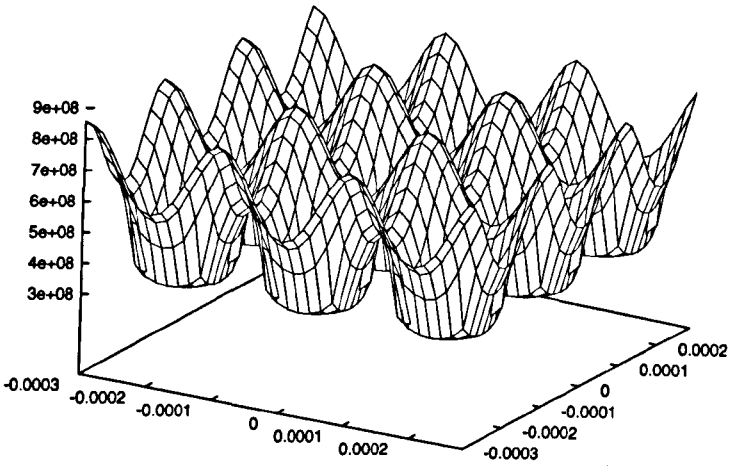

Figure 4.6: Surface Displacement Profile of a Inter-Pillar Mode

By rotating the lattice through 45°, a new set of resonance conditions can be derived in a similar manner. The spacing, d, is no longer the inter-pillar spacing but $\sqrt{2}d_p$. Hence, Bragg scattering modes will occur according to the frequency equation:

$$f_{45}^{m} = \frac{m v_s}{\sqrt{2}\, d_p} \quad \forall \quad m = 1,2,3,... \qquad \textbf{Eqn. 4.8}$$

However, the first mode, f_{45}^{1}, cannot be sustained in the matrix as it has an associated wavelength of greater than the dimensions of a unit cell. Any such mode cannot be coupled piezoelectrically since adjacent ceramic pillars would vibrate out of phase.

In summary, the first three strongly coupled inter-pillar modes for a 1-3 piezocomposite are:

1. $f_{L1} = \frac{v_s}{d_p}$ Ceramic and polymer vibrate anti-phase along any diagonal but in phase in *1* and *2* directions.

2. $f_{L2} = \frac{\sqrt{2}\, v_s}{d_p}$ Ceramic and polymer vibrate in phase along the diagonal.

3. $f_{L3} = \frac{2v_s}{d_p}$ Ceramic and polymer are alternating anti-phase along the diagonal.

This theory does not account for varying volume fractions and has been found to be more applicable to the lower volume fractions piezocomposites. Several researchers have investigated the effect of these modes on the thickness mode and have derived limiting criteria on the design of the 1-3 piezocomposite material to adequately separate the fundamental thickness mode from the first inter-pillar mode :

- Smith [49] stated the lateral mode frequency should be at least twice that of the thickness mode.
- Craciun [50] stated that the centre-to-centre spacing of the ceramic must be less than the thickness of the piezocomposite.
- Oakley [44] stated that the polymer spacing must be less than one quarter of the shear wavelength.

The criteria of Smith and Oakley are equivalent in the range of volume fractions between 20% and 80%. Another criterion was investigated in this Chapter not using a theoretical formula but using modal analysis for the different volume fractions. This has been detailed in Section 4.3.

4.2.4 Intra-Pillar Resonances

These modes occur because the boundary between the polymer matrix and the ceramic pillars represents a sufficient acoustic mismatch for resonant modes to occur with the ceramic pillars. In general, these only exist in the same frequency range as the thickness mode for aspect ratio's greater than 0.60. This is significant for higher volume fraction composites where the kerf width is correspondingly smaller, increasing the frequency of the inter-pillar modes. As high volume fraction composites are seldom used because they have no major advantage over the original ceramic, these modes are of no great interest to the transducer designer and are

ignored by most theoretical models. However, the finite element modelling design methodology does incorporate their influence on the response and this is illustrated in Table 4.4.

4.3 INVESTIGATION INTO MAXIMUM PILLAR ASPECT RATIO

For efficient homogeneous operation, the 1-3 piezocomposite must be designed so that there is sufficient separation between the efficient thickness mode and the destructive lateral modes. The application for which the material is being designed, determines the height for operational frequency and volume fraction for maximum transmission and reception. Both these variables can be selected with the use of the isostrain model as shown in Section 4.1. The remaining variable for the microstructure of the 1-3 piezocomposite is the aspect ratio of the ceramic pillars which must be chosen to ensure mode separation. This has led to the concept of maximum pillar aspect ratio (MPAR) which specifies the maximum value for a configuration of ceramic and polymer materials for a given volume fraction. If this value is exceeded, the first lateral mode would interfere with and compromise the thickness mode. The MPAR of different-shaped pillars was investigated initially using lossless modal analysis. However, the effect of mechanical loss in the high-loss polymers tends to reduce the coupling co-efficient of the lateral modes allowing the practical use of aspect ratios above the MPAR, as discussed in Section 4.4.

The inter-pillar resonances are dependent on the spacing of the pillars which is constrained by manufacturing capability. The present standard method of manufacturing the piezocomposite is the *dice-and-fill* method developed by Savakus [51] which involves dicing ceramic with a saw to form kerfs in the ceramic substrate and filling the kerfs with polymer. Hence, the smallest achievable kerf width with this method is the physical thickness of the blade. Savakus had blades varying between 0.3 mm and 1.1 mm for his work. Tests were performed at the Ultrasonics Research Group with different sized blades and it was found that for accurate dicing, 0.22 mm blade was the minimum viable value for the kerf width. This restricted the minimum

value of the aspect ratio for a given volume fraction and height. The modern technique of injection moulding has been demonstrated successfully [52] but preference is for shorter pillars to maintain rigidity during the extrusion process. Hence, both manufacturing processes become more reliable and cost-effective for larger (> 0.10) aspect ratios.

4.3.1 Square Pillar Composites

The standard pillar configuration examined was that of square pillars. To aid in the manufacture of the practical transducers for comparison with the finite element modelling, the kerf width was kept constant at 0.22 mm. Three different volume fractions for two piezocomposite materials, PZT-5A/hardset and PZT-5A/softset, were made: 10%, 20% and 40%. To increase the amount of available data, each transducer was measured for a series of different heights where the piezocomposite plate was lapped to change the height between each measurement. Table 4.2 and 4.3 summarises the defining parameters for all the experimental transducers.

The frequencies and coupling co-efficients of the fundamental thickness mode and the first two lateral modes if they could be detected, were measured and are displayed with the simulation results. For the simulation, the width of the pillars was kept constant and the height of the piezocomposite was varied to modify the aspect ratio. Figures 4.8 to 4.10 show the effect of varying the aspect ratio from 0.05 to 0.80 on the centre electrical frequency, coupling co-efficient and surface dilation quality at the fundamental electrical resonant frequency for the three sets of volume fractions. Where the thickness mode and lateral modes could be extracted from the experimental impedances for the hardset composites, they showed reasonable agreement with the finite element simulations, although depolarisation of the ceramic is evident in the lower volume fraction data. Omission of any mode indicates that identification was not possible for that configuration. This was especially true for the softset composites where the polymer matrix could not sustain the lateral modes. The softset filler has a reduced velocity compared to hardset and consequently the lateral

Table 4.2: Parameters of Experimental PZT-5A/Hardset Transducers

Name	Volume Fraction	Height (mm)	Aspect Ratio	f_{elec} (MHz)	f_{mech} (MHz)
P1S1A1	10%	4.3	0.116	0.354	0.373
P1S1A2	10%	3.5	0.143	0.402	0.438
P1S1A3	10%	2.5	0.200	0.660	0.748
P1S1A4	10%	1.5	0.333	1.021	1.182
P1S2A1	20%	3.8	0.132	0.388	0.445
P1S2A2	20%	3.5	0.143	0.415	0.475
P1S2A3	20%	2.5	0.200	0.568	0.658
P1S2A4	20%	1.5	0.333	1.068	1.204
P1S3A1	40%	5.3	0.094	0.287	0.343
P1S3A2	40%	4.5	0.111	0.331	0.405
P1S3A3	40%	3.5	0.143	0.423	0.513
P1S3A4	40%	2.5	0.200	0.582	0.715
P1S3A5	40%	1.5	0.333	0.999	1.194

resonances are expected to occur at lower frequencies. However, it can be observed in the curves for the softset filler that the analysis did not produce results with good correlation to the experiments due to the high mechanical loss in the softset.

The frequencies predicted by the Bragg scattering theory were also included on the appropriate curves. As indicated in Figure 4.9(e), surface dilation quality of the fundamental thickness mode deteriorates rapidly with increasing pillar aspect ratio. Indeed, for aspect ratios above 0.50 in the 20% composite, reliable detection of the thickness mode is no longer possible, with surface displacement dominated by the now more strongly coupled lateral modes. At higher volume fractions the lateral resonances are shifted up the spectrum, away from the desired thickness mode and the degradation is much less significant for any given pillar aspect ratio. For efficient

Table 4.3: Parameters of Experimental PZT-5A/Softset Transducers

Name	Volume Fraction	Height (mm)	Aspect Ratio	f_{elec} (MHz)	f_{mech} (MHz)
P2S1A1	10%	5.4	0.093	0.277	0.345
P2S1A2	10%	3.5	0.143	0.402	0.474
P2S1A3	10%	2.5	0.200	0.511	0.650
P2S1A4	10%	1.5	0.333	0.858	1.104
P2S2A1	20%	4.0	0.125	0.304	0.449
P2S2A2	20%	3.5	0.143	0.374	0.490
P2S2A3	20%	2.5	0.200	0.543	0.656
P2S2A4	20%	1.5	0.333	0.782	1.088
P2S3A1	40%	5.7	0.088	0.253	0.304
P2S3A2	40%	4.5	0.111	0.312	0.377
P2S3A3	40%	3.5	0.143	0.410	0.499
P2S3A4	40%	2.5	0.200	0.515	0.632
P2S3A5	40%	1.5	0.333	0.790	1.042

and uniform thickness mode operation, it is necessary to achieve a surface dilation quality (preferably at the transducer centre frequency) that is close to unity, while at the same time maximising the thickness mode coupling coefficient within any constraints imposed by the composite structure. This requires effective isolation of the thickness resonance, permitting the composite to behave as a homogeneous medium. The situation may be clarified by considering Figure 4.11 which shows the variation in thickness mode coupling factor as a function of the separation between the first lateral and thickness electrical resonance frequencies for PZT-5A/hardset composites with volume fractions between 10% and 40%.

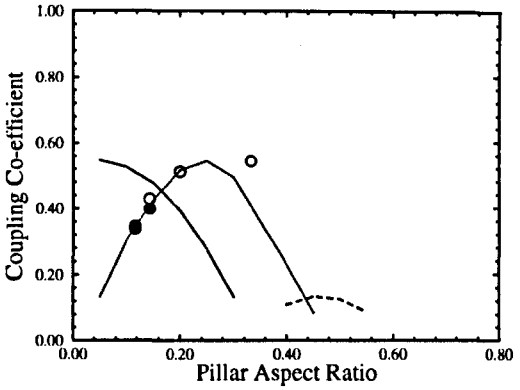

(a) Hardset Composite

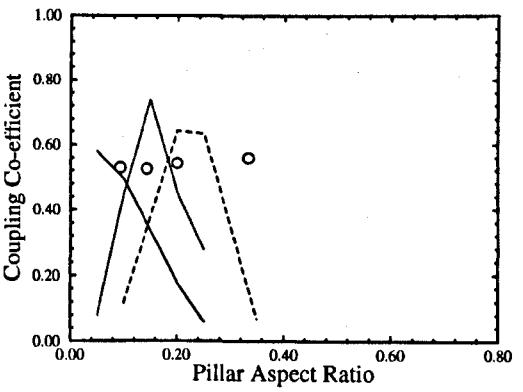

(b) Softset Composite

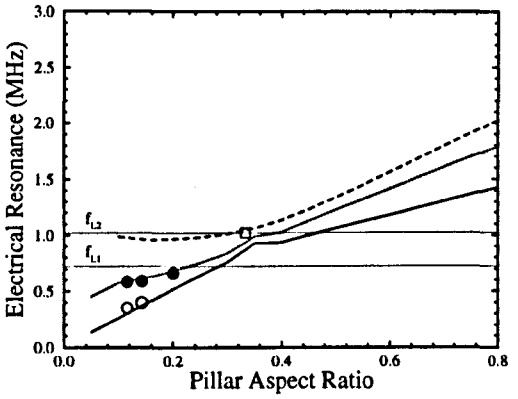

(c) Hardset Composite

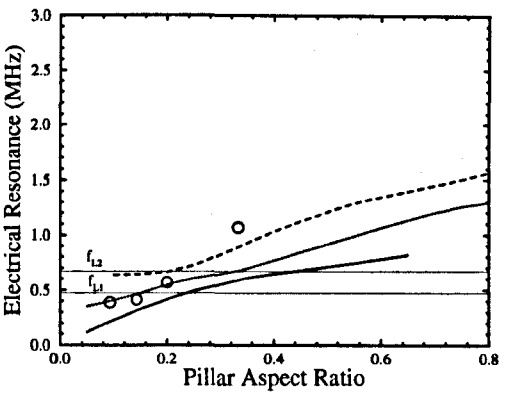

(d) Softset Composite

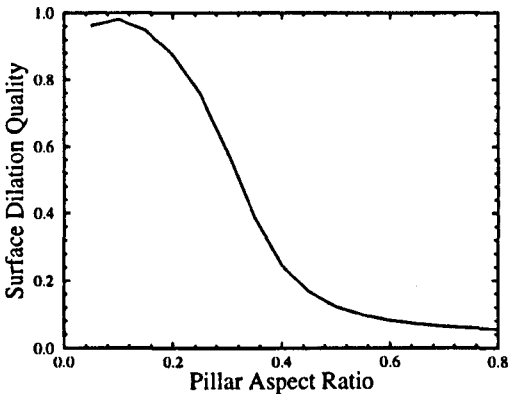

(e) Hardset Composite

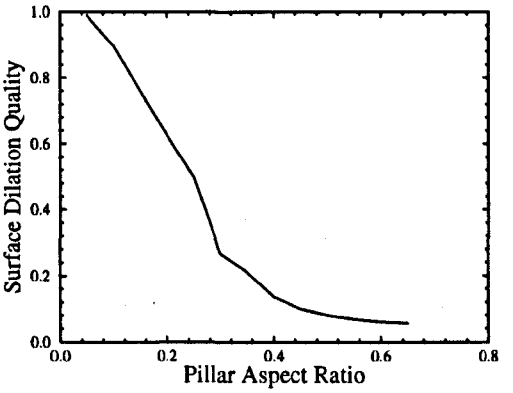

(f) Softset Composite

Figure 4.8: Transducer Characteristics as a function of Aspect Ratio for 10% VF Composite

Key:			
	Thickness Mode	— Theory	O Experiment
	First Lateral Mode	" " Theory	● Experiment
	Second Lateral Mode	---- Theory	□ Experiment

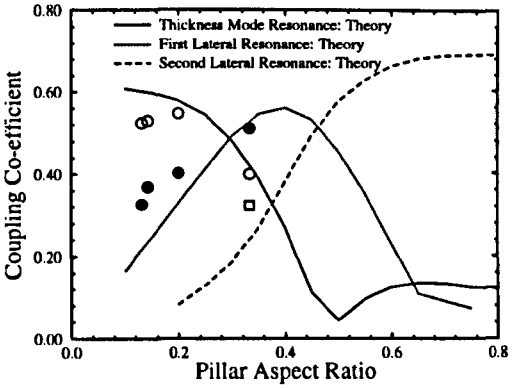

(a) Hardset Composite

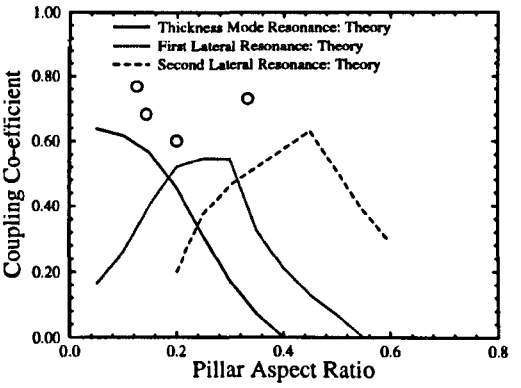

(b) Softset Composite

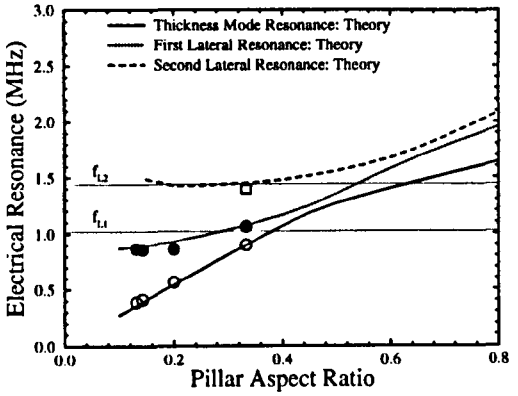

(c) Hardset Composite

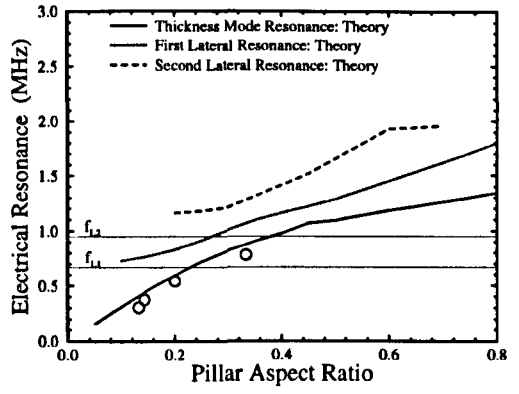

(d) Softset Composite

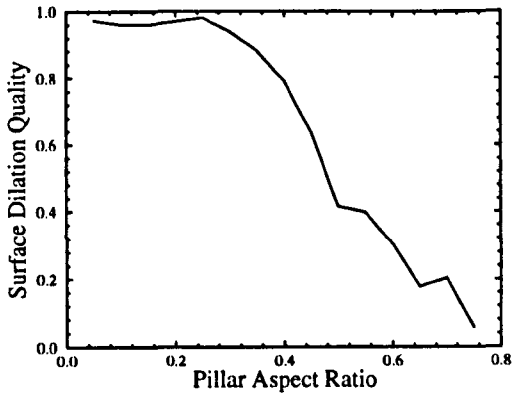

(e) Hardset Composite

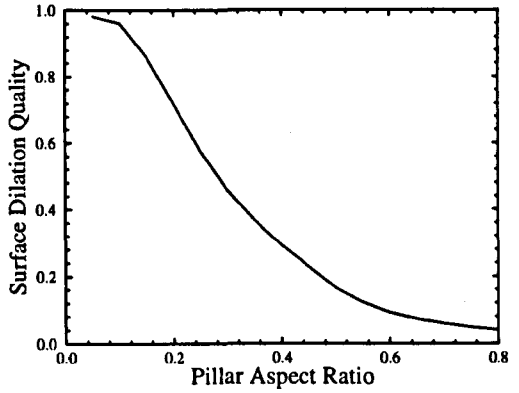

(f) Softset Composite

Figure 4.9: Transducer Characteristics as a function of Aspect Ratio for 20% VF Composite

Key: Thickness Mode — Theory ○ Experiment
First Lateral Mode - - - Theory ● Experiment
Second Lateral Mode ---- Theory □ Experiment

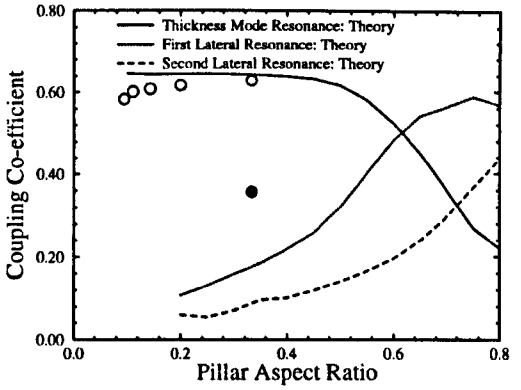

(a) Hardset Composite

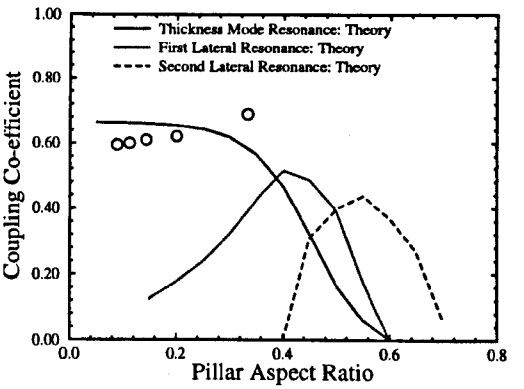

(b) Softset Composite

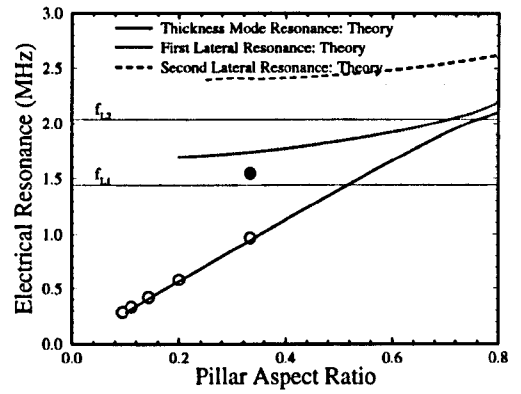

(c) Hardset Composite

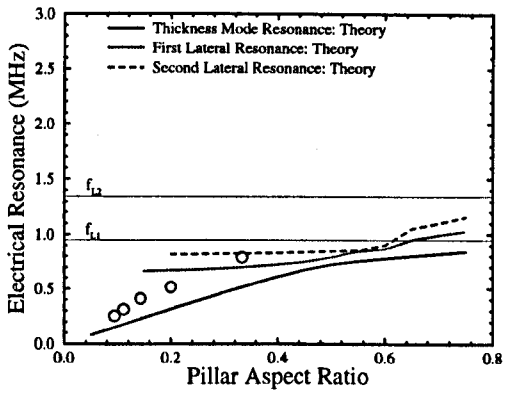

(d) Softset Composite

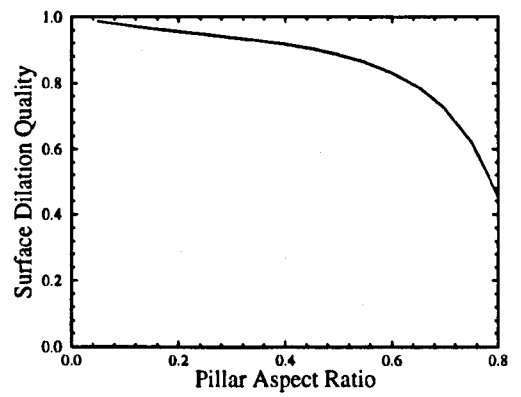

(e) Hardset Composite

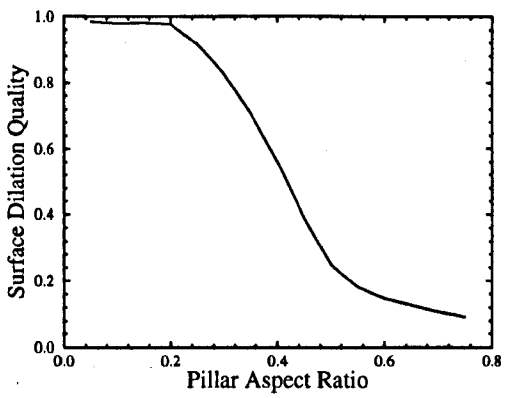

(f) Softset Composite

Figure 4.10: Transducer Characteristics as a function of Aspect Ratio for 40% VF Composite

Key:			
	Thickness Mode	— Theory	○ Experiment
	First Lateral Mode	- - Theory	● Experiment
	Second Lateral Mode	---- Theory	□ Experiment

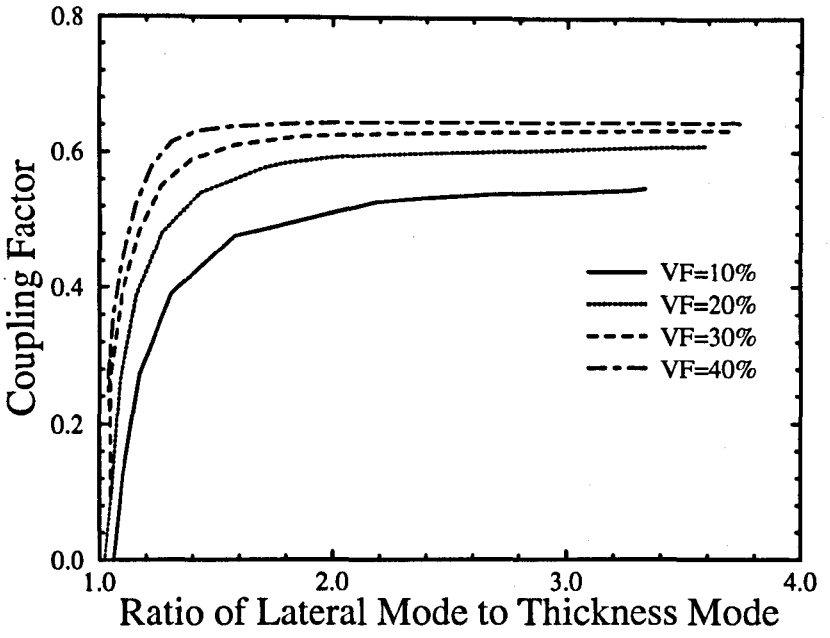

Figure 4.11: Graph showing Coupling Factor for Different Frequency Ratios of the Lateral Mode to the Thickness Mode

It is apparent that for volume fractions greater than and equal to 20%, a separation factor of 2 is sufficient to maximise the coupling coefficient. This agrees well with the comments of Smith [49] and conveniently corresponds to the null at the second harmonic of the thickness mode spectrum. However for volume fractions below 20% the coupling coefficient is reduced and stronger lateral mode interference is evident. Consequently the following criteria were adopted for selection of MPAR:

- $Q_{dil} > 0.900$
- $f_{L1} > 2f_{elec}$ for VF > 20%
- $f_{L1} > 3f_{elec}$ for VF < 20%

Finite element simulations were then repeated at different volume fractions for hardset and softset fillers and the critical pillar aspect ratios were determined in each case in conjunction with thickness mode coupling coefficient and surface dilation quality factor. The results are shown in Table 4.4 for the volume fraction range 10% to 90%.

Table 4.4: MPAR for Different Volume Fractions with Square Pillars

	Hardset Composites			Softset Composites		
VF	MPAR	k_t	$Q_{dil}@f_{elec}$	MPAR	k_t	$Q_{dil}@f_{elec}$
10%	0.07	0.541	0.963	0.05	0.579	0.991
20%	0.17	0.590	0.974	0.12	0.603	0.927
30%	0.23	0.624	0.954	0.16	0.635	0.938
40%	0.30	0.643	0.935	0.21	0.653	0.967
50%	0.39	0.653	0.915	0.28	0.663	0.975
60%	0.46	0.656	0.905	0.38	0.669	0.948
70%	0.47	0.651	0.920	0.47	0.670	0.926
80%	0.50	0.638	0.931	0.50	0.661	0.930
90%	0.55	0.605	0.942	0.52	0.633	0.945

From the Table it may be noted that the thickness mode coupling displayed the expected variation for homogeneous behaviour across the volume fraction range with surface dilation quality always greater than 0.900. While the data shown in Table 4.4 provides a useful design guideline, it is only valid for the particular filler material and piezoelectric ceramic under consideration for in-air analysis. The possible variations are illustrated by the differences in the MPAR for the two fillers, where the softset had a reduced MPAR over the full range of volume fractions. Since the two phases are now more independent, the coupling factor is increased, with dilation quality reduced, reflecting the more independent ceramic displacement in the softer material. However, here it is worth emphasising the fact that modal analysis neglects the influence of propagation loss within the polymer and only provides a valid comparison for low loss fillers, or where the operating frequencies are such that the influence of loss may be neglected. The difference in MPAR is not as large at the higher volume fractions because the aspect ratio is not constrained by the inter-pillar spacing but rather intra-pillar modes. This is why the MPAR is practically constant

for volume fractions greater than 70% in that the modes are internal to the pillar and are independent of the polymer phase.

4.3.2 Cylindrical Pillar Composites

Table 4.5: MPAR for Different Volume Fractions with Cylindrical Pillars

	Hardset Composites			Softset Composites		
VF	MPAR	k_t	$Q_{dil}@f_{elec}$	MPAR	k_t	$Q_{dil}@f_{elec}$
10%	0.08	0.531	0.965	0.06	0.568	0.985
20%	0.18	0.583	0.980	0.13	0.594	0.918
30%	0.24	0.618	0.965	0.17	0.627	0.911
40%	0.30	0.637	0.948	0.21	0.647	0.919
50%	0.36	0.649	0.934	0.25	0.659	0.946
60%	0.43	0.654	0.922	0.30	0.665	0.978

The cylindrical shape was proposed because the pillars would not have any parallel sides meaning that the only structure giving rise to lateral modes was the periodic position of the pillars. If the injection moulding technique of piezocomposite manufacturing [52] is used, then cylindrical pillars are easier to manufacture than square pillars. The MPAR results are summarised in Table 4.5 with the slightly enhanced MPAR at 10% compared to square pillars due to the closer proximity of the cylinders allowing safe operation at a correspondingly higher frequency. In all other respects, a comparison with Table 4.4 indicates strong similarity and no significant gain in MPAR. The reason that Table 4.5 contains values of volume fractions not exceeding 60% is that above these volume fractions, the cylinders would overlap. The same phenomena applies with the triangular pillars which limit the volume fraction of the triangular pillar composite to 40%.

4.3.3 Triangular Pillar Composites

The triangular pillar configuration shown in Figure 3.9 has the advantage over square pillars that there are no parallel facing sizes. The aspect ratio was defined in Section 3.6.2 as the minimum of b and c over the height of the pillar where b and c are related through the angle, θ:

$$\tan\left(\frac{\theta}{2}\right) = \frac{b}{2c} \qquad \textbf{Eqn. 4.9}$$

The optimal angle can be described as the angle which ensures that the lateral resonances are shifted furthest away from the thickness mode, for a given aspect ratio. As there is a set of lateral modes associated with each lateral dimension of the unit cell, the optimal value of the angle is that for which b and c are equal giving:

$$\tan\left(\frac{\theta}{2}\right) = \frac{1}{2} \qquad \textbf{Eqn. 4.10}$$
$$\theta = 53.13^{o}$$

The frequencies of the thickness mode and the first two lateral modes for a triangular pillar composite with angles: 50°; 53°; and 56°, were generated by modal analysis and are shown in Table 4.6. The piezocomposite consisted of 25% VF, 0.10 AR, 1.0 mm high, PZT-5A/hardset material.

Table 4.6: Frequency of Lateral Modes for Triangular Pillars

Angle	Thickness Mode (kHz)	1st Lateral Mode (kHz)	2nd Lateral Mode (kHz)
50°	853	1660	1675
53°	853	1708	1716
56°	853	1646	1715

Table 4.7: MPAR for Different Volume Fractions with Triangular Pillars

	Hardset Composites			Softset Composites		
VF	MPAR	k_t	$Q_{dil}@f_{elec}$	MPAR	k_t	$Q_{dil}@f_{elec}$
10%	0.10	0.542	0.965	0.06	0.587	0.990
20%	0.23	0.594	0.973	0.15	0.616	0.945
30%	0.31	0.624	0.959	0.19	0.643	0.950
40%	0.38	0.639	0.947	0.25	0.653	0.947

Using an angle of 53°, the MPAR results for different volume fractions were generated from modal analysis and are shown in Table 4.7 from which it is evident that the MPAR has increased when compared with the alternative composite structures. From the Table, the MPAR is increased by a factor of 43% at 10% volume fraction, to 27% at 40% volume fraction, when compared with the doubly periodic square pillar configuration. However, while there is comparable thickness mode efficiency for the triangular structure at 10% volume fraction, a corresponding reduction of 15% at 40% volume fraction is more significant. Consequently, the triangular arrangement would be advantageous for low (<25%) volume fraction composites and would be suited to the manufacture by injection moulding where the increased MPAR could constitute a distinct advantage. Also the triangular structure lends itself very well to interleaving, whereby 2 40% VF composites can be interleaved prior to encapsulation, to produce a single 80% VF device. This is important for the injection moulding process, which cannot produce high volume fraction devices in a single run.

4.4 INFLUENCE OF POLYMER LOSS

As stated previously, shear loss mechanisms in the polymer are expected to influence both the surface dilation quality and thickness mode efficiency. For lossy polymers, the lateral modes are relatively weak, with the consequent decoupling between

ceramic and polymer degrading dilation quality and at the same time increasing the apparent thickness mode efficiency [46].

4.4.1 Effect of Polymer Loss on Performance

It was found that while modal analysis was adequate at predicting results for composites with the hardset as the filler, it was not for softset composites because of the relatively high mechanical loss. Under experimental conditions, no evidence of lateral activity could be found and although the fundamental thickness mode resonance is predicted reasonably well as a function of aspect ratio, there is no evidence of degradation in electromechanical coupling coefficient as predicted by the modal analysis. The high experimental coupling coefficients provide a clear indication that the ceramic is acting independently of the polymer, with minimal degradation from lateral modes.

To evaluate the influence of polymer loss, harmonic analysis was performed to predict the electrical impedance of the composite as a function of frequency. Here the damping was systematically adjusted until a good correlation was obtained between theoretical and experimental impedance data. Thereafter the damping was maintained constant for that particular filler material during further theoretical analysis. Typical results are shown in Figures 4.12 and 4.13 for the transducers P1S2A1 and P2S2A2 respectively. P1S2A1 is a 20% VF 0.13 AR PZT-5A/hardset composite and P2S2A2 is a 20% VF 0.14 AR PZT-5A/softset composite. For the hardset composite, two strong modes are evident, corresponding to the thickness and first lateral resonances. Reasonable correlation between theory and experiment may be observed in the impedance curve. The softset composite displays quite different behaviour, with almost uni-modal behaviour that is predicted quite well by the finite element theory. The reason that the correlation between results from the finite element model and P2S2A2 transducer is not as close as for the P1S2A1 transducer is that the lateral mode, L1, is coupled with the thickness mode. The ANSYS package has the capability of only modelling with a single damping co-efficient per material so cannot

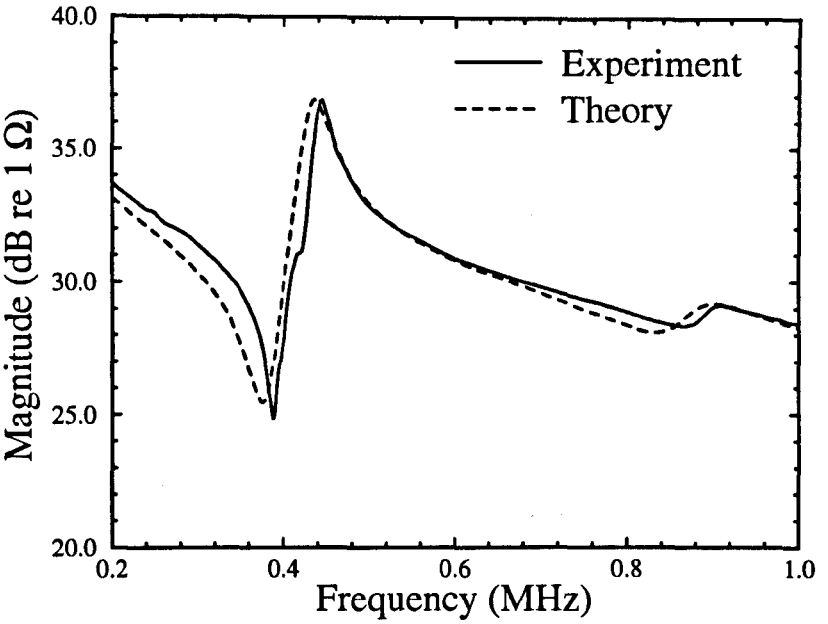

Figure 4.12: Impedance Magnitude of the Transducer P1S2A1

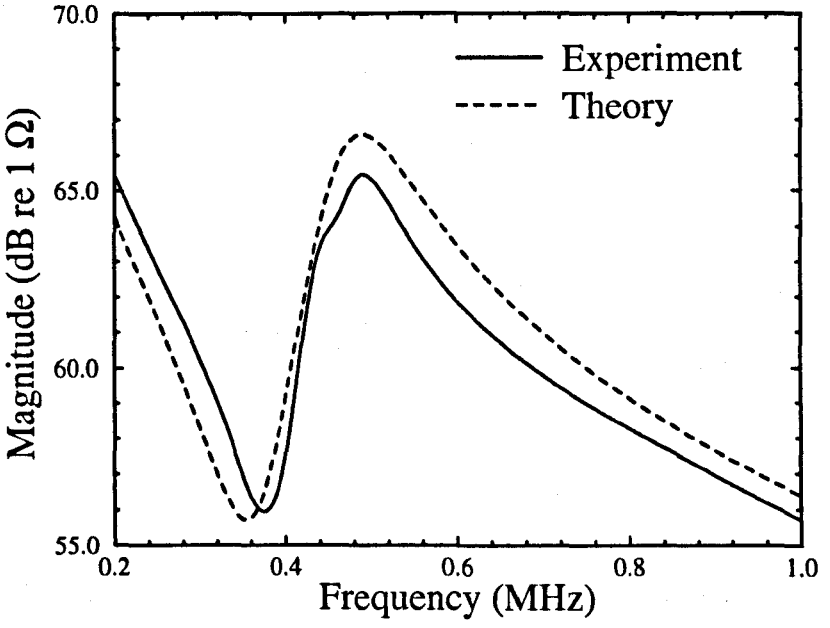

Figure 4.13: Impedance Magnitude of the Transducer P2S2A2

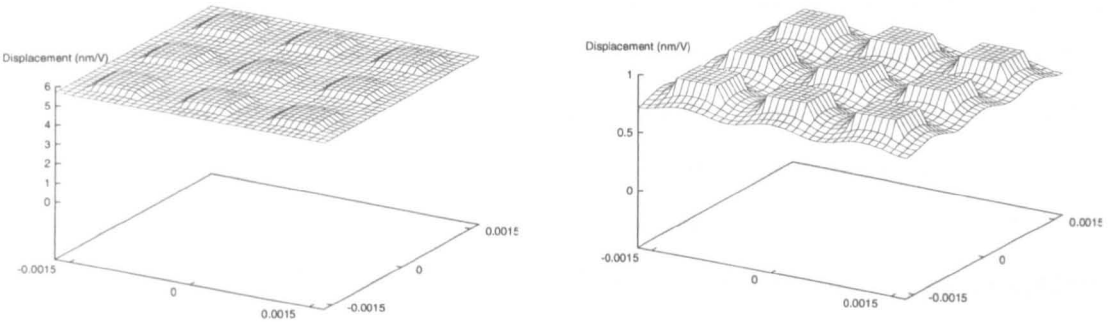

(a) P1S2A1 (b) P2S2A2

Figure 4.14: Surface Displacement Profiles for the two 20% VF PZT-5A Composites

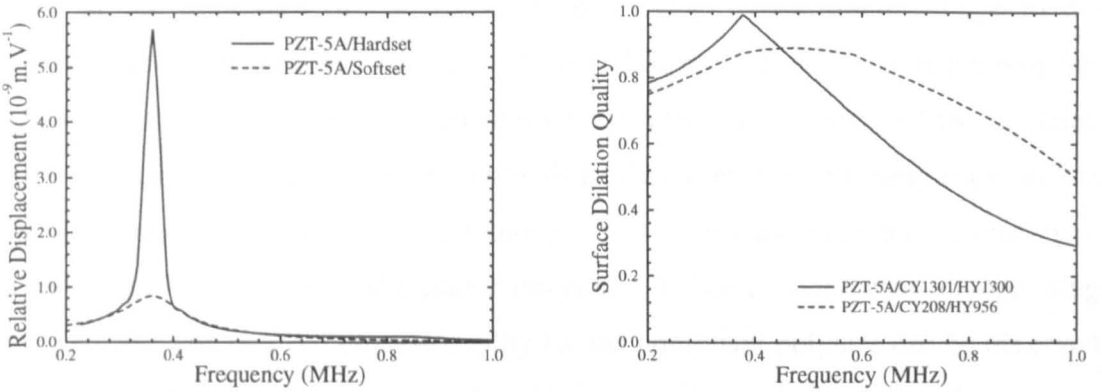

(a) Displacement (b) Dilation Quality

Figure 4.15: Surface Motion for the two 20% VF PZT-5A Composites

incorporate both the longitudinal loss associated with the thickness mode and shear loss associated with the lateral mode.

It is evident that the previous definition for MPAR is no longer valid for softset fillers which cannot sustain significant lateral wave propagation. Here the MPAR is not constrained by shear scattering within the lattice, but by intra-pillar modes occurring internally within the pillars. These are only significant for aspect ratios in the range 0.70-5.00 according to Hossack [34], suggesting that the effective MPAR can be larger than in the case for low-loss devices. However, this argument ignores the influence of lossy polymers on the surface dilation quality. As indicated previously, decoupling of the ceramic phase results in independent pillar vibration and depending on the polymer Poisson ratio, ceramic and polymer may even vibrate in an anti-phase manner. The surface displacement profiles for three by three ceramic pillars in the polymer matrix at the thickness mode electrical resonance frequency are shown in Figures 4.14(a) and (b) for the hardset and softset composite respectively. The units of the abscissa are nanometres per volt and is the displacement of each node at the front face of the transducer normalised to the input voltage to the material. It can be observed that the ceramic pillars move further out of the polymer matrix for the more compliant filler. Also the displacement is retarded by the damp filler. This is clearly shown in the normalised displacement with frequency for the two composites in Figure 4.15(a). Although the softset composite does demonstrate a reduced displacement at the centre frequency, it has a wider band of operating frequencies. The reduced dilation quality for the compliant polymer can be observed in Figure 4.15(b) which compares the dilation quality with frequency for the two transducers.

The dilation quality at the electrical resonance frequencies for the composites with aspect ratios of the MPAR detailed in Tables 4.4, 4.5 and 4.7 were estimated using harmonic analysis incorporating loss. The results are given in Table 4.8. No unambiguous thickness mode could be detected for the 10% VF softset composite transducers and hence, the correct dilation quality could not be determined.

Table 4.8: Dilation Qualities with Loss at the MPAR for Different Composites

	Hardset			Softset		
VF	SQR	CYL	TRI	SQR	CYL	TRI
10%	0.923	0.915	0.924	-	-	-
20%	0.922	0.918	0.926	0.790	0.762	0.827
30%	0.922	0.922	0.926	0.834	0.805	0.871
40%	0.918	0.917	0.924	0.860	0.835	0.888
50%	0.908	0.912		0.872	0.861	
60%	0.900	0.907		0.877	0.876	
70%	0.927			0.890		
80%	0.942			0.921		
90%	0.956			0.959		

The dilation qualities for the hardset composites were similar to those generated without the loss mechanisms. However, the softset composite had significantly reduced values except at the higher volume fractions where the displacement of the ceramic pillars dominates the expression.

The dilation quality behaviour as a function of aspect ratio is shown in Figure 4.18 for the three pillar shapes at a volume fraction of 10% using the hardset as the filler for the solid line and softset for the dotted line. The surface dilation quality for the 10% VF softset configurations were taken as the maximum value in the operational frequency band. As before, the triangular pillar composite provided superior dilation quality over the range of aspect ratios and the extent of this improvement has been increased by the inclusion of loss in the polymer phase. Interestingly, the MPAR may be increased by 10% over the volume fraction range, although dilation quality is compromised slightly when compared with the lossless case of Table 4.8.

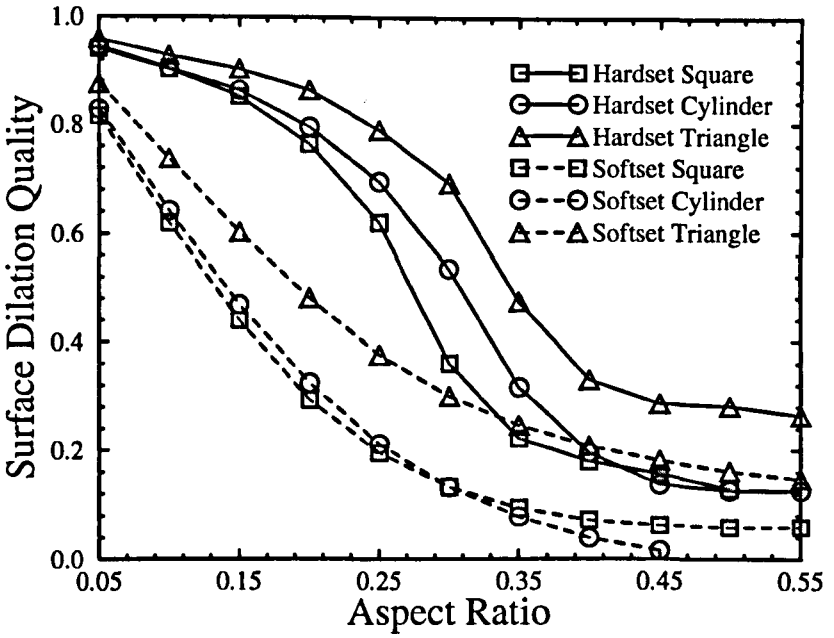

Figure 4.16: Comparison of Surface Dilation Quality for Different 10% Composites

For the softset composite, the dilation quality falls off rapidly with increasing pillar aspect ratio, and using this as a measure of thickness mode quality, no significant increases in MPAR are apparent when compared with the data shown in Table 4.6.

Figure 4.17(a) shows the variation in surface dilation quality at the fundamental thickness mode across the range of aspect ratios and including the influence of the lateral resonances, for different volume fraction PZT-5A/hardset composites. The volume fractions were from 10% to 40% and these simulations included the influence of polymer loss. It can be seen that as the aspect ratio increases and the first lateral mode becomes the dominant mode rather than the thickness mode, the dilation quality decreases sharply. The curve representing the results from the 30% VF configuration were not displayed to reduce the amount of information in the diagram. The degradations in dilation quality for the softset compared to the hardset filler occur at a lower aspect ratio as would be expected. The reduction is influenced considerably by the internal damping and Poisson ratio of the polymer phase. Similar curves shown in the solid line in Figure 4.17(b) are obtained with the softset filler material replacing the hardset in the previous configurations. The curves with the dotted lines

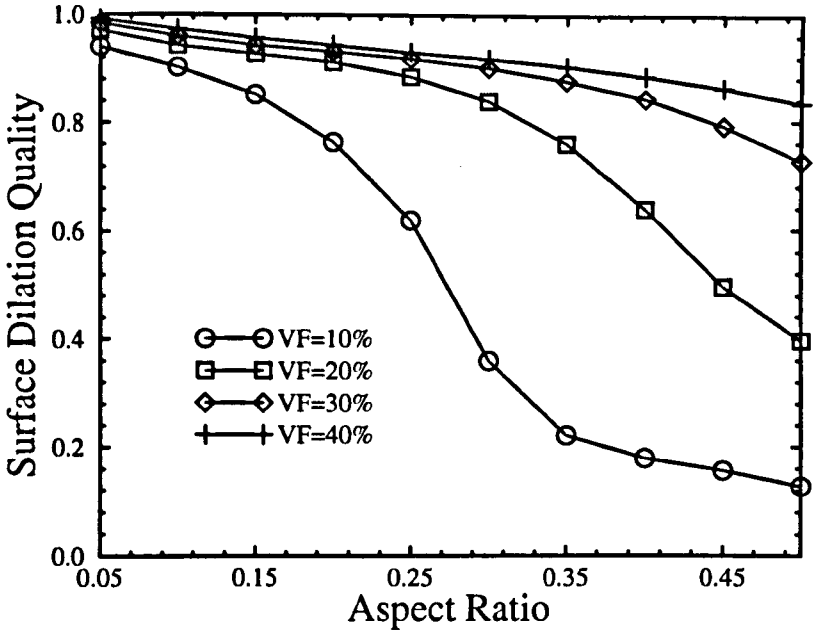

Figure 4.17(a): Comparison of Surface Dilation Quality as a Function of Aspect Ratio for PZT-5A/Hardset Composites

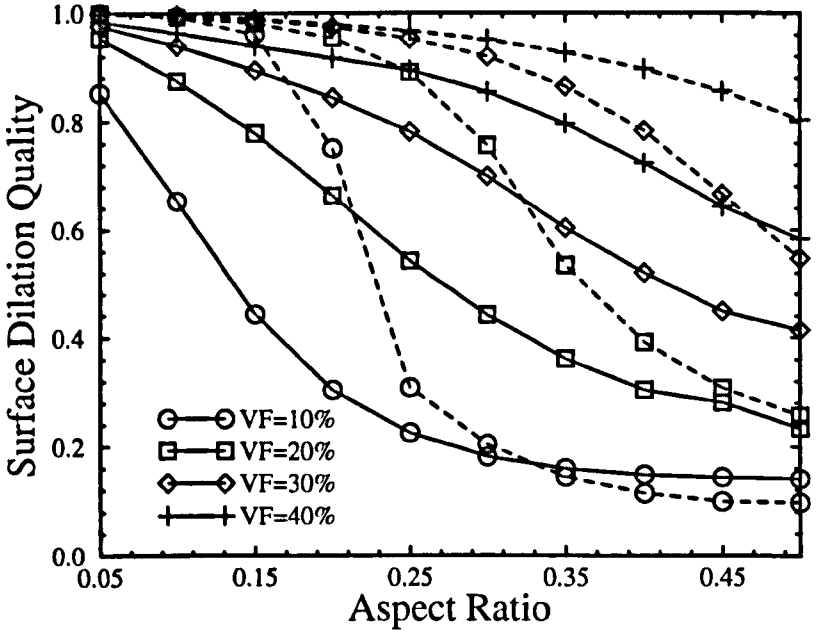

Figure 4.17(b): Comparison of Surface Dilation Quality as a Function of Aspect Ratio for PZT-5A/Softset Composites. Dashed line indicates analysis with stiffening plates.

in Figure 4.17(b) are the results obtained using the configuration with the same marker but with the addition of stiffening plates on the top and bottom surfaces of the piezocomposite. This was to increase the surface dilation quality and hence, the MPAR for the material. The plates were modelled as aluminium sheets with a thickness 0.1 that of the piezocomposite material. The plates are then sufficiently thin so that they do not unduly compromise thickness mode operation. The improvement in dilation quality is apparent with the MPAR increased to 0.15 for 10% volume fraction. Such a configuration was used by Powell [53] in his development of a flexible transducer array for operation into a solid test medium.

A similar analysis was performed with the hardset piezocomposite transducers but the strong inter-pillar resonance led to a reduction rather than an improvement of MPAR. Hence, this method is only applicable where high-loss polymers are used as the passive phase. A further in-depth investigation is required to examine the enhancement of operation into solid media and this has been included in Section 7.2 as a suggestion for future work.

4.5 ANALYSIS OF ANCILLARY COMPONENTS

The previous sections evaluated the influence of the microstructure on the behaviour of the piezocomposite material as a whole in the absence of any other components involved in the construction of the transducer. This section covers the analysis of the influence of these other components on the transducer behaviour. The components are:

- Backing Block;
- Matching layer; and
- Fluid loading

The square pillar shape was used as the example to quantify the effects of the addition of the ancillary components on the behaviour of the piezocomposite where

the composites under analysis are those detailed in Table 4.4. As the behaviour of the transducer is not solely a function of the piezocomposite material, the concept of the coupling factor is not applicable to characterise the performance of the device. Rather, the behaviour of the transducer incorporating loss can be characterised under operation by the following parameters which were examined in Chapter 3:

- The maximum dilation quality (Q_{dil}) within the operational band;
- The maximum transmit sensitivity (S_{TX} expressed in decibels) and its associated fractional bandwidth (BW expressed as percentage -3 dB bandwidth) normalised to the centre frequency; and
- The maximum receive sensitivity (S_{RX} expressed in decibels) and its associated fractional bandwidth (BW expressed as percentage -3 dB bandwidth) normalised to the centre frequency.

The sensitivities displayed in this Section are not the values for practical devices but those for the finite element model. Hence, the relative values between different configurations and not the absolute values are of interest to the reader. The bandwidth can be considered more representative for the practical devices. The operational frequency band is defined as the range of frequencies between the lower limit of the fundamental width-dilational mode and the upper limit of the third harmonic of the thickness mode. The second harmonic was not chosen as the limit because there is usually a null in the response spectrum at this frequency [16]. For the purpose of the modelling, this operational range was taken as being the frequency range covered from 100 kHz to 3.0 MHz.

Table 4.9 gives the values for these quantities for the piezocomposites incorporating loss with no additional components, operating into an air (vacuum) medium. This was simulated as a zero-stress boundary. The Table is used as the baseline for the comparison in the analysis for different components. From the Table, the trends are:

Table 4.9: Behaviour of Different Volume Fraction PZT-5A Composites in Air

	Hardset					Softset				
VF	Q_{dil}	S_{TX}	BW	S_{RX}	BW	Q_{dil}	S_{TX}	BW	S_{RX}	BW
10%	0.991	135	18	-160	17	0.852	120	113	-173	-
20%	0.972	141	13	-163	14	0.844	126	76	-175	78
30%	0.979	144	11	-163	10	0.888	129	60	-176	52
40%	0.976	146	9	-162	8	0.914	131	52	-176	40
50%	0.975	148	8	-162	7	0.940	132	48	-177	34
60%	0.957	148	8	-163	5	0.966	133	47	-178	31
70%	0.950	148	8	-164	6	0.975	133	49	-179	31
80%	0.938	147	9	-166	5	0.977	132	47	-180	28
90%	0.969	146	10	-168	6	0.990	135	27	-178	15

- The maximum surface dilation quality for all the hardset composites was greater than 0.900. This can be compared to the low volume fraction (< 40%) softset composites where the dilation quality never exceeded 0.900 across the operational band. The reason that the dilation quality for the 10% softset configuration is greater than the 20% softset configuration is that the fundamental transmit resonance occurred at a lower frequency. This means that the transducer vibrates in a more piston-like fashion. These dilation qualities exceeded the dilation qualities at the electrical resonance showing that the most uniform surface displacement occurs between the electrical and mechanical resonance. A larger dilation quality produces a wide beamwidth as the transducer moves in a more piston-like manner.
- The transmit sensitivity increases for increasing volume fractions below 30%. The peak is reached around 60% volume fraction. However, if the response of the 10% and 20% VF configurations are ignored, the difference between volume fractions is relatively small. This indicates that the 10% and 20% configurations should not be used as transmitters or transceivers.
- The receive sensitivity decreases slightly with volume fraction other than at very high (90%) volume fractions but the difference between the levels for volume

fractions ranging from 20% to 70% is not large. This indicates that the 10% configurations would make the best receivers but in conjunction with the previous observation, the optimal transceivers are between 30% and 70% if the combined transmit/receive levels are considered.

- The levels for the hardset configurations were approximately 15 dB greater than for the softset devices across the volume fraction range. The levels for the hardset devices were approximately 10 dB greater than for the equivalent softset configurations.
- The bandwidths for the transmit and receive cases decreased with increasing volume fraction. This indicates that the optimal transceiver configuration is between 30% and 40% volume fraction for operation into air. The bandwidths for the softset configurations far exceeded those for the hardset devices but this was expected as the damping within the softset device was much larger. Hence, the designer must consider the damping of the polymer filler as a trade-off between sensitivity and bandwidth. The hardset filler gave the increased sensitivity but reduced bandwidth compared to the softset filler.

4.5.1 Analysis of Backing Block

The influence of the backing impedance on the behaviour of transducers has been well investigated both in Section 3.6.4 and in the reference by DeSilets [23]. However, none of this analysis has considered the effect on the surface dilation quality. In Figure 4.18, it can be seen that by backing the example configuration of 25% VF 0.10 AR PZT-5A/softset composite with a backing block with a specific acoustic impedance of 4 MRayls and height of 2.0 mm, the dilation quality increased from 0.920 to greater than 0.980. The dilation quality displayed in this Figure is not that at the electrical resonance but the maximum value across the operational frequency band. This value is still above the prescribed limit of 0.900 for all the different backing impedances showing that the composite is acting as a homogenous medium. A better understanding of the influence of the backing block is gained by varying the aspect ratio of the hardset configuration from 0.05 to 0.80. Figure 4.19

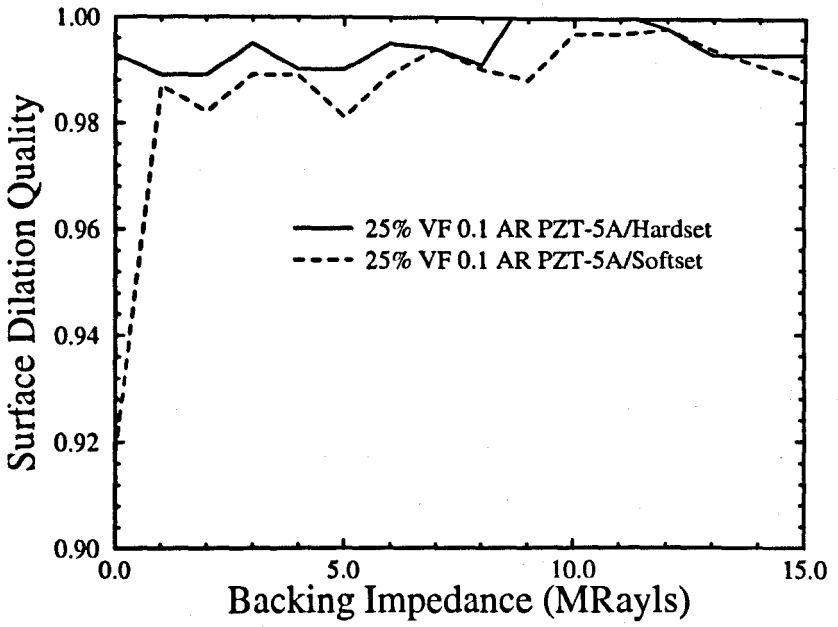

Figure 4.18: Effect of Backing Impedance on Dilation Quality

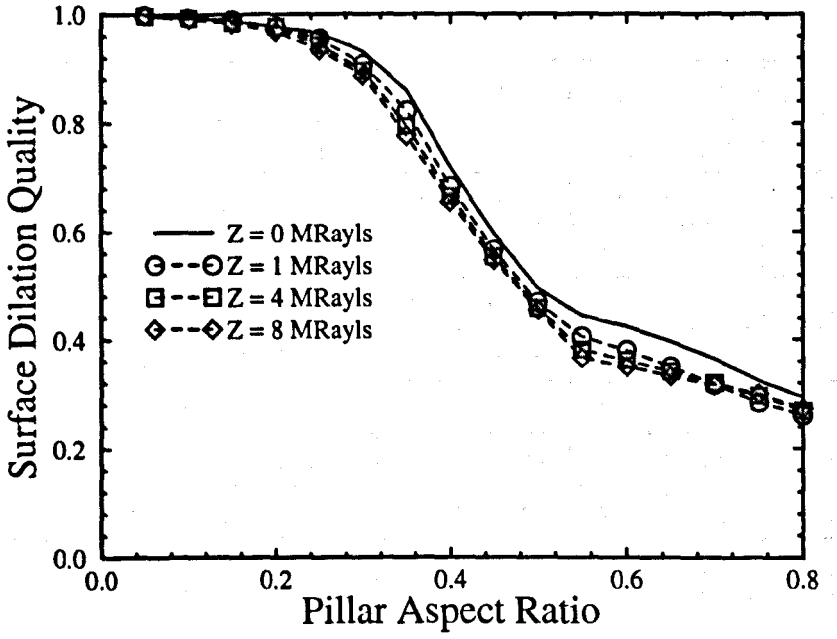

Figure 4.19: Comparison of Dilation Quality for Different Aspect Ratios

shows the curve from an unbacked configuration where the quality is above 0.900 for aspect ratios below 0.27. The curve then dips sharply to values in the region of 0.30. For the case including a backing block, the curve passes through the 0.900 limit at a lower aspect ratio depending on the specific acoustic impedance of the backing block. Hence, the effective MPAR of the transducer device is reduced by the addition of the backing block.

The effect of backing was finally examined by comparing the results of the simulations with backing blocks shown in Table 4.10 with those for the unbacked configurations as given in Table 4.9. The standard models were modified to included backing blocks with acoustic impedance half that of the active material which was determined to a suitable compromise in Chapter 3. It can be seen that:

Table 4.10: Behaviour of Different Volume Fraction Backed PZT-5A Composites in Air

	Hardset					Softset				
VF	Q_{dil}	S_{TX}	BW	S_{RX}	BW	Q_{dil}	S_{TX}	BW	S_{RX}	BW
10%	0.983	116	42	-179	40	0.847	107	136	-185	-
20%	0.965	121	35	-181	35	0.832	112	90	-188	-
30%	0.974	124	29	-182	27	0.876	115	75	-189	73
40%	0.970	125	26	-183	21	0.902	117	66	-190	56
50%	0.971	127	23	-183	19	0.928	118	61	-191	47
60%	0.962	127	21	-184	17	0.953	119	59	-192	43
70%	0.954	128	21	-185	15	0.973	119	60	-193	42
80%	0.942	128	21	-186	14	0.979	119	59	-194	40
90%	0.969	127	20	-188	16	0.991	120	37	-193	25

- Similar trends were obtained to those for the unbacked configurations. Except for the low (<40%) volume fraction softset configuration, the maximum dilation quality exceeded 0.900. The transmit sensitivity increased with volume fraction and the receive sensitivity decreased with volume fraction. The bandwidths decreased

with volume fraction. The dashes in the receive bandwidth include that the bandwidth could not be accurately measured because of low-frequency extraneous modes caused by the addition of the backing block. However, the fractional percentage bandwidths exceeded 120%.

- The large bandwidths associated with the 10% VF hardset configuration are anomalous. Examination of the model response indicates that the effective backing impedance is more than half that of the piezocomposite material. This also explains why there is a large drop in sensitivity for the this configuration.
- Compared to the unbacked transducers, the backed transducers displayed reduced sensitivities but increased bandwidth. The sensitivities of the hardset configurations were decreased by approximately 20 dB and those for the softset configurations by approximately 15 dB across the volume fraction range. The bandwidths were increased by approximately 15%. For the hardset configurations, this represented a more than doubling in value. This was an expected feature of the addition of the backing block.
- The surface dilation quality was decreased compared to the unbacked configurations for low (<50%) volume fraction and increased for the higher volume fractions.

In conclusion, the selection for a low volume fraction for a receiver, higher volume fraction for a transmitter and between 30% and 40% VF for a transceiver remains valid after the inclusion of backing. However, the selection between different polymers is not as important as it was with the unbacked devices.

4.5.2 Analysis of Matching Layer

The matching layer in a transducer is used as a mechanical impedance transformer between the piezoelectric material and the load medium. The effects of the thickness and specific acoustic impedance of the layer were examined by varying the values while keeping the piezocomposite material constant between each simulation. The speed of sound in the matching layer was also kept constant at 1000 $m.s^{-1}$. The output

parameters for the analysis were taken as the maximum transmit sensitivity and the transmit bandwidth. The specific acoustic impedance of the matching layer was varied from 0.02 to 0.18 MRayls in steps of 0.04 MRayls. Four matching layers were chosen to match the frequencies of maximum transmission and reception of the hardset and softset configurations according to Equation (2.28). Two extra matching layers were chosen, one to be slightly thicker and the other to be slightly thinner than the original four. Hence the thickness of the six layers were:

- 0.210 mm which was thicker than all the other layers.
- 0.189 mm which matched 1.322 MHz, the maximum transmission frequency for the 25% VF 0.1 AR 1.00 mm thick PZT-5A/softset configuration.
- 0.180 mm which matched 1.388 MHz, the maximum transmission frequency for the 25% VF 0.1 AR 1.00 mm thick PZT-5A/hardset configuration.
- 0.161 mm which matched 1.554 MHz, the maximum reception frequency for the softset configuration.
- 0.146 mm which matched 1.712 MHz, the maximum reception frequency for the hardset configuration.
- 0.130 mm which was thinner than all the other layers.

It was found that the maximum dilation quality was not greatly affected by the different acoustic impedances and the different polymer fillers in the composite structure. However, it did affect the transmit sensitivity as shown for the hardset composites in Figure 4.20(a) and for the softset composite in Figure 4.20(b). For both Figures, the thicker layers produced a slightly enhanced response for the lowest acoustic impedances. However, for the hardset configurations and at the higher impedances, the response was reduced so that the thickest matching layer produced the worse response. Hence, the specific acoustic impedance of the matching layer should be minimised for in-air operation but this has been a well-established fact. Furthermore, the matching layer should be thicker than calculated as a quarter-wavelength for the electrical resonance of the device to enhance the response.

The influence of the matching layer for different aspect ratios for the same configuration was investigated and the results are displayed in Figure 4.21 for the surface dilation quality and Figure 4.22 for the transmit sensitivity. Two 25% VF 0.10 AR piezocomposite configurations with PZT-5A/hardset and PZT-5A/softset were simulated with the thickness of the material fixed at 1.0 mm. The thickness of the matching layer was chosen to be quarter wavelength at the electrical resonance of the device. This was 0.180 mm for the layer on the hardset device and 0.189 mm for the layer on the softset device. The damping co-efficient within the matching layer was varied between the value used for the analysis for Figure 4.20 of -70 and -80. It was found that the damping co-efficient of the matching layer and the choice of the filler material in the piezocomposite did not have a significant effect on the surface dilation quality. Aspect ratios less than 0.24 achieved a surface dilation quality of greater than 0.900 for the highly damped matching layer with softset configuration. This was extended to aspect ratios less than 0.44 for the less damped matching layer with the hardset configuration. The transmit sensitivity shown in Figure 4.22 did not vary for aspect ratios less than 0.40 and increased slightly for the higher aspect ratios. The less damped matching layer promoted an enhanced response for both filler materials. However, the disadvantage of matching layers with small damping co-efficient is the increased lateral mode activity. Hence, highly damped layers are normally used but this is at the expense of sensitivity.

The comparison set of configurations were simulated with the matching layer on both the front and back surfaces of the transducer. The thickness of the matching layer was selected to be quarter wavelength at the frequency of maximum transmit sensitivity. These frequencies were available as part of the results from the simulations in Table 4.9. The specific acoustic impedance of the matching layers was chosen to be the geometric mean of that for the piezocomposite material and that for the air medium (taken as 427 Rayls). The results of the simulations are displayed in Table 4.11. An extra set with the matching layer on one surface and the backing block as specified in the previous section, were also simulated and the results are given in Table 4.12.

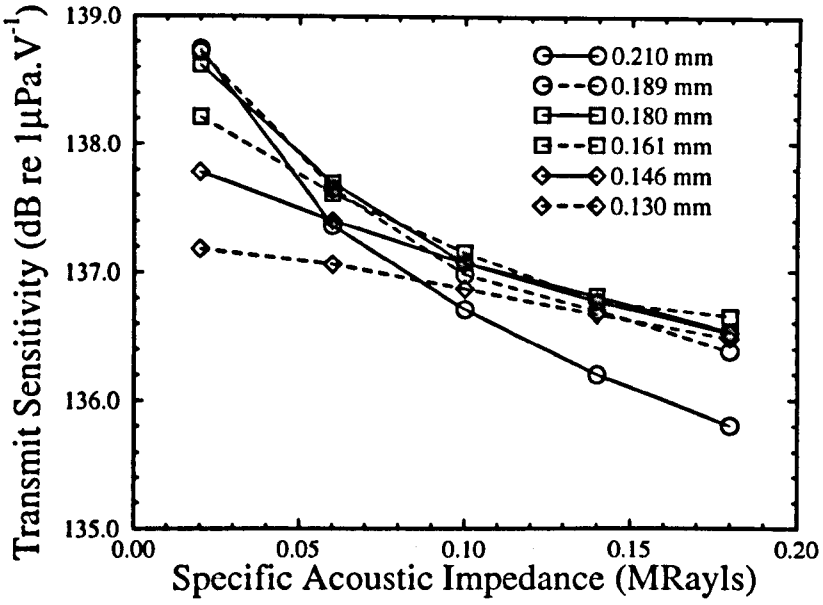

Figure 4.20(a): Maximum Transmit Sensitivity for Different PZT-5A/Hardset Configurations

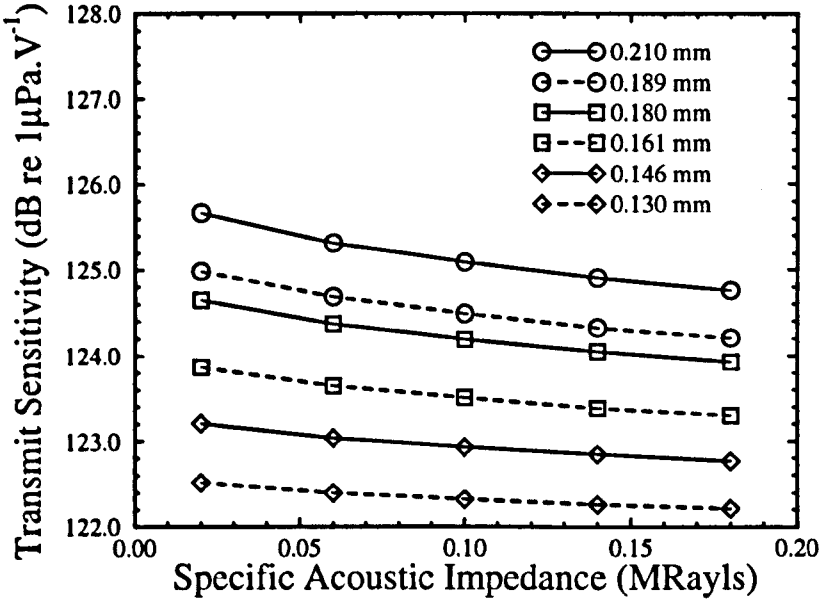

Figure 4.20(b): Maximum Transmit Sensitivity for Different PZT-5A/Softset Configurations

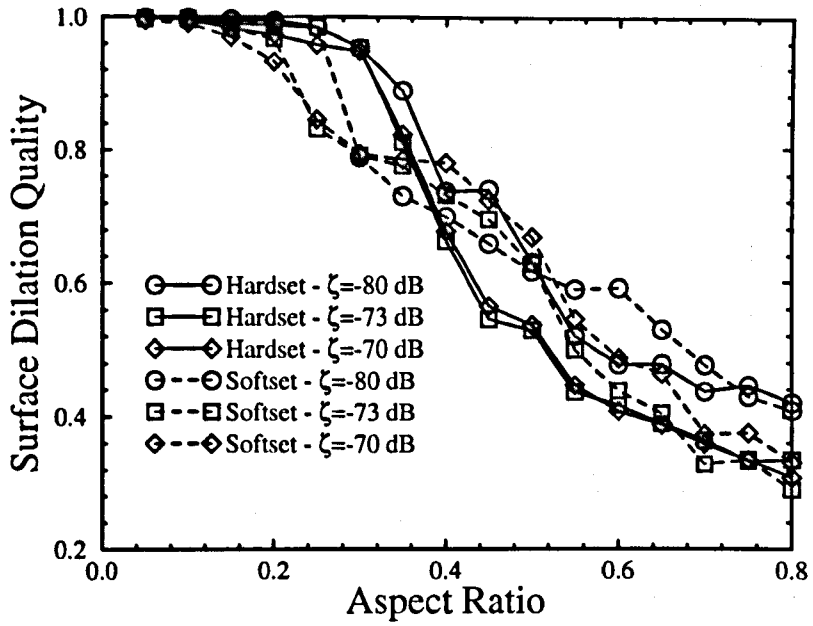

Figure 4.21: Comparison of Surface Dilation Quality for Varying Aspect Ratio

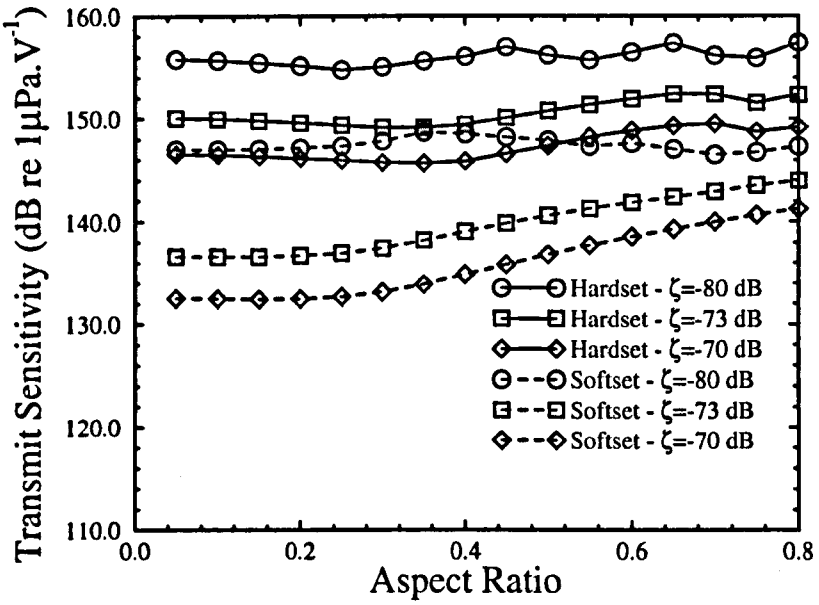

Figure 4.22: Comparison of Transmit Sensitivity for Varying Aspect Ratio

Table 4.11: Behaviour of Different Volume Fraction Matched PZT-5A Composites in Air

	Hardset					Softset				
VF	Q_{dil}	S_{TX}	BW	S_{RX}	BW	Q_{dil}	S_{TX}	BW	S_{RX}	BW
10%	0.995	138	23	-158	26	0.989	126	71	-167	72
20%	0.974	143	19	-161	24	0.988	131	60	-170	60
30%	0.974	147	15	-162	19	0.974	134	53	-171	51
40%	0.970	148	15	-162	14	0.976	136	48	-172	45
50%	0.961	150	13	-163	12	0.977	137	45	-173	39
60%	0.966	151	10	-163	12	0.972	137	44	-174	36
70%	0.971	151	11	-163	8	0.968	137	45	-175	35
80%	0.976	150	12	-164	9	0.980	136	45	-176	32
90%	0.960	149	12	-167	11	0.996	138	28	-175	17

It can be seen from Table 4.11 that:

- The sensitivities were increased by about 3 dB by the addition of the matching layer. This can be increased if the zero-stress boundary was replaced by a fluid column of air. However, the increase would be minimal.
- The bandwidths for the hardset configurations have been increased by the addition of the matching layer while for the softset configurations, most bandwidths were decreased. The configuration most affected was the 10% VF softset which had such a large receive bandwidth unmatched that it could not be calculated accurately. When matched, the receive bandwidth was 73%. The bandwidths for the hardset configurations have increased by between 2% and 5% for transmit and by approximately 10% for receive case. The bandwidths for the softset configurations have decreased by a similar amount. This is because the matching layer acts as a stiffening plate for the softset configurations which is shown by the accompanying increase in the maximum dilation quality. This would also explain why there was not large increase in sensitivity.

It can be seen from Table 4.12 that:

Table 4.12: Behaviour of Different Volume Fraction Matched and Backed PZT-5A Composites in Air

	Hardset					Softset				
VF	Q_{dil}	S_{TX}	BW	S_{RX}	BW	Q_{dil}	S_{TX}	BW	S_{RX}	BW
10%	0.995	121	40	-173	40	0.989	113	71	-179	82
20%	0.973	126	35	-177	37	0.986	118	64	-183	66
30%	0.973	128	30	-178	31	0.976	120	58	-184	58
40%	0.971	130	26	-179	24	0.976	122	54	-185	52
50%	0.967	131	24	-179	21	0.976	123	51	-186	47
60%	0.959	132	22	-180	19	0.966	124	50	-187	44
70%	0.973	132	21	-181	18	0.960	123	51	-188	43
80%	0.979	132	21	-182	16	0.977	123	51	-190	40
90%	0.971	131	21	-184	16	0.995	124	36	-190	26

- The effect of matching on the backed configurations is similar to the effect of matching on the unbacked configurations. The sensitivities have been increased by approximate 5 dB. The bandwidths have remained between the two sets of simulation.
- The dilation qualities have been increased compared to the backed configurations but are similar to those obtained for the matched simulation. This shows that the dilation quality is primarily affected by the material properties of the matching layer.

4.5.3 Analysis of Fluid Loading

It was found in Chapter 3 that there was no ideal implementation of the fluid loading component using the present version of ANSYS. However, it was decided to use the model type C from Section 3.6.6 to detect trends in the dilation quality for different configurations with fluid loading. It must be emphasized that this is not a perfect

implementation and the results produced are not necessarily exact. However, it is expected that the trends can be detected allowing the selection of design guidelines.

The influence of the aspect ratio on the surface dilation quality was investigated with the fluid loading of a water medium. The chosen configurations were 10%, 20% and 40% VF PZT-5A composites with hardset and softset as the filler material. The hardset configurations are shown in Figure 4.23(a) where the results with fluid loading are indicated by a solid line. The softset configurations are shown in Figure 4.23(b). It can be seen from the results that:

- For the hardset configurations, the effect of the fluid loading was to reduce the dilation quality but the amount was only significant for the 10% volume fraction composite. The decrease was caused by the enhanced inter-pillar modes between the filler material and the fluid loading. Hence, there is increased coupling between these modes and the thickness mode resulting in a reduced dilation quality.
- For the softset configurations, the effect of the loading was to increase the dilation quality by a small amount. The softset configurations can be considered as ceramic pillars operating in a lossy medium as shown in Figure 4.14(b). The introduction of the increased front load would retard the movement of the ceramic pillars while having less effect on the displacement of the polymer phase. Hence, the dilation quality would increase slightly as the displacement of the ceramic and polymer phase approach each other. There are no significant inter-pillar modes in the softset filler because it is too highly damped. Thus, there are no lateral modes in the polymer matrix to be enhanced by the water medium and interfere with the thickness mode as with the hardset filler.

The standard set of comparison simulations for the different configurations were used to examine the effect of the water loading component being incorporated in the model. The results are given in Table 4.13 for comparison with the in-air results shown in Table 4.9. These simulation configurations were then matched and backed according to the developed design guidelines. The acoustic impedance of the backing

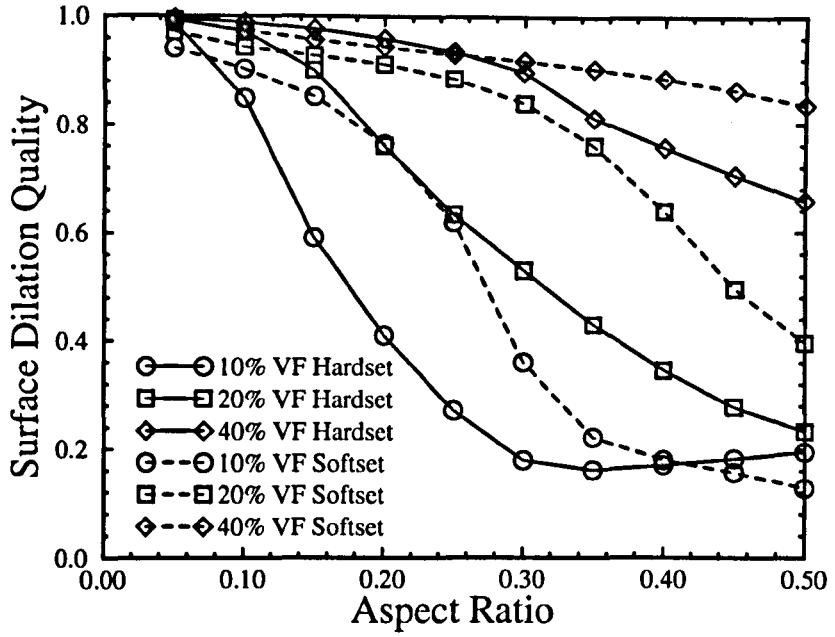

Figure 4.23(a): Surface Dilation Quality of PZT-5A/Hardset Configuration

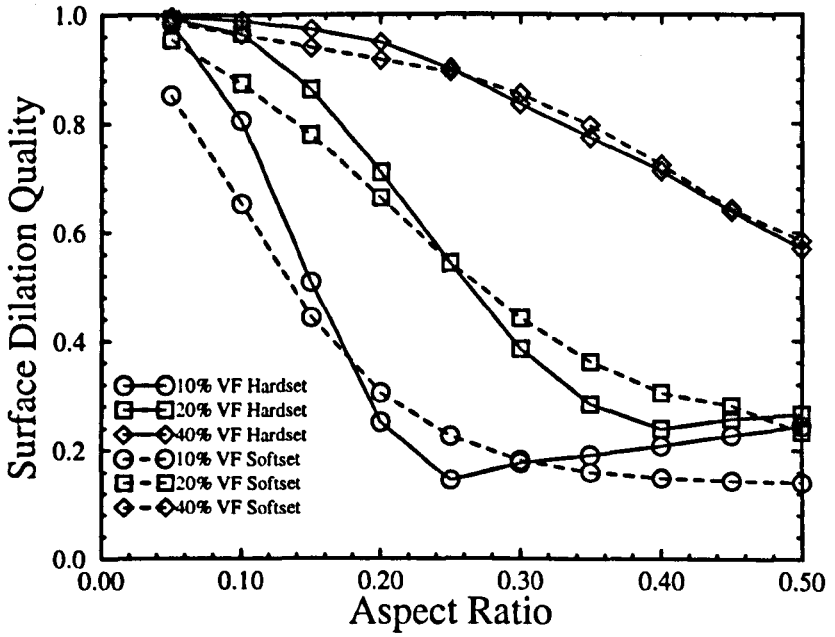

Figure 4.23(b): Surface Dilation Quality of PZT-5A/Softset Configuration

block was selected as half that of the piezocomposite and that of the matching layer was chosen as the geometric mean of the acoustic impedance of the piezocomposite and water. The specific acoustic impedance of water was taken as 1.5 MRayls. The thickness of backing block was 2.0 mm in all cases and the thickness of the matching layer was chosen to be a quarter wavelength at the electrical resonance. The results are presented in Table 4.13 and should be compared to the results in Table 4.12.

Table 4.13: Behaviour of Different Volume Fraction PZT-5A Composites in Water

	Hardset					Softset				
VF	Q_{dil}	S_{TX}	BW	S_{RX}	BW	Q_{dil}	S_{TX}	BW	S_{RX}	BW
10%	0.991	190	19	-175	19	0.863	173	-	-191	90
20%	0.982	199	15	-174	18	0.844	183	-	-188	58
30%	0.975	203	13	-173	14	0.886	187	88	-187	44
40%	0.980	206	13	-172	10	0.915	190	70	-186	37
50%	0.982	209	11	-170	9	0.937	192	61	-185	32
60%	0.971	211	9	-171	11	0.957	195	62	-184	29
70%	0.973	210	9	-171	8	0.970	196	72	-184	29
80%	0.954	210	10	-171	5	0.990	197	64	-184	26
90%	0.972	209	12	-175	11	0.990	200	29	-182	15

From Table 4.13, it can be observed that:

- The dashes for the bandwidths in the table for the softset configuration indicate that the transmit sensitivity did not decrease by the necessary 3 dB for the bandwidth calculation within the operational frequency band. The bandwidth can calculated by modelling the device at much higher frequencies but this would not present the reader with extra information.
- The transmit sensitivity for the hardset and softset configurations were increased by between 50 and 60 dB compared to the in-air analysis because of the better acoustic match of the water to the piezocomposite transducer over that between

the air (modelled as a vacuum) to piezocomposite. The transmit sensitivity for a softset transducer in water was about 10 dB less than that for the equivalent hardset transducer which is 5 dB more than for the in-air scenario. The water loading has a similar effect to that of the backing block in that they both reduce the influence of the polymer properties on the performance of the device.

- The receive sensitivity for the hardset transducers has been reduced by approximately 10 dB by the increased fluid loading and by approximately 8 dB for the softset transducers. The receive sensitivity is reduced compared to the in-air analysis because while the same pressure impinges on the surface of the transducer, less energy is transferred in the case of in-air operation but the energy reverberates more because of the larger mis-match in acoustic impedances. The reduction for the softset devices is less due to the soft polymer being highly damped so that the energy does not reverberate for in-air operation.
- The bandwidths for both the transmit and receive scenarios have been increased but the amount is only significant for the softset configurations. Theoretically, the bandwidths should increase as the maximum sensitivity at the resonances is reduced compared to the sensitivities off resonance. The small increase in the transmit bandwidth is assumed to be caused by the inexact implementation of the fluid column.

For the final set in Table 4.14, the following trends can be observed:

- The sensitivities of the transducers have been decreased by the addition of the backing block and the matching layer with the water loading. However, the bandwidth has been greatly increased compared to Table 4.13, especially for the hardset configurations. The sensitivities for the hardset devices were decreased by approximately 20 dB and for the softset devices were decreased by approximately 12 dB. The effect of the matching with in-water operation is less than with the in-air operation as the acoustic mis-match between the piezocomposite and the water medium is less than that between the piezocomposite and the air medium.

Table 4.14: Behaviour of Matched and Backed PZT-5A Composites in Water

	Hardset					Softset				
VF	Q_{dil}	S_{TX}	BW	S_{RX}	BW	Q_{dil}	S_{TX}	BW	S_{RX}	BW
10%	0.996	170	84	-194	61	0.982	161	114	-202	81
20%	0.970	178	73	-194	77	0.967	171	95	-200	69
30%	0.968	182	62	-194	61	0.966	174	83	-200	61
40%	0.961	185	53	-194	50	0.961	177	76	-199	57
50%	0.955	187	47	-193	39	0.951	180	69	-199	53
60%	0.945	189	42	-193	33	0.928	182	66	-198	50
70%	0.952	189	38	-193	30	0.917	183	66	-198	48
80%	0.960	190	35	-194	28	0.940	184	63	-199	44
90%	0.962	191	33	-194	26	0.976	186	47	-198	33

- As was expected, the sensitivity of the softset device approached that of the hardset devices. This is supported as the bandwidths produced from the two different fillers were similar with the softset configurations having a slightly large value. This emphasizes the fact that the addition of the ancillary components reduces the influence of the filler material.
- The optimum volume fraction for both receive and transmit/receive is between 30% and 40% for the water loading. The lower volume fractions have large associated bandwidths but at decreased sensitivity. The reason that the 20% VF configurations are not part of the selection set as with the in-air analysis is because of the increased acoustic impedance of the water medium.

4.6 CONCLUDING REMARKS

This Chapter dealt with an investigation using finite element modelling into the behaviour of piezocomposite transducers to develop a set of guidelines for their design. The finite element modelling was compared with the uni-dimensional isostrain model of Smith and Auld and good correlation was obtained for most values of volume fractions. The isostrain model was found to be inexact at both very low and very high volume fractions. Also, where lateral modes coupled with the thickness mode operation of the transducer, the assumption used to derived the isostrain model were no longer valid. There are two important types of lateral modes: inter-pillar that occur in the polymer matrix and are encountered in low volume fraction composites and intra-pillar that occur within the ceramic pillar and are generally encountered in high volume fraction composites. The limit to minimise the coupling between the modes of the geometry for different configurations was determined and was named the maximum pillar aspect ratio (MPAR). For volume fractions below 60%, this is highly dependent on volume fraction and encourages the application of higher volume fraction devices. Above 60%, the lateral modes are intra-pillar and the limit is approximately an aspect ratio of 0.60. The shape of the ceramic pillar also affects the MPAR and it was found that triangular pillars allowed a larger aspect ratio than the equivalent cylindrical and square pillars for low volume fractions.

The influence of the ancillary components on the performance of the different configurations was also investigated. Using the design guidelines, a set of configurations for the MPAR at the different volume fractions and for the two different polymers, hardset and softset, were simulated for each design stage. It was found that with each additional component, the influence of the filler material was reduced indicating that the choice of the filler material does not have a significant effect on the performance of a matched and backed piezocomposite operating into a water medium. Simulations with the piezocomposite material operating into air showed that volume fraction for devices to be used as transmitters should be greater than or equal to 30%. The volume fraction for receivers should be between 20% and

70%. Considering the combined transmit/receive levels, the volume fraction for transceivers should be between 30% and 70%. If large bandwidth is important, the transceiver volume fraction should be between 30% and 40%. These volume fraction values were the same for in-water operation.

The addition of the backing block was found to increase the bandwidth but at the expense of the sensitivity. A compromise value for the specific acoustic impedance of the backing block to be half that of the active material was selected. While the addition of the backing block reduced the dilation quality, it did not have a significant effect on the MPAR of the device. Several different matching layers were simulated and the dilation quality was unaffected by the acoustic impedance of the layer or the filler used. The transmit sensitivity was improved by the addition of a less damp layer but this would be at the expense of uni-modal behaviour.

It was found that the receive sensitivities produced by the in-water analysis were reduced by approximately 20 dB for hardset devices and 12 dB for the softset devices compared to the equivalent in-vacuum analysis. The increased fluid loading reduced the dilation quality but it was only significant for the low (<30%) volume fractions. The transmit sensitivity was greatly increased compared to the in-air analysis because of the reduced acoustic mis-match. The receive sensitivity was unchanged for the stiff filler material. For hardset fillers, the dilation quality was reduced because of the increased lateral activity. For softset fillers, the dilation quality was increased because of the reduced movement of the ceramic pillar.

CHAPTER FIVE

DESIGN OF 1-3 PIEZOCOMPOSITE HYDROSTATIC TRANSDUCERS

CHAPTER OBJECTIVE

1-3 piezocomposites were originally developed because of their perceived good performance under hydrostatic operating conditions and for design evaluation, several researchers have devised constrained-dimensional models that are valid over a restricted operating range. The aim of this Chapter is to extend the finite element model originally developed for thickness mode operation to incorporate hydrostatic behaviour. A materials comparison for both the ceramic and polymer phase is performed using the finite element model, from which the desired properties of each phase can be determined. Other techniques for enhancing the performance of the hydrophone such as stiffening plates to reduce the lateral stress in the polymer matrix are considered in conjunction with the influence of electrical loading on low volume fraction composite hydrophones. Finally to demonstrate the ability of the model to be extended to model other configurations, a brief investigation into the requirements for a 1-3-1 hydrophone is performed.

5.1 INTRODUCTION

One of the important applications for ultrasonic transducers is for underwater hydrophones in the hydrostatic mode of operation [54]. Piezoelectric transducers can be operated in two possible modes for underwater operation:

- Resonant where the transducer is designed to function at one of its efficient piezoelectric resonant modes; and

- Hydrostatic or off-resonance operation where the transducer is operated at, for example, frequencies between the relatively low-frequency width-dilational modes and the fundamental thickness mode.

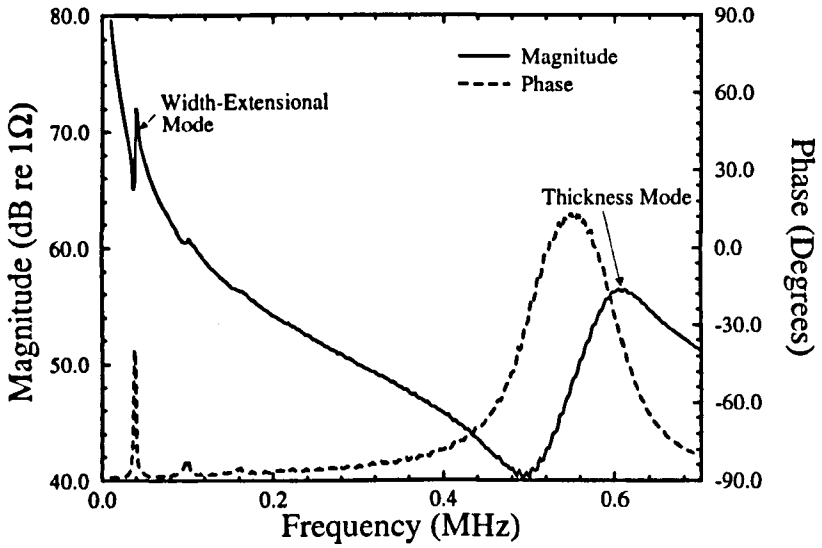

Figure 5.1: Impedance Profile of 50% VF PZT-5A/Hardset Composite in Castor Oil

The resonance mode is exemplified by high efficiency but narrow band of operational frequencies while the hydrostatic mode has a much wider band of frequencies but at a lower sensitivity. Also the phase response of the transducer in the thickness mode changes rapidly with change of frequency making it unsuitable for wide-band imaging applications. In the hydrostatic case, as the hydrophone is operated ideally in a region containing no resonances, both the phase and magnitude spectrum of the response

should be intuitively constant. The measured impedance curve of a 50% volume fraction (VF) 0.22 aspect ratio (AR) PZT-5H/Hardset piezocomposite in castor oil over a large frequency range is shown in Figure 5.1. Between the resonances at 20 kHz and 400 kHz, there is minimal modal activity giving a potential operating range of 380 kHz or a fractional bandwidth of 181% normalised to a centre frequency mid way between 20 kHz and 400 kHz. The input capacitance of the transducer varies by less than 30% and the phase varies by less than 10 degrees over this range.

5.1.1 Hydrophone Material Type Selection

Both major types of piezoelectric material, piezoceramics and piezopolymers, have been used for hydrophones with varying success [54]. Most piezoceramics have a relatively poor hydrostatic response because of the strong coupling of the lateral modes. Recent improvements, for example calcium modified lead titanate [$(Pb,Ca)TiO_3$], have provided an enhanced hydrostatic response by reducing the lateral coupling [11]. However, a disadvantage in general with the piezoceramics is the high intrinsic density making large-area and correspondingly heavy hydrophones impractical. According to Ting [54], future hydrophones will be large-area to reduce the influence of flow noise for operation on modern deep-sea submarines which precludes the application of piezoceramics.

Low density piezopolymers have a superior piezoelectric voltage constant, g_h, component when compared with the piezoceramics because of the low permittivity but demonstrate a greatly reduced piezoelectric strain constant, d_h. They were also found to be unsuitable as hydrophones because of the temperature dependence of their piezoelectric properties.

Piezoelectric composites, especially 1-3 connectivity, were developed as a compromise between the two piezoelectric types in that a passive polymer matrix was included in the microstructure to absorb lateral pressure allowing the ceramic to respond mainly in the its thickness direction, taking full advantage of the large

piezoelectric strain component. As the polymer phase has a significantly lower density (similar to that of water) than the piezoceramics, the employment of large-area hydrophones are feasible. The permittivity of the piezocomposite is also much lower than that of the constituent ceramic allowing an increased g_h component. Other significant advantages are improved matching to water and enhanced bandwidth. Importantly all of the characteristics can be configured to the application by adjusting the ceramic/polymer volume fraction. Ting [54] performed extensive measurements of the pressure and temperature dependence of the hydrostatic response of different 1-3 piezocomposite hydrophones and the properties were found to be stable with time and pressure.

5.2 THEORY

5.2.1 Measurement of Hydrostatic Response

A major modelling implication of hydrostatic operation is that the transient pressure changes in the surrounding fluid occur sufficiently slowly in time and space that they do not only apply a force in the *3* direction of the transducer but also in the lateral dimensions, significantly modifying the response of the transducer from that of its thickness mode. However, the introduction of piezocomposites, with their reduced lateral coupling in many cases compared to the constituent piezoceramic, reduces the detrimental effect of lateral forces leading towards a viable design. The hydrostatic response of the transducer is not characterised by the piezoelectric strain constant, d_{33}, and the piezoelectric voltage constant, g_{33}, but by the hydrostatic equivalents [55]:

- **Hydrostatic piezoelectric strain constant (d_h [$m.V^{-1}$])** - which can be calculated as:

$$\begin{aligned} d_h &= d_{33} + d_{31} + d_{32} \\ &= d_{33} + 2d_{31} \end{aligned} \qquad \textbf{Eqn. 5.1}$$

as the transducer is assumed to have the same response in the *1* and *2* directions. It is important to note that the two co-efficients, d_{31} and d_{33}, have opposing signs meaning that d_h is reduced compared to d_{33}. This expression was derived from the fact that the transducer is operated in its linear region so that its resultant response is the sum of all the responses to individual pressures.

- **Hydrostatic piezoelectric voltage constant (g_h [$V.m.Pa^{-1}$])** - which can be calculated from the standard voltage constants as:

$$g_h = g_{33} + 2g_{31} \qquad \textbf{Eqn. 5.2}$$

or from the hydrostatic strain constant as:

$$g_h = \frac{d_h}{\varepsilon_{33}^T} \qquad \textbf{Eqn. 5.3}$$

- **Hydrostatic Figure of Merit (HFOM [Pa^{-1}])** - which is a combination of the other two constants to describe the overall operational efficiency of the hydrophone. It is calculated as follows:

$$HFOM = d_h g_h \qquad \textbf{Eqn. 5.4}$$

5.2.2 Hydrostatic Constrained-Dimensional Models

Two models are discussed and compared in this Section:

- Smith's extension [56] to the isostrain model for thickness model developed by Smith and Auld.
- Parallel-series connectivity model of Haun-Newnham [57] which partitions the unit cell into a half-cell which is only polymer and a half-cell with 2-2 connectivity. The models for each half-cell can be easily derived and the two sub-models are combined to form the theory for the whole unit cell.

In Chapter 4, Smith's model for the operation of 1-3 piezocomposite in the thickness mode was discussed. Smith has extended the thickness mode model to include the hydrostatic effects where he utilised similar assumptions made by Haun and Newnham for their hydrostatic model. The defining assumption to differentiate Smith's extension from the original isostrain model was that there is resultant strain of the unit cell in the *1* and *2* direction i.e. $S_1 \neq 0$, $S_2 \neq 0$. In thickness mode operation, the applied field is varying sufficiently rapidly that the composite does not have sufficient time to expand or contract i.e. $S_1 = S_2 = 0$. However, for low frequency hydrostatic operation, the composite can react to the applied field leading to a resultant strain in the lateral dimensions.

Hence, the assumptions made by Smith for the hydrostatic model were:

1. Some standard assumptions about the variables in the transducer system were made: the electric field was only non-zero in the thickness direction; and there were no shear modes within the composite.
2. The wavelength of the pressure wave is larger than the composite plate implying that the displacement and electric field is constant within the entire material phase for the unit cell.

3. The lateral spacing between the centres of the pillars within the composites are sufficiently small that the thickness (*3*) strains in the ceramic and polymer do not differ significantly.
4. The electric field in the two phases are identical.
5. The lateral stresses are assumed to be constant between the two phases and hence, the total lateral strain is the sum of the two lateral strains in each phase. This assumes that the lateral stresses are evenly distributed through the unit cell.
6. The composite is assumed to move significantly in the *3* direction and hence, the effective stress and electric displacement in this direction are the summation of the components in each phase.

Using these assumptions, simplified expressions for the required parameters, d_{33}, d_{31} and ε_{33}^{T} of the piezocomposites can be derived. In the following expressions, the equivalent piezocomposite parameters are indicated by a superscripted bar, the inactive polymer by the p superscript and the piezoceramic by the usual E, C and T superscript. The expressions for the thickness strain constant and thickness permittivity under constant stress are identical for the two models. The formula for the equivalent thickness strain constant of the piezocomposite can be considered as being generated from the force that is applied directly to the piezoceramic pillar and is as follows:

$$\begin{aligned}\bar{d}_{33} &= \upsilon d_{33}^{C}\frac{\bar{s}_{33}^{E}}{s_{33}^{E}} \\ &= \frac{\upsilon d_{33}^{C}}{s_{33}^{E}}\cdot\frac{1}{\dfrac{\upsilon}{s_{33}^{E}} + \dfrac{1-\upsilon}{s_{11}^{p}}} \\ &= \frac{\upsilon d_{33}^{C} s_{11}^{p}}{\upsilon s_{11}^{p} + (1-\upsilon)s_{33}^{E}}\end{aligned} \qquad \textbf{Eqn. 5.5}$$

where υ is the ceramic volume fraction;

d_{33}^{C} is the piezoelectric strain constant of the piezoceramic;

s_{11}^{p} is the *11* compliance of the polymer; and

s_{33}^{E} is the *33* compliance of the ceramic under short-circuit conditions.

The formula for equivalent constant-stress permittivity is similar to that the equivalent constant-strain permittivity derived for the original isostrain model and is as follows:

$$\bar{\varepsilon}_{33}^{T} = \upsilon\left[\varepsilon_{33}^{T} - d_{33}^{C\,2}.\frac{1-\upsilon}{\upsilon s_{11}^{p} + (1+\upsilon)s_{33}^{E}}\right] + (1-\upsilon)\,\varepsilon_{11}^{p} \qquad \textbf{Eqn. 5.6}$$

where ε_{11}^{p} is the dielectric permittivity of the polymer.

In a similar fashion, the dielectric permittivity is the average permittivity from the two constituent phases and includes the reducing effect of the charge produced by the applied force on the piezoceramic. The expression for the lateral (31) strain constant can be partitioned into two terms:

$$\bar{d}_{31} = \alpha d_{31}^{c} + \beta d_{33}^{c} \qquad \textbf{Eqn. 5.7}$$

where α is the fractional direct contribution from the piezoceramic lateral strain constants and β is the fractional indirect contribution from the piezoceramic thickness strain constant. The second term is caused by the fact that the polymer will expand in the *3* direction due to its non-zero compressibility when compressed in the *1* and *2* direction. This will generate a stress, T_3, at the ceramic which is converted into a charge through the constant, d_{33}.

The two models agree for the expression for β:

$$\beta = \upsilon(1-\upsilon)\frac{\left(s_{12}^{p} - s_{13}^{E}\right)}{\upsilon s_{11}^{p} + (1-\upsilon)s_{33}^{E}} \qquad \textbf{Eqn. 5.8}$$

Where the two models do disagree is for the derived value of α. Smith's extension to the isostrain model has the simple formula,

$$\alpha_{SI} = \upsilon \qquad \textbf{Eqn. 5.9}$$

where α_{SI} is the constant derived for Smith's isostrain model.

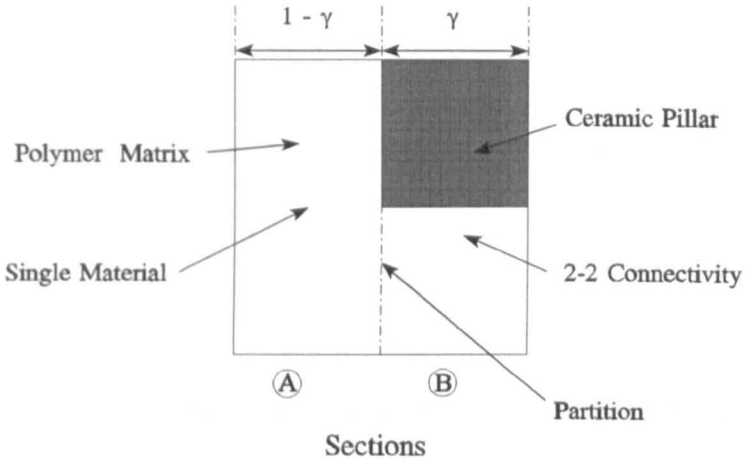

Figure 5.2: Partitioned Unit Cell used for Haun-Newnham Model

The Haun-Newnham analysis partitions the unit cell into two segments connected in parallel as shown in Figure 5.2. The first section (A) consists of a single material, the polymer matrix. The second section (B) is a series-connectivity composite of the two phases. The equivalent $\overline{s}_{11}^{E}$ of section B was derived using a Maxwell model as discussed in Section 2.1.2. This analysis is only valid for square pillars and not for cylindrical or triangular pillars because section B must have only a single straight boundary between the ceramic and polymer phase.

The two sections are combined as a Voigt model to derive the final expression for α_{HN} (the constant derived from the Haun-Newnham model) :

$$\alpha_{HN} = \frac{\upsilon\gamma s_{11}^{p}}{(\upsilon - \gamma\upsilon)s_{11}^{E} + (\gamma - \upsilon + \gamma\upsilon)s_{11}^{p}} \qquad \textbf{Eqn. 5.10}$$

where γ is given by the ratio of the width of the ceramic pillar to width of the unit cell.

The factor, γ, is related to Π as used in the Haun and Newnham reference [57] by the formula:

$$\Pi = \frac{4\upsilon}{\gamma^2} \qquad \textbf{Eqn. 5.11}$$

For square pillars, the value of γ can be determined from Figure 5.2 as:

$$\gamma = \sqrt{\upsilon} \qquad \textbf{Eqn. 5.12}$$

and Equation (5.10) can re-written as:

$$\alpha_{HN} = \frac{\upsilon s_{11}^{p}}{(\sqrt{\upsilon} - \upsilon)s_{11}^{E} + (1 - \sqrt{\upsilon} + \upsilon)s_{11}^{p}} \qquad \textbf{Eqn. 5.13}$$

Hence, α_{SI} will be greater than α_{HN} for most volume fractions and is dependent on the ratio of the stiffness of the two materials. For a polymer significantly more compliant than the piezoceramic pillar which is normally the case, $s_{11}{}^{P} >> s_{11}{}^{E}$ and Equation (5.13) can be simplified further as:

$$\alpha_{HN} = \frac{\upsilon}{1 - \sqrt{\upsilon} + \upsilon} \qquad \textbf{Eqn. 5.14}$$

The ratio of the two constants can be calculated as:

$$\frac{\alpha_{SI}}{\alpha_{HN}} = 1 - \sqrt{\upsilon} + \upsilon \qquad \textbf{Eqn. 5.15}$$

This equation was plotted relative to the volume fraction and the curve is shown in Figure 5.3. It can be seen that the ratio is close to one for very low and very high

volume fractions indicating good correlation between the two models. However, at volume fractions from 10% to 50%, there is a large discrepancy between the values produced from the two models. This is caused by the imposed boundary between the two sections of the unit cell creating extra lateral stress in the ceramic pillar. Both models are compared with each other and the finite element model in the next Section.

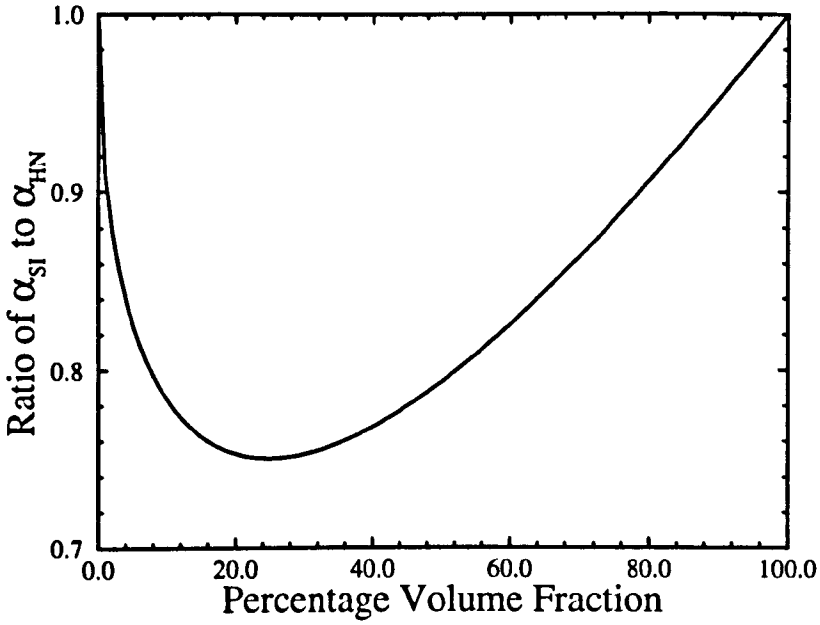

Figure 5.3: Curve Showing the Ratio of α_{SI} to α_{HN}

5.3 DEVELOPMENT OF FINITE ELEMENT MODEL

The finite element model was developed by extending the eighth-symmetry model described in Chapter 3 for the piezocomposite unit cell. As the frequency of operation for a hydrophone is normally well below that of the thickness mode, the acoustic properties of the fluid did not have a significant influence on the behaviour of the hydrophone. Hence, the fluid loading aspect of the model was ignored for the finite element analysis in this Chapter. This assumption was verified in Appendix C where the equations of motion for a piezoelectric transducer are derived and it is shown that the acoustic impedance is only important around the resonances.

The hydrostatic pressure in the finite element model was generated by applying equal force in each of the three dimensions of the model directly to the boundaries of the unit cell. This removed the requirement for symmetric boundaries about the outer surfaces of the unit cell since the forces were themselves symmetrical. Symmetric boundaries were still required through the centre of the unit cell to reduce the number of nodes in the model. The resultant finite element model is shown in Figure 5.4.

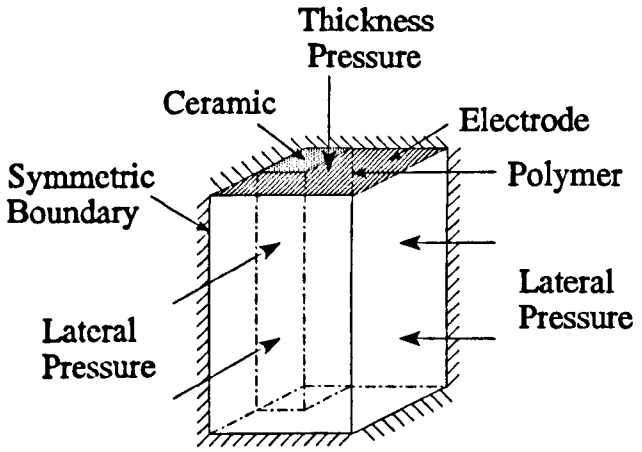

Figure 5.4: Finite Element Model of 1-3 Piezocomposite Hydrophone

Another effect of the low operational frequency is that the influence of the mass and loss matrices in the finite element Equation (3.6) is insignificant compared to the stiffness matrices. The former two matrices are proportional to the frequency and in general, only have large values at and above the fundamental thickness mode. Thus static analysis as discussed in Section 3.3.2 which solves the finite element equation with zero velocity and acceleration vectors, was used to simplify and increase the speed of the analysis process. This assumption was checked by comparing the results from the static analysis with harmonic analysis at different frequencies below that of the thickness mode and all the results were found to be equal.

The desired output of the analysis is to obtain sufficient parameters in order to calculate the HFOM for a particular piezocomposite hydrophone configuration. The hydrostatic strain co-efficient, d_h, can be calculated as the displacement of the surface

of the composite produced by a given electric field under open-circuit conditions but this cannot be calculated accurately as the movement across the surface is not constant because the polymer phase displaces with a different amplitude to that of the ceramic phase. Such results have been observed in Chapter 4. Hence, another definition of d_h was required. It was calculated as the current density at the surface produced by the unity force under short-circuit conditions. This is identical to the definition used by Richard [55] for the development of his finite element model. The hydrostatic voltage constant, g_h, was calculated as the electric field produced in the *3* direction of the transducer by the unity force under open-circuit conditions. The electric field was approximated as the ratio of the voltage produced between the two electrodes to the distance between the electrodes. This is valid as the divergence of the charge density field is zero within the piezoelectric material and separate charge can only exist at the electrodes. Then the electric field will be constant through the material with the value taken as the ratio of the voltage that exists at the open-circuit electrode to the distance between the plates. Hence, the same hydrostatic model must be analyzed under two different electrical loadings: short-circuit to calculate the strain constant; and open-circuit to calculate the voltage constant. From these two parameters, the HFOM and hydrostatic permittivity can be estimated from Equations (5.3) and (5.4).

5.3.1 Verification of the Finite Element Model

Two differing piezoelectric ceramics, PZT-5H and MPT, were selected to examine the behaviour of the finite element model and to compare the results with the extended isostrain model and the Haun-Newnham model. These ceramics were similar to the two ceramics used as examples by Smith [56] in his reference and the material parameters for the ceramics are defined in Appendix B. PZT-5H is the member of the lead zirconate titanate [$Pb(Zr,Ti)O_3$] family with the highest permittivity and largest thickness mode coupling factor available commercially at the present time but also has significant coupling between the thickness and lateral

directions. Compared to it, MPT has low lateral coupling ($-d_{31} \ll d_{33}$) and reduced permittivity but reduced coupling factor.

The finite element model was first used to analyze the response of a cube of the piezoceramic for each hydrostatic condition. d_{31} and d_{33} were generated by applying a force only in the *1* and *3* direction respectively and the g constants were generated in a similar fashion. It is important to remember that the piezoelectric matrix used to represent the material's response for the finite element model is that of the piezoelectric stress (*e*) matrix and not the strain (*d*) or voltage (*g*) matrix. The results are shown in Table 5.1.

Table 5.1: Verification of Finite Element Model

PZT-5H	d_{33}	d_{31}	d_h	g_{33}	g_{31}	g_h
Ref [9]	593	-274	46	19.7	-9.1	1.5
FEM	593	-274	46	19.5	-9.0	1.5
MPT						
Ref [9]	68.2	-3.2	61.8	36.9	-1.7	33.4
FEM	68.3	-3.2	61.9	36.1	-1.7	32.7

Good correlation is evident between the theoretically derived values and the results obtained from the finite element model for the piezoceramics. Table 5.2 compares the results of the finite element modelling with a set of experimental results supplied by Smith and Ting [58]. The depoling of the experimental ceramic is accounted for by reducing the piezoelectric action within the ceramic phase so that the modelled d_{33} was matched to the experimentally measured d_{33}. This was an attempt to reduce the error caused by variations in the ceramic properties between samples. The ceramic phase was Toshiba C-24 modified lead titanate for samples 503, 485 and 509 and was Honeywell PZT278, a PZT-5 derivative, for samples 491, 487 and 512. The polymer phase for all the piezocomposite samples was the Spurr epoxy and the properties of

all three materials are given in [56]. In Table 5.2, VF indicates volume fraction expressed as a percentage and AR indicates the pillar aspect ratio. The four columns of results are: EXP for experimental; FEA for finite element analysis; SI for the extended isostrain model; and HN for the Haun-Newnham model. This shows reasonable correlation between the finite element model and the experimental results.

Table 5.2: Comparison of the HFOM Results from Different Models

Sample	VF	AR	Hydrostatic Figure of Merit [$10^{-15}Pa^{-1}$]			
			EXP	FEA	SI	HN
503	16	0.17	940	945	1050	778
485	18	0.10	940	921	1080	784
509	26	0.13	1300	1303	1355	970
491	12	0.11	1120	1049	1267	1183
487	19	0.11	900	818	1151	1070
512	26	0.10	560	544	660	602

Figure 5.5 shows the hydrostatic figure of merit (HFOM) as calculated by the extended isostrain model, Haun-Newnham model and the finite element analysis for EC-97 modified lead titanate and PZT-5H with the two polymers, hardset and softset. EC-97 was used in preference to the C-24 material because reliable characterised material parameters for the EC-97 was supplied by Howarth of USRD, NRL, Orlando, USA. Also, finite element modelling of the very low (<5%) volume fraction piezocomposites of C-24 produced extremely high voltage constants compared to Smith extension to the isostrain model. The three curves for the finite element analysis results in each graph are for three different aspect ratios: 0.10, 0.20 and 0.30. As can be seen, both constrained models incorrectly estimated the values compared to the finite element model. The response of the piezocomposites using EC-97 with lower lateral coupling (d_{31}/d_{33}=-0.23) showed less effect from varying the aspect ratio than the PZT-5H composites where the lateral coupling in the ceramic was -0.46.

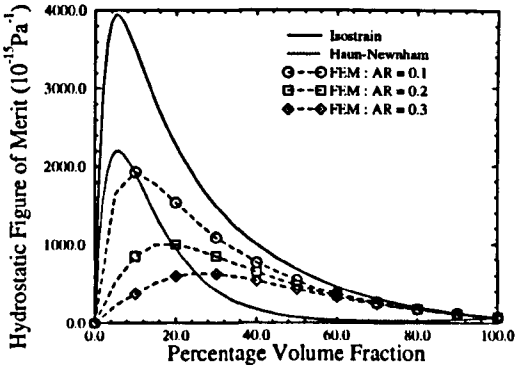

(a) PZT-5H/Hardset Composite

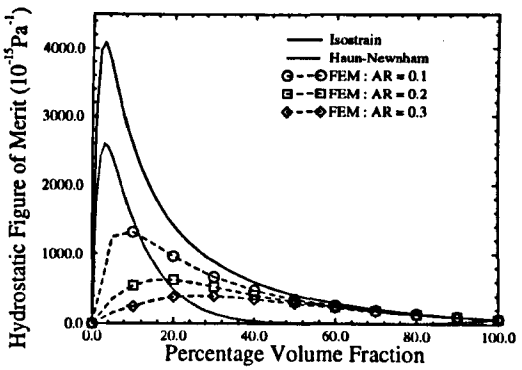

(b) PZT-5H/Softset Composite

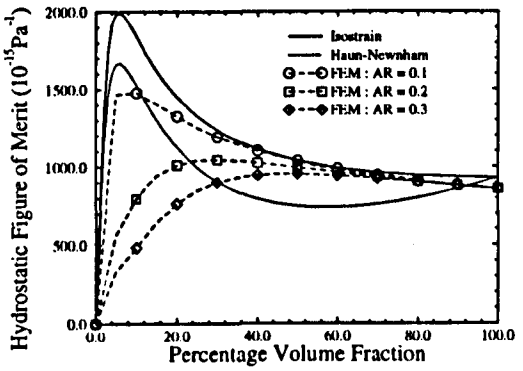

(c) EC-97/Hardset Composite

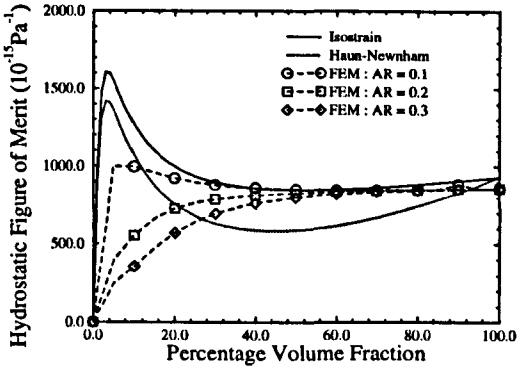

(d) EC-97/Softset Composite

Figure 5.5: Comparison of Hydrostatic Figure of Merit Produced by Different Models

Also the effect of the aspect ratio is only significant at low volume fraction. As the aspect ratio is decreased, the response was enhanced although it did not reach the peak predicted by both theoretical models.

5.4 HYDROPHONE MATERIAL SELECTION

This Section deals with the design of a 1-3 piezocomposite hydrophone using the finite-element model. The model was initially used to compare different piezoceramics and polymer to show the desired material properties for each phase. This modelling was then extended to include stiffening plates on the top and bottom surface of the hydrophones to reduce the lateral movement in the polymer matrix while not reducing the thickness direction response.

5.4.1 Ceramic and Polymer Materials

The piezoceramics chosen for the selection process were PZT-5H, PZT-4, PZT-7, Barium Titanate (BT) and EC-97. Using a ceramic phase of PZT-5H, the properties of the polymer phase were varied:

- Elastic modulus from 1.0 MPa to 3.0 MPa; and
- Poisson ratio from 0.35 to 0.45.

These simulations were not repeated using the modified lead titanate as the piezoceramic because such hydrophones have a response similar to the constituent ceramic for most volume fractions independent of the properties of the polymer phase. The density of the polymer was kept constant at 1150 $Kg.m^{-3}$ and the aspect ratio of 0.10 was assumed for all simulated piezoceramics. The curves are shown in Figure 5.6 and the results can be summarised as:

- *Ceramic* - While the PZT piezoceramics and especially PZT-5H produced the largest strain constants, the very low permittivity of the EC-97 and Barium Titanate meant they had the largest voltage constants. The largest HFOM was produced by the

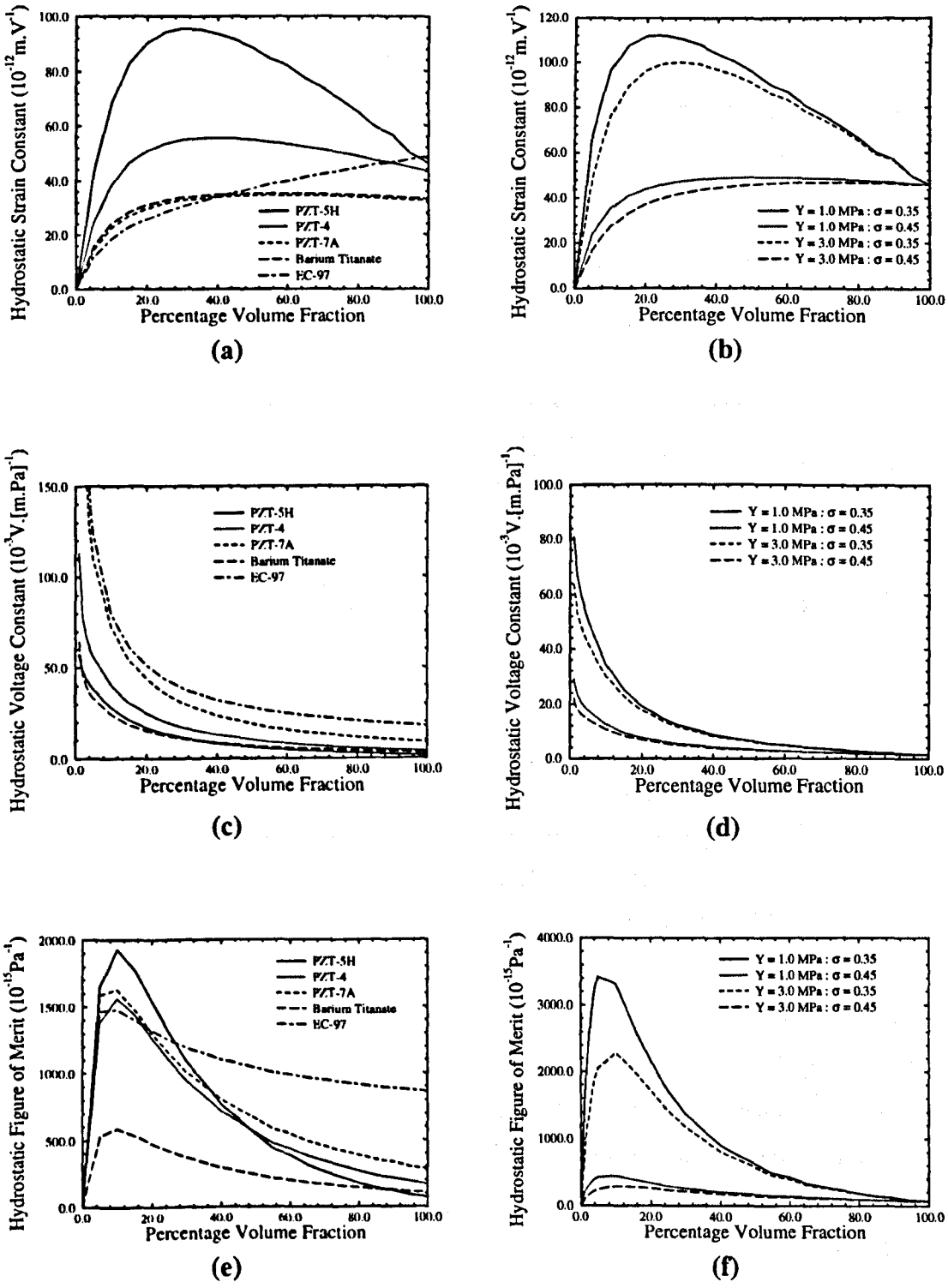

Figure 5.6: Comparison of Different Piezoceramics and Polymers under Hydrostatic Conditions

PZT-5H piezocomposite at low volume fractions but the response decreased below that of EC-97 for higher volume fractions (>25%).

- *Polymer* - The desired properties are low elastic modulus and low Poisson ratio, ideally zero or less. These are normally opposing conditions for viscoelastic materials but Figure 5.6(b) indicates that the compressibility of the polymer matrix has more influence on the hydrostatic response than its compliance.

5.4.2 Effect of Pillar Shape

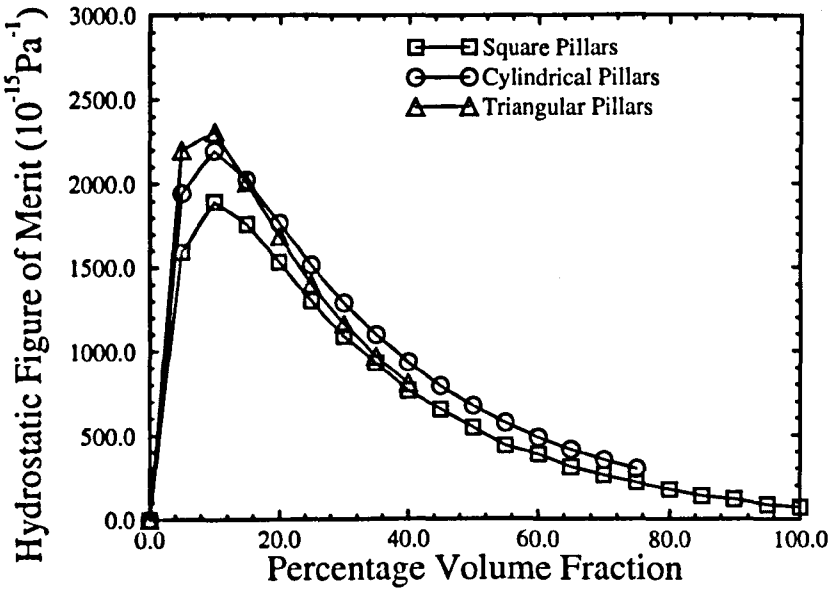

Figure 5.7: Hydrostatic Response of PZT-5H/Hardset Composites with Different Shaped Pillars

The ceramic pillars in the polymer matrix do not have to be regular hexahedrons. The effect of the shape of pillar was investigated by generating results for different shaped pillars: square, cylindrical and triangular pillars. In Chapter 4, it was found that the triangular pillars had an increased maximum pillar aspect ratio compared to the other two configurations for thickness mode operation at low volume fractions. As can be seen in Figure 5.7, the HFOM generated from the three shapes were similar indicating that the ceramic acts as a stiff rod in the compliant polymer and hence the relative volume of the ceramic is more important than the shape of the pillar. This has the implication that the pillar shape for hydrophones is selected by the

manufacturing process and not by the design process. In the shape simulations, the ceramic and the polymer phases were PZT-5H and softset respectively.

5.4.3 Stiffening Plates for the Hydrophones

A thin mechanical plate can be placed on the top and bottom surface of the 1-3 piezocomposite plate to reduce lateral movement while not affecting thickness movement. The hydrostatic response of PZT-5H with the polymer, Y=1 MPa and σ=0.35, chosen from Figure 5.6(f), was estimated with the following stiffening plates: no plates; hardset plates; aluminium plates; and titanium carbide plates. The thickness of all the plates was 0.10 of that of the height of the piezocomposite material placed above and below the active material.

Examining the results in Figure 5.8, it can be concluded that the plate should be as stiff as possible to reduce any lateral movement. This is why the aluminium and titanium carbide plate produced a better response than the hardset plate. The aluminium and titanium carbide plate simulations produced similar results although the latter has a significantly higher modulus and hence, would be stiffer for the same thickness. This was because neither deformed under the hydrostatic stress and hence, the more cost-effective material, aluminium, may be used for application as the stiffening plates.

The effect of the stiffening plate was illustrated graphically for a 25% VF, 0.10 AR PZT-5H piezocomposite. Figure 5.9 shows the shape of the finite element model of the unit cell under hydrostatic pressure with no plate and with aluminium plates. The shapes are the cross-sectional views through the centre of the unit cell for a square pillar. This shows that the aluminium plates are undistorted by the hydrostatic pressure. The surface dilation quality of the top of the ceramic pillar has been increased by the addition of the stiffening plate which shows that there is less lateral strain in the ceramic pillar. The strains have been multiplied so that they are easily visible to the reader.

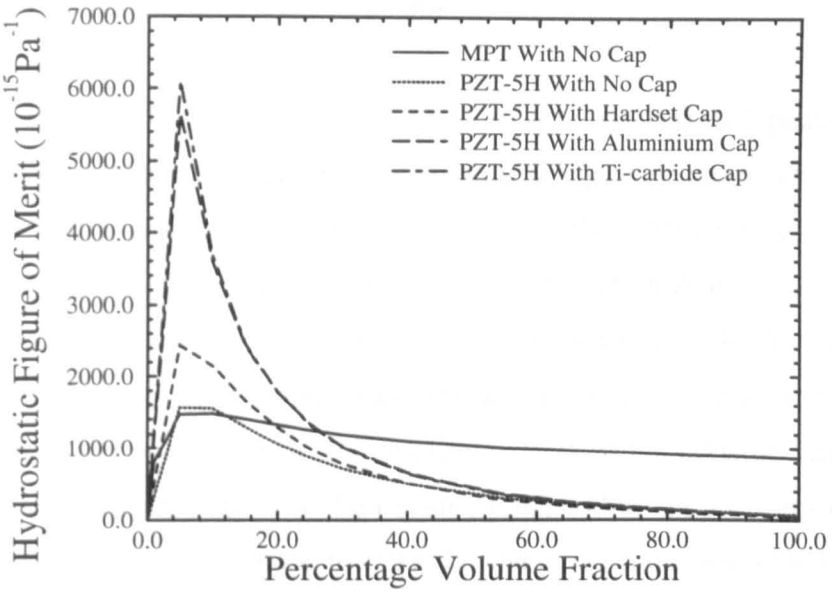

Figure 5.8: Comparison of Different 1-3 Piezocomposite Hydrophones

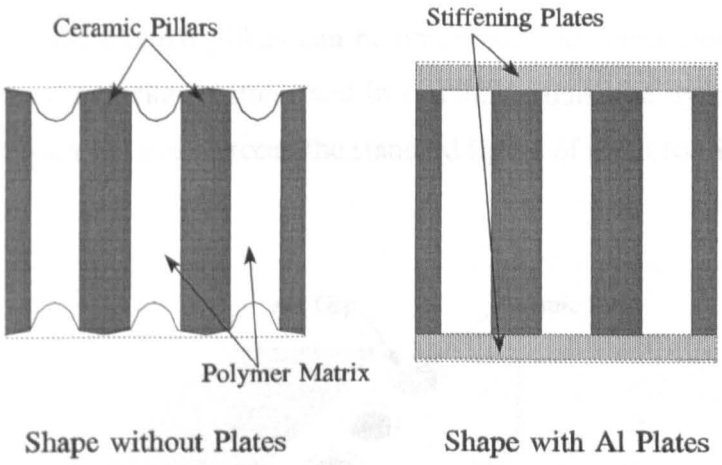

Figure 5.9: Diagram showing Displacement for Different Hydrophones

5.4.4 1-3-1 Connectivity Piezocomposites

Richard et al. [59] developed a modification to the standard 1-3 piezocomposite hydrophone in an attempt to enhance the hydrostatic figure of merit. The theoretical limit for the value is defined by the value from Smith's extension to the isostrain model. This is obtained by using an extremely low aspect ratio or needle-like pillars which makes the devices very fragile and difficult to manufacture. Richard considered the reason for this requirement and concluded that it was to maximise the transfer of lateral stress in the polymer matrix to thickness stress of the ceramic pillars and to reduce the applied lateral stress in the ceramic pillars. Optimal transfer of this form occurs at aspect ratios very close to 0.00. To overcome this requirement, Richard proposed to remove any direct contact between the polymer matrix and the ceramic pillars but rather connect the stresses through stiffening plates. He achieved this by leaving air gaps around the pillars and called this connectivity *1-3-1* where the second 1 represents the connectivity of the air. The structure is shown in Figure 5.10 where the air-gap around the circular pillars can be observed. The lateral stress within the polymer enhances the thickness stress and in certain designs, the hydrostatic figure of merit can approach and even exceed the standard figure of merit for the constituent ceramic.

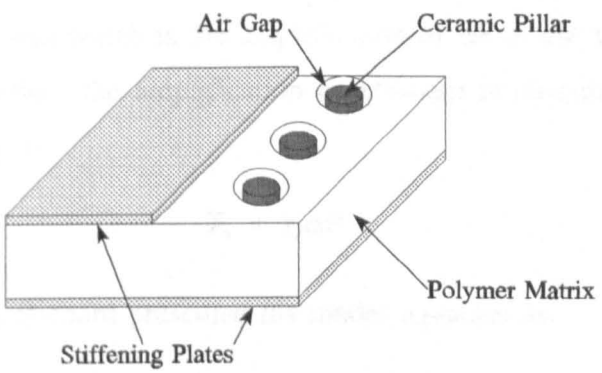

Figure 5.10: 1-3-1 Connectivity Piezocomposite Hydrophone

This is because of the lever action created on the stiffening plate by the polymer matrix. When the polymer matrix is compressed by the lateral pressure, the polymer material collapses because it is very compliant. It then bulges towards the ceramic pillar due to its large Poisson ratio, acting as a fulcrum levering the plate up from the ceramic pillar. This lever action is sufficient to exceed the hydrostatic pressure and produce an enhanced response as shown in Figure 5.11.

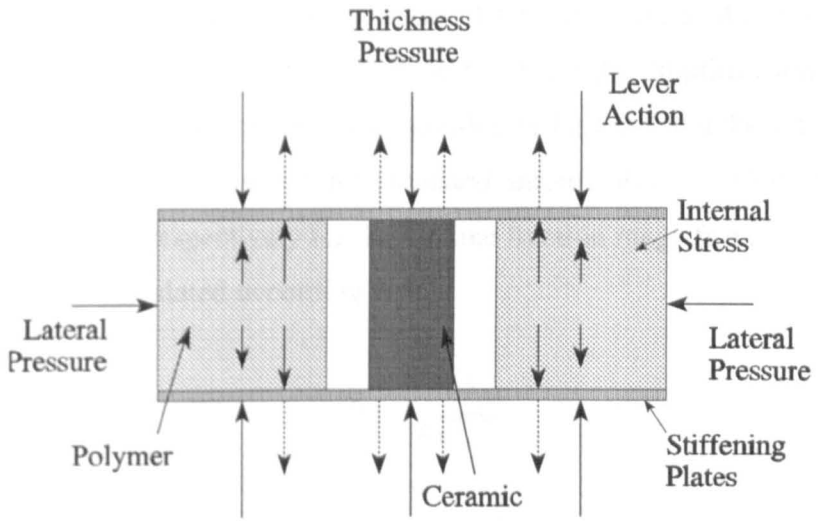

Figure 5.11: Illustration of Lever Action of Stiffening Plate

Hence, the stress applied on the ceramic rod is only in the *3* direction and exceeds that of the applied transient hydrostatic pressure, ΔP. The air-gap acts as a stress-free boundary for the circular ceramic pillar. Richard developed the concept of an amplification co-efficient which is the amplification of ΔP to the applied stress, T_3. Using Richard's notation, the amplification co-efficient is designated by χ and is given mathematically as:

$$T_3 = \chi.\Delta P \qquad \textbf{Eqn. 5.16}$$

In the reference [59], Richard presented his model equation as:

$$\begin{aligned} \bar{g}_h &= \chi g_{33}^{ceramic} \\ \bar{d}_h &= \chi \upsilon d_{33}^{ceramic} \\ \therefore HFOM &= \chi^2 \upsilon g_{33}^{ceramic} d_{33}^{ceramic} \end{aligned} \qquad \textbf{Eqn. 5.17}$$

where the bar denotes the response of the hydrophone; and

the label *ceramic* denotes the values of the constituent ceramic.

Richard investigated the effect of the thickness of the plate and the ratio of the diameter of the air gap to the diameter of the rod on the value of χ. The finite element model for a 1-3 piezocomposite hydrophone with stiffening plates was extended to incorporate the air-gap. The influence of three parameters: the aspect ratio (AR) of the ceramic pillars; the ratio of air-gap to pillar diameter (RA); and thickness of the aluminium stiffening plate (AL), on the amplification co-efficient were investigated on a hydrophone configuration of PZT-5H and the softset polymer. Figure 5.12(a) and 5.12(b) show the estimated amplification co-efficient for AL of 0.1 mm and 0.3 mm respectively for the volume fraction range from 1% to 10%. The co-efficient was calculated according to:

$$\chi = \frac{\bar{g}_h}{g_{33}^{ceramic}} \qquad \textbf{Eqn. 5.18}$$

where $g_{33}^{ceramic}$ for PZT-5H is 19.6×10^{-3} Vm.Pa^{-1}.

Comparing the two graphs, it can be observed that:

- From the two figures, increased response was obtained with a thinner stiffening plate.
- The effect of increasing air-gap dimensions was to increase the amplification co-efficient but its influence was not as important as the aspect ratio.
- The influence of the aspect ratio was to increase χ with decreasing aspect ratio. This indicates that the best response would be obtained by needle-like pillars with very small aspect ratio.
- According to the curves, the volume fractions should be minimised but both the effect of the electrical loading discussed in Section 5.5 and the volume fraction in Equation (5.17) would emphasize a higher volume fraction.

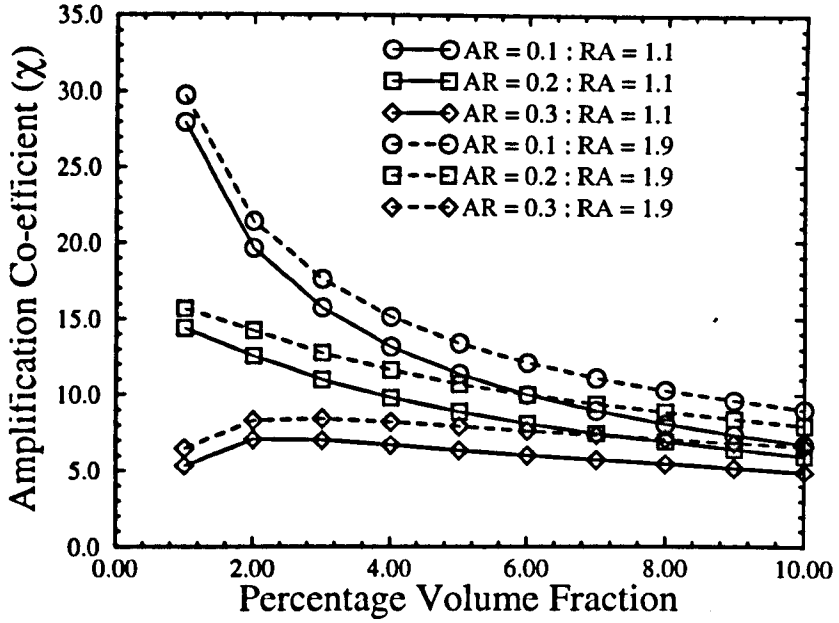

Figure 5.12(a): Results of 1-3-1 FE Model with SL=0.1mm

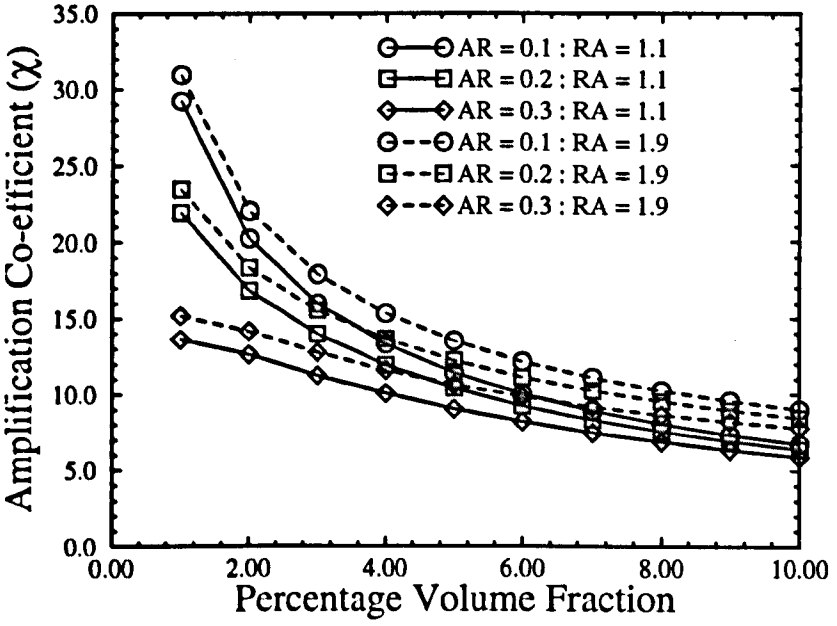

Figure 5.12(b): Results of 1-3-1 FE Model with SL=0.3mm

The best theoretical HFOM for a 1-3 piezocomposite hydrophone is the product of the d_{33} and g_{33} of the constituent ceramic. The minimum β produced by any of the modelled configurations with volume fractions less than 10% was 5.0 which implies that independent of aspect ratio, the 1-3-1 configuration produced a HFOM of at least 2.5 times that of the equivalent best 1-3 piezocomposite configuration. This shows that Richard achieved his aim of removing the requirement for a very small aspect ratio to obtain a good response.

The design guidelines for 1-3-1 piezocomposite hydrophones given by Richard in his Thesis [55] were:

- Sufficient stiffening plate thickness for the plate not to bend;
- Wide air gap (large RA); and
- Soft and compliant polymer matrix with high Poisson ratio.

These are similar conclusions that were drawn from Figure 5.12.

5.5 ELECTRICAL LOADING OF PIEZOCOMPOSITE HYDROPHONES

It can be observed in Figure 5.6(c) and 5.6(d) that with the finite element methodology, there seems to be no limit on the value of g_h as the volume fraction tends to zero. This is because even though d_h tends to zero, the permittivity also tends to zero with reducing volume fraction. However, the theoretical method of calculating g_h for the figure does not include any of the electrical loading caused by the attached cable and the input impedance of the receive amplifier. The transmit situation can be considered identical to the receive scenario and hence, an identical result would be obtained after the derivation.

The equivalent electrical circuit for the hydrophone can be derived from the alternative form of the constitutive equation for linear piezoelectricity with the electric charge density as the subject of the formula:

$$\underline{D} = [d]\underline{T} + [\varepsilon^T]\underline{E} \qquad \textbf{Eqn. 5.19}$$

where $\underline{D}$ is the electric charge density vector;

[d] is the piezoelectric charge matrix relating stress and charge density;

$\underline{T}$ is the mechanical stress vector;

$[\varepsilon^T]$ is the permittivity matrix under constant stress; and

$\underline{E}$ is the electric field vector.

As the hydrophone is under hydrostatic pressure, the stress vector becomes:

$$\underline{T} = [\Delta P \;\; \Delta P \;\; \Delta P \;\; 0 \;\; 0 \;\; 0] \qquad \textbf{Eqn. 5.20}$$

where ΔP is the transient hydrostatic pressure.

The electric field vector becomes:

$$\underline{E} = [0 \;\; 0 \;\; -E_3] \qquad \textbf{Eqn. 5.21}$$

where the negative sign indicates that the electric field is generated to oppose the applied pressure.

Hence the charge density generated in the thickness direction is:

$$D_3 = d_h \Delta P - \varepsilon_{33}^T E_3 \qquad \textbf{Eqn. 5.22}$$

The charge, Q_{hydro}, produced by the hydrophone is then:

$$\begin{aligned} Q_{hydro} &= A_{exp} D_3 \\ &= A_{exp} d_h \Delta P - A_{exp} \varepsilon_{33}^T E_3 \end{aligned} \qquad \textbf{Eqn. 5.23}$$

giving a current, I_{out}, of:

$$I_{out} = j\omega Q_{hydro}$$
$$= j\omega A_{exp} d_h \Delta P - j\omega A_{exp} \varepsilon_{33}^{T} \frac{V_{out}}{t_3} \qquad \textbf{Eqn. 5.24}$$

where ω is the operating radial frequency;

t_3 is the thickness of the transducer; and

V_{out} is the voltage produced by the hydrophone and is approximated by the product of t_3 and the electric field, E_3.

C_{imped} is the low-frequency capacitance of the hydrophone and is the electrical impedance of the device below the thickness mode frequencies. This result can be derived from Mason's model as described in Chapter 2. The capacitance is given by:

$$C_{imped} = \varepsilon_{33}^{T} \frac{A_{exp}}{t_3} \qquad \textbf{Eqn. 5.25}$$

where A_{exp} is the surface area of the hydrophone.

Equation (5.25) allows Equation (5.24) to be modified:

$$I_{out} = j\omega A_{exp} d_h \Delta P - j\omega C_{imped} V_{out}$$
$$= I_{hydro} + I_{imped} \qquad \textbf{Eqn. 5.26}$$

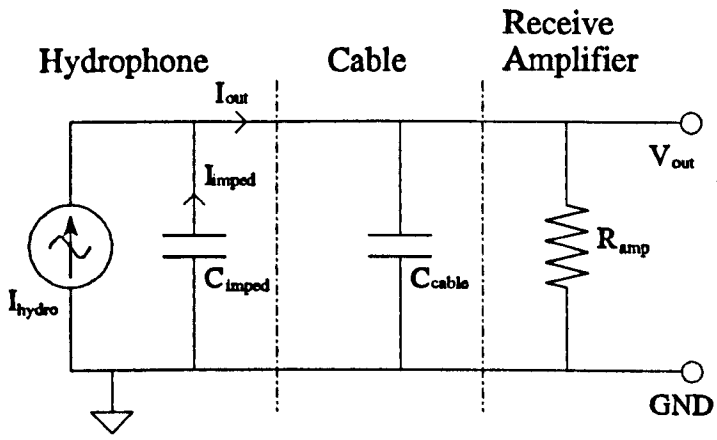

Figure 5.13: Electrical Circuit for Receiver Hydrophone

The derived circuit from Equation (5.26) is shown in Figure 5.13 where the three currents are as shown. It is important to note the direction of I_{imped} which is why the sign is inverted in Equation (5.26). For a normal design, the impedance of the cabling and receive amplifier is sufficiently greater than that of the hydrophone capacitance such that a major portion of the current generated in the hydrophone flows through the hydrophone's internal impedance. From Equation (5.24), an expression for the voltage can be derived for this simplified case as:

$$\begin{aligned} I_{imped} &= -I_{hydro} \\ C_{imped}V_{out} &= A_{exp}d_h\Delta P \\ V_{out} &= \frac{A_{exp}}{C_{imped}}d_h\Delta P \end{aligned} \qquad \textbf{Eqn. 5.27}$$

However, the hydrostatic voltage constant can be calculated as the ratio of the voltage produced to the thickness of the transducer and the applied pressure:

$$g_h = \frac{V_{out}}{t_3.\Delta P} \qquad \textbf{Eqn. 5.28}$$

Substituting Equation (5.18) into Equation (5.26):

$$\begin{aligned} V_{out} &= \frac{t_3}{\varepsilon_{33}^T}d_h\Delta P \\ \therefore\ g_h &= \frac{d_h}{\varepsilon_{33}^T} \end{aligned} \qquad \textbf{Eqn. 5.29}$$

which agrees with Equation (5.3).

However, when the static capacitance is reduced to the extent that current flows out of the hydrophone, V_{out} is reduced and the measured g_h is smaller than the theoretical value. C_{cable} represents the capacitance of the cable, the capacitance caused by the practical connections to the electrodes of the hydrophone and the input capacitance of the amplifier. At the operating frequencies of the hydrophone, the combined value is normally in the order of several 100 pFs. As the input resistance of the amplifier,

R_{amp}, can normally be modified to reduce its loading effect on the system, the limiting case occurs when the static capacitance has a similar value to the cable capacitance.

For cases where the cable capacitance is significant, Equation (5.26) can be modified to include its influence:

$$j\omega C_{cable} V_{out} = j\omega A_{exp} d_h \Delta P - j\omega C_{imped} V_{out}$$

$$\therefore V_{out} = \frac{A_{exp} d_h}{C_{cable} + C_{imped}} \Delta P \qquad \textbf{Eqn. 5.30}$$

$$\therefore g_h^{loaded} = \frac{C_{imped}}{C_{cable} + C_{imped}} g_h^{unloaded}$$

where g_h^{load} is the constant measured at the end of the cable; and

$g_h^{unloaded}$ is the constant measured at the transducer as described in Eqn (5.28).

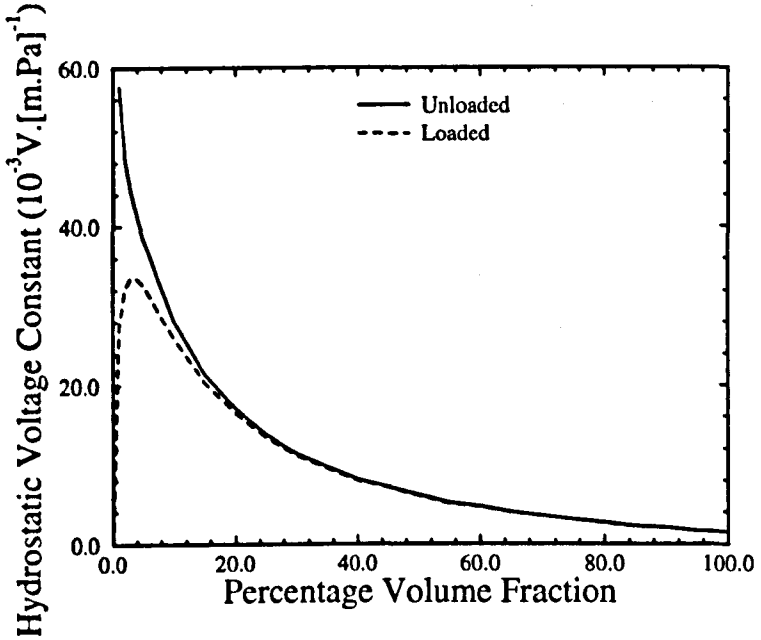

Figure 5.14: Effect of Electrical Loading on Voltage Constant

This expression tends to zero for C_{imped} approaching zero. To illustrate the effect of the cable capacitance on the g_h constant, C_{cable} was assumed to be 100 pF and the loaded and unloaded g_h are graphed in Figure 5.14 for volume fractions below 10%. The piezocomposite was PZT-5H/hardset with aspect ratio 0.10. It can be seen that the measured g_h would not reach infinity but decreases at volume fractions below 4%.

5.6 CONCLUDING REMARKS

This chapter dealt with the development of a finite element model for 1-3 piezocomposite hydrophones which enables further designs to be investigated with this technique. The finite element model was an extension of the model developed in Chapter 3 with the inclusion of lateral and thickness forces applied to the model under different electrical loading. The hydrostatic figure of merit was calculated by estimating the hydrostatic strain and voltage constant from the model.

The model was compared to two constrained-dimensional models, the Haun-Newnham model and Smith's extension to the isostrain model, and to experimental values. As the finite element model included the effect of the aspect ratio, it understandably produced better results than the other models for piezocomposite with the large lateral coupling in the ceramic phase. It is expected that more encouraging results would be obtained for the modelling if the ceramic and polymer phase were more completely characterised for the experimental hydrophone. The finite element model was then used to evaluate the piezoceramic and polymer phases for the composite microstructure. The best piezoceramic from the selection list was PZT-5H and the response at low (~10%) volume fraction was enhanced by the addition of stiffening plates. The material properties of the plates was not important as long as the plate was sufficiently thick not to be flexible. The aspect ratio of the ceramic pillars should be minimised to optimise the stress transfer from the polymer matrix to the ceramic pillars. The polymer phase should be compliant and possess the lowest possible Poisson ratio.

To demonstrate that the finite element model developed for hydrophones could be used to investigate different configurations, an analysis of the 1-3-1 connectivity composites developed by Richard was performed. The geometrical requirements for a large amplification co-efficient were determined for a configuration of PZT-5H/softset composite with aluminium stiffening plates.

The effect of the electrical loading of the receive amplifier was also examined theoretically and it was shown that there is a minimum useable value for volume fraction to generate sufficient charge to drive the cable and amplifier. This is because at extremely low volume fraction, the capacitance of the cabling shorts the static capacitance of the hydrophone and limits the produced voltage. This in turns limits the value of the hydrostatic voltage constant and hence the hydrostatic figure of merit.

CHAPTER SIX

DESIGN OF 1-3 PIEZOCOMPOSITE ARRAY TRANSDUCERS

CHAPTER OBJECTIVE

Due to the reduced lateral mode activity within the polymer matrix compared to a monolithic ceramic plate, 1-3 piezocomposite transducers are ideally suited for array applications. Other authors have shown using constrained dimensional modelling, that an efficient array can be constructed from a PZT ceramic/stiff polymer composite. Finite element modelling is utilised in this Chapter to further extend the analysis. The response of the individual element can be characterised by the sensitivities and the beamwidth for use in a standard array analysis package. The algorithms for calculating the different sensitivities were presented in Chapter 3 but an algorithm for the beamwidth needs to be derived for use in this Chapter.

Once verified, the fully-developed finite element model can also be used in an investigation into the preferred element size for the array. This analysis needs to include the effect of adding a matching layer, backing block and the increased fluid loading of water on the performance of the device. The elements should also operate in a piston-like fashion so techniques for increasing the dilation quality need to be considered. Finally, the influence of the different parameters in the design on the beamwidth and cross-coupling of energy can be investigated.

6.1 TRANSDUCER ARRAY DESIGN

There is a growing requirement for real-time two-dimensional acoustic imaging for applications in biomedicine, underwater imaging and non-destructive evaluation [41]. However, despite widespread success and the extensive application range, practical implementation has been largely limited to one-dimensional array configurations where the transducer elements are arranged in a single row to produce a two-dimensional image. The extension into two-dimensional arrays to produce complete three-dimensional images has been largely unsuccessful due to a number of factors. Recent advances in VLSI techniques and concurrent processing architectures have allowed the feasibility of low cost electronic interfacing and real time processing of the image data. The remaining problems are concerned with the transducer technology and are covered in this Chapter.

A constraint for high-frequency ultrasonic transducer arrays is that the elements must be closely spaced to obtain sufficient resolution so they are normally placed on the same piezoelectric material plate. Hence, the behaviour of each element is not only a function of the material design but also a function of the coupling between the individual elements of the array through the spacing material. Thus the finite element model must not only include the primary element being simulated but also the space between the elements and the surrounding elements.

6.1.1 Simulation of Array Design

The simulation of the operational array has historically been performed in two stages [41]:

A. Simulation of the individual element behaviour using a constrained-dimensional model for both transmission and reception; and

B. Simulation of all the elements, the surrounding medium and the targets assuming that the elements act in an "ideal" fashion according to the assumptions of the constrained-dimensional models.

The output from each stage is correlated to obtain the complete response of the system. An example of such a simulation package is *TAPES* (Two-dimensional Array Processing Evaluation Software) developed by Hall [60]. The linear systems model [36] is used for the element simulation and assumes only thickness mode vibration, not inter-element coupling. The spatial impulse response of the system is simulated in stage B taking into account the diffractions, refractions and reflections of the acoustic waves.

Both packages have been verified through extensive experimentation for configurations where the assumptions are valid. There are two major flaws in this methodology which are addressed in this Chapter:

- The diffraction from the element is assumed to be generated by piston-like movement from the element surface. As will be shown in later Sections, this is seldom the case. A non-piston movement modifies the beam profile of the element.
- The modelling of the individual elements does not account for the mechanical cross-coupling between the elements. This also modifies the beam profile of the different elements.

Hence, if the finite element model is to be used for the first stage of these simulation packages, it must be able to estimate the following for extra processing to be justified: the full beam profile of the element including all the pressures that are produced in the surrounding fluid; and the effect of the cross-coupling on the behaviour of the individual element.

The finite element model can then be used in two ways:

- It can be used to determine the limits for which the assumptions of the constrained-dimensional models are still valid. Array transducers operated in this region have normally been optimally designed as the cross-coupling tends to degrade the array performance as shown by Kino and DeSilets [61].
- In cases where constraints on the design are such that the array elements do interact through cross-coupling, it can be used to compare different techniques to reduce the coupling and to determine the exact extent of the effect of the coupling.

6.1.2 Description of PZ-Flex Package

It was found that the ANSYS package could not analyse the necessary finite element model accurately for certain array configurations to obtain the desired information. For this reason, the PZ-Flex package produced by Weidlinger Associates [62] was obtained at a late stage of the work. Hence, this package was not used for all of the array modelling. PZ-Flex is a finite element package designed to analyse the response of continua subjected to time-varying dynamic or static loads. It was developed for application in a wide range of problems including geotechnical, seismic wave propagation, soil-structure interaction and weapon effects, which can be solved using wave propagation. The current version used was 1-H.4 revised on 10 November 1994. It is similar to ANSYS in that it can model the piezoelectric ceramic, the purely mechanical polymer matrix and the surrounding fluid medium. However it differs from the ANSYS package in that it was not developed to be a general-purpose package allowing any type of modelling but package design decisions were made to maximise speed. For this reason, an explicit time integration technique which avoids the difficulties of manipulating large assembled matrices for the model, was used. This approach restricts the computational time step to be less than the Courant stability criteria but the necessary value for the whole model is estimated by the package and a safety factor of 0.8 of the generated time step is used. If the model is

sufficiently small, this integration technique can be operated using in-core memory which gives a 2-4 times increase in solution speed. To solve a similar model in the ANSYS package would take up to ten times the processing time. However, the package cannot perform modal or harmonic analysis. All the modelling performed with this package was with time-domain models.

The package also has the enhanced capabilities for fluid loading and mechanical loss mechanisms for viscoelastic polymers which were the areas where the ANSYS package was weak. The fluid loading elements are implemented as mechanical elements with no shear wave motion as fluids do not have the necessary regular lattice structure to sustain such waves. The loss in the fluid had to be modified to duplicate the effect of shear loss caused by the viscosity within the fluid. The code designers did not develop boundary elements as discussed in Chapter 3 but allowed the operator to place an absorbing boundary at any position in the model. Two mechanisms are available for the implementation of mechanical loss:

- *Static damping* which is similar to the mechanism used by the ANSYS package but the exponent for the frequency dependence can be defined to be different from that of unity for the ANSYS package. The damping can be given in terms of nepers which is the normal unit for acoustic damping or as the percentage of the critical damping. Separate values can be defined for the shear and longitudinal waves.
- *Viscoelastic damping* which simulates the movement of the molecular strands in the polymer structure. It has the same frequency response as shown in Figure 2.3. This damping should be used for high-loss components as there is no frequency-dependence at the high frequencies. The loss is specified in the same manner as with the static damping.

This means that the PZ-Flex package has the required features that the present release of ANSYS lacked. PZ-Flex also has the capability of including simple electrical circuits to the electrodes, either for transmission or reception, allowing the modelling of the pulser unit and receive pre-amplifier.

6.1.3 Verification of PZ-Flex Package

PZ-Flex was used to model two different transducers that previously had been modelled using the ANSYS package:

- *Transducer P1S2A1* which is a 0.13 aspect ratio (AR) 20% volume fraction (VF) PZT-5A/hardset piezocomposite. The response is shown in Figure 6.1 and was produced by the post-processing module of the PZ-Flex package. In order of left to right and top to bottom, the diagrams are: (a) the input voltage signal applied to the active electrode which was half-cycle at a frequency of 1.6 MHz; (b) the charge produced on the active electrode with time; (c) the impedance magnitude in the frequency range calculated from the voltage and charge functions displayed previously; and (d) the impedance phase with frequency. The experimental results have been included in Figure 6.1(c) and (d) as the dotted line. It is important for this time analysis to ensure that the time length was sufficient for the charge function to reach a steady state value of zero. This is why the time length of the voltage function is minimised without containing much energy at the very high frequency (>20 Mhz) components. It can be observed that the finite element analysis correctly modelled both the thickness mode and first lateral resonance with a single damping function.

- *50% VF 0.22 AR PZT-5A/hardset piezocomposite in air and castor oil* as shown in Figure 6.2. In order of left to right and top to bottom, the diagrams are: (a) the impedance magnitude of the transducer in air; (b) the impedance magnitude of the transducer in castor oil; (c) the phase of the transducer in air; and (d) the phase of the transducer in castor oil. Good correlation between the finite element results in the solid line and the experimental results in the dotted line can be seen. The surface dilation quality was generated from the in-oil analysis and was compared to that produced from the ANSYS package in Figure 6.3. It can be seen that the effect of the fluid loading on the dilation quality was to slightly reduce the dilation quality around the operational frequencies. This is in agreement with the results presented in Section 4.5.3.

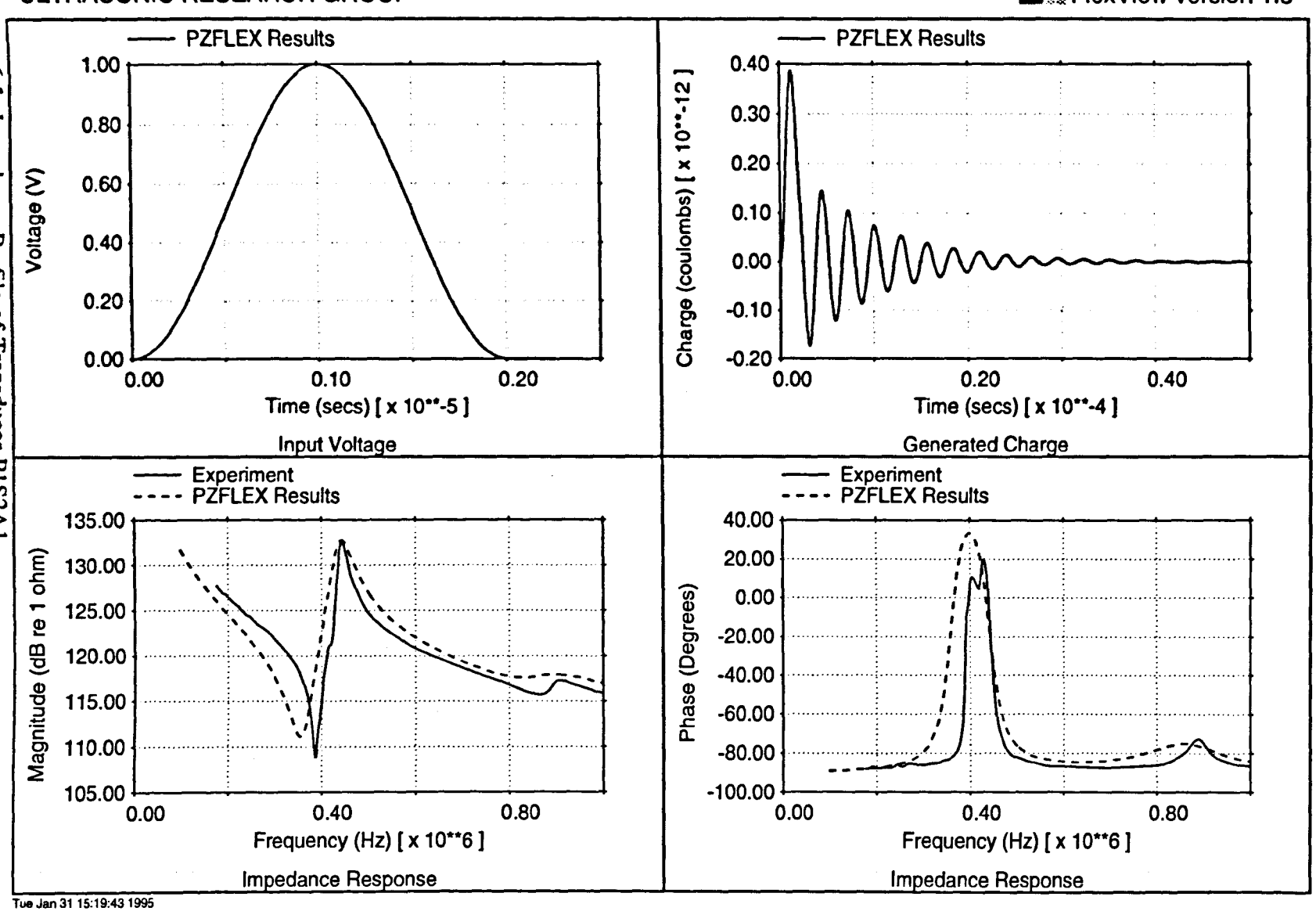

Figure 6.1: Impedance Profile of Transducer P1S2A1

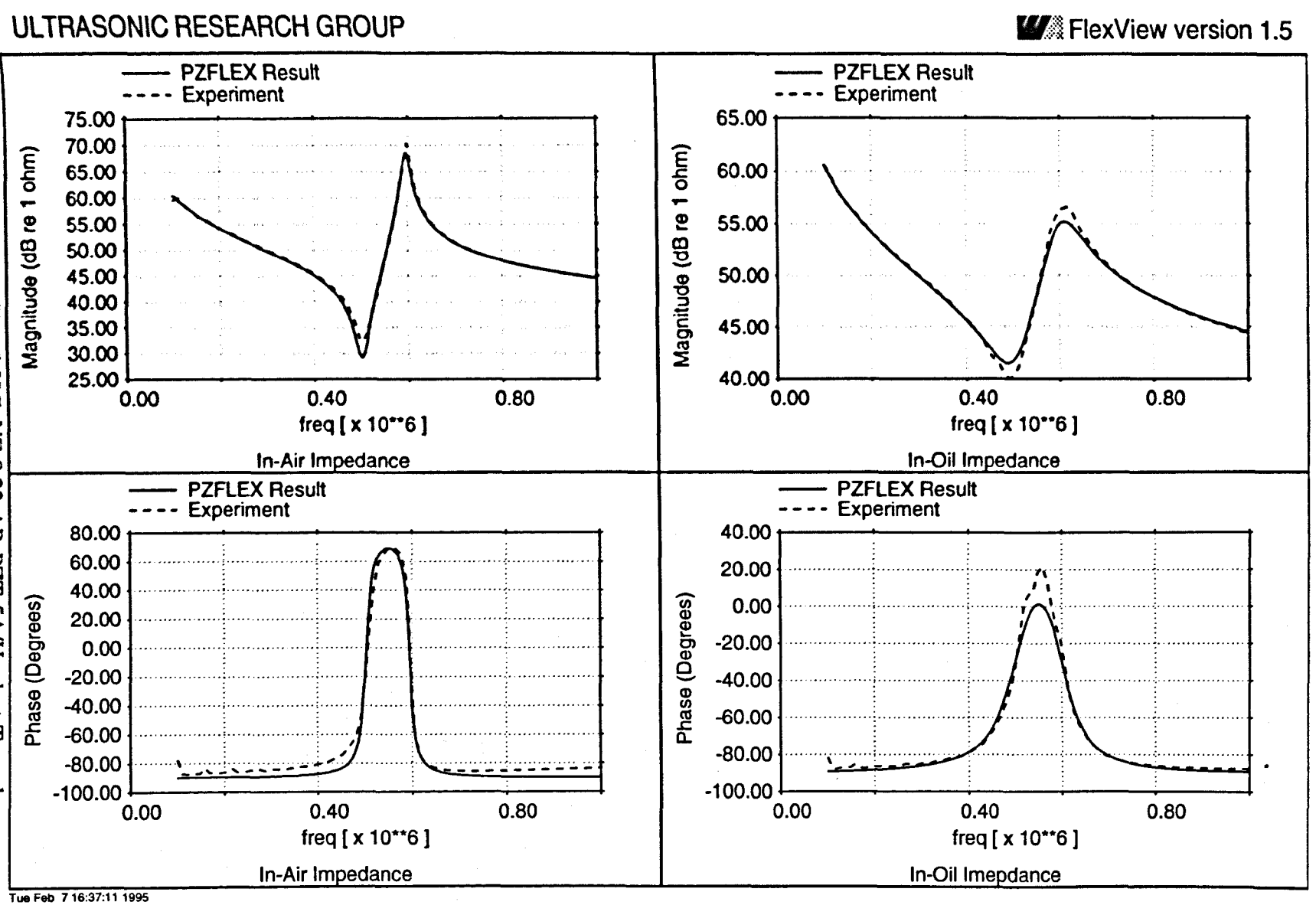

Figure 6.2: Impedance Profile of 50% VF 0.22 AR PZT-5A/Hardset Transducer

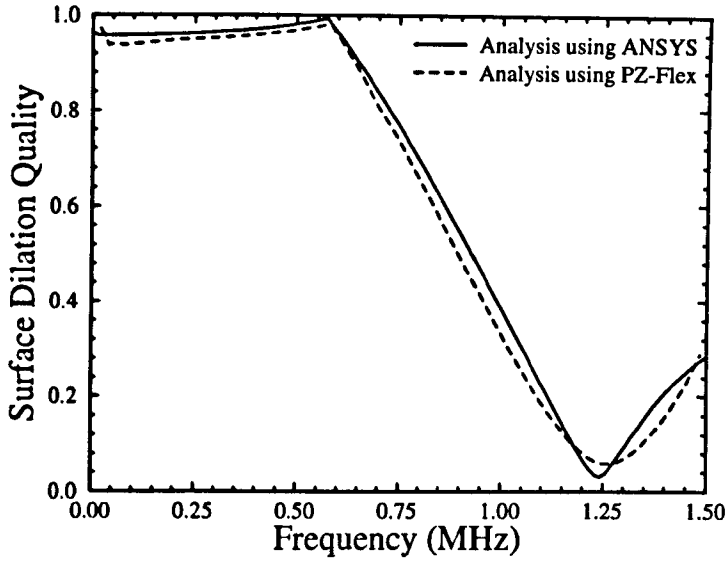

Figure 6.3: Surface Dilation Quality for 50% VF 0.22 AR PZT-5A/hardset Transducer in Castor Oil

6.2 EXTENSION OF FINITE ELEMENT MODEL

The ANSYS package was used where possible in the analysis of array transducers. The finite element model developed in Chapter 4 was extended to include the effect of the size of the electrode for the element and the space between the electrodes. This implied that the model had to include more than the symmetrical segment of the unit cell of the original model. The command defining the active electrode of the model was modified to include only the surface of the selected pillars. This was to be representative of the finite size of the electrode pattern on the surface of the active material. The concept of the model is illustrated in Figure 6.4 where the un-electroded pillars between the elements act as a spacing between the elements in an attempt to reduce the cross-coupling mechanisms. The symmetrical boundaries are retained. The piezocomposite in the diagram has a volume fraction of 25%.

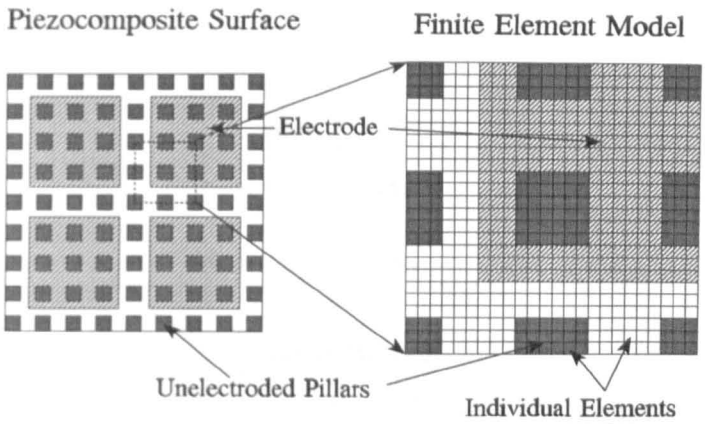

Figure 6.4: Electrode Pattern for 3x3 Pillar Element

6.2.1 Beam Profile of Transducer Element

The beam profile for a transducer element is defined as the set of values for the pressure in the far-field (at a distance from the transducer that can be considered to be infinite) with relation to the angle from the acoustic axis of the transducer. The beamwidth of the element is then determined from the pressure profile as the difference angle between the two angles at which the pressure level is half that of the pressure on the centre axis [63]. As the beam profile is normally displayed as a one-dimensional curve, the algorithm was developed for the two-dimensional case for x and z axis where z is the height above the transducer and x is in plane with the transducer surface as illustrated in Figure 6.5. The extension of the algorithm to account for the three-dimensional nature of the array elements is included as one of the suggestions for future work.

The algorithm for calculating the beam profile is derived with the aid of Huygen's principle [64]. This states that the radiation from a given object, in this case the transducer surface, can be considered as being the interference pattern generated from a series of radiating point sources on the surface of the object, each emitting spherical waveforms. This is of importance, since in the finite element modelling the pressure

in each element on the surface of the transducer, S_0 in Figure 6.5, can be considered as a point source.

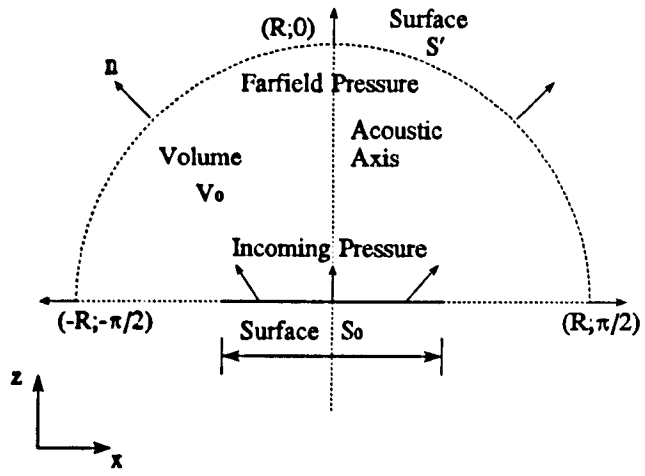

Figure 6.5: Diagram for Calculation of Beam Profile

Nagai [64] discussed a similar problem in his derivation of image reconstruction algorithms for an acoustic imaging system. The incoming pressure wave is assumed to enter the volume V_0 through the "aperture" S_0 and leaves through the surface S'. Elsewhere along the surface of V_0, the pressure function is assumed to be zero. It is also assumed that there were no reflectors or refractors within the contained volume V_0 so that the pressure waves travel through V_0 according to the solution to the free-space Helmholtz equation:

$$\left(\nabla^2 + k^2\right) G\left(\omega, \left|\underline{r} - \underline{r_0}\right|\right) = 0 \qquad \textbf{Eqn. 6.1}$$

where ∇ is the gradient of the vector function;

k is the wave number and is related to the frequency and speed of sound;

$\underline{r_0}$ and $\underline{r}$ are the starting and ending position of the travelling wave respectively;

G is the Green's function with frequency and distance and is the solution to the above equation.

The absolute vector function in Equation (6.1) is replaced by a scalar value R which is the distance between the points. The general solution for three dimensions to Equation (6.1) is that of a spherical spreading function for the wave and is given by:

$$G(\omega,R) = \frac{e^{jkR}}{4\pi R} \qquad \textbf{Eqn. 6.2}$$

Achenback [65] integrated this solution over the full range of the third dimension (in this case, *y*) from negative infinite to positive infinite and derived the two-dimensional expression for cylindrical co-ordinates:

$$G(\omega,R) = \frac{j}{4}H_0^{(1)}(kR) \qquad \textbf{Eqn. 6.3}$$

where $H_0^{(1)}$ is the zero-order Hankel function of the first kind.

The origin of the co-ordinate system is taken as the point where the acoustic axis cuts the surface S_0 and the zero angle was aligned with the acoustic axis. The exact equation for a Hankel function is a complex formula involving an integral of exponential cosh function but can be approximated for kR >> 1 to be:

$$H_0^{(1)}(kR) = \sqrt{\frac{2}{j\pi kR}}\, e^{-jkR} \qquad \textbf{Eqn. 6.4}$$

This approximation was valid for this algorithm as the surface S' is in the farfield for the pressures propagating from surface S_0 making R relatively large compared to k. Substituting Equation (6.4) into Equation (6.3), the approximate formula for the Green's function in two dimensions is:

$$G(\omega,R) = \frac{1}{4}\sqrt{\frac{2j}{\pi kR}}\, e^{-jkR} \qquad \textbf{Eqn. 6.5}$$

According to Equation (65) of Nagai reference [64], the pressure function is then:

$$p_{\infty}(\omega,\theta) = -\int_{S_0} p(x_0)\frac{\partial}{\partial \underline{n}}G(\omega,R)dx_0 \qquad \textbf{Eqn. 6.6}$$

where $\underline{n}$ is the normal vector to the surface S_0 and is the equivalent of the variable R for the partial differentiation.

Differentiating Equation (6.5) with respect to R yields:

$$\frac{\partial}{\partial \underline{n}}G(\omega,R) = -\sqrt{\frac{j}{8\pi kR}}\cos(\underline{n},\underline{r})e^{-jkR}\left[\frac{1}{2R} - jk\right] \qquad \textbf{Eqn. 6.7}$$

For large values of R, Equation (6.7) can be simplified to:

$$\frac{\partial}{\partial \underline{n}}G(\omega,R) = \sqrt{\frac{k}{j8\pi R}}\cos(\theta)e^{-jkR} \qquad \textbf{Eqn. 6.8}$$

where θ is the angle between the normal to the surface S' ($\underline{r}$) and the acoustic axis ($\underline{n}$).

Substituting this expression into Equation (6.6), the pressure profile can be estimated as:

$$p_{\infty}(\omega,\theta) = \sqrt{\frac{k}{j8\pi R}}\cos(\theta)\int_{S_0} e^{-jkR}p(x_0)dx_0 \qquad \textbf{Eqn. 6.9}$$

Equation (6.9) is called the Rayleigh-Sommerfeld diffraction formula and if the assumptions made in this Section are valid, it has been shown to produce the correct pressure profile in the farfield. It can be further simplified in this specific case by assuming that the surface S' is defined by $R\rightarrow\infty$. The beam profile is normalised so that the calculated pressure on the acoustic axis of the transducer, $p_{\infty}(\omega,0)$, is 1.0:

$$\bar{p}_{\infty}(\omega,\theta) = \frac{\sqrt{\frac{k}{j8\pi R}}\cos(\theta)\int_{S_0} p(x_0)e^{-jkR}dx_0}{\sqrt{\frac{k}{j8\pi R}}\,\bar{p}_{\infty}(\omega,0)} \qquad \textbf{Eqn. 6.10}$$

The expression for the complex exponential can be simplified by considering the diagram in Figure 6.6. Only rays that propagate in parallel straight lines from the surface S_0 at an angle of θ will influence the pressure on S' at that angle. Then, the complex exponential depends only on the difference in the length of the ray impinging at different points of the surface. This can be related to the distance along the x-axis from the acoustic axis where the different rays intersect the axis. Using simple Euclidean geometry, the difference in ray length, ΔR, for two rays intersecting the axis at a distance of x_0 can be approximated as:

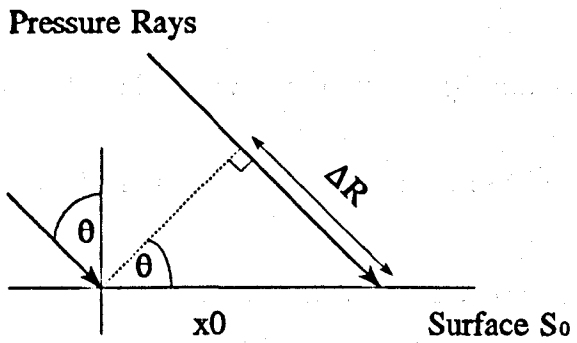

Figure 6.6: Angles Involved with Propagating Pressure Rays

$$\Delta R = x_0 \sin(\theta) \qquad \textbf{Eqn. 6.11}$$

It can be seen that for an angle of 0°, there is no difference in length between the rays, which agrees with the denominator of Equation (6.10). Substituting Equation (6.11) into Equation (6.10) gives:

$$\bar{p}_{\infty}(\omega,\theta) = \frac{\cos(\theta)\int_{S_0} p(x_0)e^{-jk\sin(\theta)x_0}dx_0}{\int_{S_0} p(x_0)dx_0} \qquad \textbf{Eqn. 6.12}$$

6.2.2 Implementation of Beam Profile Algorithm

Equation (6.12) is a continuous equation but the pressure data from the FE model is only available at discrete points along the surface. Hence, the equation needs to be discretised into a form that can be implemented in a computer program:

$$\bar{p}_j(\theta) = \cos(\theta)\frac{\sum_i^N p_i e^{jk_j\sin(\theta)x_i}}{\sum_i^N p_i} \qquad \textbf{Eqn. 6.13}$$

where $\bar{p}_j(\theta)$ is the normalised beam profile at frequency with wavenumber k_j; and

p_i is the pressure at the position $(x_i,0)$ where i varies from 1 to N.

The numerator of Equation (6.13) is of the form of a spatial discrete Fourier transform which can be implemented efficiently with the use of the fast Fourier transform (FFT) algorithm. Thus, the complete implementation of the algorithm has three steps:

A. The discrete pressure function is converted to a ray amplitude function by an FFT routine.

B. The amplitude function is normalised so that the value at an angle of 0° is 1 unit to account for the effect of the denominator.

C. The amplitude function is weighted by the obliquity factor, cos(θ).

All that remains in the algorithm is to convert the discrete spatial frequency series to the equivalent angular series. The spatial frequency difference, ΔF, between sampling frequency points is related to the spatial sampling distance, Δx, by the formula:

$$\Delta F = \frac{1}{N\Delta x} \qquad \textbf{Eqn. 6.14}$$

where N is the number of sample points along the surface.

From Equation (6.13), the angle is related to the spatial frequency through the formula:

$$\begin{aligned} \frac{2\pi F_i}{k_j} &= \sin(\theta_{i,j}) \\ \frac{2\pi i \Delta F}{2\pi/\lambda_j} &= \sin(\theta_{i,j}) \\ \therefore \theta_{i,j} &= \arcsin\left(\frac{ic}{N\Delta x f_j}\right) \end{aligned} \qquad \textbf{Eqn. 6.15}$$

where f_j is the temporal frequency of the signals; and
c is the speed of sound in the fluid.

The assumptions made for the derivation of Equation (6.13) place a requirement on the finite element model that the S_0 in the model must include all the surfaces that produce non-zero pressure wave values on the surface of the transducer. This is especially relevant for array transducers where shear waves propagate along the boundary between the monolithic structure and the surrounding fluid at a faster speed than the waves in the fluid. This phenomena has the effect of increasing the apparent aperture of the element from the size of the electrode and hence, reduces the beamwidth of the element.

The algorithm was initially tested for a piston-like element movement. The sampling distance for the frequency in question was taken as:

- $\Delta x = \lambda/8$ where λ is the wavelength of the propagating wave in the fluid; and
- the number of sample points was taken as: N = 256.

Then, $\lambda\Delta F = 1/32$. The size of the element was set at 1λ which was represented by 8 points of amplitude 1 for the sampling series. The results from the output of the algorithm were compared with those from the theory of Selfridge [63] in Figure 6.7. The equivalent equation from the theory is:

$$\bar{p}_{\infty}(\theta) = \frac{\sin\left(\frac{\pi W}{\lambda}\sin(\theta)\right)}{\frac{\pi W}{\lambda}\sin(\theta)}\cos(\theta) \qquad \textbf{Eqn. 6.16}$$

where W is the width of the element.

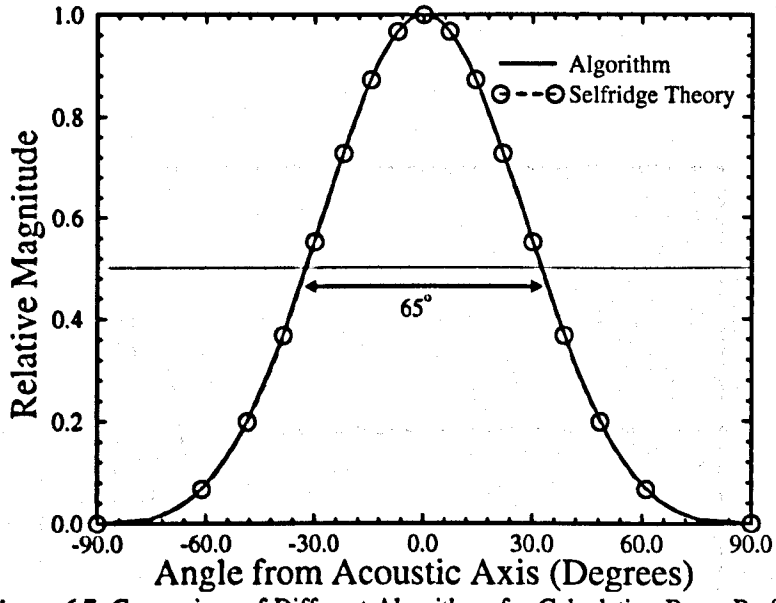

Figure 6.7: Comparison of Different Algorithms for Calculating Beam Profile

It can be seen that the algorithm produced results identical to the theory. From Figure 6.7, the beamwidth of the element can be calculated as 65°. The output of the algorithm was further investigated by modelling a two-dimensional representation of a monolithic slab of 25% VF, 0.2 AR, PZT-5H/hardset composite in water with an electrical resonance of 1.380 MHz. The active electrode covered three ceramic pillars and the polymer filler between them. The pressure generated by pillars away from

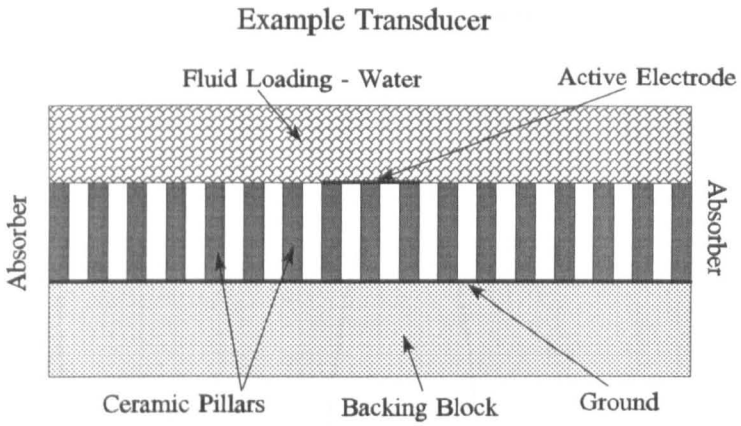

(a) Diagram of Example Transducer

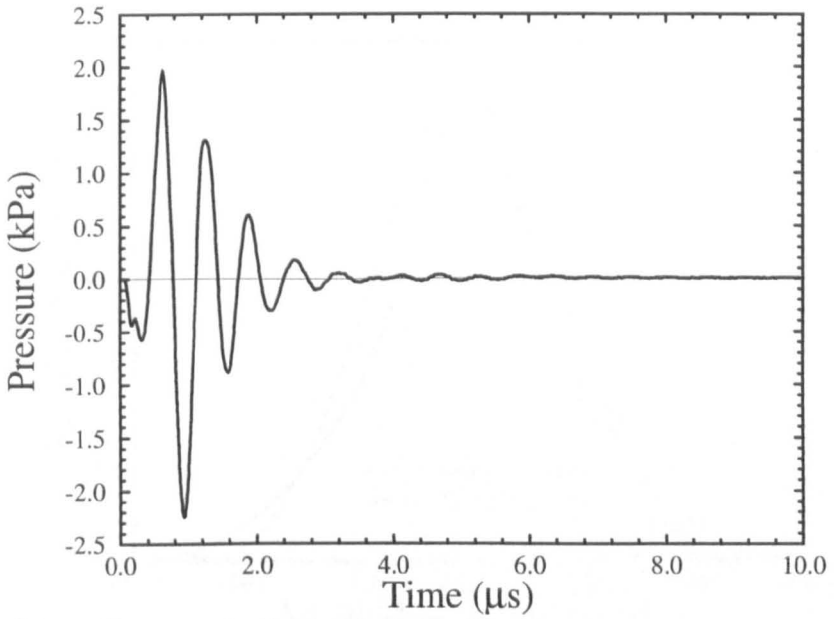

(b) Pressure in front of Electrode

Figure 6.8: Pressure Produced by Example Transducer

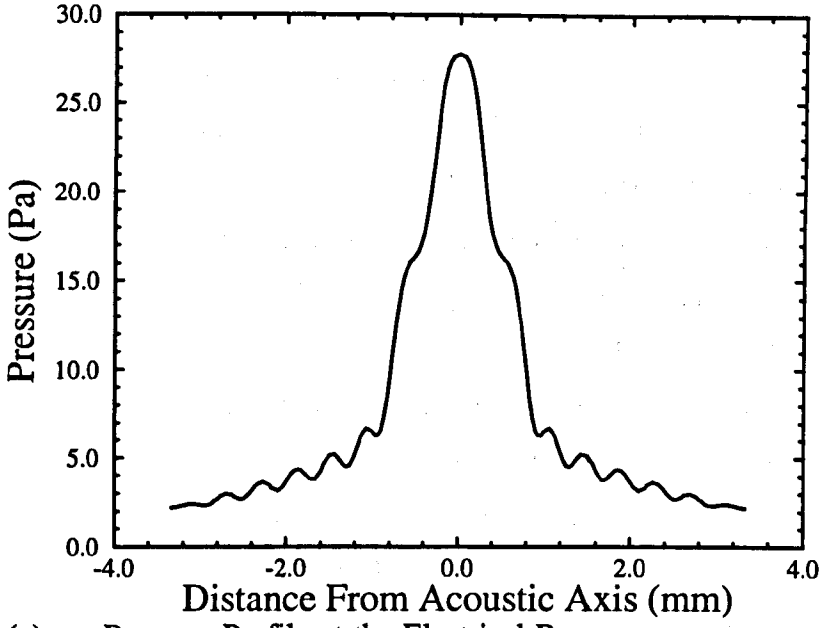

(c) Pressure Profile at the Electrical Resonance

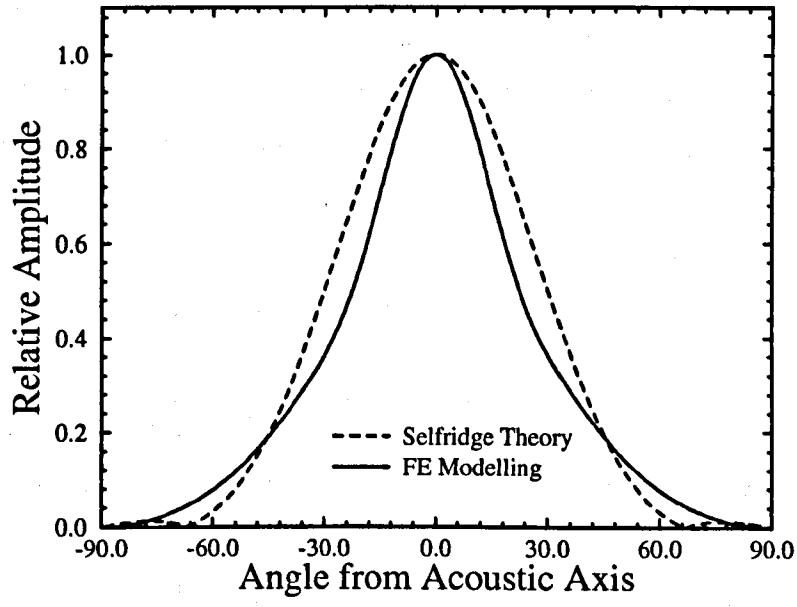

(d) Beam Profile at the Electrical Resonance

Figure 6.8: Pressure Produced by Example Transducer

the electrode was included in the algorithm. The model included no matching layer but did incorporate a backing block of specific acoustic impedance of 4.737 MRayls to reduce the signal ringing time of the device. This value of acoustic impedance is half that of the piezocomposite material. The appearance of the model is shown in Figure 6.8(a). The size of the active electrode is 1.0 mm which at 1.380 MHz, is 1.087 λ. Absorbing boundaries were placed on all four sides to remove any standing waves in the model. A single voltage cycle at the electrical resonance of the device with the backing block was applied to the active electrode of the element and the pressures produced at the surface were passed to the algorithm. The pressure generated at the centre of the surface of the centre pillar is shown in Figure 6.8(b) with time as the abscissa. The pressure profile across the equivalent surface S_0 for the electrical resonance frequency is displayed in Figure 6.8(c). The beam profile at this frequency was generated from the above algorithm and is in Figure 6.8(d) where the beamwidth for the array element can be seen to be 55°. The beam profile assuming that the centre pillar transmitted as a piston with no cross-coupling, is also shown in Figure 6.8(d) and is named *Selfridge Theory*. It can be seen from Figure 6.8(c) that the response was similar to that of a piston above the electrode but pressure is generated away from the electrode by the waves travelling through the composite material and through the backing block. This resulted in a smaller beamwidth than a piston with the same length as the electrode.

6.2.3 Verification of Array Model

The finite element model for different sized array elements was analysed and compared to an experimental configuration. The piezocomposite transducer consisted of PZT-5H and hardset with the geometric parameters of 40% volume fraction, 0.3 aspect ratio and height of 3.41 mm. The material parameters for the ceramic phase in the model were adjusted to match those of the experiment. Four elements of 2x2, 3x3, 4x4 and 5x5 pillars were created at different positions on the piezocomposite plate as shown in Figure 6.10. Figure 6.9(a), (b), (c) and (d) show the electrical impedance trace for the four different configurations. The damping co-efficients used

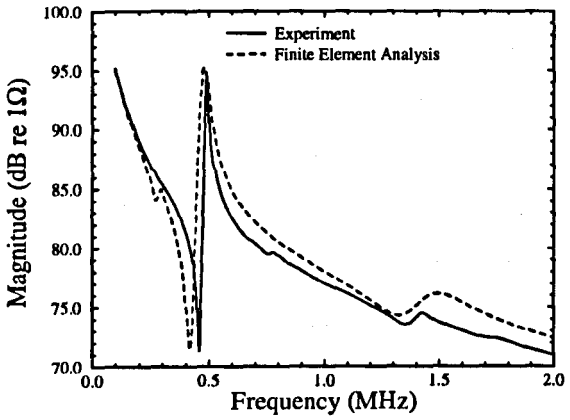

(a) 2x2 Pillars Under the Electrode

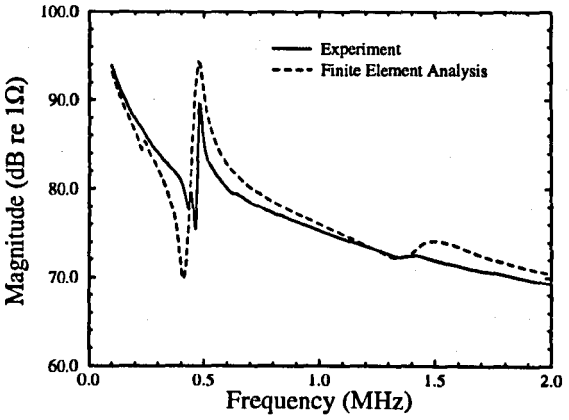

(b) 3x3 Pillars Under the Electrode

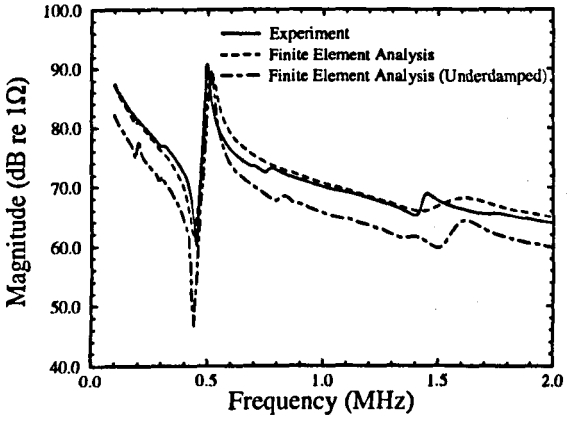

(c) 4x4 Pillars Under the Electrode

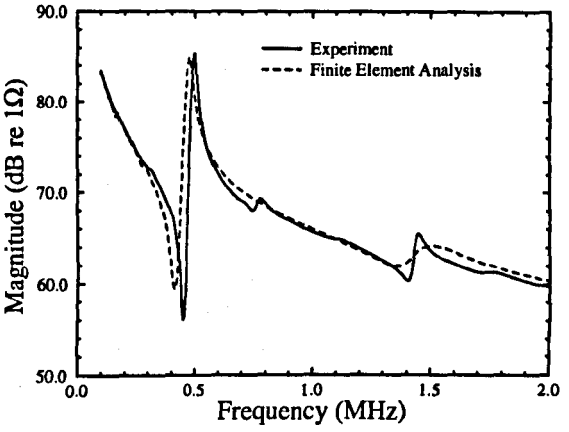

(d) 5x5 Pillars Under the Electrode

Figure 6.9: Impedance Profile of Different Sized Array Element

for the model become very important in that there are now significant lateral modes excited by the laterally varying electric field. This set of figures show that the finite element model produces a reasonable fit for the electrical impedance to the experimental device and can be used to compare different two-dimensional configurations for 1-3 piezocomposites. Several of the lateral modes in the experimental data did not appear in the finite element response because of too high damping of the shear modes in the polymer. The ANSYS package allows only a single damping co-efficient and this is normally set to the longitudinal value. This value is normally larger than the shear value because for longitudinal modes, the polymer acts as a damper rather than a medium in which the mode is sustained as with the shear modes. The effect of reducing the damping co-efficient is illustrated in Figure 6.9(c) where an extra curve is included for the results from an underdamped finite element model. The impedance of the curve has been decreased by 5 dB deliberately to separate it from the other curves so that the features can be seen. The lateral modes are now present in the results from the finite element model.

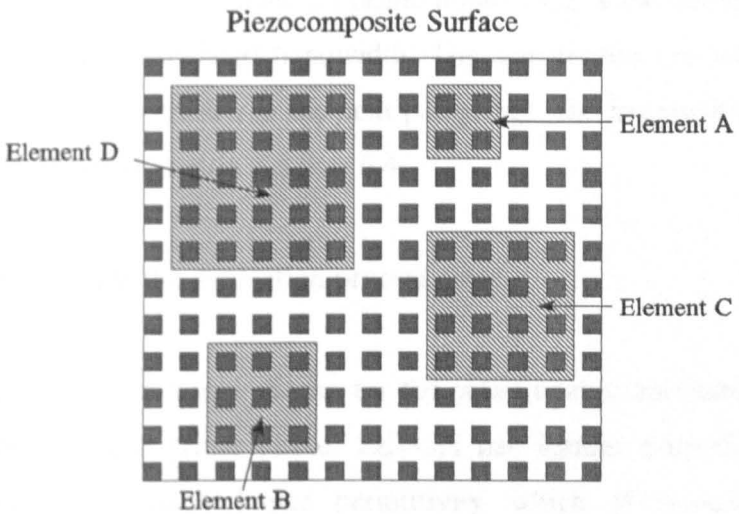

Figure 6.10: Electrode Pattern for Experimental Transducer

Initial analysis can be performed using modal analysis on the multi-pillar finite element models developed from the ANSYS package. However the value of this process would be limited as mode coupling can be incorporated with the finite element model. Hence, this analysis was not performed but a similar investigation has been reported upon in Hall [41]. The results indicated that the minimum number of pillars under the electrode for this configuration is 3x3 in order to obtain a sufficiently large coupling factor. Hall introduced a safety factor and selected the size of the electrode to be 4x4.

6.3.1 Evaluation of Array Element Performance

The application of finite element analysis to the modelling of array transducers allows the designer to select the output integrated parameters with which to evaluate the performance of the array elements. Of prime importance is the transmit and receive sensitivity with their associated bandwidth. The sensitivities are tabulated for the different configurations chosen in the next paragraph. The beamwidths for different configurations are discussed in Section 6.4.

The configurations for the evaluation process were:

- **Material**: PZT-5H was chosen for the piezoceramic and hardset epoxy was chosen as the polymer phase. PZT-5H has similar properties to PZT-5A except for a much larger permittivity which is important for array applications.
- **Volume Fraction**: Several values were chosen for the simulation set:
  - 20% for receiver applications; and
  - 30%, 35% and 40% for pulse-echo applications.
- **Aspect Ratio**: three aspect ratios were chosen for each volume fraction: one below, one at and one above the maximum pillar aspect ratio.

These are:

For 20% VF : 0.14, 0.17 and 0.20

For 30% VF : 0.20, 0.23 and 0.26

For 35% VF : 0.24, 0.27 and 0.30

For 40% VF : 0.28, 0.31 and 0.34

- **Backing Block** - the acoustic impedance of the backing block was selected to be half that of the active material.
- **Matching Layer** - the optimal material as defined in Chapter 2 was used as the matching layer for the simulations.
- **Number of Pillars under the Electrode**: the number was varied from 2x2 to 5x5 which is the maximum size that could be modelled with the ANSYS package with the academic licence. The electrode size of 1x1 was not simulated as it was found experimentally before this analysis that this pattern did not produce a good response. The response for an electrode covering the full surface of the transducer is also included as a base for comparison.
- **Number of Pillars between the Electrode**: for all the configurations, the number of pillars was kept at one.

		Transmit Sensitivity					Receive Sensitivity				
VF	AR	Full	2x2	3x3	4x4	5x5	Full	2x2	3x3	4x4	5x5
20	0.14	144	140	140	141	141	-164	-168	-168	-166	-166
20	0.17	144	139	141	141	142	-164	-169	-168	-167	-166
20	0.20	144	140	142	142	143	-165	-169	-168	-167	-167
30	0.20	147	141	144	144	145	-164	-169	-168	-167	-167
30	0.23	147	143	145	145	145	-164	-169	-168	-167	-167
30	0.26	147	144	146	146	147	-165	-168	-167	-167	-167
35	0.24	148	143	145	146	147	-164	-169	-167	-167	-166
35	0.27	148	144	146	147	148	-165	-168	-167	-166	-166
35	0.30	148	146	147	147	148	-165	-167	-167	-166	-166
40	0.28	149	145	147	147	148	-164	-168	-167	-167	-166
40	0.31	149	146	148	148	149	-165	-168	-167	-166	-166
40	0.34	149	147	148	149	148	-165	-167	-167	-166	-166
		Transmit Bandwidth					Receive Bandwidth				
20	0.14	14	23	32	17	21	13	16	14	14	14
20	0.17	14	35	17	19	17	15	24	19	17	16
20	0.20	14	19	15	16	15	17	28	24	22	21
30	0.20	12	31	16	17	16	10	15	15	14	13
30	0.23	12	17	14	15	14	11	19	16	15	14
30	0.26	12	14	12	12	12	12	18	15	15	14
35	0.24	11	17	15	15	13	9	12	11	10	10
35	0.27	11	16	12	12	11	10	14	12	11	11
35	0.30	11	13	11	11	11	10	13	12	11	11
40	0.28	10	15	14	13	12	8	12	11	10	10
40	0.31	10	14	12	11	10	8	13	11	10	10
40	0.34	10	12	10	10	11	9	12	11	10	10

Table 6.1: Results for In-Air Analysis with No Components

		Transmit Sensitivity					Receive Sensitivity				
VF	AR	Full	2x2	3x3	4x4	5x5	Full	2x2	3x3	4x4	5x5
20	0.14	121	123	122	123	123	-185	-185	-185	-185	-184
20	0.17	121	123	123	123	124	-185	-185	-185	-184	-184
20	0.20	121	123	124	124	124	-185	-184	-184	-184	-184
30	0.20	123	125	125	126	126	-187	-187	-186	-185	-185
30	0.23	123	125	126	126	126	-187	-186	-185	-185	-185
30	0.26	123	126	127	127	127	-187	-185	-185	-184	-185
35	0.24	124	126	127	127	127	-188	-187	-186	-186	-185
35	0.27	124	126	127	127	128	-188	-186	-185	-185	-185
35	0.30	124	127	128	128	128	-188	-185	-185	-185	-185
40	0.28	125	127	128	128	128	-188	-186	-186	-186	-186
40	0.31	125	127	128	128	128	-188	-186	-185	-185	-185
40	0.34	125	128	128	128	128	-188	-185	-185	-185	-185
		Transmit Bandwidth					Receive Bandwidth				
20	0.14	56	38	52	39	38	58	48	58	40	39
20	0.17	59	58	40	41	40	60	58	44	43	43
20	0.20	65	54	39	41	38	64	38	40	41	42
30	0.20	50	47	32	33	33	48	40	33	32	31
30	0.23	50	45	30	32	31	48	31	31	31	30
30	0.26	51	32	30	31	30	49	28	28	29	29
35	0.24	47	43	28	31	30	44	30	28	27	27
35	0.27	47	31	28	29	28	45	26	26	26	26
35	0.30	48	28	28	28	28	45	24	25	25	25
40	0.28	44	32	27	28	27	40	25	24	24	24
40	0.31	45	27	26	27	27	41	23	23	22	23
40	0.34	45	26	26	27	27	41	21	22	22	22

Table 6.2: Results for In-Air Analysis with Backing Block

		Transmit Sensitivity					Receive Sensitivity				
VF	AR	Full	2x2	3x3	4x4	5x5	Full	2x2	3x3	4x4	5x5
20	0.14	147	155	157	159	157	-163	-152	-153	-150	-148
20	0.17	147	154	156	158	158	-163	-155	-152	-150	-149
20	0.20	146	159	158	158	158	-164	-153	-149	-147	-148
30	0.20	150	159	160	161	161	-164	-153	-149	-151	-151
30	0.23	150	159	161	160	161	-164	-152	-154	-152	-153
30	0.26	150	161	161	162	161	-165	-152	-155	-153	-153
35	0.24	151	156	161	162	161	-165	-155	-149	-149	-150
35	0.27	151	164	164	164	162	-165	-152	-150	-150	-152
35	0.30	151	160	161	162	165	-165	-151	-151	-150	-151
40	0.28	152	160	165	164	163	-165	-154	-149	-147	-148
40	0.31	152	165	164	164	163	-165	-150	-151	-151	-152
40	0.34	152	165	163	161	162	-165	-153	-155	-153	-151
		Transmit Bandwidth					Receive Bandwidth				
20	0.14	19	8	7	8	11	24	5	17	8	5
20	0.17	19	12	12	10	11	26	12	8	5	7
20	0.20	20	8	11	12	11	29	23	6	4	5
30	0.20	16	9	7	11	10	19	9	5	13	8
30	0.23	16	11	10	13	10	20	15	11	12	6
30	0.26	16	7	10	10	10	21	6	35	16	13
35	0.24	15	29	10	10	11	17	7	5	5	6
35	0.27	15	6	9	9	12	19	5	9	5	9
35	0.30	16	11	13	10	5	20	9	8	7	7
40	0.28	15	12	6	9	9	15	10	5	4	5
40	0.31	14	5	9	9	10	16	4	7	8	8
40	0.34	14	7	10	14	11	16	15	17	9	10

Table 6.3: Results for In-Air Analysis with Matching Layer

		Transmit Sensitivity					Receive Sensitivity				
VF	AR	Full	2x2	3x3	4x4	5x5	Full	2x2	3x3	4x4	5x5
20	0.14	201	178	178	174	172	-176	-195	-195	-197	-199
20	0.17	202	179	176	172	171	-176	-197	-198	-200	-201
20	0.20	203	177	174	172	170	-176	-200	-202	-204	-206
30	0.20	205	180	177	174	172	-175	-195	-196	-197	-199
30	0.23	206	178	174	171	170	-175	-197	-199	-201	-202
30	0.26	207	176	173	170	168	-175	-201	-204	-206	-207
35	0.24	207	178	175	173	171	-176	-196	-197	-199	-200
35	0.27	207	176	172	170	168	-175	-199	-201	-203	-205
35	0.30	208	174	171	169	167	-175	-205	-207	-209	-211
40	0.28	208	176	173	170	169	-175	-198	-200	-201	-203
40	0.31	208	173	170	168	166	-175	-202	-204	-206	-208
40	0.34	209	172	169	167	165	-175	-209	-211	-213	-215
		Transmit Bandwidth					Receive Bandwidth				
20	0.14	15	33	38	43	40	16	16	16	14	13
20	0.17	15	31	33	35	35	18	16	14	13	12
20	0.20	16	24	27	25	26	21	14	13	13	12
30	0.20	14	31	32	32	33	12	12	10	10	9
30	0.23	13	33	37	38	37	13	10	9	9	9
30	0.26	13	27	27	18	18	15	10	10	9	9
35	0.24	14	29	31	31	18	13	9	8	8	6
35	0.27	13	32	36	36	36	14	7	7	7	7
35	0.30	13	17	14	13	13	15	10	9	8	8
40	0.28	14	29	16	16	16	12	8	7	7	5
40	0.31	14	33	16	15	14	13	6	6	6	6
40	0.34	13	14	11	10	11	14	11	8	8	8

Table 6.4: Results for In-Water Analysis with No Ancillary Components

			One Pillar Spacing				Two Pillar Spacing				Diced Elements			
VF	AR	Full	2x2	3x3	4x4	5x5	2x2	3x3	4x4	5x5	2x2	3x3	4x4	5x5
20%	0.14	0.990	0.803	0.860	0.852	0.868	0.856	0.866	0.890	0.851	0.916	0.823	0.874	0.832
20%	0.17	0.979	0.835	0.816	0.877	0.842	0.830	0.913	0.887	0.882	0.907	0.808	0.855	0.808
20%	0.20	0.978	0.801	0.824	0.844	0.839	0.851	0.877	0.865	0.868	0.912	0.787	0.839	0.818
30%	0.20	0.984	0.877	0.870	0.904	0.898	0.900	0.921	0.914	0.913	0.929	0.856	0.900	0.867
30%	0.23	0.986	0.857	0.879	0.889	0.881	0.898	0.912	0.896	0.905	0.926	0.841	0.887	0.853
30%	0.26	0.974	0.843	0.885	0.856	0.865	0.914	0.887	0.890	0.896	0.926	0.831	0.880	0.853
35%	0.24	0.987	0.880	0.881	0.890	0.887	0.910	0.924	0.911	0.915	0.935	0.869	0.908	0.878
35%	0.27	0.982	0.872	0.883	0.883	0.877	0.923	0.913	0.906	0.912	0.933	0.858	0.899	0.877
35%	0.30	0.976	0.854	0.886	0.870	0.885	0.908	0.891	0.880	0.885	0.943	0.848	0.894	0.890
40%	0.28	0.988	0.911	0.910	0.910	0.909	0.929	0.930	0.922	0.927	0.941	0.883	0.917	0.891
40%	0.31	0.979	0.894	0.892	0.885	0.885	0.918	0.906	0.899	0.904	0.939	0.873	0.914	0.882
40%	0.34	0.977	0.872	0.893	0.889	0.891	0.918	0.893	0.881	0.896	0.947	0.874	0.912	0.882

Table 6.5: Dilation Qualities of Different In-Air Analyses

6.3.2 In-Air Analysis with No Ancillary Components

This analysis was performed to evaluate the performance of the active material in isolation of any other component of the transducer. The results are given in Table 6.1. It can be seen that the sensitivities of the array elements were slightly reduced compared to that of the full electrode. The transmit sensitivity for the full electrode case varied from 144 dB at 20% VF to 149 dB at 40% VF. For the 20% VF array elements, the sensitivity ranged from 139 dB for 2x2 pillars at 0.17 AR to 143 dB for 5x5 pillars at 0.20 AR. For the 40% VF array elements, the sensitivity ranged from 145 dB for 2x2 pillars at 0.28 AR to 149 dB for 5x5 pillars at 0.31 AR. The receive sensitivity for the full electrode case varied from -164 dB at 20% VF to -165 dB at 40% VF. For the 20% VF array elements, the sensitivity ranged from -169 dB for 2x2 pillars at 0.17 AR to -166 dB for 5x5 pillars at 0.20 AR. For the 40% VF array elements, the sensitivity ranged from -168 dB for 2x2 pillars at 0.28 AR to -166 dB for 5x5 pillars at 0.31 AR. The larger sized elements and larger volume fractions were more sensitive for the transmit case. This is probably because the damping effect of the unelectroded pillars between the elements would be strongest for the smallest elements. The aspect ratio did not have a significant effect on the response and the receive sensitivities did not vary by a large amount over the range. The bandwidths for the element transducers exceeded that of the full electrode and the bandwidth decreased with increasing size of element. All the bandwidths decreased with volume fraction. The percentage fractional transmit bandwidth for the full electrode configuration ranged between 10% and 14% while the receive bandwidth ranged from 8% to 17%. However, in general, the receive bandwidth was slightly less than for the transmit bandwidth of the same transducer. The range for the electroded elements was much greater: 35% for a 20% VF transmit case to 10% for a 40% VF case. In summary, the elements should have at least 4x4 pillars under the electrode to obtain a good response. There is only a small advantage to be gained from increasing the element to 5x5 pillars.

6.3.3 In-Air Analysis with Backing Block

This analysis was performed to evaluate the effect of the addition of the backing block on performance of the active material. The results are given in Table 6.2. It can be seen that the addition of the backing block reduced the sensitivity of the full electrode configurations and all the elements. The sensitivities of the full electrode configurations decreased by approximately 20 dB for both the transmit and receive case. However, the sensitivities of the electrode elements exceeded that of the full electrodes by approximately 3 dB. This shows that the effect of the backing block was reduced for the limited size elements. This theory is supported by reduced bandwidths for the limited size elements compared to those for the full electrode configurations. The bandwidths are increased compared to the unbacked case. The range for the transmit bandwidth of the full electrode configurations is from 65% for the 20% VF case to the 44% for the 40% VF case. The receive bandwidths varied from 64% for the 20% VF to the 40% for the 40% VF case. For the limited sized electrodes, the transmit bandwidth varies from 26% to 58% and the receive bandwidth varies from 21% to 58%. However, the effect of the enhanced lateral modes caused by the finite size of the electrode on the results can be observed in the seemingly random values for the bandwidths. This is demonstrated by the receive frequency response for the transducers of the 20% VF 0.20 AR configuration shown in Figure 6.11. As the element size is made larger, the response approaches that of the full electrode which can be consider optimal in this case. The conclusion from the analysis is that the values for the 5x5 pillar element and for several of the 4x4 pillar elements are similar to that of the full electrode. The results indicated that at least a 4x4 pillar element if not a 5x5 pillar element should be chosen for minimal lateral mode activity.

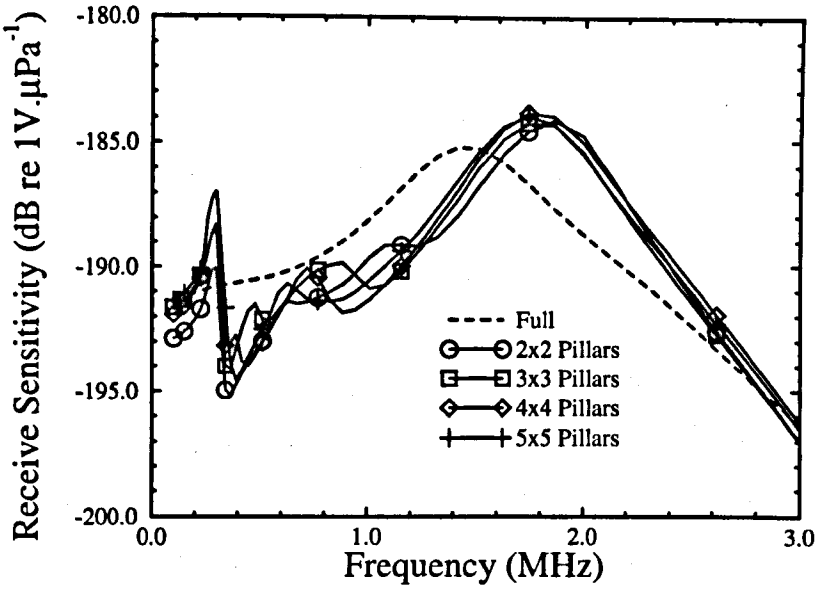

Figure 6.11: Receive Sensitivity for 20% VF 0.2 AR PZT-5H/Hardset Composites with Backing

6.3.4 In-Air Analysis with Matching Layer

This analysis was to evaluate the performance of the active material when it is matched to the surrounding medium. The results are given in Table 6.3. It can be seen that the addition of the matching layer increased the sensitivity and bandwidth of the full electrode configurations and of all the different elements. While the increase in transmit and receive sensitivities were approximately 3 dB and 0 dB respectively for the fully electroded devices, the transmit and receive sensitivities for the finite sized elements was approximately 15 dB and 16 dB respectively. These results support the conclusion made in the previous Section that the preferred choice for the number of pillars under the electrode is 4x4. The response is similar to that of the 5x5 configurations but is superior to that of the 2x2 and 3x3 configurations. The influence of the lateral modes in the matching layers is evidenced by the different values for the bandwidths of similar configurations. However, in general, the bandwidths were slightly (1%-2%) greater than for the unmatched cases. The range for the limited size elements was: 5% to 29% occurring for different 35% VF configurations for the transmit bandwidth and 5% to 35% for the receive bandwidth occurring for different 30% VF configurations.

6.3.5 In-Water Analysis with No Ancillary Components

This analysis was performed to evaluate the performance of the active material incorporating the influence of fluid loading. The results of the analysis are given in Table 6.4. It can be seen that while the receive sensitivity is similar to that for the configurations into air for the full electrode, the transmit sensitivity is vastly increased because of the better acoustic matching between the piezocomposite material and the water medium. However, the sensitivities of the array elements is dramatically reduced compared to that of the full electrode. Also the transmit bandwidths are increased by the water loading. It is not known whether this is a feature of the inexact implementation of the fluid loading. However, it could be caused by the fact that the force produced by the array elements compared to the full electrode is small because of the smaller surface area of the transmitting surface. Interestingly, the smaller elements were more sensitive than the large elements. This would result from a reduced displacement at the surface and hence, a reduced sensitivity. The transmit and receive sensitivities for the fully electroded configurations were from 201 dB to 209 dB and from -175 dB to -176 dB respectively. In comparison, the transmit and receive sensitivities for the finite sized elements covered a much larger range and were from 165 dB to 180 dB and from -195 dB to -215 dB respectively. The receive bandwidths were similar between the two types of electrodes and similar to those produced for the in-vacuum scenario.

6.3.6 Effect of Increased Spacing between Elements

The simulations discussed in the previous Sections were been performed with a single row of pillars between the elements. In practice, this would lead to relatively large cross-coupling between the elements. The coupling can be decreased by increasing the space between the elements by adding an additional row of pillars. It was found that there was little gain in transmit sensitivity and in the bandwidths compared to the equivalent single pillar scenario. However, the receive sensitivity has been reduced compared to the configurations with narrower spacing. Examining the

sensitivity with frequency response for the configurations with different spacing, it was found that the coupling between the thickness mode and the first lateral mode was stronger for the closely spaced elements. The combined mode produced a better receive sensitivity and a wider band than the weakly coupled modes. However, the disadvantage with the strongly coupled lateral mode is the reduction in the dilation quality which can be seen in Table 6.5. This indicates that the increased spacing would improve the beamwidth of the element.

6.3.7 Effect of Dicing the Elements

Another technique for reducing the cross-coupling and increasing the dilation quality is to dice the transducer elements or remove the space between the elements. The diced air-gap between the elements can be simulated by placing a stress-free boundary on the sides of the finite element model. The surface dilation qualities for the in-air analysis of diced array elements with no additional components are shown in Table 6.5. It can be seen that this technique did not decrease the receive sensitivity as did the technique of widening the inter-element spacing. For most configurations, the dilation qualities were found to be similar to those produced by the previous set of simulations. However, for the 2x2 pillar elements, the dilation quality of the diced element was significantly larger than with either previous case. The thickness mode coupling factors were also examined and it was found that the coupling factors for the diced elements were larger than for the other two cases. This indicates that the preferred method of enhancing the performance of the array elements is dicing the space between the elements.

6.4 INVESTIGATION USING THE PZ-Flex PACKAGE

The composite material used for the investigation was the 35% VF PZT-5H/hardset configuration which was found to be optimal for pulse-echo applications [66]. Different parameters were varied for a 1.00 mm thick transducer operating in a fluid medium. The resultant beamwidths were calculated according to the algorithm

derived in Section 6.2.2 and the results are tabulated in Table 6.6 for the in-water analysis and Table 6.7 contains a comparison with diced elements operating into the water and undiced elements operating for into an air medium. An electrode was placed on the second neighbouring pillar from the active electrode. The peak-to-peak voltage at this pillar was taken as the measure of the energy contained in the pressure waves travelling through the composite material allowing for an inter-element spacing of one ceramic pillar. The voltages generated at the extra electrode are given in Table 6.8 for in-water analysis as the ratio of the peak-to-peak generated voltage to the peak-to-peak input voltage expressed in decibels. Due to the nature of the fully diced element model (zero-stress boundaries on the sides of the elements), no cross-coupling voltage was produced for the diced element simulations. The analysis was performed for electrode size varying from 2 pillars to 5 pillars. The parameters that were varied, are:

A. The aspect ratio was varied from 0.1 to 0.5 in steps of 0.1.

B. For the aspect ratio set of 0.24, 0.27 and 0.30

- No ancillary components
- Backing block as used in Section 6.3.3.
- Matching layer as used in Section 6.3.4 in conjunction with the backing block.

This is not a conclusive study but was performed to indicate what parameters are important to the array designer. A complete study was not performed because the optimal array element is determined by the specific application for which the array will be used. Thus the designer should do specific simulations for the final design.

AR	2 Pillars	3 Pillars	4 Pillars	5 Pillars
0.10	50°	50°	67°	72°
0.20	35°	35°	29°	29°
0.30	23°	19°	18°	17°
0.40	14°	13°	12°	11°
0.50	13°	12°	11°	10°
No Ancillary Components				
0.24	33°	23°	24°	21°
0.27	54°	21°	24°	19°
0.30	23°	19°	18°	17°
Backing Block Analysis				
0.24	58°	35°	32°	27°
0.27	47°	30°	28°	23°
0.30	39°	27°	24°	21°
Backing Block and Matching Layer				
0.24	65°	47°	37°	31°
0.27	56°	40°	32°	27°
0.30	56°	37°	30°	25°

Table 6.6: Beamwidth of Elements for Different Configurations

AR	2 Pillars	3 Pillars	4 Pillars	5 Pillars
In-Water Undiced Elements				
0.24	33°	23°	24°	19°
0.27	54°	21°	24°	19°
0.30	23°	19°	18°	17°
In-Water Diced Elements				
0.24	87°	61°	45°	36°
0.27	81°	55°	41°	32°
0.30	75°	50°	37°	29°
In-Air Undiced Elements				
0.24	17°	12°	9°	7°
0.27	15°	10°	8°	7°
0.30	14°	9°	7°	6°

Table 6.7: Beamwidth of Elements for the Comparison

AR	2 Pillars	3 Pillars	4 Pillars	5 Pillars
0.10	-18 dB	-17 dB	-18 dB	-19 dB
0.20	-21 dB	-22 dB	-22 dB	-22 dB
0.30	-25 dB	-26 dB	-27 dB	-27 dB
0.40	-26 dB	-27 dB	-27 dB	-27 dB
0.50	-27 dB	-28 dB	-28 dB	-28 dB
No Ancillary Components				
0.24	-24 dB	-24 dB	-24 dB	-25 dB
0.27	-26 dB	-26 dB	-27 dB	-27 dB
0.30	-25 dB	-26 dB	-27 dB	-27 dB
Backing Block Analysis				
0.24	-25 dB	-26 dB	-27 dB	-27 dB
0.27	-29 dB	-30 dB	-31 dB	-31 dB
0.30	-26 dB	-27 dB	-28 dB	-28 dB
Backing Block and Matching Layer				
0.24	-27 dB	-29 dB	-29 dB	-29 dB
0.27	-31 dB	-31 dB	-32 dB	-33 dB
0.30	-27 dB	-28 dB	-29 dB	-29 dB

Table 6.8: Cross-Coupling Voltage for Different Configurations in Water

6.4.1 Influence on Beamwidth

The beamwidths in Table 6.6 decrease with both aspect ratio and number of pillars. This is because the beamwidth is inversely proportional to the size of the aperture according to Equation (6.16). However, the beamwidths for the 5 pillar elements are similar to those of the 4 element for most aspect ratios. No attempt was made to normalise the beamwidth to the size of the array element because the height and the volume fraction of the piezocomposite are determined by the application. The remaining design parameter for the material is then the aspect ratio. Hence, the requirement of large beamwidth encourages the designer to use small aspect ratio and a smaller sized aperture for the element for a set height. This is especially true for aspect ratios around the MPAR of the configuration where it can be seen that the beamwidth changes from 33° to 23° for a change in aspect ratio from 0.24 to 0.30 for 2 pillar element. The large beamwidth (54°) for the in-water operation of 2 pillars at 0.24 AR is due to the amplitude of the sidelobes approaching that of the main lobe. The addition of the backing block and the matching layer increased the beamwidth as the internal reverberations of the singal is reduced. An interesting point is that the addition of the matching layer reduces the influence of the aspect ratio. Table 6.7 shows a comparison between different forms of the array elements. It can be seen that dicing the elements increased the beamwidth as was expected from Table 6.5. For the 2 pillar 0.24 AR example mentioned earlier, the beamwidth have increased from 33° to 87°. Also, operating the elements into an air medium as compared to a water medium decreases the beamwidth to 17° because of the reduced wavelength in air.

6.4.2 Influence on Cross-Coupling Voltage

The results in Table 6.8 show that while the cross-coupling decreases with aspect ratio, it is independent of the size of the element. It was mentioned in the previous Section that the height and volume fraction was kept constant between simulations. Hence, the electrodes of different elements are close together for smaller aspect ratios

and the cross-coupling would be larger. When a backing block and a matching layer are added to the transducer, extra cross-coupling channels are included in the system. However, the damp nature would make the channel through the backing block attenuative as well as reducing the overall energy contained within the system. Hence, the backing block did not have a large effect on the values for the cross-coupling. The cross-coupling for the 0.24 AR 2 pillar configuration was modified from -24 dB for the unbacked case to -25 dB for the backed case. The matching layer was not as attenuative but would have a good match with the surrounding medium. This is shown in the slight decrease in the cross-coupling voltage of approximately 2 dB across the range. The cross-coupling for the 0.24 AR 2 pillar configuration with matching layer and backing block was -27 dB.

6.5 CONCLUDING REMARKS

This Chapter has covered the development of different finite element models for characterisation of two-dimensional ultrasonic arrays. They were used to investigate the design of electrode patterns for low volume fraction piezocomposites. The parameters used to compare the different configurations were:

- Transmit and receive sensitivities with their associated bandwidths; and
- Beamwidth of the transmitting element.

The algorithms for generating the former quantities were presented in Chapter 3 but the algorithm for the latter quantity was derived in this Chapter. Part of the derivation involved determining the requirements for the model such as the model must include all vibrating surfaces including the those a distance away from the active electrode.

It was found from the simulations that the number of pillars under the electrode should be at least 4x4. The addition of the backing block and the matching layer did not have such a dramatic effect on the finite sized elements as it did for the full electrode configurations. The water loading on the element was found to increase the

transmit bandwidth but it was not known whether this is due to the inexact implementation of the fluid loading. Also the smaller elements were more sensitive than the larger elements.

Two techniques for increasing the dilation quality were considered: increasing the inter-element spacing; and dicing between the elements. It was found that although increasing the inter-element spacing increased the dilation quality, it decreased the sensitivity of the element. Dicing the element produced similar dilation qualities to the previous method but not at the expense of element sensitivity.

The PZ-Flex package was used to determine the influence of different parameters on the beamwidth and cross-coupling voltage. For a constant volume fraction and height for the piezocomposite material, the aspect ratio should be chosen to be less than the maximum pillar aspect ratio to obtain a large beamwidth. The addition of the ancillary components increased the angle but only by a small amount compared to varying the aspect ratio. However, the matching layer did reduce the sensitivity of the beamwidth to the aspect ratio. While the cross-coupling decreased with aspect ratio, it was independent of element size (number of pillars under the electrode). The addition of the backing block and matching layer decreased the cross-coupling by approximately 1 dB and 2 dB respectively.

CHAPTER SEVEN

CONCLUSIONS AND SUGGESTIONS FOR FUTURE WORK

CHAPTER OBJECTIVE

The aim of this chapter is to review the objectives and findings of the work presented in the thesis and to make recommendations for future work. In chapter 1, the problem statement and the concepts that would be used to overcome the problem were defined. This included specifying the contributions made by this thesis to the field of ultrasonic transducer modelling. The background to the problem was covered in chapter 2 and included a discussion on the properties for piezoelectric and viscoelastic materials, constrained-dimensional modelling and ancillary components used to modify the response of piezoelectric transducers. The finite element model for 1-3 piezocomposite was developed in chapter 3 in conjunction with the integrated parameters that were used to evaluate the different designs investigated in chapter 4. The finite element modelling system was then used for the development of a system for hydrophone design in chapter 5 and for high-frequency array transducer design in chapter 6.

7.1 MAIN FINDINGS

The principal new findings of the work were:

- A set of finite element models for 1-3 piezocomposite transducers including the backing block, matching layer and fluid loading under operational conditions were developed. These were used to generate a set of design guidelines for 1-3 piezocomposite transducers.

- The main design guidelines were:
  - To obtain an undistorted thickness mode oscillation from a piezocomposite transducer, the aspect ratio of the material must be less than the "*Maximum Pillar Aspect Ratio*" (MPAR). Tables for the MPAR of different PZT-5A piezocomposite are given in Chapter 4.
  - The volume fraction for devices to be used as transmitters should be greater than or equal to 30%. The volume fraction for receivers should be between 20% and 70%. Considering the combined transmit/receive levels, the volume fraction for transceivers should be between 30% and 70%. If large bandwidth is important, the transceiver volume fraction should not be greater than 40%.
  - Low volume (<10%) fraction composites of PZT-5H make good hydrophones but the performance can be enhanced by the addition of cover plates. The aspect ratio of the ceramic pillars should be minimised and the polymer phase should be compliant and possess the minimum Poisson ratio.
  - The number of pillars under the electrode for an array element should be at least 4x4 pillars to obtain good sensitivity and sufficient dilation quality.

- For a piezocomposite with a high loss polymer, the material does not act as a homogeneous medium but as a set of ceramic pillars in a dense medium. However, the effect of the high damping is reduced by the addition of a backing block and a matching layer.

7.2 CONCLUSIONS FROM EACH CHAPTER

It was shown in Chapter 2 that the features required for the finite element model for the analysis of 1-3 piezocomposite transducers were:

- *Model Components* - the finite element model must include the effect of the microstructure geometry on 1-3 piezocomposites and should not model the material as homogenous as in the case of the constrained-dimensional models.
- *Integrated Parameters* - the finite element model must be defined in such a manner that the post-processing analysis produces individual measures of performance.
- *Array Characterisation* - the finite element model for the array transducer must also include the ability to estimate the crosstalk between neighbouring elements and the beam profile of an element.

The finite element model for 1-3 piezocomposites was developed in Chapter 3 with the above considerations in mind. For efficient thickness mode operation, the thickness mode must be sufficiently separated from the first lateral mode. It was concluded that the maximum pillar aspect ratio (MPAR) was the maximum aspect ratio for which:

- $Q_{dil} > 0.9$
- $f_{L1} > 2f_{elec}$ for VF > 20%
- $f_{L1} > 3f_{elec}$ for VF < 20%

Square, cylindrical and triangular pillars were compared and for volume fractions of less than 40%, the triangular pillars possessed the highest MPAR. The analysis was performed on a high loss polymer but the results did not correlate with those obtained by experiment as mechanical loss was not included in the model. The parameters for the components of backing block and matching layer were considered. It was found that the damping within the backing block affected its specific acoustic impedance.

The addition of the backing block increased the dilation quality and bandwidth but decreased the sensitivity of the device. The matching layer had minimal effect on the surface dilation quality but the transmit sensitivity was determined by the damping of the matching material. Problems were encountered with the implementation of the fluid loading as the finite element package, ANSYS, did not have the correct form of boundary elements. Several methods were investigated to implement such elements and it was concluded that there were no optimal solutions. However, an approximation of absorbing boundaries on all open boundaries was used to determine the influence of the fluid loading on the dilation quality of the composite. The dilation quality was decreased for less damp fillers and increased for the more damp fillers. However, anomalies were produced by the in-water analysis such as a reduction in receive sensitivity.

A hydrostatic finite element model was developed and compared with experimental data. It was then used to compare different ceramics and filler material to obtain a high hydrostatic figure of merit (HFOM). From the selection list of ceramics, it was found that PZT-5H produced the best HFOM at low volume fractions but above 25% VF, the modified lead titanate, EC-97, was the best. The desirable properties for the filler are high compliance and low compressibility. These are normally opposing conditions for viscoelastic materials but the compressibility is more important. The performance of the hydrophones can be further enhanced by the addition of stiffening plates. Chapter 5 included a study of the effect of electrical loading on the measurement of transducer values. Formulae for accounting for the decrease in performance were developed so that the finite element results could be modified to improve correlation with experiment.

From simulations of array elements, it was found that the effect of the limited size of the electrode was to enhance the coupling of the lateral modes leading to a significant reduction of dilation quality at lower volume fractions. The effect was reduced for higher volume fractions indicating their application. The number of pillars under the electrode did not influence the dilation quality but the sensitivity did

increase with increasing number of pillars. As with the single transducer simulations, the dilation quality decreased with increasing aspect ratio indicating the maximum pillar aspect ratio concept was also applicable for array design. The simulation results demonstrated that no significant gain in performance was achieved by increasing the element size above 4x4 pillars. However, smaller elements did not perform as well and 4x4 pillar configuration was chosen as the preferred size of an element. Analysis of the beamwidth and cross-coupling voltage showed that the optimal aspect ratio for a piezocomposite for array applications is the maximum pillar aspect ratio. The addition of the ancillary components had negligible effect on the beamwidth. While the size of the element had minimal influence on the cross-coupling voltage, the addition of the backing block was found to significantly increase it.

In summary, the mission objective for the work as stated in section 1.1 has been achieved and the work was completed successfully. The system has been used to generate the results for several academic papers as can be seen by the list of references from this work. While the author realises that the finite element system is not complete and will never be, it is in a state that can be used for many different applications and this is emphasized by the following section.

7.3 SUGGESTIONS FOR FUTURE WORK

There are several areas connected with the work presented in this thesis that would complement the work. It was decided that they were not crucial to the objective of the thesis. None of the suggestions would require major development of the finite element system.

7.3.1 Characterisation of Materials

There cannot be a close correlation between the response of the finite element model and that of an experimental transducer unless the properties of the materials in the experimental transducer have been fully characterised. The properties of the

piezoceramics can vary as much as 10% from the manufacturer's data and are frequency dependent. Being viscoelastic, the polymers have properties that are also frequency dependent. These include the damping co-efficients.

7.3.2 Three-Dimensional Beam Profiles

An algorithm for the calculation of two-dimensional beam profiles from two-dimensional finite element models was derived and presented in section 6.2.1. The work can be extended to generate three-dimensional beam profiles from complete three-dimensional models. However, the mathematical complexity and the difficulty in displaying and interpreting the results meant that this was not included in the work done for the thesis. As all the array elements considered in Chapter 6 were symmetrical about the *1* and *2* axes, the beam profiles would be symmetrical and could be derived from the two-dimensional beam profiles.

7.3.3 Effect of Ancillary Components on Cross-Coupling Between Array Elements

It was shown in Chapter 6 that energy is coupled in the material through the ancillary components and most importantly, through the backing block. While the properties of the fluid cannot be modified, the loss and speed of sound in the other two components can be adjusted within limits while their specific acoustic impedance remains constant.

It is suggested that an investigation into the influence of the adjustable properties of these components on the cross-coupling and its phasing between array elements be performed. The modelling should include all the cross-coupling mechanisms in an attempt to produce destructive interference between the energy travelling along the different channels.

7.3.4 Modelling of 1-3 piezocomposites Operating into Solids

All the modelling of 1-3 piezocomposites in this thesis has been operating into low impedance media such as water and air. There exist many applications for high frequency transducer arrays operating into solids such as the monitoring of structures described in the reference [67]. The present solution involves using monolithic ceramic arrays which have the disadvantage of strong cross-coupling. It is foreseen that high volume fraction piezocomposites can be used effectively in such situations but with low cross-coupling between elements. This has been demonstrated practically by the work of Powell [53] for a 90% VF 4.0 AR PZT-5A/softset composite acting as the transmitter into an aluminium pipe.

It is suggested that an investigation similar to that performed in Chapter 4 be repeated but with the surrounding fluid replaced by a solid material such as aluminium. The concept of maximum pillar aspect ratio for operation into solids is not as important because the lateral modes could not be strongly coupled at the boundary between the piezocomposite and the solid material. The use of stiffening plates has been shown to enhance the performance into solids as they allow the composite material to act as a homogenous medium and not as ceramic pillars in a soft filler. An investigation similar to that performed in Chapter 5 to determine the desired properties of the stiffening plates is required.

REFERENCES

1. ANSYS Inc., "Ansys Users Manual for Revision 5.0 Vol I-IV", DN-R300:50, 1992, P.O.Box 65, Johnston Road, Houston, PA 15342-0065, USA.
2. H.Kutruff, "Ultrasonics Fundamentals and Applications", ISBN 1-85166-553-6, Elsevier Science Publishers, 1991.
3. W. Smith, "New Opportunities in Ultrasonic Transducers Emerging from Innovations in Piezoelectric Materials" *1992 SPIE International Symposium in New Developments in Ultrasonic Transducers and Transducer Systems*, San Diego, CA, USA, 21-22 July 1992, pp 3 - 26
4. H.A.Smith, "A Student Introduction to Engineering Design" Pergamon Unified Engineering Series, Pergamon Press Inc. 1975 ISBN 0-08-017103-6
5. H.Allik and T.J.R.Hughes, "Finite Element Modelling for Piezoelectric Vibration", *Int. Journal of Numerical Methods of Engineering*, Vol 2, 1970, pp 151-157
6. R.Lerch, "Simulations of Piezoelectric Devices by Two- and Three-Dimensional Elements", *IEEE Transactions on Ultrasonics, Ferroelectric and Frequency Control*, Vol 37, No. 3, 1990, pp 233-247
7. A-C Hladky-Hennion and J-N Decarpigny, "Finite Element Modelling of Active Periodic Structures: Application to 1-3 Piezocomposites", *Journal of the Acoustic Society of America* Vol 94, No 2, 1993, pp 621-635
8. D.Vaughan and E.Richardson, "FLEX User's Manual" 1-H.4, Nov. 10 1994, Weidlinger Associates, 4410 El Camino Real, Suite 110, Los Altos, CA 94022
9. D.A.Berlincourt, D.R.Curran and H.Jaffe, "Piezoelectric and Piezomagnetic Materials and Their Function in Transducers", pp 169-270 in *Physical Acoustics, Volume 1A*, edited by W.P.Mason, Academic Press, New York, NY, USA, 1966

10. J.Hyslop, J.Bennett and G.Hayward, "An Investigation into the Design of High frequency Two-Dimensional Arrays", *Proc. IEEE Ultrasonic Symposium*, Cannes, France 1994, pp 1515-1518

11. T.Takahashi, "Lead Titanate Ceramics with Large Piezoelectric Anisotropy and their Applications", *Ceramics Bulletin*, Vol. 69, No. 4, 1990, pp 691-695

12. E.Fukada and T.Furukawa, "Piezoelectricity and Ferroelectricity in Polyvinylidene Fluoride", *Ultrasonics*, Jan 1981, pp 31-39

13. R.Newnham, D.Skinner and L.Cross, "Connectivity and Piezoelectric-Pyroelectric Composites", *Material Results Bulletin*, Vol 13, No 5, 1970, pp 525-536

14. D.W.Van Krevelen, "Properties of Polymers: Their Estimation and Correlation with Chemical Structure", 2nd Edition, Elsevier Scientific Publishing Company, Amsterdam, ISBN 0-444-41467-3, 1976

15. R.Capps, "Elastomeric Materials for Acoustical Applications", Naval Research Laboratory, Washington, DC 20375-5000, September 15, 1989

16. G.Hayward, "Time and Frequency Modelling of the Piezoelectric Transducer", *Ph.D. Thesis*, University of Strathclyde, Glasgow, Scotland, UK, 1981

17. M.Redwood, "Transient Performance of a Piezoelectric Transducer", *Journal of the Acoustical Society of America*, Vol 33, No 4, 1961, pp 527-536

18. M.Brissaud, "Characterisation of Piezoceramics", *IEEE Transactions on Ultrasonics, Ferroelectrics and Frequency Control*, Vol 38, No. 6, 1991, pp 603-617

19. G.S.Kino, "Acoustic Waves: Devices, Imaging and Analog Signal Processing", Prentice-Hall Inc., New Jersey, 1987, ISBN 0-13-003-47-3 025

20. Editor P.D.Edmonds, "Methods of Experimental Physics: Vol 19 Ultrasonics", Academic Press, New York, USA, 1981, ISBN 0-12-475961-0

21. Institute of Electrical and Electronic Engineering Standard on Piezoelectricity, Std 176-1978, 345 East 47 Street, New York, NY 10017, USA

22. R. Krimholtz, D.Leedom and G.Matthaei, "Equivalent circuits for Transducers having Arbitrary Even-or-Odd Symmetry Piezoelectric Excitation", *IEEE Transactions on Sonics and Ultrasonics*, Vol SU-18, 1971, pp 128-141

23. C.S.DeSilets, J.Fraser and G.S.Kino, "The Design of Efficient Broad-band Piezoelectric Transducers", *IEEE Transactions of Sonics and Ultrasonics* Vol SU-25, No. 3, 1978, pp 115-125

24. L.Augustine and J.Andersen, "An Algorithm for the Design of Transformless Broadband Equalizers of Ultrasonic Transducers", *Journal of the Acoustical Society of America*, Vol 66, No 3, 1979, pp 629-635

25. M.Jackson, "Simulation and Control of Thickness-Mode Piezoelectric Transducers", *Ph.D Thesis*, University of Strathclyde, Glasgow, Scotland, UK, 1984

26. O.Zienkiewicz, "The Finite Element Method", McGraw-Hill, London, England, 1971 CSN: 07 094138 6

27. O.C.Zienkiewicz and R.L.Taylor, "The Finite Element Method Volume 2: Solid and Fluid Mechanics: Dynamics and Non-linearity", 4th Edition, McGraw-Hill Book Company, London, 1991, ISBN 0-07-084175-6

28. C.Rajakumar, A.Ali and S.M.Yunus, "A New Acoustic Interface Element for Fluid-Structure Interaction Problems", *International Journal for Numerical Methods in Engineering*, Vol 33, No 2, 1992, pp 369-386

29. Private Correspondence with C.Rajakumar, Swanson Analysis Systems Incorporated, Houston, PA 15342-0065, USA

30. A.Jennings and J.J. McKeown, "Matrix Computation", 2nd Edition, John Wiley and Sons Inc., England, 1992, ISBN 0-471-93598-0

31. R.J.Bobber, "Underwater Electroacoustic Measurements", U.S. Government Printing Office, Washington, DC, 1970

32. G.Kossoff, "The Effects of Backing and Matching on the Performance of Piezoelectric Ceramic Transducer", *IEEE Transactions on Sonics and Ultrasonics*, Vol 13, No 1, 1966, pp 20-30

33. L.L.Beranek, "Acoustics", 1st British Edition, McGraw-Hill, New York, 1954

34. J.Hossack, "Modelling Techniques for 1-3 Composite Transducers", *Ph.D. Thesis*, University of Strathclyde, Glasgow, Scotland, UK, March 1990

35. G.Hayward and J.Hossack, "Finite Element Analysis of 1-3 Composite Piezoelectric Transducers", *IEEE Transactions on Ultrasonic, Ferroelectrics and Frequency Control*, Vol 38, No 6, 1991, pp 618-629

36. G.Hayward and J.A.Hossack, "Unidimensional Modelling of 1-3 Composite Transducers", *Journal of the Acoustic Society of America*, Vol 88, No 2, 1990, pp 599-608

37. D.Ostergraad and T.Pawlak, "Three Dimensional Finite Element Elements for Analysing Piezoelectric Structures", *Proc. IEEE Ultrasonics Symposium*, Williamsburg, VA, USA, November 1986, pp 639-644

38. A.Gachagan, J.Bennett and G.Hayward, "A Finite Element Modelling Approach into the Influence of Mechanical Matching and Damping in 1-3 Piezocomposites", *Proc. IEEE Ultrasonic Symposium*, Cannes, France, 1994, pp 995-998

39. T.R.Gururaja, W.A.Schulze, L.E.Cross, R.E.Newnham, "Piezoelectric Composite Material for Ultrasonic Transducer Applications. Part II: Evaluation of Ultrasonic Medical Applications", *IEEE Transactions of Sonics and Ultrasonics*, Vol SU-32, 1985, pp 499-513

40. K.Ingard, "Fundamentals of Waves and Oscillations", Cambridge University Press, 1988, ISBN 0-521-32734-2

41. D.Hall, "The Modelling and Design of Two-Dimensional Composite Matrix Arrays for Underwater Imaging Applications", *Ph.D. Thesis*, University of Strathclyde, October 1994

42. A.Selfridge, "Approximate Material Properties in Isotropic Material", *IEEE Transactions on Sonics and Ultrasonics*, Vol SU-32, No. 3, 1985, pp 381-394

43. W.Smith and B.A.Auld, "Modelling 1-3 Composite Piezoelectrics: Thickness-Mode Oscillations", *IEEE Transactions on Ultrasonics, Ferroelectrics and Frequency Control*, Vol UFFC-38, 1991, pp 40-47

44. C.Oakley, "Analysis and Development of Piezoelectric Composites for Medical Ultrasound Transducer Applications", *Ph.D. Thesis*, The Pennsylvania State University, PA, USA May 1991

45. G.Hayward, J.Bennett and R.Hamilton, "A Theoretical Study on the Influence of Some Constituent Material Properties on the Behaviour of 1-3 Connectivity Composite Transducers", Accepted for publication to *Journal of the Acoustic Society of America*

46. T.R.Gururaja, W.A.Schulze, L.E.Cross, R.E.Newnham, B.A.Auld and Y.J.Wang, "Piezoelectric Composite Material for Ultrasonic Transducer Applications. Part I: Resonant Modes of Vibration of PZT Rod-Polymer Composites", *IEEE Transactions of Sonics and Ultrasonics*, Vol SU-32, 1985, pp 481-498

47. R.J.Guyan, "Reduction of Stiffness and Mass Matrix", *American Institute of Aeronautics and Astronautics Journal*, Vol 3, No 2, February 1965, pp 380

48. B.Auld and Y.Wang, "Acoustic Wave Vibrations in Periodic Composite Plates", *Proc. IEEE Ultrasonics Symposium*, Dallas, TX, USA, November 1984, pp 528-532

49. W.Smith, A.Shaulov and B.Auld, "Tailoring the Properties of Composite Piezoelectric Materials for Medical Ultrasonic Transducers", *Proc. IEEE Ultrasonics Symposium*, Chicago, IL, USA, October 1988, pp 617-622

50. F.Craciun, L.Sorba, E.Molinari and M.Pappalardo, "A Coupled-Mode Theory for Periodic Piezoelectric Composites", *IEEE Transactions on Ultrasonics, Ferroelectrics and Frequency Control*, Vol 36, No. 1, 1989, pp 50-55

51. H.P.Savakus, K.A.Klicker and R.E.Newnham, "PZT-Epoxy Piezoelectric Transducers: A Simplified Fabrication Procedure", *Material Research Bulletin*, Vol 16, 1981, pp 677-680

52. L.J.Bowen, "Fabrication of Piezoelectric Ceramic Polymer Composites by Injection Moulding", *Proc. IEEE Symposium on Applications of Ferroelectrics*, 1992, CH 155, pp 160-163

53. D.J.Powell, "Flexible Ultrasonic Transducer Arrays", *Ph.D. Thesis*, University of Strathclyde, March 1994

54. R.Y.Ting, A.A.Shaulov and W.A.Smith, "Evaluation of Properties of 1-3 Piezocomposites of a New Lead Titanate in Epoxy Resins", *Ferroelectrics*, Vol 132, 1992, pp 69-77

55. C.Richard, "Étude Expérimentale et Théorique de Composites Piézoélectriques de Connectivité 1.3.1 pour Hydrophone", *Ph.D. Thesis*, Devant L'Institut National des Sciences Appliquées de Lyon, 16 June 1992

56. W.A.Smith, "Modelling 1-3 Composite Piezoelectrics: Hydrostatic Response" *IEEE Transactions on Ultrasonics, Ferroelectrics and Frequency Control*, Vol 40, No. 1, 1993, pp 41-48

57. M.Haun and R.Newnham, "Experimental and Theoretical Study of 1-3 and 1-3-0 Piezoelectric PZT-Polymer Composites for Hydrophone Applications", *Ferroelectrics*, Vol 68, 1986, pp 123-139

58. W.A.Smith and R.Y.Ting, Private communications concerning the hydrostatic measurement of 1-3 piezocomposites

59. C.Richard, P.Eyraud, L.Eyraud, M.Richard and G.Grange, "1-3-1 PZT-Polymer Composites for High Pressure Hydrophone Application", *Ferroelectrics*, Vol. 134, 1992, pp 59-64

60. D.D.N.Hall, J.T.Bennett and G.Hayward, "The Design and Evaluation of Ultrasonic Arrays using 1-3 Connectivity Composites", *SPIE International Symposium Proceedings*, San Diego, CA, USA, 1992, Vol 1733, Ch 29, pp 216-227

61. G.S.Kino and C.S.DeSilets, "Design of Slotted Transducer Arrays with Matched Backings", *Ultrasonic Imaging*, Vol 1, 1979, pp 189-209

62. G.Wojcik and D.Vaughan, Discussions concerning the application and usefulness of the PZ-Flex package, Los Altos, CA, USA, 14-22 November 1994

63. A.Selfridge, "The Design and Fabrication of Ultrasonic Transducers and Transducer Arrays", *Ph.D. Thesis*, Stanford University, Stanford, CA, USA, July 1982

64. K.Nagai, "Synthetic Aperture Ultrasonic Imagery", *Advances in Electronics and Electron Physics*, Vol 70, pp 215-313, Academic Press, 1988

65. J.Achenbach, "Wave Propagation in Elastic Solids", North Holland, 1973, CSN: 0371268X

66. J.E.Hyslop, "A Theoretical Study of Transducer Material Performance in Monolithic Piezoelectric Arrays for Underwater Imaging Applications", *M.Phil Thesis*, University of Strathclyde, Nov 1994

67. K.Kirk, A.McNab and G.Hayward, "Monolithic Arrays for Monitoring Industrial Plant at High Temperatures", *Proc. IEEE Ultrasonic Symposium*, Cannes, France 1994, pp 1125-1128

68. *ANSYS News*, Third Issue, 1994, Swanson Analysis System Inc - This is a regular magazine supplied to users of the ANSYS package

69. R.Holland, "Representation of Dielectric, Elastic and Piezoelectric Losses by Complex Coefficient", *IEEE Transactions on Sonics and Ultrasonics*, Vol SU-14, 1967, pp 18-20

APPENDIX A
PROGRAMS FOR FINITE ELEMENT ANALYSIS

A.1 INTRODUCTION

This appendix describes the software library of routines used for extracting the results from the finite element modelling. Programs which use the library to analyse the results and extract the important parameters, have also been included. The programs are written in ANSI C V2.0 rather than the language generally used for mathematical processing, Fortran 77, because of the ability to define the size of the arrays at run-time and advanced programming structures. The language is also normally delivered as part of the operating software for a modern workstation so the programs presented in this appendix can be used on any workstations that run the ANSYS package. The system used in this case was a SUN Sparc 10/51 running Solaris 1.1 (SunOS 4.1.3) with the GNU C compiler *gcc 2.6.3*. ANSYS is available for a myriad of different computing systems varying from supercomputers such as Crays and Convex, through workstations such as Silicon Graphics to PCs running Windows NT [68].

Swanson Associates System Incorporated, the developers of the ANSYS finite element code, included the source for a set of simple FORTRAN 77 routines for reading and writing files in their proprietary format. These routines were ported from Fortran to the C language and modified to allow multiple file access. A immediate layer of library routines were also developed to aid in the extraction of any necessary information from the results file that the programmer would require. This kept the actual program code short and did not require the programmer to know the structure of the ANSYS file format.

Three separate programs are discussed in this appendix: one for the static analysis, one for the modal analysis and one for the harmonic analysis. There are variants on each to handle specific cases that differed. The complete theory for the extraction

process is detailed in Chapter 5 for the static analysis program and Chapter 3 for the other two programs. The finite element model for array transducers was designed in such a way that the standard harmonic analysis program could be used with minor modifications. This was achieved by storing a line of information with each results file, which described the type of analysis and the necessary information for the post-processing. All the examples used to illustrate the output of the programs were of the 25% volume fraction, 0.1 aspect ratio, 1.0 mm high, PZT-5A/hardset 1-3 piezocomposite used as the example for the investigation in Chapter 4.

A.2 DESCRIPTION OF SOFTWARE

A.2.1 Library Routines

All the programs use a set of library routines for reading the results file produced by the analysis phase of the finite element method. Included with this library is a C header file that contains the definitions of the structures used for reading the information. They were:

Name	Description
CMPLX	This allows complex double numbers required for harmonic analysis to be used with ANSI C.
F_INFO	This contains the file information for an open result file. It also includes the buffer used to speed the reading and writing of the array data between the computer core memory and the disk.
SDATA	This contains the extracted information from the harmonic analysis of a single frequency step.
STORE	This contains the co-ordinates of the nodes so that the area and volume of the elements can be calculated.

The routines included in this library are:

a) *initans* reads the result file and returns the header data of the file

Parameter	Description
F_INFO *initans(	The routine returns the file information structure so that the file can be passed to other software routines.
char [],	The filename of the results file to be read - it is an input parameter.
int [],	A buffer array used for reading large records from the results file.
char [],	The title of the analysis which normally contains a short description of the parameters used in the analysis. If the title is of a standard form, these parameters can be extracted and be displayed by the program.
char *,	A character defined in the pre-processing module to specify the type of analysis. This is used to confirm that the right post-processing program is being used to analyse the data.
int *,	A flag indicating whether the analysis was done with scalar or complex values which is needed for the allocation of the data arrays.
int *,	The number of datasets that are contained in the results file This indicates the number of loops required to read the complete file.
int *,	The number of nodes in the analysis which indicates the size of the data arrays.
STORE *,	The co-ordinate of the nodes in the finite model.
double *,	The surface area of the transducer at the plane specified in the pre-processing phase.

double *,	The distance between the two electrodes of the transducer which is required for calculation of the electric field in the active material and is the parameter t_3.
double *)	The specific acoustic impedance of the surrounding medium which is specified at the pre-processing phase.

b) *rdsolu* reads a specified dataset from a result file

Parameter	Description
int rdsolu(	Returns -1 if an error occurs during the reading of the record.
F_INFO *,	The file information structure containing the information on the results file from which the dataset must be read.
int,	The index number of the dataset to be read.
int *,	The temporary buffer for reading in the dataset before it is analysed to extract the required information.
float *,	The exact frequency or time for the dataset depending on the analysis type.
float [],	The displacements at each node - these are UX, UY and UZ and if the analysis is complex, another set of components are also included.
CMPLX *,	The average UZ displacement at the surface plane which is taken as the average displacement of the surface.
CMPLX *,	The potential difference between the two electrodes of the transducer.
CMPLX *)	The charge produced at the active electrode.

c) *SetAngle* converts an angle in radians into an angle in degrees between -180° and 180°

Parameter	Description
double SetAngle(	Returns the value in degrees.
double)	The angle in radians.

d) *TotalPress* calculates the total pressure generated by the transducer model at the surface plane

Parameter	Description
double TotalPress()	Returns the root-mean-square pressure across the surface.

Other routines have been included in the library to aid the extracting of certain information required for the generation of the surface displacement profiles. These are: a routine to sort the nodes into a rectangular grid; and a routine to extract the frequencies of all the datasets.

A.2.2 Programs for Post-Processing

Three programs are covered in the appendix:

a) *static* for the post-processing for hydrostatic transducers

Input
(Optional)
- Result filename
- Output filename

Example Output:

```
0.25 0.10   60.7   17.59    1067.6   389.6
```

Columns in the output

i) Volume fraction.

ii) Aspect ratio.

iii) Piezoelectric strain constant for the model definition.

iv) Piezoelectric voltage constant for the model definition.

v) Figure of merit for the model definition.

vi) Relative permittivity for the model definition.

Algorithm

1) Open the results file using *initans*.
2) Check that the analysis was scalar and static.
3) Extract the value of the volume fraction and aspect ratio from the title.
4) Read the first dataset using *rdsolu* which is the analysis with open-circuit electrodes to estimate the voltage constant.
5) Calculate the piezoelectric voltage constant according to:

$$g = \frac{volt}{height} \times 10^3 \ millivolt\ per\ metre.pascal \qquad \textbf{Eqn. A.1}$$

6) Read the second dataset using *rdsolu* which is the analysis with short-circuit electrodes to estimate the strain constant.
7) Calculate the piezoelectric strain constant according to:

$$d = \frac{charge}{surface\ area} \times 10^{12} \ picometre\ per\ volt \qquad \textbf{Eqn. A.2}$$

8) Display the results according to Example Output.
9) If an output filename is specified as a command-line parameter, append the results to the file.

b) *modal* for post-processing of the modal analysis of the transducer

Input • Result filename

(Optional) • Quality dilation limit

Example Output:

```
Processing Square VF 25 AR 0.1 MC 1 MP 1

Electrical Resonances
 Mode      Freq(MHz) Quality
   1 :     1.388 =>   0.963
   2 :     4.999 =>   0.603
   3 :     5.199 =>   0.282
   4 :     6.325 =>   0.091

Mechanical Resonances
 Mode      Freq(MHz) Quality
   1 :     1.712 =>   0.953
   2 :     5.041 =>   0.515
   3 :     5.238 =>   0.232
   4 :     6.400 =>   0.074

**** Kt = 0.624 ****
```

Columns in the Output

i) Number of mode generated.

ii) Frequency in megahertz of the mode.

iii) Dilation quality of the mode.

Algorithm

1) If no dilation quality limit was specified on the command line, then set the limit to 0.0.

2) Open the results file for the short-circuit electrode case using *initans*.

3) Check that the analysis was scalar and modal.

4) Display the title of the analysis and the label for electrical resonances.

5) For each dataset from 1 to the number of datasets:

   a) Read the dataset using *rdsolu*.

   b) Determine the maximum UZ displacement of all the nodes on the surface plane.

   c) Divide the average displacement by the maximum displacement to calculate the surface dilation quality.

   d) If the dilation quality exceeds or equals the specified limit, display the number, frequency and quality of the mode as shown in the Example Output.

6) Open the results file for the open-circuit electrode case using *initans*.

7) Check that the analysis was scalar and modal.

8) Display the message concerning mechanical resonances.

9) Repeat step 5.

10) Select the thickness modes from the electrical resonances and mechanical resonances by selecting the modes with the largest dilation qualities. From the two frequencies, the thickness mode coupling co-efficient (k_t) is calculated as follows:

$$k_t^2 = \frac{\pi f_{elec}}{2 f_{mech}} cotan\left(\frac{\pi f_{elec}}{2 f_{mech}}\right) \qquad \textbf{Eqn. A.3}$$

10) Display the value of the coupling co-efficient.

c) *harmonic* for post-processing of the transducer's behaviour with or without the electrical loading element

Input • Result filename

Example Output:

Columns in the output

i) Frequency

ii) Magnitude of the impedance in decibels relative to 1 $\Omega.mm^2$

iii) Phase angle of the impedance in degrees from -180° to 180°

iv) Surface dilation quality

v) Magnitude of the average displacement in nanometres at the surface plane per unit volt that exists between the electrodes

vi) Angle of the average displacement at the surface plane in degrees from -180° to 180°

vii) Reciprocity parameter of the transducer in decibels relative to 1.0

viii) Transmit sensitivity (S_{TX}) in decibels relative to 1 $\mu Pa.V^{-1}$

```
# Impedance analysis produced by ANSYS 5.1
# Processing Square VF 25 AR 0.1 MC 1 MP 1
# Complete sensitivity and efficiency measurement
# Maximum Impedance =  120.83
# Minimum Insertion Loss =  154.91
# Maximum TX Sensitivity =  143.01
# Maximum RX Sensitivity = -160.84
 1.000   107.30   -84.8 0.898 2.23e-01   170.2   154.91   127.61 -177.69 1.08e-01
 1.040   106.57   -83.8 0.903 2.43e-01   168.9   155.26   128.69 -177.34 1.37e-01
 1.080   105.78   -82.7 0.908 2.68e-01   167.3   155.65   129.87 -176.95 1.79e-01
 1.120   104.90   -81.1 0.913 3.00e-01   165.2   156.07   131.16 -176.53 2.42e-01
 1.160   103.93   -78.9 0.919 3.42e-01   162.5   156.52   132.59 -176.08 3.38e-01
 1.200   102.82   -75.9 0.925 3.98e-01   158.7   157.02   134.21 -175.58 4.89e-01
 1.240   101.52   -71.3 0.931 4.77e-01   153.4   157.57   136.05 -175.03 7.39e-01
 1.280   100.02   -64.0 0.937 5.89e-01   145.2   158.18   138.17 -174.42 1.19e+00
 1.320    98.37   -51.8 0.944 7.47e-01   131.9   158.86   140.49 -173.74 2.22e+00
 1.360    97.10   -31.4 0.951 9.16e-01   110.3   159.62   142.52 -172.98 4.77e+00
 1.400    97.46    -4.3 0.958 9.42e-01    81.6   160.47   143.01 -172.13 5.69e+00
 1.440    99.87    18.6 0.966 7.77e-01    56.8   161.45   141.58 -171.15 3.36e+00
 1.480   103.09    31.9 0.974 5.93e-01    40.8   162.57   139.48 -170.03 2.29e+00
 1.520   106.39    38.1 0.982 4.59e-01    31.1   163.88   137.49 -168.72 1.72e+00
 1.560   109.66    39.2 0.991 3.67e-01    24.9   165.42   135.76 -167.18 1.32e+00
 1.600   112.94    35.8 0.994 3.02e-01    20.7   167.23   134.29 -165.37 1.05e+00
 1.640   116.26    26.6 0.986 2.55e-01    17.6   169.29   133.02 -163.31 8.52e-01
 1.680   119.27     8.7 0.977 2.19e-01    15.3   171.19   131.91 -161.41 7.13e-01
 1.720   120.83   -17.6 0.969 1.91e-01    13.5   171.76   130.93 -160.84 6.11e-01
 1.760   120.27   -42.3 0.960 1.68e-01    12.1   170.33   130.05 -162.27 5.34e-01
 1.800   118.77   -58.3 0.952 1.50e-01    10.9   168.03   129.26 -164.57 4.75e-01
 1.840   117.24   -67.7 0.943 1.35e-01     9.9   165.78   128.54 -166.82 4.28e-01
 1.880   115.93   -73.4 0.934 1.22e-01     9.0   163.80   127.87 -168.80 3.90e-01
 1.920   114.83   -77.1 0.925 1.12e-01     8.3   162.08   127.25 -170.52 3.59e-01
 1.960   113.90   -79.7 0.916 1.02e-01     7.6   160.58   126.68 -172.02 3.34e-01
 2.000   113.11   -81.5 0.906 9.42e-02     7.0   159.25   126.15 -173.35 3.12e-01
```

ix) Receive sensitivity (S_{RX}) in decibels relative to 1 V.(μPa)$^{-1}$

Algorithm

1) Open the results file specified in the command line using *initans*.

2) Check that the analysis was harmonic.

3) Check that if the analysis was complex, the number of datasets is divisible by two as there would be two datasets, real and imaginery, for each frequency.

4) Open the output file which is to contain the extracted data and print the title.

5) For each dataset from 1 to number of frequency steps

   a) If the analysis was complex, read both dataset using *rdsolu* into the CMPLX variables,

      Else read one dataset using *rdsolu* into the real part of the CMPLX variables and set the imaginery parts to zero.

   b) Read the pressure output at the surface with *TotalPress*.

   c) Calculate the voltage magnitude and angle from the complex voltage.

   d) Calculate the charge magnitude from the complex charge.

e) Calculate the magnitude of the average displacement relative to the voltage magnitude.

f) Convert the charge magnitude into current magnitude using the following equation:

$$i_{mag} = q_{mag} \times \frac{2\pi freq}{surface\ area} \qquad \textbf{Eqn. A.4}$$

g) Divide the voltage magnitude by the current magnitude and convert to decibels to obtain the impedance magnitude. This is relative to 1 Ω.mm but the value can be modified to account for the surface area of the physical transducer being simulated.

h) Determine the maximum UZ displacement at the surface plane.

i) Subtract the angle of the input voltage from the angle of the average displacement to generate the true phase angle for the average displacement relative to the applied voltage.

j) Divide the average displacement magnitude by the maximum displacement to generate the surface dilation quality.

k) Calculate the reciprocity parameter, J, as:

$$J = \frac{surface\ area}{load\ medium\ impedance \times conductance} \qquad \textbf{Eqn. A.5}$$

l) Calculate the transmit sensitivity as the magnitude of the pressure divided by the magnitude of the voltage and convert into decibels relative to $1\mu Pa.V^{-1}$.

m) Calculate the power transfer ratio by squaring the transmit sensitivity and multiplying by the reciprocity parameter.

n) Calculate the receive sensitivity by multiplying the transmit sensitivity by the reciprocity parameter and converting the calculated value to decibels relative to $1V.\mu Pa^{-1}$.

6) Display results to the output file as shown in the Example Output.

APPENDIX B

MATERIAL PARAMETERS USED FOR THE THESIS

B.1 CALCULATION OF MATERIAL PARAMETERS

Two different sets of materials are detailed in this appendix:

- **Piezoceramics** - the equations for the piezoelectric relationships for the piezoceramics are defined in the IEEE Standard on Piezoelectric Measurement [21]. Most of the material constants were obtained from the standard reference [9]. However, the author would like to acknowledge the assistance of Ian Sidney and Dave Cannell of Morgan Matroc in supplying the data for the lead metaniobate (PmN) and Bob Ting and Tom Howarth from USRD, NRL, Orlando, FL, USA for supplying the data on the modified lead titanate, EC-97. The values are detailed in Table B.1. Any number within brackets have not been measured but have been estimated by the author.

- **Isotropic Materials** - all other materials encountered in this thesis were isotropic and hence, could be defined with fewer material co-efficients. The data was obtained either experimentally as denoted by * or were extracted from the reference [42]. The values are detailed in Table B.2.

TABLE B.1: PIEZOCERAMIC MATERIAL PARAMETERS								
Material	$BaTiO_3$	PZT-4	PZT-5A	PZT-5H	PZT-7A	PZT-8	$PbNb_2O_6$	EC-97
Compliance, s_{ij}^E, and stiffness, c_{ij}^E, under constant electric field								
s_{11}^E (10^{-12}Pa^{-1})	8.6	12.3	16.4	16.4	10.7	11.5	17.4	7.4
s_{12}^E (10^{-12}Pa^{-1})	-2.6	-4.1	-5.7	-4.8	-3.2	-3.4	-4.5	-1.5
s_{13}^E (10^{-12}Pa^{-1})	-2.7	-5.3	-7.2	-8.5	-4.6	-4.7	-5.8	-1.5
s_{33}^E (10^{-12}Pa^{-1})	9.1	15.5	18.8	20.8	13.9	13.5	14.4	8.6
s_{44}^E (10^{-12}Pa^{-1})	22.2	39.0	47.5	43.5	39.5	31.9	35.6	18.1
s_{66}^E (10^{-12}Pa^{-1})	22.4	32.7	44.3	42.6	29.7	27.8	40.6	17.7
c_{11}^E (10^{10}Pa)	15.8	13.9	12.0	12.7	14.8	13.7	8.4	15.0
c_{12}^E (10^{10}Pa)	6.9	7.8	7.5	8.0	7.6	6.9	3.8	3.7
c_{13}^E (10^{10}Pa)	6.8	7.4	7.5	8.5	7.4	7.2	4.9	3.2
c_{33}^E (10^{10}Pa)	15.0	11.6	11.1	11.7	12.1	12.4	10.9	12.7
c_{44}^E (10^{10}Pa)	4.5	2.6	2.1	2.3	2.5	3.1	2.8	5.5
c_{66}^E (10^{10}Pa)	4.5	3.1	2.3	2.4	3.4	3.6	2.5	5.7
Piezoelectric Coefficients, d_{ij}, e_{ij}								
d_{31} (10^{-12}C.N^{-1})	-58	-123	-171	-274	-60	-97	-10	-21
d_{33} (10^{-12}C.N^{-1})	149	289	374	593	153	225	85	91
d_{15} (10^{-12}C.N^{-1})	242	495	584	741	360	330	(90)	(95)
e_{13} (C.m^{-1})	-3.1	-5.2	-5.4	-6.5	-2.1	-4.0	3.0	-1.1
e_{33} (C.m^{-1})	14.5	15.1	15.8	23.3 **	9.5	13.8	8.4	10.2
e_{15} (C.m^{-1})	10.9	12.7	12.3	17.0	9.2	10.4	(2.5)	(5.3)
Dielectric Constants, ε_{ii} (under constant stress denoted, T, and constant strain, S)								
$\varepsilon_{11}^T/\varepsilon_o$	1300	1475	1730	3123	840	1291	(320)	(283)
$\varepsilon_{33}^T/\varepsilon_o$	1200	1300	1700	3400	425	1000	320	283
$\varepsilon_{11}^S/\varepsilon_o$	1000	730	916	1700	460	898	(265)	(200)
$\varepsilon_{33}^S/\varepsilon_o$	910	635	830	1470	235	582	265	200
Loss coefficients (electrical, tanδ, and mechanical, Q_m) and Density (ρ)								
tanδ	0.01	0.00	0.020	0.02	0.02	0.00	0.01	0.00
Q_m	400	500	75	65	600	1000	15	922
ρ	5550	7500	7750	7500	7700	7600	5900	6900

TABLE B.2: ISOTROPIC MATERIAL PARAMETERS							
Material	CY1301/ HY1300*	CY208/ HY956*	Poly-urethane	Mix 1	Mix 2	Alum-inium	Titanium Carbide
Compliance, s_{ij}, and stiffness, c_{ij}, coefficients							
s_{11} ($10^{-10}Pa^{-1}$)	2.50	5.56	6.67	0.67	5.00	0.15	0.03
s_{12} ($10^{-10}Pa^{-1}$)	-0.88	-2.22	-3.13	-0.20	-0.50	-0.05	-0.01
s_{44} ($10^{-10}Pa^{-1}$)	6.75	15.56	19.6	1.75	11.0	0.40	0.07
c_{11} ($10^{9}Pa$)	6.42	3.83	9.01	20.06	2.05	111.3	352.2
c_{12} ($10^{9}Pa$)	3.46	2.55	7.99	8.60	0.23	61.3	77.8
c_{44} ($10^{9}Pa$)	1.48	0.64	0.51	5.73	0.91	25.0	137.2
Youngs Modulus, Y, Poisson Ratio, σ, Bulk and Shear Wave Velocity, v_l and v_s							
Y ($10^{9}Pa$)	4.0	1.8	1.5	14.9	2.0	67.8	324.0
σ	0.35	0.40	0.47	0.3	0.1	0.355	0.181
v_l($m.s^{-1}$)	2370	1820	2820	3210	2020	6420	8270
v_s($m.s^{-1}$)	1140	750	670	1710	1350	3040	5160
Dielectric Constant, ε_{11}							
$\varepsilon_{11}/\varepsilon_o$	4.0	4.0	4.0	4.0	4.0	-	-
Density (ρ)							
ρ	1140	1150	1130	1950	500	2700	5150

* Material properties derived experimentally

Key for mixed, loaded polymer fillers:

MIX 1: A 75% Glass particles (average diameter 50-100μm), 25% CY1301/HY1300 mixture.

MIX 2: A 60% Glass microballoons (average diameter 70μm), 40% CY1301/HY1300 mixture.

n.b. Percentages are given with respect to weight.

B.1.1 Piezoelectric Material Parameters

The material constants that are normally measured for the piezoceramics are:

- Compliance under constant electric field matrix ($[s^E]$) which is uniquely defined by six values: s_{11}^E, s_{12}^E, s_{13}^E, s_{33}^E, s_{44}^E and s_{66}^E. The form of the matrix is:

$$[s^E] = \begin{pmatrix} s_{11}^E & s_{12}^E & s_{13}^E & 0 & 0 & 0 \\ s_{12}^E & s_{11}^E & s_{13}^E & 0 & 0 & 0 \\ s_{13}^E & s_{13}^E & s_{33}^E & 0 & 0 & 0 \\ 0 & 0 & 0 & s_{44}^E & 0 & 0 \\ 0 & 0 & 0 & 0 & s_{44}^E & 0 \\ 0 & 0 & 0 & 0 & 0 & s_{66}^E \end{pmatrix} \qquad \textbf{Eqn. B.1}$$

- Piezoelectric strain matrix ([d]) which is uniquely defined by three values: d_{31}, d_{33} and d_{15}. The form of the matrix is:

$$[d] = \begin{pmatrix} 0 & 0 & 0 & 0 & d_{15} & 0 \\ 0 & 0 & 0 & d_{15} & 0 & 0 \\ d_{31} & d_{31} & d_{33} & 0 & 0 & 0 \end{pmatrix} \qquad \textbf{Eqn. B.2}$$

- Permittivity under constant stress matrix ($[\varepsilon^T]$) which is uniquely defined by two values: ε_{11}^T and ε_{33}^T. The form of the matrix is:

$$[\varepsilon^T] = \begin{pmatrix} \varepsilon_{11}^T & 0 & 0 \\ 0 & \varepsilon_{11}^T & 0 \\ 0 & 0 & \varepsilon_{33}^T \end{pmatrix} \qquad \textbf{Eqn. B.3}$$

From these matrices, the remaining material properties can be derived as follows:

- For the stiffness under constant electric field matrix ($[c^E]$) :

$$[c^E] = [s^E]^{-1} \qquad \text{Eqn. B.4}$$

- For the piezoelectric stress matrix ([e]) :

$$[e] = [c^E][d]^t \qquad \text{Eqn. B.5}$$

- For the piezoelectric voltage matrix ([g]) :

$$[g] = [\varepsilon^T]^{-1}[d] \qquad \text{Eqn. B.6}$$

- For the compliance under constant electric density matrix ([s^D]) :

$$[s^D] = [s^E] - [d][g] \qquad \text{Eqn. B.7}$$

- For the piezoelectric current matrix ([h]) :

$$[h] = [g][s^D]^{-1} \qquad \text{Eqn. B.8}$$

- For the permittivity matrix under constant strain matrix ([ε^S]) :

$$[\varepsilon^S] = [\varepsilon^T] - [d][e] \qquad \text{Eqn. B.9}$$

where the superscript t is for matrix transpose; and
the superscript -1 is for inverse matrix.

B.1.2 Mechanical Material Parameters

The mechanical material properties are normally defined as: Young's modulus (Y) for strength; Poisson ratio (σ) for compressibility; and density (ρ). The compliance matrix ([s]) is generated as:

$$\begin{aligned} s_{11} &= \frac{1}{Y} \\ s_{12} &= -\frac{\sigma}{Y} \\ s_{44} &= 2(s_{11} - s_{12}) \end{aligned} \qquad \text{Eqn. B.10}$$

As the materials are assumed to be isotropic, the compliance matrix is given by:

$$[s] = \begin{pmatrix} s_{11} & s_{12} & s_{12} & 0 & 0 & 0 \\ s_{12} & s_{11} & s_{12} & 0 & 0 & 0 \\ s_{12} & s_{12} & s_{11} & 0 & 0 & 0 \\ 0 & 0 & 0 & s_{44} & 0 & 0 \\ 0 & 0 & 0 & 0 & s_{44} & 0 \\ 0 & 0 & 0 & 0 & 0 & s_{44} \end{pmatrix}$$

Eqn. B.11

The stiffness matrix ([c]) is then the inverse of this matrix. One element of this matrix that is of interest, is c_{44} which is the shear modulus G for the material and allows the shear wave speed to be calculated.

The two wave speeds are calculated as:

$$v_l = \sqrt{\frac{c_{11}}{\rho}}$$

$$v_s = \sqrt{\frac{c_{44}}{\rho}}$$

Eqn. B.12

where v_l is the bulk wave speed; and

v_s is the shear wave speed.

APPENDIX C : DERIVATION OF PIEZOELECTRIC DISPLACEMENT EQUATION

The displacement with frequency, ω, can be derived from a modified form of the piezoelectric equations as shown by Hladky-Hennion [7]. As the electrodes are assumed to be parallel and extend into infinity, there can be no variation or movement in the *1* or *2* direction. This implies that $D_3(\omega)$ does not vary with space through the piezoelectric plate and the only non-zero strain component is $S_3(\omega)$. Hence, these two parameters are chosen as the best choice for independent variables in the piezoelectric equation:

$$\begin{aligned} T_3(\omega) &= c_{33}^D S_3(\omega) - h_{33} D_3(\omega) \\ E_3(\omega) &= -h_{33} S_3(\omega) + \beta_{33}^S D_3(\omega) \end{aligned} \qquad \textbf{Eqn. C.1}$$

where c_{33}^D is the stiffness modulus between strain and stress under conditions of constant charge density;

h_{33} is a piezoelectric constant relating the stress and the charge density; and

β_{33}^S is the dielectric impermeability under conditions of constant strain.

As the forcing functions involved with the displacement are harmonic, the displacement in the *3* direction, $u(x_3,\omega)$, must also be harmonic:

$$u(x_3,\omega) = \left(Ae^{j\frac{\omega}{v}x_3} + Be^{-j\frac{\omega}{v}x_3}\right)e^{j\omega t} \qquad \textbf{Eqn. C.2}$$

where A and B are the amplitude components of the forward and backward wave generated in the plate respectively; and

v is the wave speed.

The displacement must be related to a zero position which, for the derivation, is taken as the axis of symmetry through the centre of the plate i.e. $u(0,\omega) = 0$. Substituting this assumption back into Equation (C.2), it can be seen that B = -A giving:

$$u(x_3,\omega) = A\left(e^{j\frac{\omega}{v}x_3} - e^{-j\frac{\omega}{v}x_3}\right)e^{j\omega t}$$
$$= 2jA\sin\left(\frac{\omega}{v}x_3\right)e^{j\omega t} \qquad \textbf{Eqn. C.3}$$

and hence:

$$S_3(\omega) = \frac{\partial u(x_3,\omega)}{\partial x_3}$$
$$\therefore \int_0^{t_3/2} S_3(\omega)dx_3 = u(t_3/2,\omega) \qquad \textbf{Eqn. C.4}$$
$$= 2jA\sin\left[\frac{\omega t_3}{2v}\right]e^{j\omega t}$$

where t_3 is the height of the piezoelectric plate.

For simplification, the parameter, ω', is introduced as:

$$\omega' = \frac{\omega t_3}{2v} = \frac{\pi}{2}\frac{\omega}{\omega_{mech}} \qquad \textbf{Eqn. C.5}$$

where ω_{mech} is the fundamental mechanical radial frequency.

This simplification is similar to that performed for the β value in Mason's electrical model as discussed in Section 2.2. The voltage across the electrodes, V(ω), can be calculated using Equation (C.1):

$$V(\omega) = 2\int_0^{t_3/2} E_3(x_3,\omega)dx_3$$
$$= -4jAh_{33}\sin[\omega']e^{j\omega t} + \beta_{33}^S t_3 D_3(\omega)\Big|_{x_3=\frac{t_3}{2}} \qquad \textbf{Eqn. C.6}$$

The first part of Equation (C.1) can then be re-arranged as:

$$D_3(\omega)\Big|_{x_3=\frac{t_3}{2}} = \frac{1}{h_{33}}\left(c_{33}^D S_3(\omega) - T_3(\omega)\right)\Big|_{x_3=\frac{t_3}{2}} \qquad \textbf{Eqn. C.7}$$

but:

$$T_3(\omega) = Z_{fluid}\frac{\partial u(x_3,\omega)}{\partial t} \qquad \textbf{Eqn. C.8}$$

where Z_{fluid} is the specific acoustic impedance of the load medium at the surface of the device.

Hence, the final expression for $D_3(\omega)$ is:

$$D_3(\omega)\Big|_{x_3=\frac{t_3}{2}} = \frac{j4A}{h_{33}t_3}\left(c_{33}^D\omega'\cos[\omega'] + jZ_{fluid}\nu\omega'\sin[\omega']\right)e^{j\omega t} \qquad \textbf{Eqn. C.9}$$

Thus the magnitude of the displacement at the surface of the device relative to the voltage is:

$$\frac{u(t_3/2,\omega)}{V(\omega)} = \frac{h_{33}/4}{\left(\beta_{33}^S c_{33}^D\omega' cotan[\omega'] - h_{33}^2\right) + jZ_{fluid}\nu\omega'} \qquad \textbf{Eqn. C.10}$$

At the mechanical resonance, the normalised frequency, ω', becomes π/2 and Equation (C.10) can be simplified to:

$$\left|\frac{u(t_3/2,\omega_{mech})}{V(\omega_{mech})}\right| = \frac{h_{33}}{2\sqrt{4h_{33}^4 + \pi^2 Z_{fluid}^2\nu^2}} \qquad \textbf{Eqn. C.11}$$

For in-air analysis where Z_{fluid} is a relatively small number, the expression can be further simplified to:

$$\frac{u(t_3/2,\omega_{mech})}{V(\omega_{mech})} = \frac{1}{4h_{33}} \qquad \textbf{Eqn. C.12}$$

The relative phase between the movement at the surface and the voltage across the electrodes is 0°. The maximum displacement would occur when the denominator of

Equation C.10 is minimal. Considering the expression, this would be when the real part of the denominator is zero giving a relative phase of 90°. Equating the two expressions of the real part in Equation C.10 gives:

$$h_{33}^2 = \beta_{33}^S c_{33}^D \omega' cotan(\omega')$$

$$\therefore \quad \omega' cotan(\omega') = \frac{h_{33}^2}{\beta_{33}^S c_{33}^D} = k_t^2 \qquad \textbf{Eqn. C.13}$$

It can be seen that the solution of Equation (C.13) is the radial frequency of the electrical resonance from the definition of the coupling factor in Equation A.3. The final expression for the displacement at the electrical resonance is:

$$\left| \frac{u(t_3/2, \omega_{elec})}{V(\omega_{elec})} \right| = \frac{h_{33}}{2Z_{fluid}\omega_{elec}t_3} \qquad \textbf{Eqn. C.14}$$

The verification example of Section 3.4.1 uses a 1 mm thick plate of PZT-5A. The derived material constants for PZT-5A are:

- $h_{33} = 2.16 \times 10^9$ V.m^{-1}
- $\beta_{33}^S = 1.3607 \times 10^8$
- $c_{33}^D = 1.45 \times 10^{11}$ N.m^{-2}
- $v = 4323$ m.s^{-1}
- $k_t = 0.486$

For a height of 1 mm, the plate would have:

- $f_{mech} = 2.162$ MHz
- $f_{elec} = 1.932$ MHz

and the displacement with frequency for operation into a water medium (Z_{fluid} = 1.5 MRayl) is shown in Figure C.1.

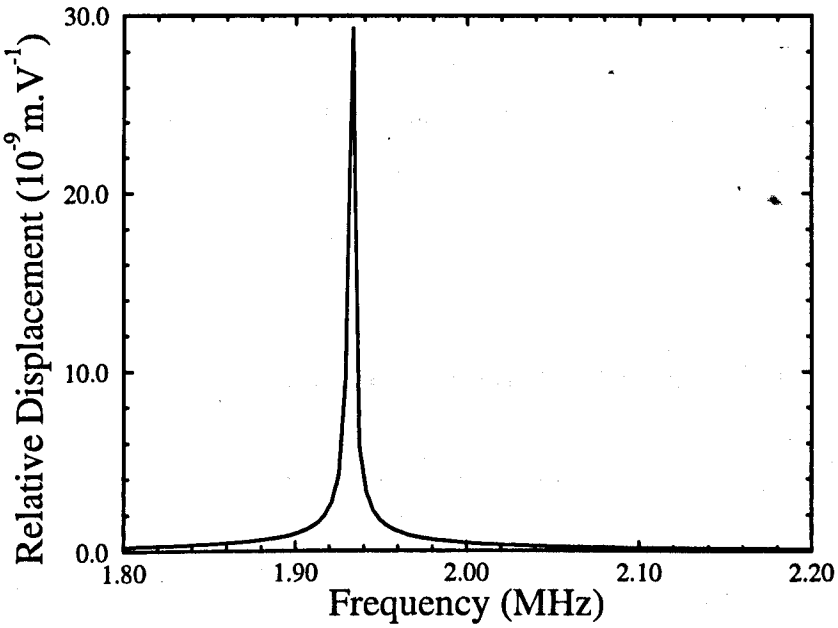

Figure C.1: Lossless Displacement of Surface in a Water Medium

For the hydrostatic response discussed in Chapter 5, the frequency of operation is far below the thickness mode frequencies so that ω' tends to zero. Considering the frequency dependent parts of Equation (C.10) in the limit to zero:

$$\lim_{\omega' \to 0} \omega' cotan(\omega') = 1$$

$$\lim_{\omega' \to 0} Z_{fluid} \nu \omega' = 0 \qquad \textbf{Eqn. C.15}$$

giving a final equation of:

$$\frac{u(t_3/2,0)}{V(0)} = \frac{h_{33}}{2\left(\beta_{33}^S c_{33}^D - h_{33}^2\right)} \qquad \textbf{Eqn. C.16}$$

For the PZT-5A example, the displacement is 0.036 nm.V^{-1} for the frequency range below resonance.

It can be seen that the value derived from Equation (C.16) is independent of the acoustic impedance of fluid so that for the hydrostatic analysis of Chapter 5, the influence of fluid loading can be ignored in the finite element model.

This analysis is incomplete in that losses are not included in Equation (C.10). However, in Holland [69], it was shown that there are three loss mechanisms associated with piezoelectric activity:

- Dielectric loss in the electrical domain represented by $\hat{\beta}_{33}^{S} = \beta_{33}^{S} + j\beta_{33}^{S''}$;
- Piezoelectric loss between the two domains represented by $\hat{h}_{33} = h_{33} + jh_{33}''$; and
- Mechanical loss in the mechanical domain represented by $\hat{c}_{33}^{D} = c_{33}^{D} + jc_{33}^{D''}$.

The finite element package, ANSYS, can only model the mechanical losses but this tends to be dominant for piezocomposites with the lossy viscoelastic matrix. This allows a modified version of Equation (C.10) to be derived:

$$\left|\frac{u(t_3/2,\omega)}{V(\omega)}\right| = \left|\frac{h_{33}/2}{\left(\beta_{33}^{S}c_{33}^{D}\omega' cotan[\omega'] - h_{33}^{2}\right) + j\left(Z_{fluid}\nu\omega' + \beta_{33}^{S}c_{33}^{D''}\omega' cotan[\omega']\right)}\right| \quad \textbf{Eqn. C.17}$$

For PZT-5A, the mechanical Q is 75 from Table B.1 which gives:

- $c_{33}^{D''} = 1.93\text{x}10^{9}\text{Pa}$
- Damping co-efficient for ANSYS = $1.1\text{x}10^{-9}$

The damping co-efficient is similar to that derived from experiment. Equation C.17 has been graphed in Figure C.2 and compared to the finite element analysis results

for the PZT-5A plate. Reasonable correlation is shown between the two theoretical approaches. The difference in frequencies between the two peaks is caused both the small inaccuracy of the finite element modelling approach and the simplified form of the loss equation in C.17.

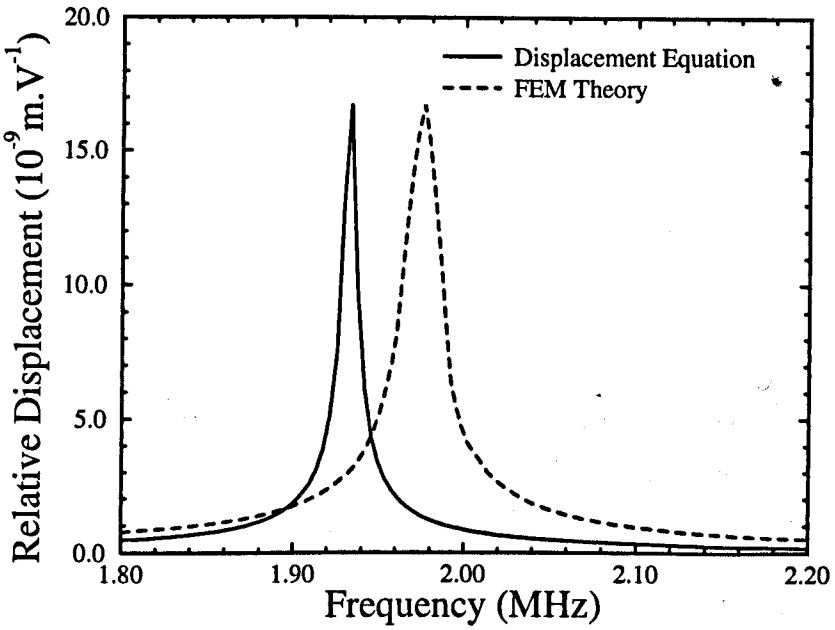

Figure C.2: Comparison of Surface Displacement for PZT-5A Plate

In conclusion, Equation (C.10) is the surface displacement with frequency for a plate of piezoelectric material with no lateral modes and no losses included. From this equation, the position of the mechanical and electrical resonances can be determined along with the surface displacement of the plate. Actual values were calculated for a PZT-5A plate that was 1 mm thick. It was also shown that the surface displacement at frequencies below the fundamental resonance is independent of the fluid loading which simplifies the modelling in Chapter 5.